Nonlinear coupling and dissipation in two-dimensional resonators

Keşkekler, A.

DOI
10.4233/uuid:d4bbe182-8021-4562-a56a-bcb7652032ef

Publication date
2023

Document Version
Final published version

Citation (APA)
Keşkekler, A. (2023). *Nonlinear coupling and dissipation in two-dimensional resonators*. [Dissertation (TU Delft), Delft University of Technology]. https://doi.org/10.4233/uuid:d4bbe182-8021-4562-a56a-bcb7652032ef

NONLINEAR COUPLING AND DISSIPATION IN TWO-DIMENSIONAL RESONATORS

NONLINEAR COUPLING AND DISSIPATION IN TWO-DIMENSIONAL RESONATORS

Dissertation

for the purpose of obtaining the degree of doctor
at Delft University of Technology,
by the authority of the Rector Magnificus Prof. dr. ir. T. H. J. J. van der Hagen,
chair of the Board of Doctorates,
to be defended publicly on Wednesday 29 November 2023 at 17:30 o'clock

by

Ata KEŞKEKLER

Master of Science in Mechanical Engineering,
Delft University of Technology, The Netherlands,
born in Istanbul, Türkiye.

This dissertation has been approved by the promotors

Prof. dr. P. G. Steeneken,	promotor
Dr. F. Alijani,	promotor

Composition of the doctoral committee:

Rector Magnificus,	chairperson
Prof. dr. P. G. Steeneken,	Delft University of Technology
Dr. F. Alijani,	Delft University of Technology
Independent members:	
Prof. M. Dykman,	Michigan State University, USA
Prof. dr. E. Scheer,	University of Konstanz, Germany
Prof. dr. Y. M. Blanter,	Delft University of Technology
Dr. S. Hanay,	Bilkent University, Türkiye
Dr. G. J. Verbiest,	Delft University of Technology
Prof. dr. ir. M. Langelaar,	Delft University of Technology, reserve member

Keywords: nanomechanics, nonlinear dynamics, graphene, two-dimensional materials, internal resonance, mode coupling, nonlinear damping, frequency combs, nonlinear reduced-order modelling, NEMS, laser interferometry, magnetic phase transition.

Printed by: ProefschriftMaken, The Netherlands.

Front: A composition made from the phase space trajectories of a dynamical system exhibiting quasi-periodic oscillations during an internal resonance, by A. Keşkekler.

Back: Ripples on a graphene membrane. Generated with Midjourney by A. Keşkekler.

ISBN 978-94-6366-781-4

An electronic version of this dissertation is available at
http://repository.tudelft.nl/.

To my beloved family, Derya, Deniz and Atilla.

CONTENTS

SUMMARY

MICRO and nanomechanical resonators are essential to the state-of-the-art communication, data processing, timekeeping, and sensing systems. The discovery of graphene and other two-dimensional (2D) materials has been a profound source of inspiration for the next generation of these devices, owing to their exceptional mechanical, electrical, and thermal properties. However, alongside their advantages, the atomically thin nature of these resonators also presents its own unique challenges, as the dynamic response of these resonators rapidly becomes nonlinear, where nonlinear coupling and dissipation processes manifest. To unleash the full potential of these resonators, a comprehensive understanding of the emerging nonlinear phenomena is crucial. In this pursuit, this thesis studies nonlinear dissipation pathways in 2D material resonators that arise from the coupling of their internal mechanical modes to each other as well as to their microscopic physics. The thesis consists of six chapters.

Chapter 1 serves as an introduction to the realm of micro/nanomechanical and 2D material resonators, providing the reader with the fundamental mathematical groundwork and forming the motivation for investigating their nonlinear dynamics and dissipation.

Chapter 2 investigates the effects of intermodal coupling on nonlinear dissipation, by studying the nonlinear dynamic response of an optothermally excited graphene nanodrum resonator. Here, experiments reveal a significant increase in the nonlinear dissipation rate at the vicinity of a parametric-direct internal resonance. The observations are explained by a coupled nonlinear two degrees-of-freedom model of the resonator with good agreement, demonstrating a clear relationship between the observed nonlinear dissipation and parameters such as drive frequency, coupling strength, and Q factor of the coupled mode.

To understand the intermodal couplings of these resonators in a more general framework, in Chapter 3, a multi-modal reduced-order modeling procedure is introduced. This approach, relying only on physically measurable quantities and utilizing finite element simulations, enables the understanding of the global dynamic response of nonlinear nanoresonators. To validate the model, the simulations of the reduced-order model are compared to experimental data from a graphene nanoresonator, resulting in a good qualitative description of the intricate nonlinear dynamics exhibited by the nanodrum, which is essential for describing the dissipation and intermodal energy pathways of the system.

Chapter 4 explores the generation of mechanical frequency combs from the nonlinear coupling of internal modes of a graphene nanodrum due to symmetry-breaking forces. By applying electrostatic forces to disrupt the out-of-plane symmetry of a graphene resonator and tuning its resonance frequencies, a one-to-two internal resonance is activated. It is found that at high drive levels, at the center of this internal resonance, quasi-periodic oscillations emerge, leading to the generation of mechanical frequency combs.

To explain the observations, a continuum mechanics model of the deflected nanodrum is constructed, offering insight into the origin of the frequency comb through simulations and revealing that it is a consequence of the Neimark bifurcation of periodic solutions.

In Chapter 5, the focus shifts to the nonlinear coupling between mechanics and microscopic physics in a 2D material resonator. The nonlinear dynamics of $FePS_3$-based heterostructure membranes undergoing a magnetic phase transition at the Néel temperature are investigated. Significant changes in the nonlinear stiffness and damping parameters are observed during the transition. An analytical model that accounts for magneto-mechanical coupling is utilized to explain these observations. The results emphasize the influence of the material's magnetic order on linear and nonlinear dynamics of the resonator, showcasing the potential for utilizing the resonator's nonlinear dynamic responses as probes for condensed-matter physics.

And finally, in Chapter 6, the conclusions and key findings of the thesis are presented. Additionally, an outlook is provided on future directions and the next steps for research in the field of nonlinear dynamics of micro/nano and 2D material resonators.

SAMENVATTING

Micro- en nanomechanische resonatoren zijn essentieel voor de nieuwste vormen van communicatie, gegevensverwerking, tijdwaarneming en detectie. De ontdekking van grafeen en andere tweedimensionale (2D) materialen is een rijke bron van inspiratie geweest voor de volgende generatie van zulke systemen. De materialen onderscheiden zich vanwege hun uitzonderlijke mechanische, elektrische en thermische eigenschappen. Naast voordelen brengt de atomair dunne aard van deze resonatoren echter ook zijn unieke uitdagingen met zich mee. De dynamische respons van deze resonatoren wordt snel niet-lineair, waardoor niet-lineaire koppeling en dissipatieve processen zich manifesteren. Om het volledige potentieel van deze resonatoren te benutten, is diepgaand inzicht in de voortkomende niet-lineaire verschijnselen cruciaal. In dit streven bestudeert dit proefschrift niet-lineaire dissipatieroutes in 2D-materiaalresonatoren die voortkomen uit de koppeling van hun interne mechanische modi met elkaar en met hun microscopische fysica. Dit proefschrift bestaat uit zes hoofdstukken.

Hoofdstuk 1 dient als inleiding tot het rijk van micro/nanomechanische en 2D-materiële resonatoren, die de lezer voorziet van de fundamentele wiskundige grondslag en de motivatie vormt voor het onderzoek naar hun niet-lineaire dynamiek en dissipatie.

Hoofdstuk 2 onderzoekt de effecten van intermodale koppeling op niet-lineaire dissipatie, door het bestuderen van de niet-lineaire dynamische respons van een optothermisch aangedreven grafeen nanodrum resonator. Hier onthullen experimenten een significante toename van de niet-lineaire dissipatie in de buurt van een parametrisch-directe interne resonantie. De observaties worden met goede overeenstemming verklaard door een gekoppeld niet-lineair model van de resonator met twee vrijheidsgraden, waaruit een duidelijke relatie blijkt tussen de waargenomen niet-lineaire dissipatie en parameters zoals aandrijffrequentie, koppelingssterkte en Q-factor van de gekoppelde modus.

Om de intermodale koppelingen van deze resonatoren in een algemener kader te begrijpen wordt in hoofdstuk 3 een multimodale modelleringsprocedure van gereduceerde orde geïntroduceerd. Deze benadering, die alleen vertrouwt op fysiek meetbare grootheden en gebruik maakt van eindige elementen methodes, maakt het mogelijk om de globale dynamische respons van niet-lineaire nanoresonatoren te begrijpen. Om het model te valideren, worden de simulaties van het gereduceerde-orde model vergeleken met experimentele data van een grafeen nanoresonator, wat resulteert in een goede kwalitatieve beschrijving van de ingewikkelde niet-lineaire dynamica die de nanodrum vertoont. Dit is essentieel voor het beschrijven van de dissipatieve en intermodale energieoverdrachten van het systeem.

Hoofdstuk 4 onderzoekt hoe mechanische frequentiekammen voortkomen uit de niet-lineaire koppeling van interne modi van een grafeen nanodrum ten gevolge van symmetrie brekende krachten. Door elektrostatische krachten toe te passen om de perpendiculaire symmetrie van een grafeen resonator te verstoren en de resonantiefrequenties af te stemmen, werd een één-op-twee interne resonantie geactiveerd. Er blijken bij hoge aandrijfniveaus, in het midden van deze interne resonantie, quasi-periodieke oscillaties te ontstaan, wat leidt tot het genereren van mechanische frequentiekammen. Om de waarnemingen te verklaren, wordt een continuümmechanica model voor een gebogen nanodrum geconstrueerd, die inzicht biedt in de oorsprong van de frequentiekam door middel van simulaties, en onthult dat deze het gevolg is van een Neimark-bifurcatie van periodieke oplossingen.

In hoofdstuk 5 verschuift de focus naar de niet-lineaire koppeling tussen mechanica en microscopische fysica in een 2D-materiaalresonator. De niet-lineaire dynamica van FePS3-gebaseerde heterostructuurmembranen die een magnetische faseovergang ondergaat bij de Néel temperatuur wordt onderzocht. Significante veranderingen in de niet-lineaire stijfheid en demping worden waargenomen tijdens de overgang. Een analytisch model dat rekening houdt met magneto-mechanische koppeling wordt gebruikt om deze waarnemingen te verklaren. De resultaten onderstrepen de invloed van de magnetische orde van het materiaal op lineaire en niet-lineaire dynamica van de resonator, die het potentieel toont voor het gebruik van de niet-lineaire dynamiek van de resonator reacties als sonde voor de vaste stof fysica.

Tot slot worden in hoofdstuk 6 de conclusies en belangrijkste bevindingen van het proefschrift gepresenteerd. Daarnaast wordt er een vooruitblik gegeven op toekomstige richtingen en de volgende stappen voor onderzoek op het gebied van niet-lineaire dynamica van micro/nano- en 2D-materiaalresonatoren.

ÖZET

MİKRO ve nanomekanik rezonatörler iletişim, veri işleme, zaman ölçümü ve algılama sistemlerinin en ileri teknolojik gelişmelerinde temel bir rol oynamaktadır. Grafen ve diğer iki boyutlu (2B) malzemelerin keşfi, bu malzemelerin üstün mekanik, elektriksel ve termal özellikleri sebebiyle gelecek nesil cihazlar için derin bir ilham kaynağı olmuştur. Avantajlarının yanı sıra, 2B rezonatörlerin atomik derecede ince yapısı kendi benzersiz zorluklarını beraberinde getirmektedir. Bu cihazların dinamik tepkisi kolayca doğrusal olmayan bir hale gelmekte ve mekanik doğal modları arasında doğrusal olmayan bağlaşım ve sönümleme süreçleri ortaya çıkmaktadır. Bu cihazların tam potansiyelini açığa çıkarmak için, doğrusal olmayan bu fenomenlerin kapsamlı şekilde anlaşılması hayati öneme sahiptir. Bu amaçla, bu tez, 2B rezonatörlerin iç mekanik modlarının birbiriyle ve mikroskobik ölçekteki süreçlerle olan bağlaşımından kaynaklanan doğrusal olmayan sönümleme yollarını incelemektedir. Tez altı bölümden oluşmaktadır.

Birinci bölüm, mikro/nanomekanik ve 2B rezonatörlere giriş olarak hizmet ederek, okuyucuya doğrusal olmayan dinamikleri ve sönümlemeyi incelemek için gerekli matematiksel temeli sunmakta ve araştırmanın motivasyonunu açıklamaktadır.

İkinci bölüm, iç doğal modlar arası bağlaşımın doğrusal olmayan sönümleme üzerindeki etkilerini inceleyerek, optotermal olarak uyarılmış bir grafen nanodavul rezonatörünün doğrusal olmayan dinamik tepkisini incelemektedir. Burada deneyler, bir parametrik-direkt içsel rezonansın (internal resonance) yakınında, doğrusal olmayan sönümleme hızında önemli bir artışın olduğunu göstermektedir. Gözlemler, rezonatörün doğrusal olmayan bağlaşımlı, iki serbestlik dereceli bir modeli ile açıklanmış ve doğrusal olmayan sönümleme ile sürücü frekansı, bağlaşım gücü ve bağlaşan modun Q faktörü gibi parametreler arasındaki açık bir ilişkiyi göstermiştir.

Bu rezonatörlerin iç modları arasındaki bağlaşımları ve etkileşimleri daha genel bir çerçevede anlamak için, üçüncü bölümde bu rezonatörlerin çoklu modlu indirgenmiş derece modellemesi (reduced-order modelling) sunulmaktadır. Bu yaklaşım tamamen fiziksel olarak ölçülebilir niceliklere dayanmaktadır ve sonlu elemanlar simülasyonları kullanarak doğrusal olmayan nanorezonatörlerin dinamik tepkisinin bütünsel olarak anlaşılmasını amaçlamaktadır. Modelin doğrulanması için, indirgenmiş derece modelin simülasyonları bir grafen nanorezonatöründen elde edilen deneysel verilerle karşılaştırılmaktadır. Model, nanodavulun gösterdiği karmaşık doğrusal olmayan dinamiklerin nitel bir açıklamasını başarılı bir şekilde sunar ve bu, bu sistemlerdeki iç modlar arası enerji yollarının ve sönümlemenin kökenlerinin kapsamlı bir bakış açısından anlaşılması için esastır.

Dördüncü bölüm, bir grafen nanodavulunda doğal modların, simetri bozan kuvvetler sayesinde ortaya çıkan doğrusal olmayan bağlaşımından meydana gelen mekanik frekans tarağı oluşumunu incelemektedir. Bu bölümde, bir grafen rezonatörünün düzlem dışı simetrisini bozmak ve rezonans frekanslarını ayarlamak için elektrostatik kuvvetler uygulanmakta ve bu sayede iki doğal mod arası bir bire-iki içsel rezonans etkinleştiril-

mektedir. Yüksek sürücü seviyelerinde, bu içsel rezonansın merkezinde, kuazi-periyodik salınımların ortaya çıktığı ve mekanik frekans tarağı oluşturduğu gözlemlenmektedir. Gözlemleri açıklamak için, eğik nanodavulun sürekli ortamlar mekaniği modeli oluşturulmaktadır. Bu sayede, modelin simülasyonları aracılığıyla frekans tarağının kökeni anlaşılmış ve bunun periyodik salınımların Neimark çatallanmasının bir sonucu olduğu ortaya koyulmuştur.

Beşinci bölüm, 2B rezonatörlerde mekanik ve mikroskobik fizik arasındaki doğrusal olmayan bağlaşıma odaklanmaktadır. Néel sıcaklığında manyetik bir faz geçişine uğrayan $FePS_3$ tabanlı heteroyapı membranların doğrusal olmayan dinamikleri incelenmektedir. Geçiş sırasında doğrusal olmayan sertleşme ve sönümleme parametrelerinde önemli değişiklikler gözlenmektedir. Bu gözlemleri açıklamak için, manyeto-mekanik bağlaşımı hesaba katan analitik bir model oluşturulmuştur. Sonuçlar, malzemenin manyetik düzeninin, rezonatörün doğrusal ve doğrusal olmayan dinamiği üzerindeki etkisini açığa çıkartmakta ve rezonatörün doğrusal olmayan dinamik tepkisinin yoğun madde fiziği araştırmaları için potansiyel bir araç olduğunu sergilemektedir.

Son olarak, altıncı bölümde tezin çıkarımları ve anahtar bulguları sunulmaktadır. Ayrıca, mikro/nano ve 2B rezonatörlerin doğrusal olmayan dinamikleri alanında gelecek yönelimler ve araştırma adımlarına dair bakış açıları ele alınmaktadır.

1

INTRODUCTION

WHETHER it is to study the motion of celestial bodies, growth of a cell or a chemical reaction, predicting the future states of a dynamical system is essential to many scientific disciplines. From the perspective of mechanics, this state is defined by the displacement of an object and its time derivatives. In his foundational works on classical mechanics, given their initial condition and forces acting on them, Newton demonstrated that it is possible to relate an object's current state to its future states. On a deeper level, this meant that, it might be possible to claim (as Laplace did [1]), at a certain moment in time, having complete knowledge of the forces in nature, together with the position and velocity of every single particle in the universe, in principle, one would have all the ingredients, not only to know all the future states of the universe, but also all the past. Consequences of this claim went beyond the boundaries of science and even raised philosophical questions regarding the existence of free will. The problems with this exciting but ambitious statement became apparent in many works later on, but even at the conceptual level, the idea is still inspiring.

However, in the practical sense, even in a scenario where all of the fundamental forces could be described in simple mathematical forms, a student of dynamics will quickly realize that it is still non-trivial how the resulting motion will be determined, specially when nonlinear forces and multiple interacting objects are involved. It is almost ironic that even the simplest looking dynamics problems in nature, such as three particles interacting via gravity, the famous three-body problem, has no general analytical closed form solution. Nevertheless, with the development of theory of dynamical systems, pioneered by Henri Poincaré and later further advanced by many others, numerous methods have been established in order to gather valuable information about a system's dynamics, without having to exactly solve them [2]. Benefits of these methods expand beyond mechanics, and were used to virtually study any dynamical system that could be expressed with differential equations, let it be the prey-predator population dynamics, electrical circuits or the weather forecasting.

If we set aside slightly complicated (!) problems like solving the equation of motion for the universe, for certain conditions, many dynamical systems in nature locally show well defined periodic responses with a characteristic frequency. It is even possible to find many instances where there is an emerging symmetry in this periodicity between interacting systems, where we can talk about a dynamical order, in spite of what the second law of thermodynamics dictates in the long run [3]. In fact, this dynamical order is the reason I am able to write these words, thanks to the thousands of pacemaker cells that are periodically firing in synchrony to keep my heart beating.

The mathematical framework for analyzing such periodic responses has been thoroughly developed, not only to understand how nature operates, but also to take advantage of these principles in technology. Great examples are the oscillators that we use, whether these are old pendulum clocks on the wall of our grandparents' house, RLC circuits in radio receivers, quartz crystals in our computers or micro and nanoelectromechanical oscillators.

1.1. MICRO/NANOELECTROMECHANICAL OSCILLATORS

Micro and Nanoelectromechanical oscillators are essential for cutting-edge technological applications like modern communication, data processing, and time-keeping systems[4], [5]. They are micro/nanoscale structures that are used for reliable generation of stable and periodic electromechanical signals from kHz up to GHz frequencies, to synchronize operations and track time. Because of their high stability and longevity, they are frequently preferred to their purely electrical analogues. These devices have been pushed down to sub-nanometer scale as a result of recent advancements in manufacturing processes, which have reduced their volume and energy requirements while increasing their output frequency. All oscillators mainly consist of two core components, a resonator and an amplifier. The resonator, is the heart of the oscillator, which in Micro/Nanoelectromechanical systems (MEMS/NEMS), is a mechanical structure that can vibrate efficiently at its resonance frequency. An amplifier provides the drive for the resonator, in a feedback loop, to drive the resonator at its resonance where it generates a high amplitude, stable electromechanical signal. In this thesis, we will focus on the thinnest mechanical resonators ever made.

1.1.1. GRAPHENE RESONATORS

The discovery of the two-dimensional (2D) material graphene by Novoselov and Geim in 2004 [6] (which later earned them the Nobel Prize in Physics 2010 "for groundbreaking experiments regarding the two-dimensional material graphene") opened up a number of promising research directions in physics [7] and, for that matter, nanomechanics. Graphene is a single layer of carbon atoms organized in a hexagonal lattice and was first realized by exfoliating layers (conveniently, with a commercial adhesive tape) from natural graphite, as these layers are held by weak van der Waals forces. Along with having outstanding electrical and thermal characteristics, it also possesses a record level of mechanical strength in the plane of the lattice, being the strongest material ever measured with theoretical Young's modulus of 1 TPa, where it has shown to endure stresses up to 60 GPa experimentally [8]. Furthermore, due to being atomically thin (0.335 nm between its layers) it is extremely light and sensitive in the out-of-plane direction. Naturally, it became one of the top contenders for the upcoming nanomechanical devices. In fact, numerous studies have already shown the capabilities of graphene-based NEMS sensors, including the ability to detect mass, pressure, acceleration, light and even the movement of a single bacterium [9]–[18]. After the discovery of graphene, it was quickly realized that it is possible to make free-standing graphene structures by transferring a graphene layer on top of a cavity, that is often etched into a SiO_2 layer on top of a Si substrate. Almost all of the graphene-based NEMS devices are based on these free-standing graphene structures, including the graphene resonator [19].

These nanoscale resonators typically have resonances at the MHz frequencies. Contrary to what one might initially expect from such a pure resonator made out of a single layer of carbon atoms, experiments at room temperature have shown that they have high dissipation rates [20] compared to state of the art micro and nanomechanical resonators that are designed for sensitivity [21]. There are many studies trying to pinpoint the origins of dissipation in these resonators, but because of the unique mechanical, thermal, and electrical properties of graphene, the problem is non-trivial. Moreover, these resonators exhibit nonlinear dynamic response already at pN force levels due to their extreme out-of-plane force sensitivity, resulting in a very small linear operation range [22]. Yet for the same reason, they also provide an unrivaled framework for the experimental study of fundamental nonlinear dynamics problems, which is virtually impossible with other types of mechanical systems. Thus it is clear that, in order to use these resonators to their full potential, their response in the nonlinear regime should be well understood. However, before diving deep into their nonlinear response, let us first establish the foundations of the basic linear mechanical resonators.

1.1.2. FUNDAMENTALS OF A MECHANICAL RESONATOR

In its most basic form, a mechanical resonator can be approximated by a spring-mass system, where a mass, m, is attached to the linear spring with resulting restoring force $F_s = -k_1 x$. From Newton's second law, the fundamental equation of motion for this mechanical resonator is:

$$m\ddot{x}(t) + k_1 x(t) = 0 \tag{1.1}$$

The well known general solution to this differential equation is $x(t) = a_1 \cos(\omega_0 t) + a_2 \sin(\omega_0 t)$, where $\omega_0 = \sqrt{k_1/m}$ is the resonance frequency of the resonator and a_1 and a_2 are coefficients depending on the initial conditions $x(0) = x_0$ and $\dot{x}(0) = v_0$. In this form, the equations are conservative, where no energy goes in or out of the system. However, in reality, energy is being lost to the environment continuously. Typically to model this energy being loss, a linear damping force $F_d = -c\dot{x}$ is considered. A more intuitive way of describing this dissipative term is by introducing the dimensionless quality factor (Q), where the damping coefficient c can be expressed as $c = \frac{m\omega_0}{Q}$. The Q-factor can be effectively interpreted as the number of oscillation cycles a system must go through before losing most of its energy to the environment for a freely oscillating, non-driven resonator. Therefore it is a useful quantity when comparing the energy efficiency of different resonators. When the resonator is excited with a periodic force in order to sustain the motion of the resonator at a desired frequency (which is generally the resonance frequency ω_0 for maximum efficiency and signal amplitude) $F_1 = F\cos(\omega_d t)$, where F is the drive amplitude and ω_d is the drive frequency, we obtain the famous linear harmonic oscillator model, which reads as:

$$m\ddot{x} + k_1 x + \frac{m\omega_0}{Q}\dot{x} = F\cos(\omega_d t). \tag{1.2}$$

The steady-state amplitude $\bar{X}$ for the linear harmonic oscillator model can be found by assuming a motion in the form of $x = \bar{X}\cos(\omega_d t + \theta)$, where θ is a phase shift.

In the end, the steady-state amplitude $\bar{X}$ can be written as:

$$\bar{X} = \frac{F/m}{\sqrt{(\omega_0^2 - \omega_d^2)^2 + (\omega_0\omega_d/Q)^2}} \tag{1.3}$$

where the phase θ is:

$$\theta = \arctan\left(\frac{\omega_0\omega_d}{Q(\omega_d^2 - \omega_0^2)}\right) \tag{1.4}$$

Here, two important observations that can be made, which will be important for the following sections. Firstly, as the name suggests, the steady-state amplitude of the linear harmonic oscillator indeed scales linearly with the force F that is applied. Secondly, the phase of the oscillations, θ, is dependent on neither the driving force F nor the oscillation amplitude $\bar{X}$.

These two equations lay the basic principles to understand oscillators that are being employed in current day technologies, yet, not surprisingly, it is only an approximation of the governing physics that is only valid when they are operated at small amplitudes where nonlinearities aren't influencing the dynamic response. This approximation is often valid in practice, as most of the resonators cannot reach these amplitudes, either because they are too strongly damped or undergo structural failure before the onset of nonlinear response. However, recent advances in lithography techniques and material science have enabled the manufacturing of micro/nano-structures with enormous aspect ratios and record yield strengths. Naturally, these structures can safely reach relative (with respect to their characteristic length) oscillation amplitudes orders of magnitude greater than their predecessors, resulting in a dynamic response which can not be explained anymore by the well established linear harmonic oscillator model. Although nanomechanical structures with high aspect ratios can operate at greater relative amplitudes, their signal output is much weaker due to their reduced size, that might stay below the noise level of the output signal at low oscillation amplitudes. The range between the lowest linear operation amplitude above the noise level and the operation amplitude where nonlinearities emerge is called the dynamic range. In fact, for some of these resonators at the nanoscale, the dynamic range is almost non-existent and they practically can be only operated in the nonlinear regime, as their output signals are below or extremely close to the noise level for oscillation amplitudes that remain in the linear regime.

1.2. NONLINEAR MICRO/NANOMECHANICAL RESONATORS

For nonlinear micro/nanomechanical resonators, including graphene resonators, assumptions of linear stiffness and damping quickly fail at high amplitude oscillations. The experiments reveal that the effective stiffness and energy dissipation in these systems are amplitude dependent [23]. Thus generally, a modified version of the linear harmonic oscillator is employed to describe the motion of these systems, which is the so called Duffing-van der Pol oscillator:

$$m\ddot{x} + k_1 x + k_3 x^3 + \frac{m\omega_0}{Q}\dot{x} + \tau_{nl} x^2 \dot{x} = F\cos(\omega_d t). \tag{1.5}$$

where k_3 is the Duffing coefficient that defines the nonlinear cubic stiffness and τ_{nl}, the coefficient of nonlinear damping.

1.2.1. NONLINEAR STIFFNESS

Even though the origins of nonlinear effects to be encountered are numerous at the nanoscale (such as electrostatic potentials, mechanical couplings, van der Waals forces and so on), the primary root to nonlinear stiffness k_3, that is encountered in these resonators is purely geometrical, which is also the case for graphene resonators. In fact, a system with only linear springs can generate effective nonlinear stiffness purely due to geometry. The effect is very fundamental and can be intuitively demonstrated by a simple model: Imagine a mass m that is attached to two springs with stiffness k from each side to a wall at their neutral lengths L, a very basic representation of a string resonator (see Fig. 1.1). The resonator operates in the z degree-of-freedom. As the mass displaces in z, the springs will elongate such that their lengths will be $R_s = \sqrt{z^2 + L^2}$. The force per spring can be expressed as $F_s = k(L - R_s)$. The total force in the z degree-of-freedom, using the trigonometric relations, can be written as:

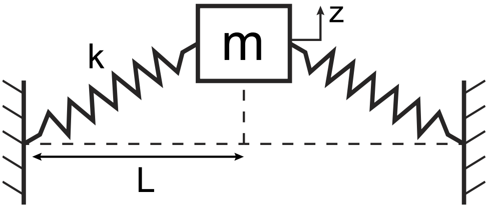

Figure 1.1: **Schematic of the toy string resonator model.**

$$F_z = 2k(L - R_s)\frac{z}{\sqrt{z^2 + L^2}} = -2\left(kz - \frac{kzL}{\sqrt{z^2 + L^2}}\right) \tag{1.6}$$

Already we can see that the linear spring forces translate to z degree-of-freedom with a linear and nonlinear part. We can Taylor expand the nonlinear force term around $z = 0$, which results in the F_z:

$$F_z = -2(kz - (kz - \frac{k}{2L^2}z^3 + O(z^5))) \approx -\frac{k}{L^2}z^3 \tag{1.7}$$

At moderately high amplitudes, the resulting force can be approximated as a cubic nonlinear spring, which is purely a consequence of geometry. This source of nonlinearity is called geometric nonlinearity, since it occurs due to the geometry, and is not caused by material nonlinearities. It is not so different for more sophisticated models of these resonators (although the mathematics is more cumbersome), which we demonstrate in the following chapters.

The consequences of this amplitude dependent stiffness on the dynamics are remarkable. Depending on the sign of k_3, as the oscillation amplitudes grow, the resonator either gets stiffer ($k_3 > 0$) or softer ($k_3 < 0$), as the effective stiffness of the system is $k_{\text{eff}} = k_1 + k_3 (x^2)_{\text{avg}}$. This amplitude dependent stiffness of the system results in an amplitude dependent resonance frequency, where the resonance of the system is a function of the oscillation amplitude (Fig. 1.2). Furthermore, the nonlinear resonance curve becomes multi-stable, for a single drive frequency, there can be found two stable and one unstable solution.

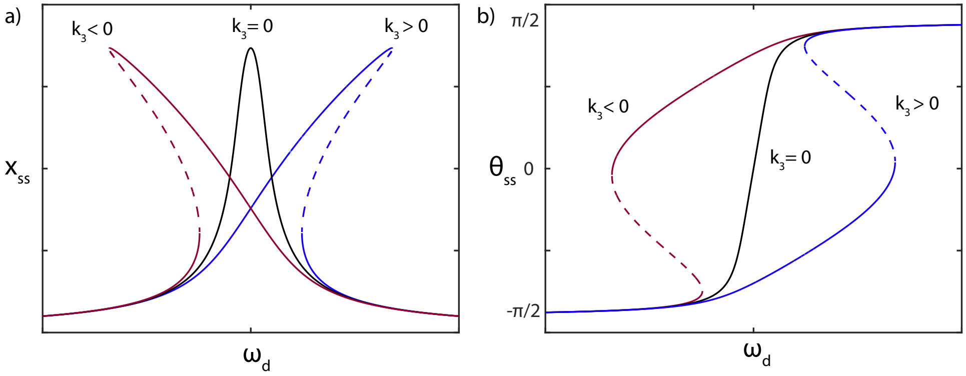

Figure 1.2: **Steady-state frequency responses of Duffing-van der Pol equation, with different Duffing coefficients.** Solid lines are stable and dashed lines are unstable solutions. a) Steady-state amplitude with respect to drive frequency. b) Steady-state phase with respect to drive frequency.

The form of this dependence can be obtained by solving for the steady-state amplitude of the Duffing-van der Pol oscillator (Eq. (1.5)). Approximations of the steady-state solution to this nonlinear differential equation can be analytically obtained by using various methods, such as secular perturbation theory, rotating wave approximation and harmonic balancing (the latter two are also used in following chapters), resulting in similar outcomes. Using secular perturbation theory [23], it is possible to obtain the equations for the steady-state amplitude x_{ss}:

$$x_{ss}^2 = \frac{\left(\frac{F}{2m\omega_0^2}\right)^2}{\left(\frac{\omega_d - \omega_0}{\omega_0} - \frac{3}{8}\frac{k_3}{m\omega_0^2}x_{ss}^2\right)^2 + \left(\frac{1}{2Q} + \frac{1}{8}\frac{\tau_{nl}}{m\omega_0}x_{ss}^2\right)^2} \tag{1.8}$$

and phase θ_{ss}:

$$\theta_{ss} = \arctan\left(\frac{\frac{m\omega_0}{2Q} + \frac{\tau_{nl}}{8}x_{ss}^2}{m(\omega_d - \omega_0) - \frac{3k_3}{8\omega_0}x_{ss}^2}\right) \tag{1.9}$$

We can obtain the nonlinear resonance frequencies of the amplitude equation using the fact that at the peak amplitude $\frac{\mathrm{d}x_{ss}^2}{\mathrm{d}\omega_d} = 0$, resulting in:

$$\omega_{nl} = \omega_0 + \frac{3}{8}\frac{k_3}{m\omega_0}x_{max}^2 \tag{1.10}$$

where ω_{nl} is the nonlinear resonance peak frequency, where x_{max} is the peak amplitude. Looking at equations (1.8), (1.9) and (1.10), one can immediately recognize the interplay between the amplitude, resonance frequency and phase of the oscillations, as they are functions of one another. Unlike the linear harmonic oscillator, this interplay results in the conversion of any noise in the driving force or amplitude of the resonator to frequency noise. This is one of the big challenges nonlinear resonators pose in terms of frequency stability [24], [25], though luckily, the origins are well understood, contrary to nonlinear damping.

1.2.2. AMPLITUDE DEPENDENT DISSIPATION

Most people are not foreign to the concept of a damping force that depends nonlinearly on the velocity, as every physics or mechanical engineering student was probably taught during fluid dynamics classes that viscous drag scales with the square of velocity. However the form of nonlinear damping $x^2\dot{x}$ we study here is special in the sense that its nonlinearity comes from the displacement x. The further you are from the equilibrium position $x = 0$, the stronger the energy is dissipated.

In the frequency response, nonlinear damping will result in a decrease of responsivity in the nonlinear oscillation amplitude, such that the peak amplitude of the resonator is not anymore linearly dependent on the force and Q factor but also a nonlinear function of the nonlinear damping coefficient τ_{nl} (Fig. 1.3a and b). Furthermore, in time domain, decay rates during ringdowns from high amplitude oscillations will be determined by both Q factor and τ_{nl}, while when the ringdown oscillations reach the linear regime, the effective decay rate will solely depend on the Q factor, like a linear resonator (Fig. 1.3c).

In the realm of carbon based nanoresonators, such as suspended carbon nanotubes and graphene membranes, nonlinear damping was first detected by the observation of drive dependent resonance linewidths $\Delta f = f_0/2Q$, where $f_0 = \omega_0/2\pi$ [26]. The observation was that, as the resonators were driven at higher amplitudes, a broadening of the resonances were observed, resulting in an increase of linewidths, which assuming linear damping, is not a function of the oscillation amplitude. This provoked the assumption of linear damping in these systems to be reexamined. In the end, the experimental results were empirically explained by the nonlinear damping model $x^2\dot{x}$, but the origins of the phenomenon were not clear. Previously, this term was proposed to explain observations of nonlinear damping in a MEMS resonator [27], based on a viscoelastic material model. The material in this model was assumed to have a complex Young's modulus, that represents a time delay between the occurrence of stresses and the associated strains, generating nonlinear damping for geometrically nonlinear motion [28], [29]. However in both studies, the nonlinear dissipation rates determined from the experiments were significantly higher than those predicted by the viscoelastic model, revealing the existence of distinct underlying physics. This provoked many others to pursue the root of this phenomenon. Other than the material properties, there were two other significant origins that were investigated. These were based on the interaction of the mechanical mode either with in-plane phonons or other internal modes of the structure. Theoretically it was shown that nonlinear damping could also emerge from these origins [30], [31], yet strong experimental evidence was only obtained for the latter [32].

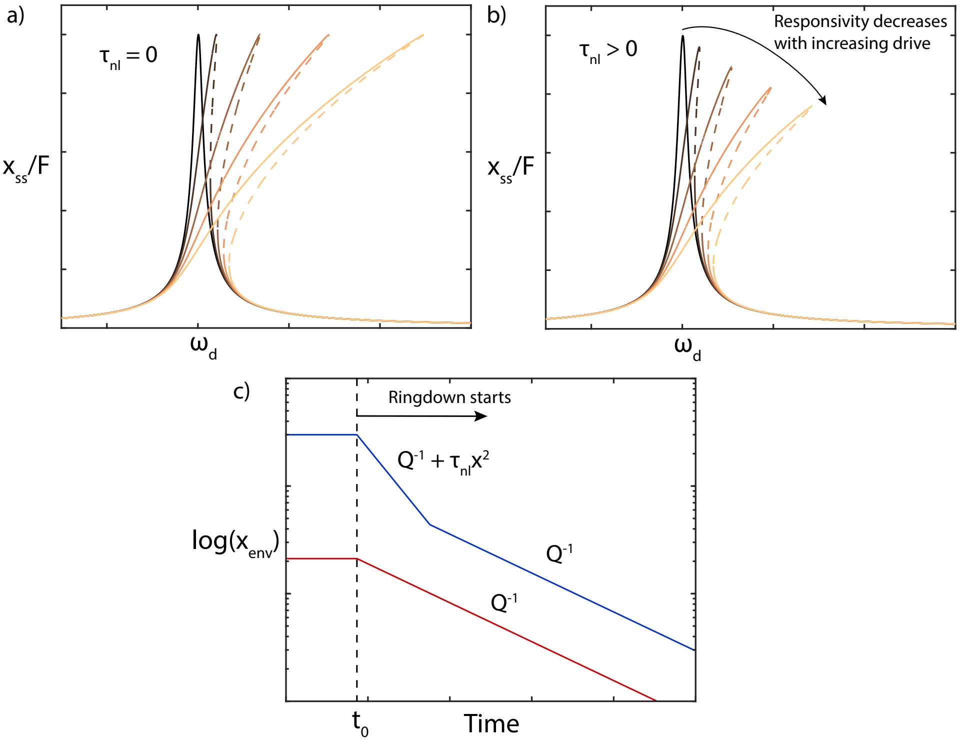

Figure 1.3: **Consequences of nonlinear damping in frequency and time domain responses.** a) Evolution of the responsivity of a forced Duffing-van der Pol oscillator with increasing driving force, in the absence of nonlinear damping. b) Evolution of the responsivity of a forced Duffing-van der Pol oscillator in the presence of nonlinear damping. As the driving force and thus oscillation amplitude increase, the responsivity of the system decrease with $\tau_{nl} > 0$. c) Ringdown of a nanoresonator with nonlinear damping (adapted from [32]), where x_{env} is the envelope amplitude of the oscillations. For ringdowns from low amplitude oscillations, the dissipation rate is constant (shown in red) and determined by the Q factor of the resonator. For the ringdowns from high amplitude oscillations (shown in blue), we can see two dissipation rates, one that is governed by both τ_{nl} and Q factor, and a second one which is governed only by the Q factor.

1.2.3. NONLINEAR INTERMODAL COUPLING AND INTERNAL ENERGY PATHWAYS

Modeling these resonators as single degree of freedom systems is based on the presumption that, in relatively small oscillation amplitudes, the linear superposition of eigenmodes is sufficient to explain these systems' overall dynamics, which are by definition orthogonal and do not transfer energy to one another. At high amplitude oscillations however, this approximation fails as the inherent nonlinear coupling of the structure becomes significant and energy that is being stored in an individual mode starts leaking to others. In nonlinear dynamics, this problem is actually one of the earliest to be explored computationally. In 1955, Fermi et. al [33], simulated a one-dimensional string by considering a chain of up to 64 masses connected by linear springs that are perturbed with quadratic and cubic nonlinear terms. It was anticipated that, if the free oscillation of the system is simulated with non-zero initial energy at an eigenmode, the energy would leak into all other modes and thermalize, leading to a state of equipartition. But in contrast to expectations, the system did not thermalize; instead, energy kept returning to the initial mode in a complicated quasi-periodic manner. Discovery of this phenomenon, later named the FPUT (Fermi-Pasta-Ulam-Tsingou) problem, gave rise to a new direction of research in nonlinear dynamics. However, the study of this problem in real-world mechanical systems is typically limited by the dissipation or the weak nonlinearity of these systems such that they are unable to retain their energy and stay at the nonlinear regime for the duration necessary to observe this phenomenon. Nevertheless, using molecular dynamic simulations it was numerically shown that, for graphene resonators, the nonlinear inter-modal energy transfer sets a fundamental lower bound for the effective dissipation of the fundamental mode [34]. To date, this was not able to be shown experimentally, as these simulations assume a closed system, which is far from reality where the environmental losses are dominant.

1.3. AIM AND OUTLINE OF THE THESIS

In the previous sections I tried to make clear that understanding the nonlinear dynamics and energy dissipation in nanomechanical resonators is crucial. Achieving this, especially for the energy dissipation, is not trivial, as a variety of potential origins have overlapping effects on the motion. Distinguishing a single dissipation mechanism is only possible by either eliminating all of the others or being able to control the strength of a single mechanism.

In this thesis, the reader will find a study of nonlinear dissipation pathways in 2-D material resonators, through the coupling of the internal mechanical modes and physics of these resonators. In most of the chapters, the resonators are brought to special dynamical and physical conditions to enhance and therefore distinguish the effects of singular nonlinear dissipation mechanisms. As these mechanisms are promoted, as a consequence, exotic nonlinear phenomena emerge in the dynamics, which are also explored.

In Chapter 2, we start by studying the nonlinear dissipation in a graphene nanoresonator that is parametrically excited. We drive the resonator at different power levels and frequencies and observe an anomalous increase in the nonlinear dissipation when the fundamental mode of the structure interacts with a higher mode. We explain the observations with an analytical two degrees-of-freedom model that links the nonlinear dissipation to the interaction. Later in Chapter 3, we provide a general framework and methodology for modelling the global nonlinear dynamics of nanoresonators. We utilize finite element simulations to build multi-modal reduced-order models of nanoresonators and compare our results to experiments on a graphene nanoresonator, with good qualitative agreement. In Chapter 4, we explore a different way to promote intermodal interactions, where we expose a graphene nanoresonator to an external electric field and break its out-of-plane symmetry. For certain conditions, this results in a strong one-to-two internal resonance amongst its modes, generating a mechanical frequency comb at higher drive levels. We study this exotic dynamic phenomenon using a continuum mechanics model and show its origins. Finally in Chapter 5, we study the dynamics of $FePS_3$-based heterostructure membranes near a magnetic phase transition, where we observe a pronounced enhancement of the resonator's nonlinear stiffness and damping parameters. We explain these observations with a model that is based on the coupling of mechanics to the magnetic order.

The combined results of these studies demonstrate the significance of nonlinear coupling for the energy dissipation in graphene and other 2-D material resonators driven in the nonlinear regime. By linking the complex dynamics of these resonators to their physics, these results not only shed light on the fundamental question of dissipation in these devices, but also provide tools in order to take advantage of their intricate nonlinear dynamics.

2

TUNING NONLINEAR DAMPING IN GRAPHENE NANORESONATORS BY PARAMETRIC-DIRECT INTERNAL RESONANCE

Mechanical sources of nonlinear damping play a central role in modern physics, from solid-state physics to thermodynamics. The microscopic theory of mechanical dissipation suggests that nonlinear damping of a resonant mode can be strongly enhanced when it is coupled to a vibration mode that is close to twice its resonance frequency. To date, no experimental evidence of this enhancement has been realized. In this chapter, we experimentally show that nanoresonators driven into parametric-direct internal resonance provide supporting evidence for the microscopic theory of nonlinear dissipation. By regulating the drive level, we tune the parametric resonance of a graphene nanodrum over a range of 40-70 MHz to reach successive two-to-one internal resonances, leading to a nearly two-fold increase of the nonlinear damping. Our study opens up a route towards utilizing modal interactions and parametric resonance to realize resonators with engineered nonlinear dissipation over wide frequency range.

This chapter has been published in Nature Communications 12, 1099 (2021).

2.1. INTRODUCTION

IN nature, from macro to nano scale, dynamical systems evolve towards thermal equilibrium while exchanging energy with their surroundings. Dissipative mechanisms that mediate this equilibration, convert energy from the dynamical system of interest to heat in an environmental bath. This process can be intricate, nonlinear, and in most cases hidden behind the veil of linear viscous damping, which is merely an approximation valid for small amplitude oscillations. In the last decade, nonlinear dissipation has attracted much attention with applications that span nanomechanics [26], materials science [28], biomechanics [35], thermodynamics [34], spintronics [36] and quantum information [37]. It has been shown that the nonlinear dissipation process follows the empirical force model $F_d = -\tau_{\text{nl1}} x^2 \dot{x}$ where τ_{nl1} is the nonlinear damping coefficient, x is the displacement and $\dot{x}$ velocity. To date, the physical mechanism from which this empirical damping force originates has remained ambiguous, with a diverse range of phenomena being held responsible including viscoelasticity [27], phonon-phonon interactions [30], [38], Akhiezer relaxation [31], and mode coupling [32]. The fact that nonlinear damping can stem from multiple origins simultaneously, makes isolating one route from the others a daunting task, especially since the nonlinear damping coefficient τ_{nl1} is perceived to be a fixed parameter that unlike stiffness [39]–[41], quality factor [42], and nonlinear stiffness [43]–[45], cannot be tuned easily. Amongst the different mechanisms that affect nonlinear damping, intermodal coupling is particularly interesting, as it can be enhanced near internal resonance (IR), a special condition at which the ratio of the resonance frequencies of the coupled modes is a rational number [46]. This phenomenon has frequently been observed in nano/micro-mechanical resonators [47]–[56]. At internal resonance, modes can interact strongly even if their nonlinear coupling is relatively weak. Interestingly, internal resonance is closely related to the effective stiffness of resonance modes, and can therefore be manipulated by careful engineering of the geometry of mechanical systems, their spring hardening nonlinearity [22], [57], and electrostatic spring softening [48]. Internal resonance also finds its route in the microscopic theory of dissipation proposed back in 1975, where it was hypothesized to lead to a significantly shorter relaxation time if there exists a resonance mode in the vicinity of twice the resonance frequency of the driven mode in the density of states [58]. Here we demonstrate that nonlinear damping of graphene nanodrums can be strongly enhanced by parametric-direct internal resonance, providing supporting evidence for the microscopic theory of nonlinear dissipation [31], [58]. To achieve this, we bring the fundamental mode of the nanodrum into parametric resonance at twice its resonance frequency, allowing it to be tuned over a wide frequency range from 40-70 MHz. We extract the nonlinear damping as a function of the parametric drive level, and observe that it increases as much as 80 % when the frequency shift of the parametric resonance brings it into internal resonance with a higher mode. By comparing the characteristic dependence of the nonlinear damping coefficient on parametric drive to a theoretical model, we confirm that internal resonance can be held accountable for the significant increase in nonlinear damping.

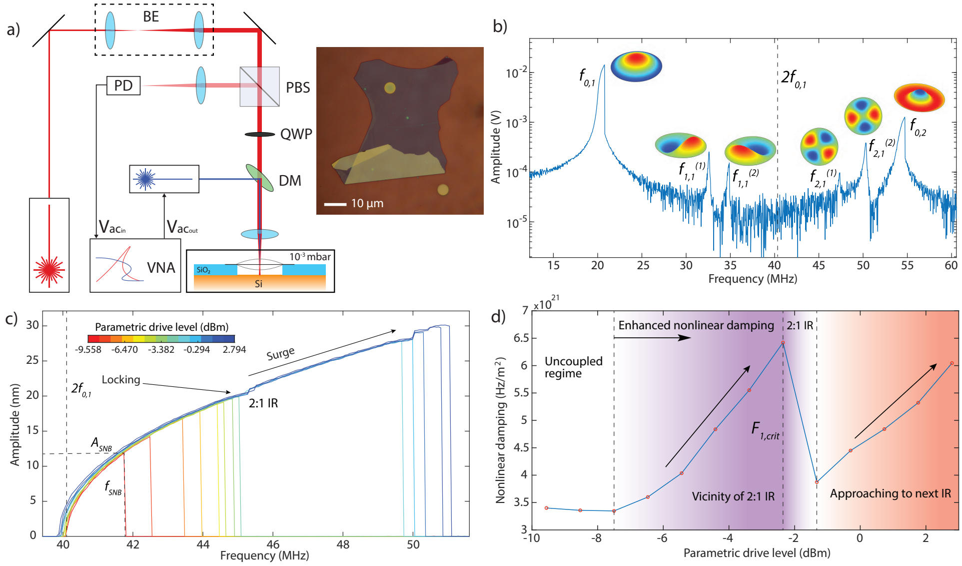

Figure 2.1: **Nonlinear dynamic response of a graphene nanodrum near 2:1 internal resonance.** (a) Fabry–Pérot interferometry with thermomechanical actuation and microscope image of the graphene. Experiments are performed in vacuum at 10^{-3} mbar. Red laser is used to detect the motion of the graphene drum and the blue laser is used to optothermally actuate it. In the figure; BE: Beam expander, QWP: Quarter wave plate, PBS: Polarized beam splitter, PD: Photodiode, DM: Dichroic mirror, VNA: Vector network analyzer, $\mathrm{V}_{\mathrm{ac}_{\mathrm{in}}}$: Analyzer port, $\mathrm{V}_{\mathrm{ac}_{\mathrm{out}}}$: Excitation port. In the device schematic, Si and SiO_2 layers are represented by orange and blue colors, respectively. (b) Direct frequency response curve of the device(motion amplitude vs. drive frequency), showing multiple resonances (Drive level = -12.6 dBm). The mode shapes are simulated by COMSOL. Resonance peaks are associated with $f_{m,n}^{(k)}$ where m represents the number of nodal diameters, n nodal circles and $k = 1,2$ stand for the first and second asymmetric degenerate modes. Dashed line shows $2f_{0,1}$, which is the drive frequency where the parametric resonance of mode $f_{0,1}$ is activated. (c) Parametric resonance curves(calibrated motion amplitude vs. drive frequency), driven at twice the detection frequency. As the parametric resonance curves approach the 2:1 internal resonance(IR), f_{SNB} first locks to 2:1 IR frequency and consecutively saddle-node bifurcation surges to a higher frequency and amplitude. A_{SNB} and f_{SNB} stand for the amplitude and frequency of saddle-node bifurcation. (d) Variation of the nonlinear damping $\tau_{\mathrm{nl}1}$ as a function of drive F_1. Dashed lines represent different regimes of nonlinear damping. White region represents a constant nonlinear damping, purple region an increase in nonlinear damping in the vicinity of 2:1 IR and orange region an increase in nonlinear damping due to IR with a higher mode.

2.2. FREQUENCY RESPONSE MEASUREMENTS ON A NONLINEAR GRAPHENE NANODRUM

Experiments are performed on a 10 nm thick multilayer graphene nanodrum with a diameter of 5 um, that is transferred over a cavity etched in a layer of SiO_2 with a depth of 285 nm. A blue laser is used to thermomechanically actuate the membrane, where a red laser is being used to detect the motion, using interferometry (see Methods for details). A schematic of the set-up is shown in Fig 1a.

By sweeping the drive frequency we obtain the frequency response of the nanodrum in which multiple directly driven resonance modes can be identified (Fig. 2.1b). We find the fundamental axisymmetric mode of vibration at $f_{0,1}$=20.1 MHz and several other modes, of which the two modes, at $f_{2,1}^{(1)}$=47.4 MHz and $f_{2,1}^{(2)}$=50.0 MHz, are of particular interest. This is because, to study the effect of internal resonance on nonlinear damping, we aim to achieve a two-to one (2:1) internal resonance by parametrically driving the fundamental mode, such that it coincides with one of the higher frequency modes. The frequency ratios $f_{2,1}^{(1)}/f_{0,1} \approx 2.3$ and $f_{2,1}^{(2)}/f_{0,1} \approx 2.4$ are close to the factor 2, however additional frequency tuning is needed to reach the 2:1 internal resonance condition.

The parametric resonance can be clearly observed by modulating the tension of the nanodrum at frequency ω_F with the blue laser while using a frequency converter in the VNA to measure the amplitude at $\omega_F/2$ as shown in Fig. 2.1c. By increasing the parametric drive, we observe a Duffing-type geometric nonlinearity over a large frequency range, such that the parametrically driven fundamental resonance can be tuned across successive 2:1 internal resonance conditions with modes $f_{2,1}^{(1)}$ and $f_{2,1}^{(2)}$, respectively.

2.2.1. EXTRACTING EXPERIMENTAL NONLINEAR PARAMETERS

In Fig. 2.1c we observe that the parametric resonance curves follow a common response until they reach the saddle-node bifurcation frequency f_{SNB} above which the parametric resonance curve reaches its peak amplitude A_{SNB} and drops down to low amplitude. We note that the value of A_{SNB} can be used to determine the degree of nonlinear damping [23]. Therefore, to extract the nonlinear damping coefficient τ_{nl1} of mode $f_{0,1}$ from the curves in Fig. 2.1c, we use the following single mode model to describe the system dynamics:

$$\ddot{x}_1 + \omega_1^2 x_1 + \gamma x^3 = F_1 x_1 \cos(\omega_F t) - 2\tau_1 \dot{x}_1 - 2\tau_{\mathrm{nl1}} x_1^2 \dot{x}_1, \tag{2.1}$$

in which $\omega_1 = 2\pi f_{0,1}$ is the eigenfrequency of the axisymmetric mode of the nanodrum, γ is its Duffing constant and F_1 and ω_F are the parametric drive amplitude and frequency, respectively. Moreover, $2\tau_1 = \omega_1/Q$ is the linear damping coefficient, with Q being the quality factor, and τ_{nl1} is the nonlinear damping term of van der Pol type that prevents the parametric resonance amplitude A_{SNB} from increasing to infinity [23], [59] at higher driving frequencies since $|A_{\mathrm{SNB}}|^2 \propto (2F_1 Q - 4)/\tau_{\mathrm{nl1}}$. To identify the parameters governing the device dynamics from the measurements in Fig. 2.1c, we use equation (2.1) and obtain good fits of the parametric resonance curves using τ_{nl1} and γ as fit parameters (see Appendix A1).

ENHANCED NONLINEAR DAMPING

As we gradually increase the drive level, f_{SNB} increases until it reaches the vicinity of the internal resonance, where we observe an increase in τ_{nl1} (Fig. 2.1d). Whereas f_{SNB} increases with parametric drive F_1, Fig. 2.1c shows that its rate of increase $\frac{\mathrm{d}f_{\mathrm{SNB}}}{\mathrm{d}F_1}$ slows down close to $f_{2,1}^{(1)}$, locking the saddle-node-bifurcation frequency when $f_{\mathrm{SNB}} \approx 45$ MHz. At the same time, τ_{nl1} increases significantly at the associated parametric drive levels, providing the possibility to tune nonlinear damping up to two-folds by controlling F_1, as seen in Fig. 2.1d.

Fig. 2.1c also shows that above a certain critical parametric drive level $F_{1,\mathrm{crit}}$, the frequency locking barrier at $f_{\mathrm{SNB}} \approx 45$ MHz is broken and f_{SNB} suddenly jumps to a higher frequency (≈ 5 MHz higher), and a corresponding larger A_{SNB}. We label this increase in the rate $\frac{\mathrm{d}f_{\mathrm{SNB}}}{\mathrm{d}F_1}$ by “surge" in Fig. 2.1c, where an abrupt increase in the amplitude-frequency response is observed to occur above a critical drive level $F_{1,\mathrm{crit}}$. Interestingly, even above $F_{1,\mathrm{crit}}$ a further increase in τ_{nl1} is observed with increasing drive amplitude, indicating that a similar frequency-locking occurs when the parametric resonance peak reaches the second internal resonance at $f_{\mathrm{SNB}} \approx f_{2,1}^{(2)}$. Similar nonlinear phenomena are also showcased in a second nanodrum undergoing parametric-direct modal interaction, confirming the reproducibility of the observed physics (see Appendix A2).

2.3. THEORETICAL MODEL: 2:1 PARAMETRIC-DIRECT INTERNAL RESONANCE

Although the single mode model in equation (2.1) can capture the response of the parametric resonance, it can only do so by introducing a non-physical drive level dependent nonlinear damping coefficient $\tau_{\mathrm{nl1}}(F_1)$ (Fig. 2.1d). Therefore, to study the physical origin of our observation, we extend the model by introducing a second mode whose motion is described by generalized coordinate x_2. Moreover, to describe the coupling between the interacting modes at the 2:1 internal resonance, we use the single term coupling potential $U_{\mathrm{cp}} = \alpha x_1^2 x_2$ (see Appendix A3). The coupled equations of motion in the presence of this potential become:

$$\begin{aligned} \ddot{x}_1 + \omega_1^2 x_1 + \gamma x_1^3 + \frac{\partial U_{\mathrm{cp}}}{\partial x_1} &= F_1 x_1 \cos(\omega_F t) - 2\tau_1 \dot{x}_1 - 2\tau_{nl1} x_1^2 \dot{x}_1, \\ \ddot{x}_2 + \omega_2^2 x_2 + \frac{\partial U_{\mathrm{cp}}}{\partial x_2} &= F_2 \cos(\omega_F t) - 2\tau_2 \dot{x}_2. \end{aligned} \tag{2.2}$$

The 2 mode model describes a parametrically driven mode with generalized coordinate x_1 coupled to x_2 that has eigenfrequency $\omega_2 = 2\pi f_{2,1}^{(1)}$, damping ratio τ_2, and is directly driven by a harmonic force with magnitude F_2.

To understand the dynamics of the system observed experimentally and described by the model in equation (2.2), it is convenient to switch to the rotating frame of reference by transforming x_1 and x_2 to complex amplitude form (see Appendix A4). This transformation reveals a system of equations that predicts the response of the resonator as the drive parameters (F_1, F_2, and ω_F) are varied. Solving the coupled system at steady-state yields the following algebraic equation for the amplitude a_1 of the first mode:

$$\left[\tau_1+(\tau_{\mathrm{nl1}}+\tilde{\alpha}^2\tau_2)\frac{a_1^2}{4}\right]^2+\left[\Delta\omega_1-\left(\frac{3\gamma}{\omega_F}+\tilde{\alpha}^2\Delta\omega_2\right)\frac{a_1^2}{4}\right]^2 = \frac{1}{4\omega_F^2}\left[F_1^2+\tilde{\alpha}^2(F_2^2+2\omega_F\Delta\omega_2 F_1F_2/\alpha)\right], \tag{2.3}$$

where $\Delta\omega_1=\omega_F/2-\omega_1$ and $\Delta\omega_2=\omega_F-\omega_2$ are the frequency detuning from the primary and the secondary eigenfrequencies, and $\tilde{\alpha}^2=\alpha^2/[\omega_F^2(\tau_2^2+\Delta\omega_2^2)]$ is the rescaled coupling strength. Essentially, the first squared term in (2.3) captures the effect of damping on the parametric resonance amplitude a_1, the second term captures the effect of nonlinear coupling on the stiffness and driving frequency, and the term on the right side is the effective parametric drive. From the rescaled coupling strength $\tilde{\alpha}$ and equation (2.3) it can be seen that the coupling $\tilde{\alpha}^2$ shows a large peak close to the 2:1 internal resonance where $|\Delta\omega_2|\approx 0$. In addition, equation (2.3) shows that mode 2 will always dissipate energy from mode 1 once coupled, and that, the 2 mode model accounts for an increase in the effective nonlinear damping parameter ($\tau_{nl\mathrm{eff}}=\tau_{\mathrm{nl1}}+\tilde{\alpha}^2\tau_2$) near internal resonance, in accordance with the observed peak in τ_{nl1} with the single mode model in Fig 1d. It is also interesting to note that, this observation in steady-state is different from what has been reported in [52] for transient nonlinear free vibrations of coupled modes where it was important that $\tau_2\gg\tau_1$ to observe nonlinear damping. The 2 mode model of equation (2.3) allows us to obtain good fits of the parametric resonance curves in Fig. 2.1b, with a constant $\tau_{\mathrm{nleff}}\approx 3.4\times10^{21}$ (Hz/m^2) determined far from internal resonance and a single coupling strength $\alpha=2.2\times10^{22}$ (Hz^2/m) which intrinsically accounts for the variation of τ_{nleff} near internal resonance. These fits can be found in Appendix A5, and demonstrate that the 2 mode model is in agreement with the experiments for constant parameter values, without requiring drive level dependent fit parameters.

We note that the extracted nonlinear damping parameter fits the Duffing response at $f_{0,1}$ with good accuracy too (See Appendix A6).

2.3.1. MODEL RESPONSE

To understand the physics associated with the frequency-locking and amplitude-frequency surge, we use the experimentally extracted fit parameters from the 2 mode model and numerically generate parametric resonance curves using equation (2.3) for a large range of drive amplitudes (see Fig. 2.2a). We see that for small drive levels, an upward frequency sweep will follow the parametric resonance curve and then will lock and jump-down at the first saddle-node bifurcation (SNB1) frequency, that lies close to $f_{\mathrm{SNB}}\approx f_{2,1}^{(1)}$. At higher parametric drive levels, the parametric resonance has a stable path to traverse the internal resonance towards a group of stable states at higher frequencies.

A more extensive investigation of this phenomenon can be carried out by performing bifurcation analysis of the steady-state solutions (see Appendix A4). The bifurcation analysis reveals two saddle-node bifurcations near the singular region of the internal resonance, one at the end of the first path (SNB1) and another at the beginning of the second path (SNB2) (Fig. 2.2b). As the drive amplitude increases, the bifurcation pair starts to move towards each other until they annihilate one another to form a stable so-

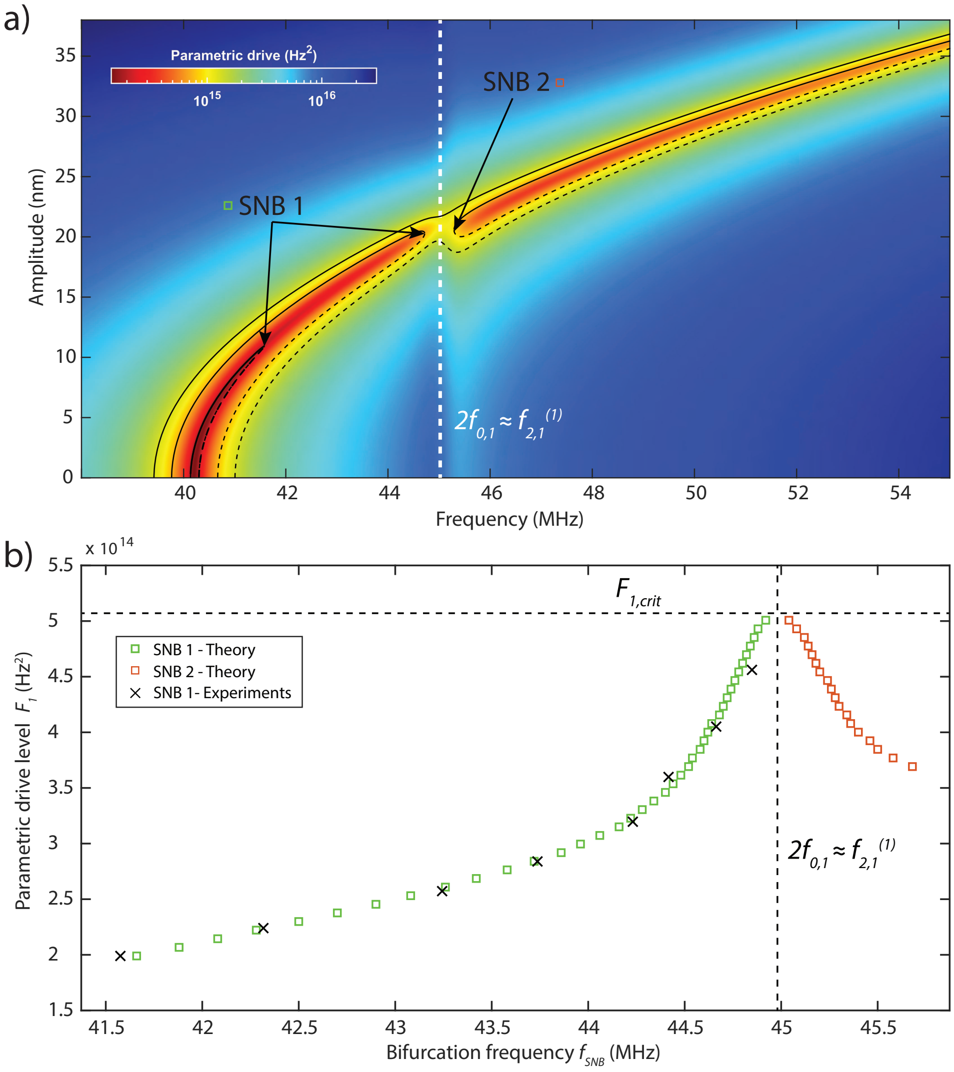

Figure 2.2: **Parametric-direct internal resonance.** (a) Color map of the analytical model response curves obtained by using the fitted parameters from experiments. Colors correspond to frequency response(motion amplitude vs. drive frequency) solutions with a certain parametric drive level. Black lines show samples from these solutions where solid lines are stable and dashed lines are unstable solutions. White dashed line is where parametric resonance meets with interacting mode and undergoes internal resonance. (b) The underlying route of the amplitude-frequency surge is revealed by tracing the evolution of saddle-node bifurcations (green and red squares represent theoretical SNB1 and SNB2, whereas experimental SNB1 is represented by crosses) of the parametric resonance curves.

lution at the connecting point, which we labeled as "surge". It is also possible to observe that the rate at which saddle-node pairs approach each other dramatically drops near the internal resonance condition, demonstrating the "locking" which we also observed in the experiments.

2.3.2. Comparison to experimental results

To check how closely the 2 mode model captures the variation of τ_{nl1} close to the internal resonance condition, we follow a reverse path, and fit the numerically generated resonance curves of Fig. 2.2a using the single mode model of equation (2.3) with τ_{nl1} as the fit parameter. In this way, we track the variation of τ_{nl1} in the single mode model with the parametric drive F_1, similar to what we observed experimentally and reported in Fig. 2.1c. The result of this fit is shown in Fig. 2.3a, where a similar anomalous change of nonlinear damping is obtained for the 2 mode model.

The variation of nonlinear damping affects the total damping (sum of linear and nonlinear dissipation) of the resonator too. It is of interest to study how large this effect is. In Fig. 2.3b we report the variation in the ratio of the linear damping τ_1 and the amplitude-dependent total damping $\tau_{\text{tot}} = (\omega_1/Q+0.25\tau_{nl\text{eff}}|x_1|^2)$ [23] in the spectral neighborhood of $f_{2,1}^{(1)}$, and observe a sudden decrease in the vicinity of internal resonance. This abrupt change in the total damping is well captured by the 2 mode model. With the increase in the drive amplitude, τ_1/τ_{tot} values of this model though, deviate from those of the experiments due to a subsequent internal resonance at $f_{2,1}^{(2)}/f_{0,1} \approx 2.4$ that is not included in our theoretical analysis. The dependence of τ_1/τ_{tot} on frequency shows that near internal resonance the total damping of the fundamental mode increases nearly by 80%.

2.4. Discussion

We note that increased nonlinear damping near internal resonance was also observed in [32]. In that work nonlinear damping was studied using ringdown measurements, with 2 modes brought close to an internal resonance by electrostatic gating. The increased nonlinear damping was attributed to a direct-direct 3:1 internal resonance, that as shown theoretically in Ref. [52] leads to a high order (quintic) nonlinear damping term. Conversely, in our work two modes are brought into parametric-direct 2:1 internal resonance by adjusting the parametric drive level. This results in a nonlinear damping term that already comes into play at smaller amplitudes because it is of lower (cubic) order, as discussed in Ref. [52]. Moreover, the nonlinear damping mechanism in [32] is approximately described by two exponential decays with crossovers from $(\tau_1+\tau_2)/2$ to τ_1, which implies that similar to [52], $\tau_2 > \tau_1$ is required to observe positive nonlinear damping. This is in contrast with the damping mechanism we describe where the effective nonlinear damping actually increases for smaller τ_2 (see equation (2.3)).

Since the tension of the nanodrum can be manipulated by laser heating, we can further investigate the tunability of the nonlinear damping by increasing the laser power and detecting the range over which 2:1 internal resonance conditions may occur. When increasing the blue laser power and modulation, we observe the parametrically actuated signal also in the direct detection mode (like in Fig. 2.1b) due to optical readout nonlin-

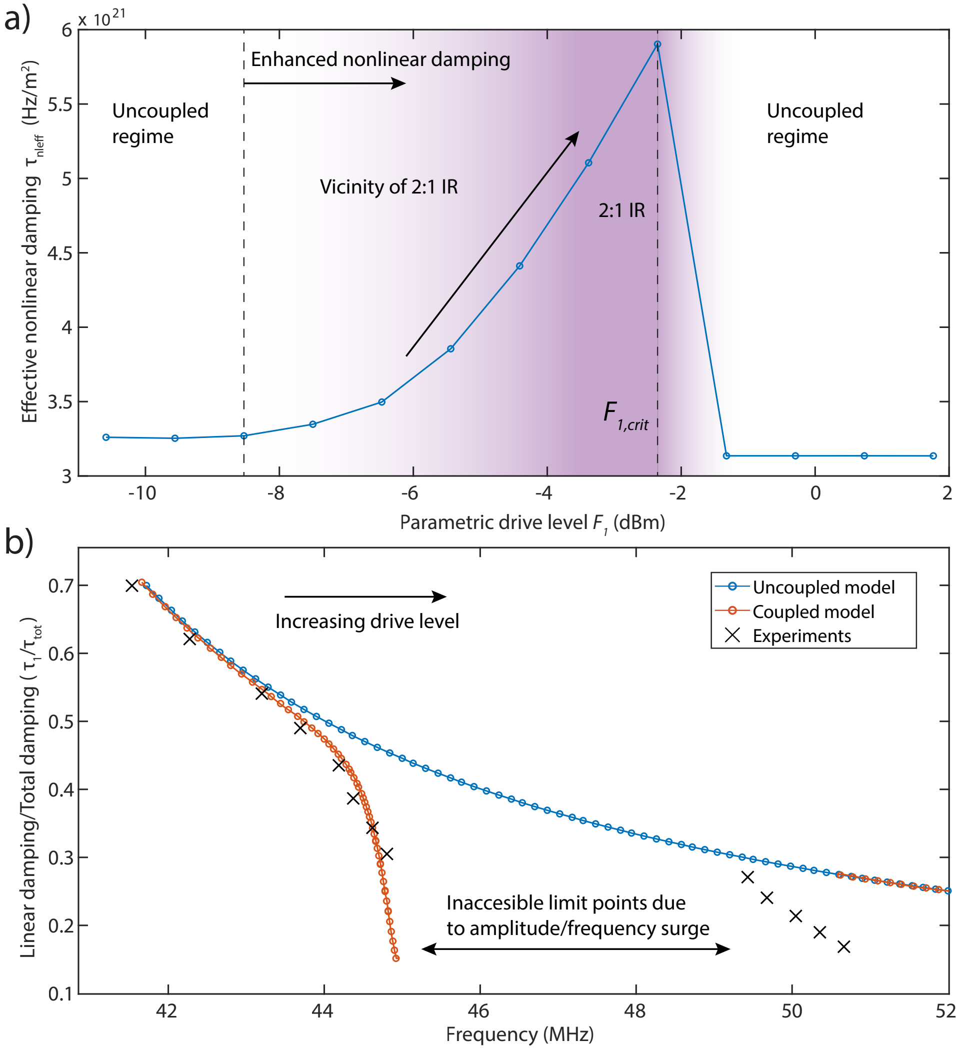

Figure 2.3: **Measurements and fits of the effective nonlinear damping.** (a) Variation of the effective nonlinear damping parameter (τ_{nleff}) with respect to parametric drive. The τ_{nleff} is obtained by fitting the numerically generated curves of Fig. 2.2a as the fit parameter. Dashed lines represent different regimes of nonlinear damping. White regions represent a constant nonlinear damping and purple region represents an increase in nonlinear damping in the vicinity of 2:1 IR. (b) Comparison of the ratio between linear damping(τ_1) and total damping(τ_{tot}). In the figure, blue and red dashed lines represent τ_1/τ_{tot} obtained from uncoupled and coupled models, whereas black crosses represent experiments.

earities [60]. As a result a superposition of Fig. 2.1b and 2.1c is obtained, as shown in Fig. 2.13. We note that the enhanced laser power increases membrane tension which moves $f_{0,1}$ upward by a few MHz, but also allows us to reach even higher parametric modulation. In this configuration we achieve a frequency shift in f_{SNB} from 40-70 MHz, corresponding to as much as 75 % tuning of the mechanical motion frequency. This large tuning can increase the number of successive internal resonances that can be reached even further, to reach modal interactions between the parametric mode $f_{0,1}$ and direct modes $f_{2,1}^{(2)}$ and $f_{0,2}$ (see Fig. 2.13). As a result, multiple amplitude-frequency surges can be detected in the large frequency range of 30 MHz over which nonlinear damping coefficient can be tuned. In summary we study the tunability of nonlinear damping in a graphene nanomechanical resonator, where the fundamental mode is parametrically driven to interact with a higher mode. When the system is brought near a 2:1 internal resonance, a significant increase in nonlinear damping is observed. In addition, the rate of increase of the parametric resonance frequency reduces in a certain locking regime, potentially stabilizing the values of f_{SNB} and A_{SNB}, which could potentially aid frequency noise reduction [49]. Interestingly, as the drive level is further increased beyond the critical level $F_{1,\mathrm{crit}}$, this locking barrier is broken, resulting in a surge in f_{SNB} and amplitude of the resonator. These phenomena were studied experimentally, and could be accounted for using a 2 mode theoretical model. The described mechanism can isolate and differentiate mode coupling induced nonlinear damping from other dissipation sources, and sheds light on the origins of nonlinear dissipation in nanomechanical resonators. It also provides a way to controllably tune nonlinear damping which complements existing methods for tuning linear damping [42], linear stiffness [39]–[41] and nonlinear

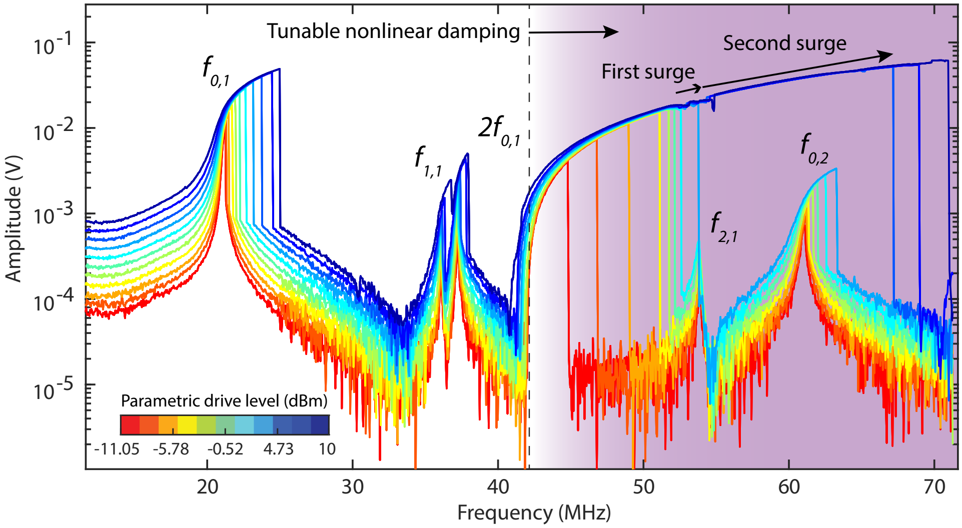

Figure 2.4: **Nonlinear frequency response measurements at high drive powers.** The parametric resonance interacts successively with multiple directly driven modes of vibration. The arrows in the figure show successive amplitude-frequency surges. Starting from the dashed line, shaded area represents the region where nonlinear damping is tunable.

stiffness[43]–[45], extending our toolset to adapt and study the rich nonlinear dynamics of nanoresonators.

2.5. METHODS

2.5.1. SAMPLE FABRICATION

Devices are fabricated using standard electron-beam(e-beam) lithography and dry etching techniques. A positive e-beam resist, ARP-6200 is spin coated on a Si wafer with 285 nm of thermally grown SiO_2. The cavity patterns ranging from 2 - 10 um in diameter are exposed using the Vistec EBPG 5000+ and developed. The exposed SiO_2 are subsequently etched away in a reactive ion etcher using a mixture of CHF_3 and Ar gas until all the SiO_2 is etched away and the Si exposed. Graphene flakes are exfoliated from natural crystals and dry transferred on top of cavities.

2.5.2. LASER INTERFEROMETRY

The experiments are performed at room temperature in a vacuum chamber (10^{-3} mbar). A power modulated blue laser ($\lambda = 405$ nm) is used to thermomechanically actuate the nanodrum. The motion is then read-out the motion using a red laser ($\lambda = 633$ nm) whose reflected intensity is modulated by the motion of the nanodrum in a Fabry–Pérot etalon formed by the graphene and the Si back mirror (Fig. 2.1a). The reflected red laser intensity from the center of the drum is detected using a photodiode, whose response is read by the same Vector Network Analyzer (VNA) that modulates the blue laser. The measured VNA signal is then converted to displacement in nanometers using a nonlinear optical calibration method [60] (see Appendix A7).

2.6. APPENDIX A

2.6.1. A1: MODEL FITS USING THE SINGLE MODE EQUATION

In this section, we use equation (2.1) to fit the experimental data. The fittings are carried out by using an algorithm that compares measurements to the analytical solution [23] to sequentially extract the model parameters. To fit the data, information about resonance frequency ω_1 and damping coefficient τ_1 are directly extracted from the measurements. The linear quality factor Q of the resonator is determined at low drive level to be 454 and has been fixed throughout the fitting procedure. Moreover, the magnitude of the parametric drive F_1 at low driving powers is estimated by tracing the locus of the pitch-fork bifurcation points (Mathieu tongue) as shown in Fig. 2.5. However, for higher power levels, the bifurcation points did not give reliable information due to frequency fluctuations. Thus, to obtain the parametric forces at high drive powers, we use lower force levels (known from Mathieu tongue) and extrapolate using the ratios between the applied voltage/power levels from the VNA and the forces such that $F_{1,\text{high}} = F_{1,\text{low}} \frac{P_{\text{high}}}{P_{\text{low}}}$. In other words, we assume that the drive levels applied in the experiments using the VNA are linearly related to the force felt by the resonator.

Once F_1 is estimated, γ is fitted by minimizing the curvatures of the hardening type nonlinearity observed in the experiments and the model. Finally, to match the peak amplitudes observed in the experiments, the nonlinear damping coefficient $\tau_{\text{nl}1}$ is used as the fitting parameter such that the saddle-node bifurcation amplitude (A_{SNB}) and frequency (f_{SNB}) are within 0.1% error of the A_{SNB} and f_{SNB} obtained experimentally. In Fig. 2.6 we report the fitted curves and their associated γ and τ_{nl1}. Fits are associated with the experimental curves (Fig. 2.1c) that are repeated with labels as Fig. 2.7 for convinience.

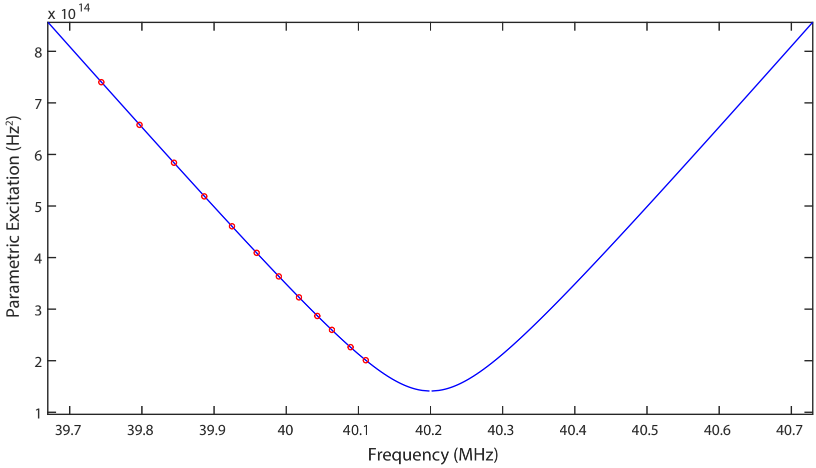

Figure 2.5: **Determination of parametric excitation levels.** The Mathieu tongue(blue) associated with the experimental pitch-fork bifurcation frequencies is used to extract parametric excitation levels(red).

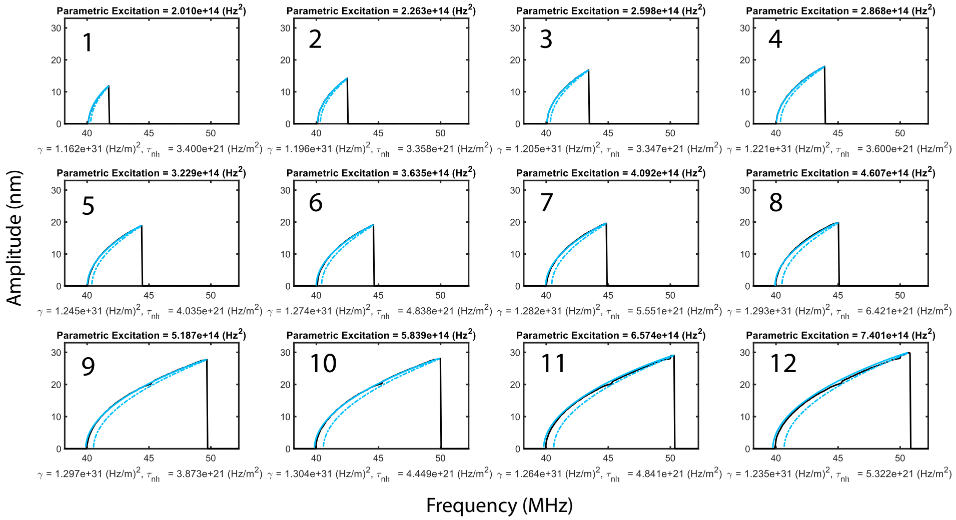

Figure 2.6: **Single mode model fits.** Frequency response measurements (black) and corresponding fits (blue) obtained by using the single mode model. The solid and dashed lines in the figure represent stable and unstable numerical solutions, respectively.

2.6.2. A2: EXPERIMENT ON A SECOND NANODRUM

Here we present additional experimental evidence of a parametric-direct internal resonance in a second graphene nanodrum that is 14 nm thick and has a radius of 2.5 μm. Fig. 2.8a shows the direct response and Fig. 2.8b the parametric resonance where the internal resonance frequency f_{IR} occurs close to 2.3 times the fundamental mode, and after which an amplitude-frequency surge is apparent.

2.6.3. A3: NORMAL FORM OF THE EQUATIONS OF MOTION

In the absence of damping and external forces, the geometrically nonlinear equations of motion for plates and membranes can be written in the following discretized form [61]

$$\ddot{x}_k + \omega_k^2 x_k + \sum_n \sum_p \alpha_{np}^{(k)} x_n x_p + \sum_n \sum_p \sum_l \gamma_{npl}^{(k)} x_n x_p x_l = 0, \quad \forall k \in \mathbb{N}, \tag{2.4}$$

where ω_k is the eigenfrequency of the k^{th} mode x_k, and $\alpha_{np}^{(k)}$ and $\gamma_{npl}^{(k)}$ are quadratic and cubic nonlinear terms, respectively. For a two mode system ($k = 2$), the nonlinear equations become

$$\ddot{x}_1 + \omega_1^2 x_1 + \alpha_{11}^{(1)} x_1^2 + \alpha_{12}^{(1)} x_1 x_2 + \alpha_{22}^{(1)} x_2^2 + \gamma_{111}^{(1)} x_1^3 + \gamma_{112}^{(1)} x_1^2 x_2 + \gamma_{122}^{(1)} x_1 x_2^2 + \gamma_{222}^{(1)} x_2^3 = 0, \tag{2.5}$$
$$\ddot{x}_2 + \omega_2^2 x_2 + \alpha_{11}^{(2)} x_1^2 + \alpha_{12}^{(2)} x_1 x_2 + \alpha_{22}^{(2)} x_2^2 + \gamma_{111}^{(2)} x_1^3 + \gamma_{112}^{(2)} x_1^2 x_2 + \gamma_{122}^{(2)} x_1 x_2^2 + \gamma_{222}^{(2)} x_2^3 = 0. \tag{2.6}$$

Note that many of the nonlinear terms in equation (2.5) and (2.6) are non-resonant, and hence, can be eliminated via a normal form transformation [62]. To recover the resonant terms (which cannot be eliminated from the normal form) in a 2:1 internal resonance condition ($\omega_2 \simeq 2\omega_1$), here instead we assume harmonic motion of the form $x_1 \approx$

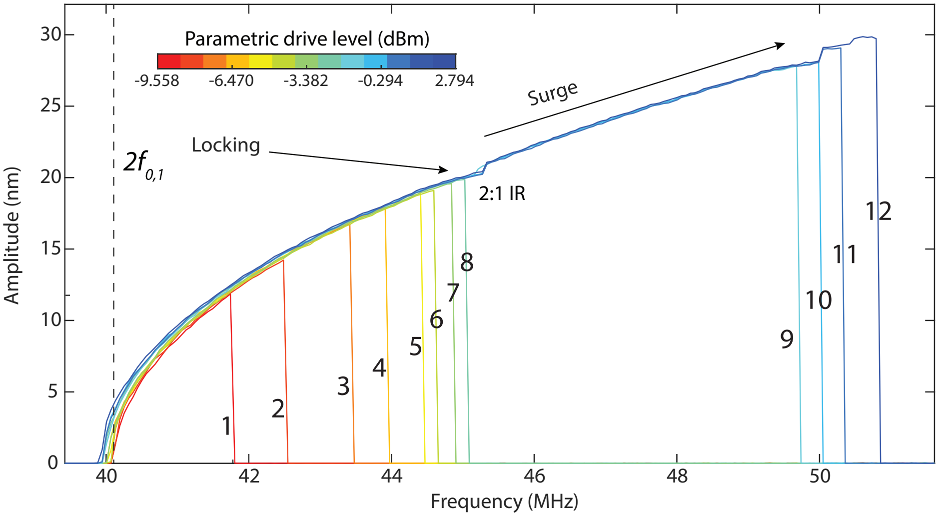

Figure 2.7: **Experimental parametric resonance curves.** Experimental frequency response curves from Fig. 2.1c, labelled to corresponding fitted curves in Fig. 2.6

$\cos(\omega_1 t)$ and $x_2 \approx \cos(2\omega_1 t)$ as a first approximation. Inserting these relations in equation (2.5) reveals that the terms $x_1^3 = \frac{3}{4}\cos(\omega_1 t) + \frac{1}{4}\cos(3\omega_1 t)$ and $x_1 x_2 = \frac{1}{2}(\cos(\omega_1 t) + \cos(3\omega_1 t))$ in the first equation of motion are trivially resonant. The same holds for the term $x_1^2 = \frac{1}{2}(1 + \cos(2\omega_1 t))$, which can be viewed as a resonant term for equation (2.6). Furthermore, in order to obtain the most simple model for the considered dynamical system, we neglect the contribution of the dispersive coupling terms $x_1 x_2^2$ in equation (2.5) and $x_2^2 x_1$ in equation (2.6) (which only shift the resonance frequency of each mode in amount that is proportional to the amplitude square of the other mode), and the Duffing nonlinearity of the second mode (which is assumed to operate below the Duffing threshold). Therefore, the governing equations of motion reduce to

$$\ddot{x}_1 + \omega_1^2 x_1 + \alpha_{12}^{(1)} x_1 x_2 + \gamma_{111}^{(1)} x_1^3 = 0, \tag{2.7}$$

$$\ddot{x}_2 + \omega_2^2 x_2 + \alpha_{11}^{(2)} x_1^2 = 0. \tag{2.8}$$

We note that equations (2.7) and (2.8) are the normal form of the conservative dynamical system of interest, with $\gamma_{111}^{(1)}=\gamma$ being the Duffing nonlinearity of the first mode, and $\alpha=\alpha_{12}^{(1)}/2=\alpha_{11}^{(2)}$ is the coupling coefficient, which stems from a single-term potential $U_{\text{cp}} = \alpha x_1^2 x_2$.

2.6.4. A4: SLOW DYNAMIC EQUATIONS AND BIFURCATION ANALYSIS

In order to investigate the experimentally observed physics in our graphene nanodrum, we use the normal form of the equations obtained in the previous section in the presence

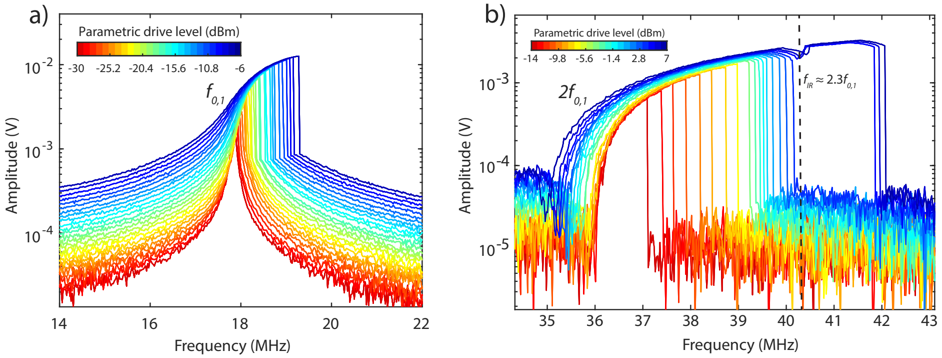

Figure 2.8: **Frequency response measurements.** Frequency response of (a) direct and (b) parametric resonance in a second graphene nanodrum, showing the parametric-direct interaction.

of damping and external forcing terms. The resulting equations then read

$$\ddot{x}_1 + \omega_1^2 x_1 + \gamma x_1^3 + 2\alpha x_2 x_1 = F_1 x_1 \cos(\omega_F t) - 2\tau_1 \dot{x}_1 - 2\tau_{nl1} x_1^2 \dot{x}_1, \tag{2.9}$$

$$\ddot{x}_2 + \omega_2^2 x_2 + \alpha x_1^2 = F_2 \cos(\omega_F t) - 2\tau_2 \dot{x}_2, \tag{2.10}$$

in which τ_1 and τ_2 are the damping coefficients associated with modes 1 and 2 , respectively. F_1 is the parametric drive, F_2 is the direct drive, and τ_{nl1} is the van der Pol type nonlinear damping term added to the equation of motion to avoid unbounded parametric resonance [23].

Applying the rotating wave approximation (RWA):

$$\begin{aligned}
x_1(t) &= A_1(t)\exp(i\omega_F t/2) + A_1^*(t)\exp(-i\omega_F t/2),\\
\dot{x}_1(t) &= (i\omega_F/2)[A_1(t)\exp(i\omega_F t/2) - A_1^*(t)\exp(-i\omega_F t/2)],\\
x_2 &= A_2(t)\exp(i\omega_F t) + A_2^*(t)\exp(-i\omega_F t),\\
\dot{x}_2 &= i\omega_F[A_2(t)\exp(i\omega_F t) - A_2^*(t)\exp(-i\omega_F t)],
\end{aligned} \tag{2.11}$$

where A_j and A_j^* are the complex-amplitude of the j^{th} mode and its complex-conjugate, respectively, and introducing the detuning parameters $\Delta\omega_1 = \omega_F/2 - \omega_1$, $\Delta\omega_2 = \omega_F - \omega_2$, we obtain the following evolution equations for the complex amplitudes

$$\dot{A}_1 = -\left[\tau_1 + \tau_{nl1}|A_1|^2 + i\left(\Delta\omega_1 - \frac{3\gamma}{\omega_F}|A_1|^2\right)\right]A_1 + \frac{2i}{\omega_F}\left(\alpha A_2 - \frac{F_1}{4}\right)A_1^*, \tag{2.12}$$

$$\dot{A}_2 = -(\tau_2 + i\Delta\omega_2)A_2 + \frac{i}{2\omega_F}\left(\alpha A_1^2 - \frac{F_2}{2}\right). \tag{2.13}$$

At steady-state $\dot{A}_j = 0$. Thus, from equation (2.13) we find that the steady-state complex-amplitude of the second mode A_{2ss} is given by

$$A_{2ss} = \frac{(i\tau_2 + \Delta\omega_2)}{2\omega_F(\tau_2^2 + \Delta\omega_2^2)}\left(\alpha A_{1ss}^2 - \frac{F_2}{2}\right). \tag{2.14}$$

Hence, by substituting equation (2.14) into equation (2.12), we obtain a single equation for the steady-state complex-amplitude of the first mode A_{1ss} as follows

$$\left[\tau_1+\left(\tau_{nl1}+\frac{\alpha^2\tau_2}{\omega_F^2(\tau_2^2+\Delta\omega_2^2)}\right)|A_{1ss}|^2\right]A_{1ss}+i\left[\Delta\omega_1-\left(\frac{3\gamma}{\omega_F}+\frac{\alpha^2\Delta\omega_2}{\omega_F^2(\tau_2^2+\Delta\omega_2^2)}\right)|A_{1ss}|^2\right]A_{1ss}$$
$$=-\frac{i}{2\omega_F}\left(F_1+\frac{\alpha(i\tau_2+\Delta\omega_2)}{\omega_F(\tau_2^2+\Delta\omega_2^2)}F_2\right)A_{1ss}^*. \quad (2.15)$$

Taking the magnitude squared of both sides of equation (2.15), we find the intensity of the non-trivial response of the first mode $4|A_{1ss}|^2\equiv a_1^2$ as the positive roots of the equation

$$\left[\tau_1+\left(\tau_{nl1}+\frac{\alpha^2\tau_2}{\omega_F^2(\tau_2^2+\Delta\omega_2^2)}\right)\frac{a_1^2}{4}\right]^2+\left[\Delta\omega_1-\left(\frac{3\gamma}{\omega_F}+\frac{\alpha^2\Delta\omega_2}{\omega_F^2(\tau_2^2+\Delta\omega_2^2)}\right)\frac{a_1^2}{4}\right]^2$$
$$=\frac{1}{4\omega_F^2}\left[F_1^2+\frac{\alpha F_2(\alpha F_2+2\omega_F\Delta\omega_2F_1)}{\omega_F^2(\tau_2^2+\Delta\omega_2^2)}\right]. \quad (2.16)$$

We note that equation (2.16) is a quadratic equation in a_1^2. Thus, in addition to the trivial solution $a_1=0$, which is always a solution, we are left with, at most, two additional positive solutions for a_1. Therefore, the non-trivial steady-state solutions of the first mode $x_1=a_1\cos\big(\omega_F t/2+\phi_1\big)$ is fully described by equation (2.16) and the following equation for the phase

$$e^{2i\phi_1}=\frac{A_{1ss}}{A_{1ss}^*}=\frac{-\frac{i}{2\omega_F}\left(F_1+\frac{\alpha(i\tau_2+\Delta\omega_2)}{\omega_F(\tau_2^2+\Delta\omega_2^2)}F_2\right)}{\tau_1+\left(\tau_{nl1}+\frac{\alpha^2\tau_2}{\omega_F^2(\tau_2^2+\Delta\omega_2^2)}\right)\frac{a_1^2}{4}+i\left[\Delta\omega_1-\left(\frac{3\gamma}{\omega_F}+\frac{\alpha^2\Delta\omega_2}{\omega_F^2(\tau_2^2+\Delta\omega_2^2)}\right)\frac{a_1^2}{4}\right]}. \quad (2.17)$$

From equation (2.14) we also find the steady-state solution of the second mode $A_{2ss}=a_2e^{i\phi_2}/2$. Thus, the solution a_1 of equation (2.16) along with equations (2.14)-(2.17) give complete description of the system non-trivial steady-state solutions. Note that the peak amplitude of the first mode A_{SNB} can be calculated by differentiation of equation (2.16) with respect to ω_F and setting $da_1^2/d\omega_F=0$. To the leading order approximation, the expression for the peak amplitude A_{SNB} is given by

$$A_{\mathrm{SNB}}^2=\frac{2\sqrt{\tau_2^2+\Delta\omega_2^2}\left[\omega_F^2(\tau_2^2+\Delta\omega_2^2)F_1^2+\alpha F_2(\alpha F_2+2\omega_F\Delta\omega_2F_1)\right]^{1/2}-4\omega_F^2(\tau_2^2+\Delta\omega_2^2)\tau_1}{\omega_F^2(\tau_2^2+\Delta\omega_2^2)\tau_{nl1}+\alpha^2\tau_2}. \quad (2.18)$$

Instability threshold of the trivial solution

In order to find the conditions under which the trivial solution of the first mode $a_1=0$ loses its stability, we linearize equations (2.12) and (2.13) around $A_{1ss}=0$, $A_{2ss}=$

$-\frac{(i\tau_2+\Delta\omega_2)F_2}{4\omega_F(\tau_2^2+\Delta\omega_2^2)}$, and obtain the eigenvalues of the resulting linear system

$$\delta\dot{A}_1 = -(\tau_1 + i\Delta\omega_1)\delta A_1 - \frac{i}{2\omega_F}\left(F_1 + \frac{\alpha(i\tau_2+\Delta\omega_2)}{\omega_F(\tau_2^2+\Delta\omega_2^2)}F_2\right)\delta\bar{A}_1, \tag{2.19}$$

$$\delta\dot{A}_2 = -(\tau_2 + i\Delta\omega_2)\delta A_2. \tag{2.20}$$

Note that equations (2.19) and (2.20) are uncoupled, and hence, we can analyze each equation separately. equation (2.20) can be readily solved to yield $\delta A_2 = \delta A_2(0)e^{-(\tau_2+i\Delta\omega_2)t}$. Consequently, δA_2 decays to zero for all $\tau_2 > 0$. Similarly, we seek a solution for equation (2.19) in the form $\delta A_1 = |\delta A_1|e^{i\delta\phi_1}e^{\lambda t}$, where $\delta\phi_1$ and λ are real. By substitution of the solution into equation (2.19) we find that

$$\lambda = -\tau_1 \pm \sqrt{\frac{1}{4\omega_F^2}\left[F_1^2 + \frac{\alpha F_2(\alpha F_2 + 2\omega_F\Delta\omega_2 F_1)}{\omega_F^2(\tau_2^2+\Delta\omega_2^2)}\right] - \Delta\omega_1^2}. \tag{2.21}$$

Thus, for $\lambda > 0$, the trivial solution of the first mode $a_1 = 0$ is unstable (i.e., there is a supercritical pitchfork bifurcation). The boundaries, which define the domains of the instability, form the Mathieu tongue and are given by

$$4\omega_F^2(\tau_1^2 + \Delta\omega_1^2) = F_1^2 + \frac{\alpha F_2(\alpha F_2 + 2\omega_F\Delta\omega_2 F_1)}{\omega_F^2(\tau_2^2+\Delta\omega_2^2)}. \tag{2.22}$$

Note that the same condition can be obtained from equation (2.16) by taking the limit $a_1 \to 0$.

Stability of the non-trivial steady-state solutions and local bifurcation analysis
To investigate the stability of the non-trivial steady-state solutions (which are found from equations (2.14), (2.16) and (2.17)), we superimpose a perturbation $\delta\mathbf{u} = (\delta A_1, \delta A_2)^T$ on the non-trivial fixed-points of equations (2.12) and (2.13) $\mathbf{u}_{ss} = (A_{1ss}, A_{2ss})^T$, linearize in terms of the perturbed variables, and obtain the following pair of linear complex evolution-equations for the perturbation $\delta\mathbf{u}$

$$\begin{aligned}\delta\dot{A}_1 = &-\left[\tau_1 + 2\tau_{nl1}|A_{1ss}|^2 + i\left(\Delta\omega_1 - \frac{6\gamma}{\omega_F}|A_{1ss}|^2\right)\right]\delta A_1 \\ &-\left[\tau_{nl1}A_{1ss}^2 + \frac{i}{\omega_F}\left(\frac{F_1}{2} - 2\alpha A_{2ss} - 3\gamma A_{1ss}^2\right)\right]\delta\bar{A}_1 + \frac{2i\alpha}{\omega_F}\bar{A}_{1ss}\delta A_2,\end{aligned} \tag{2.23}$$

$$\delta\dot{A}_2 = \frac{i\alpha}{\omega_F}A_{1ss}\delta A_1 - (\tau_2 + i\Delta\omega_2)\delta A_2. \tag{2.24}$$

Using Cartesian notations for the perturbations $\delta A_j = q_j + ip_j$, equations (2.23) and (2.24) can be written as $\dot{q}_1 + i\dot{p}_1 = f_1 + if_2$ and $\dot{q}_2 + i\dot{p}_2 = f_3 + if_4$. Thus, by taking the real and imaginary part of these equations, we obtain a set of four linear real evolution-equations for the perturbation quadratures $\dot{\eta} = \mathbf{J}\cdot\eta$, where $\eta = (q_1, p_1, q_2, p_2)^T, J_{nm} = \partial f_n/\partial\eta_m|_{A_{1ss},A_{2ss}}$. Therefore, the stability of the fixed points are determined by the eigenvalues λ of $\mathbf{J}$, which are the roots of the following characteristic polynomial

$$\begin{gathered}\lambda^4 + c_1\lambda^3 + c_2\lambda^2 + c_3\lambda + c_4 = 0\\ c_1 = -\mathrm{tr}(\mathbf{J}),\ c_2 = \frac{1}{2}(\mathrm{tr}(\mathbf{J})^2 - \mathrm{tr}(\mathbf{J^2})),\ c_3 = -\frac{1}{3}\left(\mathrm{tr}(\mathbf{J^3}) - \frac{3}{2}\mathrm{tr}(\mathbf{J}^2)\mathrm{tr}(\mathbf{J}) + \mathrm{tr}(\mathbf{J})^3\right),\ c_4 = \det(\mathbf{J}).\end{gathered} \tag{2.25}$$

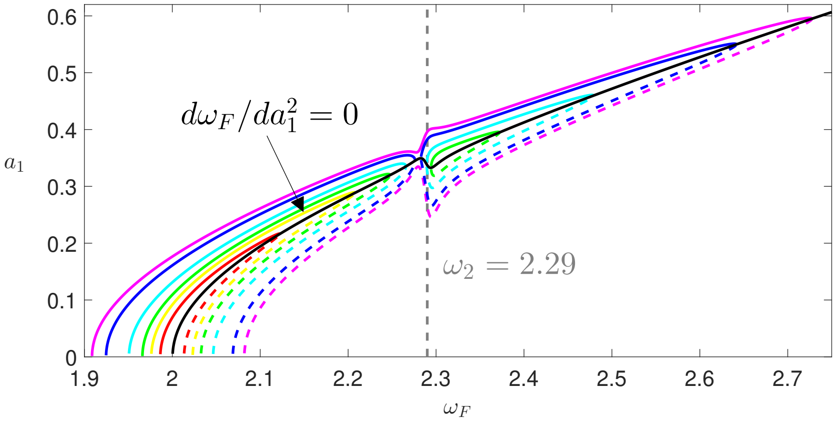

Figure 2.9: **Theoretical parametric resonance curves**. The parameter values used for the curves are: $\tau_1 = 0.0025, \tau_{nl1} = 0.175, \tau_2 = 0.00764, \alpha = 0.17, \gamma = 3.7, \omega_1 = 1, \omega_2 = 2.29, F_2 = 0.13F_1$. The magenta/dark-blue/light-blue/green/yellow/red curves are the first mode response curve for drive amplitudes $F_1 = 0.18, 0.15, 0.1, 0.07, 0.05, 0.03$. The grey vertical dashed line shows the frequency of the second mode, and the black curve show the loci of the saddle-node bifurcations.

Consequently, there is a saddle-node bifurcation whenever $c_4 = 0$, and Hopf bifurcation whenever $\Delta_3 = c_3(c_2c_1 - c_3) - c_4c_1^2 = 0$. Furthermore, near the Hopf threshold ($\Delta_3 = 0$), the frequency of the limit cycle is given by $\lambda_{1,2} = \pm i\Omega_H$, $\Omega_H^2 = c_3/c_1$. Note that the condition for the saddle-node bifurcation $c_4 = 0$ can also be obtained by differentiating equation (2.16) with respect to the drive frequency ω_F, and requiring that $d\omega_F/da_1^2 = 0$ (i.e., requirement of vertical tangency in the response curve). Fig. 2.9 shows the response curves for several values of drive amplitude F_1 along with the locus of the saddle-node bifurcations, and an indication of the second mode frequency (assuming that $\omega_2 = 2.29\omega_1$). It is clear from the figure that as the driving amplitude F_1 increases, the gap between the first two saddle-node bifurcations decreases. At a critical drive level (the magenta response curve), these two saddle-node bifurcations annihilate each other and the response becomes continuous.

2.6.5. A5: MODEL FITS USING THE COUPLED MODEL

To fit with the coupled model, equations (2.9) and (2.10) are used. The parameters from the single mode fits in the uncoupled regime (at the force levels where the coupling effects are negligible) have been taken as base parameters, since they are intrinsic to the modes themselves. This leaves only 2 additional parameters for fitting, namely the coupling strength α and the direct forcing F_2. Before the interaction, F_2 can be directly obtained from the measurements, however during the interaction the individual amplitude of the second mode is hidden beneath the parametric resonance curve. Thus, we assume a linear relation between F_1 and F_2 such that $F_2 = c_{pm}F_1$ so as to estimate the contribution of F_2 in the coupled mode dynamics. Finally, we use α as the fit parameter and minimize the error between the resonance peak (A_{SNB}) of the model and experimental data.

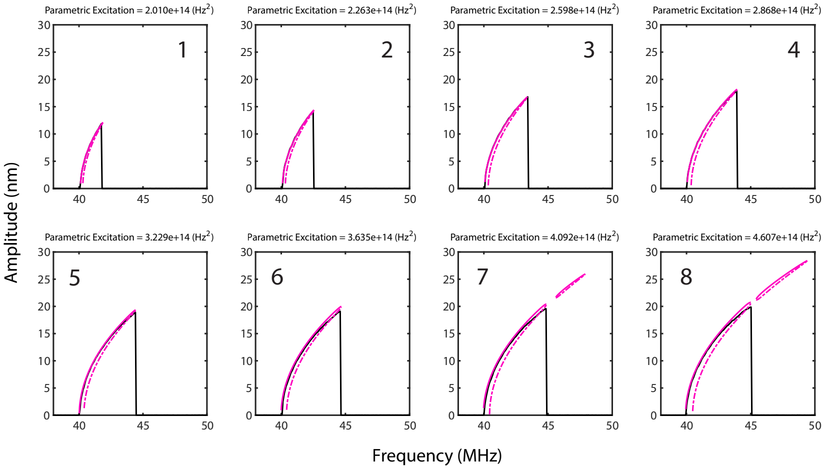

Figure 2.10: **2 mode coupled model fits.** Frequency response measurements (black) and corresponding fits (pink) obtained by using the 2 mode coupled model. The solid and dashed lines in the figure represent stable and unstable numerical solutions, respectively.

In Fig. 2.10 we report the fits to the experimental data using the coupled model(labelled to their corresponding experimental curves in Fig. 2.7), and in Table 2.1, we report the fitted values. We note that the curves with different parametric excitation are fitted with constant parameters.

Table 2.1: Parameter set extracted from the fits of Fig. 2.10

w_1	w_2	τ_1	τ_2
1.262×10^8 (rad/s)	2.841×10^8 (rad/s)	2.781×10^5 (Hz)	2.185×10^6 (Hz)
τ_{nl1}	γ	α	c_{pm}
3.139×10^{21} (Hz/m^2)	1.205×10^{31} (Hz/m)^2	2.213×10^{22} (Hz^2/m)	1.585×10^{-9} (m)

2.6.6. A6: EFFECT OF NONLINEAR DAMPING ON THE DIRECT RESONANCE

The effect of nonlinear damping can also be seen in the decaying responsivity of the Duffing response as the drive level increases(see Fig. 2.11) [23]. In order to check the consistency of the extracted nonlinear damping from parametric resonance, here we fit the direct response using the extracted intrinsic damping(τ_{nl1}) and Duffing nonlinearity(γ) reported in Table 2.1. Fig. 2.12 shows reasonably good fits for different drive levels. equation (2.1) has been used as the model for these fits with a modification of the direct drive term(considering only direct excitation i.e. $F_1 x_1 cos(\omega_F t)$ has changed to $F_1 cos(\omega_F t)$).

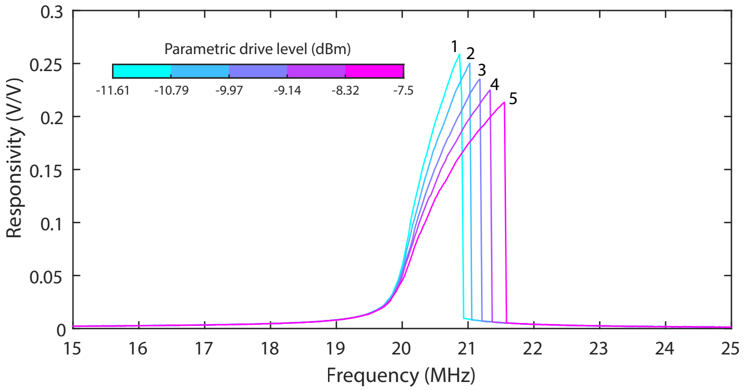

Figure 2.11: **Responsivity measurements of the direct mode.** At higher drive levels decrease in responsivity is observed due to nonlinear damping.

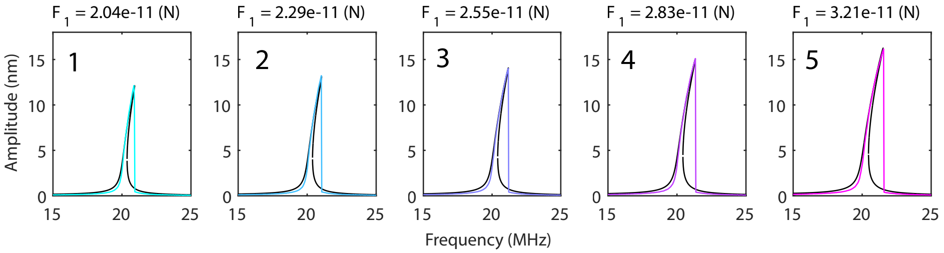

Figure 2.12: **Model fits (black) to the experimental direct resonance curves from Fig. 2.11.** Model parameters from Table 2.1 have been used for all fits.

2.6.7. A7: AMPLITUDE CALIBRATION

We measure the response of the graphene membrane in Volts from a Fabry–Pérot interferometer and convert the readings to nanometers using the nonlinear optical transduction technique presented in [60]. We note that for thin membranes and for high back-mirror reflectively, the reflected intensity $I(t)$ of the optical read-out can be approximated by

$$I(t) = A + B\cos\left(4\pi\frac{g+\bar{x}(t)}{\lambda}\right), \tag{2.26}$$

where A and B are constants, $\bar{x}(t) = x\sin(\omega_F t)$ is the membrane displacement, g is the cavity depth, and λ is the wave-length of the light used for measurement. The reflected intensity $I(t)$ in equation (2.26) is a nonlinear function of the membrane displacement, and therefore, the read-out of a monochromatic signal will contain higher-order harmonics. The amplitude of these harmonics can be obtained from a Fourier expansion of the intensity $I(t) = \sum I_{n\omega_F}\sin(n\omega_F t)$, and harmonic balancing of equation (2.26). This will lead to the following relations for the first ($I_{1\omega_F}$) and the third ($I_{3\omega_F}$) harmonics of the motion [60]:

$$I_{1\omega_F} = -B\eta x\sin(\eta g) + \frac{1}{8}Bx^3\eta^3\sin(\eta g), \tag{2.27}$$

$$I_{3\omega_F} = -\frac{1}{24}Bx^3\eta^3\sin(\eta g), \tag{2.28}$$

in which $\eta = 4\pi/\lambda$. Taking the ratio of the two harmonics, one can find the motion amplitude as follows:

$$x = \frac{2\sqrt{6}}{\eta}\sqrt{\frac{I_{3\omega_F}/I_{1\omega_F}}{1+3I_{3\omega_F}/I_{1\omega_F}}}. \tag{2.29}$$

We can then obtain the linear transduction coefficient $C_{conv} = x/I_{1\omega_F}$ by averaging multiple data points on the nonlinear resonance curves in Fig. 2.13, in order to calibrate the response where $I_{3\omega_F}$ is below the noise level. The value we obtain for our experiments is $C_{conv} = 7.92\times10^{-7}$ (m/V). We also note that, above certain amplitudes, saturation of

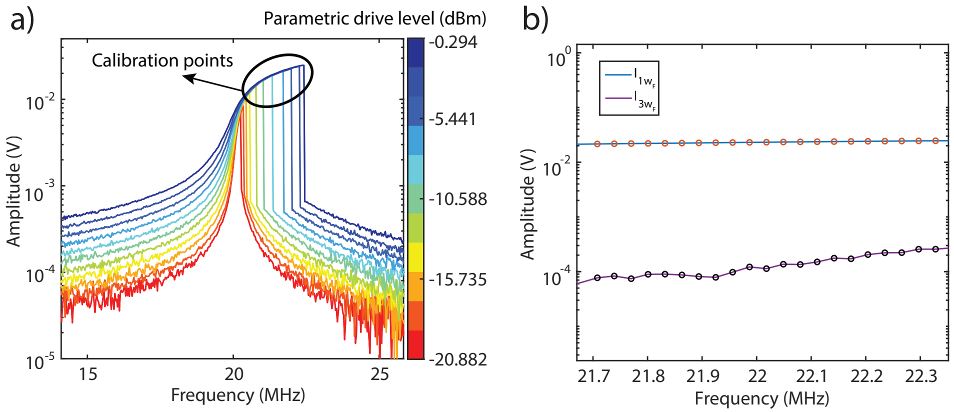

Figure 2.13: **Calibration method.** (a) Nonlinear optical effect observed in the Duffing response has been used for amplitude calibration. (b) First and third harmonics arising from optical nonlinearity. The ratio of these harmonics are used to determine oscillation amplitude.

the resonance frequency curves become apparent for which the nonlinear transduction error becomes significant. We correct for this using [60]

$$x_{nl} = \left(1 + \frac{1}{8}x^2\eta^2\right)x. \tag{2.30}$$

3

MULTI-MODE NONLINEAR DYNAMICS OF NANOMECHANICAL RESONATORS

Mechanical nonlinearities dominate the motion of nanoresonators already at relatively small oscillation amplitudes. Although single and coupled two-degrees-of-freedom models have been used to account for experimentally observed nonlinear effects, it is shown that these models quickly deviate from experimental findings when multiple modes influence the nonlinear response. Here, we present a nonlinear reduced-order modelling methodology based on FEM simulations for capturing the global nonlinear dynamics of nanomechanical resonators. Our physics-based approach obtains the quadratic and cubic nonlinearities of resonators over a wide frequency range that spans 70 MHz. *To qualitatively validate our approach, we perform experiments on a graphene nanodrum driven opto-thermally and show that the model can replicate diverse ranges of nonlinear phenomena, including multi-stability, parametric resonance, and different internal resonances without considering any empirical nonlinear fitting parameters. By providing a direct link between microscopic geometry, material parameters, and nonlinear dynamic response, we clarify the physical significance of nonlinear parameters that are obtained from fitting the dynamics of nanomechanical systems, and provide a route for designing devices with desired nonlinear behaviour.*

This chapter is under review for publication in the journal Physical Review Applied.

3.1. INTRODUCTION

NAnomechanical resonators are the devices of choice for high-performance sensing since they respond to minuscule forces [10], [63], [64]. More recently, they have emerged as ideal systems for exploring nonlinear dynamic phenomena. Thanks to their high force sensitivity they are easily driven into the nonlinear regime [65]. Their small mass leads to high resonance frequencies, which facilitates high-speed measurements and, especially in ultra-thin resonators, the high aspect ratio allows tuning of tension and resonance frequencies to explore a variety of nonlinear phenomena [66].

When nanomechancial devices are driven into resonance, already at small amplitudes Duffing nonlinearities precipitate in the motion, leading to softening- or hardening-type nonlinear responses [23]. When the nonlinear regime is traversed further, with the increase in drive amplitude, other eigenmodes begin to partake in the motion through autoparametric excitations and nonlinear intermodal couplings [46]. In this nonlinear domain, many studies have reported significant impact of these nonlinear couplings on the effective dissipation and stiffness of the vibration modes [32], [67]. A number of exotic nonlinear phenomena have also been showcased, ranging from frequency noise suppression [49] and intermodal storage of mechanical energy [51], [68], to the generation of mechanical frequency combs [53], [69].

Efforts made to date in explaining nonlinear phenomena often rely on proposing analytical nonlinear low-degrees-of-freedom (DOFs) models that are fit to the experimental data to prove their validity. However, since there is no direct link between the magnitude of the resulting fit parameters and the geometry or material properties of the nanomechanical device, it is difficult to evaluate whether these models are the only ones that can account for the experimental data, and which parameters are the most relevant. Moreover, since there is no direct link between the model parameters and the underlying physics, it is difficult to extract device information from the fitting. A realistic description of the complex nonlinear dynamics of nanoresonators with pure analytical methods such as rotating-wave approximation [70] or harmonic balancing [22] is not always sufficiently accurate, because analytical methods are constrained to a limited number of DOFs. Purely numerical methods such as molecular dynamics or dynamic nonlinear Finite Element Method (FEM) simulations may resolve this issue, yet they are computationally expensive [34], [71] and provide less insight. Therefore, an intermediate approach, whereby analytical multi-mode nonlinear dynamic models are constructed from the physical device properties using numerical methods, can be extremely valuable for the precise and fast analysis of the nonlinear dynamics of nanomechanical systems.

In this article we develop and utilize a physics-based Reduced-Order Model (ROM) to characterize multi-mode nonlinear dynamics of nanomechanical resonators over a wide frequency range. Our approach makes use of FEM simulations to probe the geometric nonlinearities of nanoresonators for a large number of coupled vibrational modes. To validate our method, we perform experiments on a graphene nanodrum that is driven opto-thermally into the strong mode coupling regime. We show that the physics-based model can capture the response of the seven directly excited and two parametrically excited modes of the graphene nanodrum from linear to nonlinear regime, in a frequency range that spans 70 MHz. The model uses the Young's modulus and pre-stress to obtain the coupling coefficients, thus providing insight into the influence of geometric and

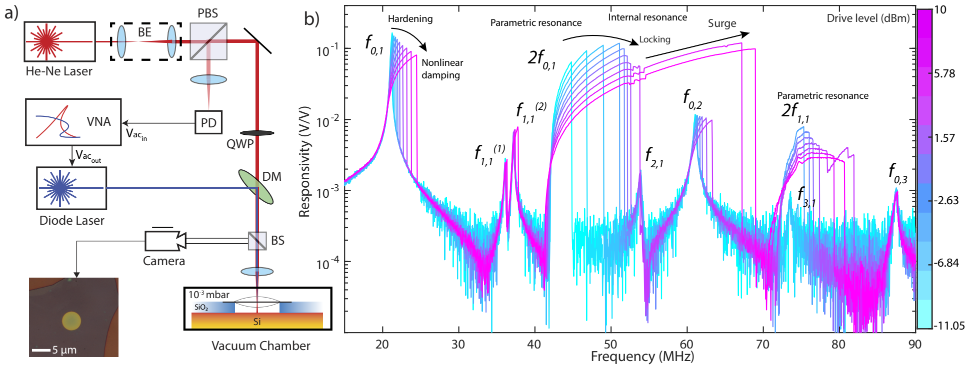

Figure 3.1: **Measuring the motion of a nonlinear graphene nanodrum.** (a) Schematic of the measurement setup. BE, PBS, BS, QWP, DM and VNA stand for beam expander, polarized beam splitter, beam splitter, quarter-wave plate, dichroic mirror and vector network analyzer, respectively. (b) Measurements reveal a range of nonlinear dynamic phenomena for the graphene nanodrum at relatively small amplitudes. At high drive levels, graphene nanodrum exhibits complex nonlinear behavior where the frequency response shows hardening nonlinearity, signatures of nonlinear damping, parametric resonance, mode couplings and internal resonances. The labels $f_{\mathrm{p,m}}$ are frequencies associated with circular drum mode shapes that are found from FEM simulations. Here, p stands for the number of nodal lines and m is the number of nodal circles.

physical parameters on the coupled dynamics of nanomechanical resonators. Since the method is FEM-based, it can be applied further to nanomechanical devices of virtually any geometry, allowing predicting and designing a variety of nonlinear phenomena.

3.1.1. EXPERIMENTAL MODEL SYSTEM

As an experimental model system for demonstrating the method, we probe the complex dynamics of a graphene nanodrum resonator. The resonator is fabricated by dry transfer of $h = 10$ nm thick multi-layer graphene over a $d = 5$ µm diameter and 285 nm deep circular cavity, etched in a layer of SiO_2 on a Si substrate. To study the mechanical vibrations of the nanodrum, we opto-thermally drive it using a blue laser ($\lambda = 405$ nm) and measure its response by a red laser ($\lambda = 633$ nm) using laser interferometry (Fig. 3.1a). At low drive powers, a linear set of resonance peaks can be obtained, showing the activation of multiple modes of vibration that we can identify easily using FEM simulations. As the drive level is increased, the nanoresonator quickly shows signs of nonlinearity (Fig. 3.1b). It is possible to observe the well-studied Duffing (hardening type) nonlinearity in several modes already at relatively small amplitudes (below -6 dBm).

By further increasing the drive level, we notice rapid activation of a plethora of nonlinear dynamic responses. For instance, when the excitation frequency is tuned to twice the resonance frequency of the modes $f_{0,1}$ and $f_{1,1}$, it is possible to detect strong parametric resonances [59]. Since the tension of the nanodrum is directly related to its stiffness, modulation of the tension via opto-thermal actuation parametrically excites the nanodrum. Consequently, for conditions where the drive is strong enough, period doubling instabilities emerge, resulting in parametric resonances [59]. These resonances can reach high amplitudes and span wide frequency ranges thanks to the Duffing hardening nonlinearity. Especially at drive frequencies where the frequencies of these modes satisfy internal resonance conditions [46], they strongly interact with other modes of vibration. This can be observed in Fig. 3.1b at drive levels above 2 dBm, around the region where the parametrically driven $f_{0,1}$ and the directly driven $f_{2,1}$ are interacting. As the parametric response of $f_{0,1}$ approaches $f_{2,1}$, it is also possible to observe a decrease in the responsivity as well as a reduction in the rate of increase in the nonlinear frequency of the parametric resonance – a phenomenon that we label as "locking" in Fig. 3.1b. Only after a certain drive level is reached, this "locking" barrier is surpassed, and the parametric resonance surges to a higher amplitude and frequency [67]. Other than this apparent interaction, a similar coupled dynamic response can be noticed in the neighborhood of the parametrically driven $f_{1,1}$ and directly driven $f_{3,1}$.

Another interesting observation is the decrease in the responsivity of the nanoresonator for the directly driven modes of vibration with the increase in drive level (see the nonlinear response around $f_{0,1}$ and $f_{0,2}$ in Fig. 3.1b for instance). This reduction, which is a result of the emergence of nonlinear dissipation [23], was first observed in resonators that can reach strong nonlinear regime [26]. It was recently shown that such nonlinear dissipation process could also be mediated when two modes of vibration are coupled via internal resonance [67]. Capturing such nonlinear dissipation processes by analytical means, however, when multiple modes are contributing to the response, is far from being trivial. In order to deepen our understanding of these complex multi-modal interactions, we thus introduce a FEM-based ROM model [72].

3.2. REDUCED-ORDER MODELLING PROTOCOL

The method for modelling the complex dynamics showcased in Fig. 3.1b consists of five steps, starting with the generation of a FEM model of the nano device (step I in Fig. 3.2). For this purpose, any FEM software package that can handle geometric nonlinearities can be used (we have chosen to use COMSOL in this work). The FEM model of the circular graphene nanodrum resonator uses plate elements and fixed boundary condition. We use the literature values for the mass density and Poisson's ratio of graphene to be $\rho = 2267\,\mathrm{kg\,m^{-3}}$ and $\nu = 0.16$. As the geometry of the resonator is already known from optical microscopy and Atomic Force Microscopy (AFM) measurements, this leaves only two unknown parameters to be determined for building the model, namely the pre-tension and the Young's modulus of the nanodrum. Since the linear resonance frequencies of the graphene membrane are dominated by the pre-tension, we can extract its value from frequency response measurements at low drive levels. However, if only the fundamental frequency is taken into account when determining the pre-tension, it is not possible to explain the splitting of the asymmetric modes, like $f_{1,1}^{(1)}$ and $f_{1,1}^{(2)}$ in Fig. 3.3a. In a perfectly symmetric drum, these eigenmodes are degenerate, i.e., they have the same frequency. But in practice, there is a mismatch in the tension along the in-plane axes that causes these modes to have slightly different frequencies. The frequencies of the first degenerate mode, together with the fundamental frequency, are enough to extract the tension in the membrane by matching the experimental linear resonance frequencies of the first three modes in the FEM analysis. By doing this we found the pre-tension in the membrane to be $T_x = 0.321\,\mathrm{N\,m^{-1}}$ and $T_y = 0.257\,\mathrm{N\,m^{-1}}$ for two perpendicular axes in the plane. To find Young's modulus of the graphene nanodrum we then used the linear resonance frequencies of the higher modes following the method described

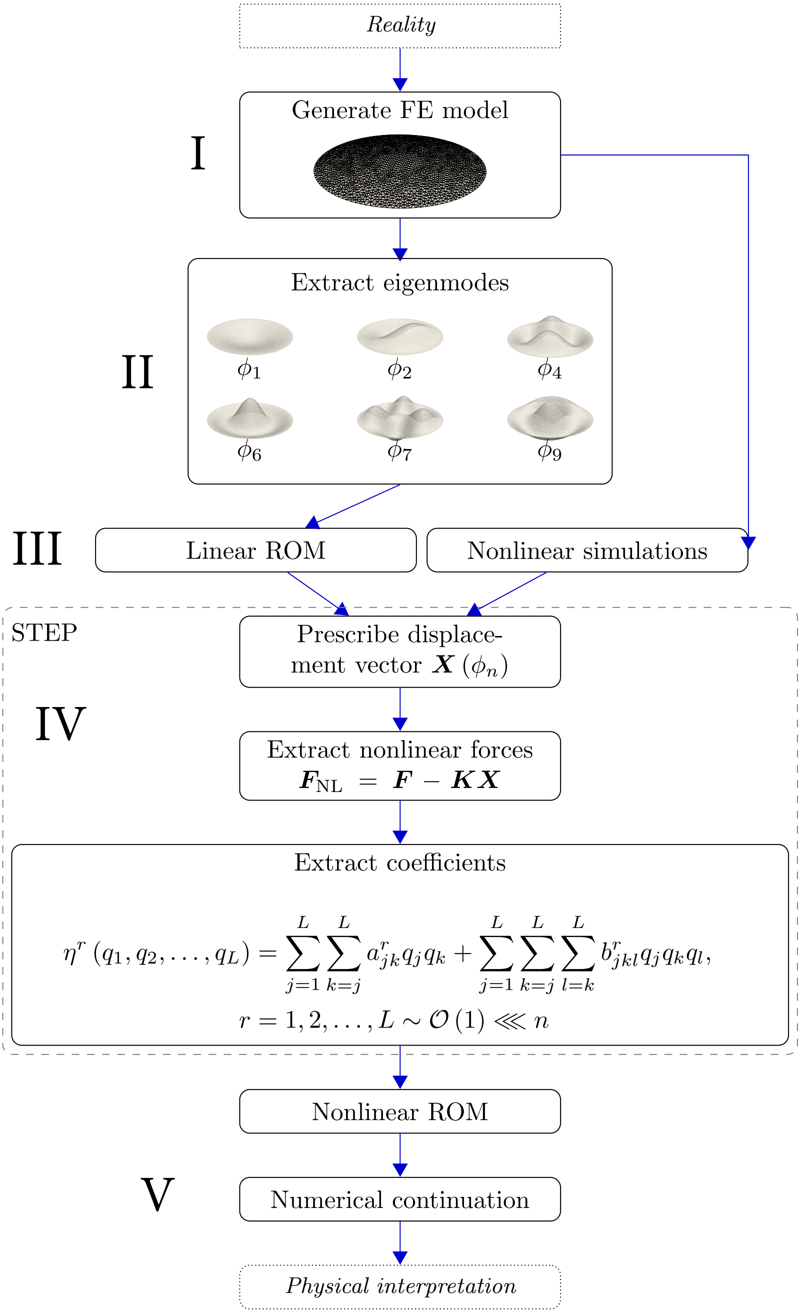

Figure 3.2: **The flowchart of the ROM procedure for nonlinear dynamic simulations.** The frequency response and AFM measurements are used to extract the physical parameters for building the FE model, which is then utilized to obtain linear and nonlinear reaction forces of the device, given prescribed displacements in terms of superposition of eigenmodes. These forces are then used for extracting the coefficients of nonlinear terms in the ROM [72]. Finally the nonlinear multi-mode model is simulated numerically to obtain the full nonlinear dynamic response.

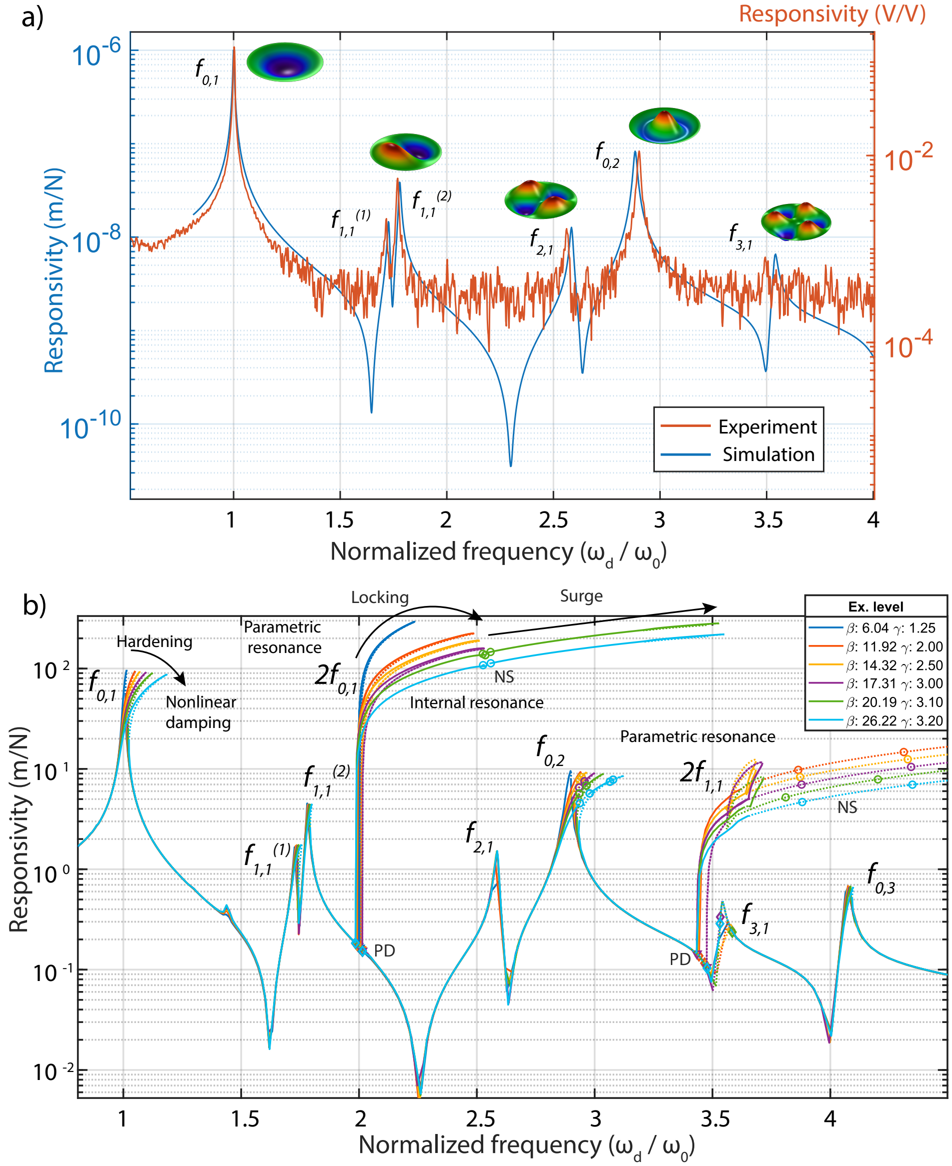

Figure 3.3: **The simulated linear and nonlinear dynamic responses of the ROM.** a) Frequency response measurements at linear regime are used for extracting the pre-tension and Young's Modulus of the membrane. b) The simulated nonlinear frequency response of the graphene nanodrum, where β is the direct drive intensity and γ is the parametric drive intensity. It is possible to capture the experimentally observed nonlinear phenomena using the ROM , such as hardening nonlinearities, parametric resonances and internal resonance induced physics such as frequency locking and amplitude surge. Bifurcation points are also detected during numerical simulations, diamond indicators stand for period doubling bifurcations (PD), whereas circles stand for the Neimark-Sacker bifurcation (NS).

in [73]; we found a Young's modulus of 410 MPa (Fig. 3.3a), which is within the values reported in the literature [74], [75].

By performing linear vibration analysis in the FEM software, we can now obtain the $n \times n$ linear mass and stiffness matrices (K and M, respectively), as well as the eigenvalues ω_n and eigenmode matrix Φ, where n is the number of DOFs used in the FEM simulations (step II in Fig. 3.2). Therefore, for an n-dimensional displacement vector X in the FEM model, we obtain the following set of discrete equations:

$$M\ddot{X}(t) + C\dot{X}(t) + KX(t) + H(X(t)) = F(t), \tag{3.1}$$

where $\ddot{X}$ denotes acceleration, $\dot{X}$ velocity, H the nonlinear force vector, and $F(t)$ is the nodal force vector. Here, the linear damping matrix C accounts for dissipation. Currently nonlinear damping is not yet included in the equation of motion, although viscous material damping might be added via an imaginary term in the material's Young modulus. Evidently, in a finely meshed FEM model, the large number of degrees of freedom n in Eq. (3.1) in combination with the wide frequency range, makes it practically impossible to use the FEM for simulating nonlinear dynamic responses like those in Fig. 3.1b. Therefore, we use a subset L of the n eigenmodes for explaining the observed physics, where $L \ll n$. This mathematically means reducing the number of DOFs to only a few that are capable of replicating the nonlinear dynamics of the full model. To do so, we use the modal coordinate transformation $X = \Phi q$, expressing the displacement as a superposition of eigenmode shapes, and only select a subset $\Phi_{n\times L}$ of eigenvectors, such that q is the L-dimensional modal amplitude vector. Using this transformation, Eq. (3.1) can be re-written in modal coordinates as

$$\tilde{M}\ddot{q}(t) + \tilde{C}\dot{q}(t) + \tilde{K}q(t) + \eta(q(t)) = \tilde{F}(t), \tag{3.2}$$

where $\tilde{M} = \Phi^T M\Phi$, $\tilde{C} = \Phi^T C\Phi$, $\tilde{K} = \Phi^T K\Phi$, $\eta = \Phi^T H$ and $\tilde{F}(t) = \Phi^T F(t)$.

From the linear FEM eigenmode simulation, all these matrices and vectors except η can be determined (step I-III in Fig. 3.2). To obtain this nonlinear matrix we perform multiple nonlinear stationary FEM simulations, with suitably chosen displacements X_c along the Stiffness Evaluation Procedure (STEP, see IV in Fig. 3.2) that we briefly outline in what follows and along the lines of Ref. [72].

For any nodal displacement vector $X = X_c$, the reaction forces can be transformed into the modal domain and used for the extraction of nonlinear internal forces of the nanodrum. We do this by carefully prescribing nodal displacement vectors X_c, to calculate the corresponding linear reaction forces F_{L} since $F_{\mathrm{L}} = KX_c$. After finding the linear reaction forces, we perform a full nonlinear static analysis in the FEM package, considering that the nanodrum is subjected to the same displacement vector X_c, and obtain the total nodal reaction force F_{T}. By subtracting the linear reaction forces from this full static solution, i.e., $F_{\mathrm{NL}} = H(X_c) = F_{\mathrm{T}}(X_c) - KX_c$, we then obtain the nonlinear reaction force and map that on the subset of eigenmodes selected as follows: $\eta = \tilde{F}_{\mathrm{NL}} = \Phi^T F_{\mathrm{NL}}$ (see steps III and IV in Fig. 3.2). We finally expand this nonlinear reaction force for every mode of vibration in terms of quadratic and cubic nonlinear terms as follows:

$$\eta^{(r)} = \sum_{j=1}^{L}\sum_{k=j}^{L} \alpha_{jk}^{(r)} q_j q_k + \sum_{j=1}^{L}\sum_{k=j}^{L}\sum_{l=k}^{L} b_{jkl}^{(r)} q_j q_k q_l, \tag{3.3}$$

where r stands for the rth equation of motion also associated with the rth mode, and j, k, l are the mode numbers. Furthermore, L is the number of modes that is being considered in the ROM. We note that these cubic and quadratic nonlinear terms for single or two-mode models are commonly used to simulate nonlinear dynamics of nanomechanical resonators. However, here we extract them purely from geometric nonlinearities and can expand that to any number of modes of vibration, up to the number of DOFs that is being considered in the FEM simulations.

The procedure explained above enables us to generate a set of linearly independent F_{NL} equations by applying different displacement vectors $X_c(\phi_r)$, $r = \{1, \dots L\}$; these are selected such that they are superpositions of eigenvectors ϕ_r where each combination provides unique information about a nonlinear term through simulations, e.g., $X_c = \pm\phi_j q_j \pm \phi_k q_k \pm \phi_l q_l$. In order to obtain information about the nonlinear reaction forces, the modal amplitudes in the displacement vector X_c should be chosen such that the nano device reaches the geometric nonlinear regime.

3.2.1. EXTRACTION OF NONLINEAR FORCES

To clarify the procedure outlined above, we demonstrate how the nonlinear coefficients of the ROM can be derived for two hypothetical generalized coordinates, q_1 and q_2. We start by determining the uncoupled nonlinear coefficients of the system. For the first generalized coordinate q_1, we construct displacement vectors X_c from ϕ_1, such that only nonlinear terms associated with q_1 are activated:

$$X_1 = +\phi_1 q_1, \tag{3.4}$$
$$X_2 = -\phi_1 q_1. \tag{3.5}$$

This results in two equations with two unknowns:

$$\tilde{F}^{(1)}_{\mathrm{NL}}(X_1) = \alpha^{(1)}_{11} q_1^2 + b^{(1)}_{111} q_1^3, \tag{3.6}$$
$$\tilde{F}^{(1)}_{\mathrm{NL}}(X_2) = \alpha^{(1)}_{11} q_1^2 - b^{(1)}_{111} q_1^3, \tag{3.7}$$

which can be solved to obtain $\alpha^{(1)}_{11}$ and $b^{(1)}_{111}$, that are namely the quadratic and cubic uncoupled nonlinear terms for the modal coordinate q_1. Similarly, by prescribing the system to move on its second eigenmode ϕ_2 we can obtain $\alpha^{(2)}_{22}$ and $b^{(2)}_{222}$. Next, in order to determine the coupled terms, we use the superposition of the eigenmodes as follows:

$$\begin{aligned} X_3 &= +\phi_1 q_1 + \phi_2 q_2, \\ X_4 &= -\phi_1 q_1 - \phi_2 q_2, \\ X_5 &= +\phi_1 q_1 - \phi_2 q_2, \end{aligned} \tag{3.8}$$

which results in the following set of 3 equations with a_{12}, b_{112}, b_{211} as unknowns:

$$
\begin{aligned}
\tilde{F}_{\mathrm{NL}}^{(1)}(X_3) &= \alpha_{11}^{(1)} q_1^2 + b_{111}^{(1)} q_1^3 + \alpha_{12}^{(1)} q_1 q_2 + \alpha_{22}^{(1)} q_2^2 \\
&\quad + b_{112}^{(1)} q_1^2 q_2 + b_{122}^{(1)} q_1 q_2^2 + b_{222}^{(1)} q_2^3, \\
\tilde{F}_{\mathrm{NL}}^{(1)}(X_4) &= \alpha_{11}^{(1)} q_1^2 - b_{111}^{(1)} q_1^3 + \alpha_{12}^{(1)} q_1 q_2 + \alpha_{22}^{(1)} q_2^2 \\
&\quad - b_{112}^{(1)} q_1^2 q_2 - b_{122}^{(1)} q_1 q_2^2 - b_{222}^{(1)} q_2^3, \\
\tilde{F}_{\mathrm{NL}}^{(1)}(X_5) &= \alpha_{11}^{(1)} q_1^2 + b_{111}^{(1)} q_1^3 - \alpha_{12}^{(1)} q_1 q_2 + \alpha_{22}^{(1)} q_2^2 \\
&\quad - b_{112}^{(1)} q_1^2 q_2 + b_{122}^{(1)} q_1 q_2^2 - b_{222}^{(1)} q_2^3.
\end{aligned}
\tag{3.9}
$$

Since all of the uncoupled parameters ($\alpha_{jk}^{(r)}$ and $b_{jkl}^{(r)}$ where $j = k = l$) are already known thanks to the previous step, the coupling terms between two modes ($\alpha_{jkl}^{(r)}$ and $b_{jkl}^{(r)}$ where $j = k \neq l$, etc.) can be found by solving these three linearly independent equations (Eq. (3.9)). In case of coupling between 3 modes of vibration, the third mode's eigenvector shall also be included in the prescribed displacement, i.e., $X_c = \phi_j q_j + \phi_k q_k + \phi_l q_l$, and a similar procedure shall be followed to obtain $b_{jkl}^{(r)}$, where $j \neq k \neq l$. We note that this procedure can be generalized and easily applied to a system with L number of modes.

The number of eigenmodes to consider depends on the complexity of the problem and the dynamic range of interest. In our study, and in order to replicate the nonlinear dynamics observed in Fig. 3.1b, we used 11 out-of-plane modes in a frequency range that spans 20 MHz to 90 MHz. For convenience, we compare in Tab. 3.1 the coupling terms for the first two axisymmetric modes of an ideal (with uniform tension) nanodrum, obtained analytically (see Appendix BI) [69] with the FE-based ROM approach explained here. We also provide the quadratic and cubic nonlinear terms of the experimentally tested graphene nanodrum for seven modes of vibration in Appendix B2. As additional examples, we also provide the nonlinear ROM parameters extracted from this protocol for various other nanomechanical systems such as nanomechanical strings and rectangular membrane resonators in Appendix B2.

It is important to mention that the ROM approach sketched here can also account for the influence of in-plane modes of vibration on the nonlinear terms associated with out-of-plane DOFs. This is of great importance for probing nonlinear stiffness terms with accuracy since it has been shown that neglecting the influence of in-plane modes could result in overestimation of the stiffness [22], [76]. In the analytical setting, effects of in-plane modes could be condensed into the out-of-plane modes by assuming zero in-plane inertia since they have orders of magnitude higher frequencies, thus from the frame of reference of out-of-plane modes, act almost instantaneously. In this way they can be treated statically and their effects can be condensed into the out-of-plane modes, without having to calculate their inertial effects [77]. Instead of including the in-plane modes, the FEM method described here can automatically include their effect more efficiently by leaving the in-plane displacements free (instead of fixed) while applying the out-of plane membrane displacement X_c. As such, in-plane effects are automatically condensed into the nonlinear parameters out-of-plane modes. After the construction of η and the nonlinear ROM, we incorporate the coupled nonlinear differential equa-

	Analytic		STEP	
	Mode 1	Mode 2	Mode 1	Mode 2
b_{111}	2.84	-0.57	2.84	-0.57
b_{222}	-3.32	22.76	-3.29	22.9
b_{112}	-1.73	9.25	-1.71	9.27
b_{122}	9.25	-9.96	9.27	-9.85

Table 3.1: Comparison of the nonlinear coupling coefficients for the first two axisymmetric modes of the graphene nanodrum obtained by an analytical method and the ROM approach. Coefficients are normalized by $c = Eh/r^2$ where E is the Young modulus, h is the thickness and r is the radius of the membrane. We note that the quadratic coupling terms are all zero for a flat symmetric membrane.

tions in a numerical continuation package (AUTO) [78] and obtain the steady-state response for different drive frequencies and drive levels, i.e., the frequency response (step V in Fig. 3.2). We utilize the numerical continuation software also to detect bifurcations in the system, which are crucial for understanding the complex nonlinear dynamics of nanoresonators.

3.3. SIMULATIONS OF THE REDUCED-ORDER MODEL

We simulate the ROM for different direct and parametric drive levels, $\tilde{F}^{(r)}(t) = F^{(r)}_{\text{dir}} + F^{(r)}_{\text{par}}$, where $F^{(r)}_{\text{dir}} = J^{(r)}\beta\cos(\omega_d t)$ and $F^{(r)}_{\text{par}} = J^{(r)}q_r\gamma\cos(\omega_d t)$, with γ denoting the parametric drive intensity, β the direct drive intensity, and J the force mapping vector. We shall note that in order to obtain the modal forces $J^{(r)}$ we use the Duffing shift in the frequency of the high amplitude saddle-node points per drive level. For simplicity, in our simulations we use the Q factor of the fundamental mode ($Q = 180$) for all the modes.

Fig. 3.3b shows the simulated frequency response of the nonlinear ROM for various drive levels. Simulations are in good qualitative agreement with the experimental frequency responses in both linear and nonlinear regimes. Although it was attempted to obtain quantitative agreement in the nonlinear regime, this was not fully achieved, possibly due to small imperfections in the membrane that deviate its behavior from the FE model. Similar to experiments, it is possible to observe period doubling bifurcations of modes $f_{0,1}$ and $f_{1,1}$ around $\omega_d = 2f_{0,1}$ and $\omega_d = 2f_{1,1}$ caused by the parametric drive. When the first parametric resonance reaches the vicinity of the second asymmetric mode $f_{2,1}$, it suffers a reduction in the simulated responsivity in Fig. 3.3b which is consistent with the experimental observation in Fig. 3.1b. We also see the frequency locking at the internal resonance. With further increase in the drive level, similar to the experiments, we observe that the frequency locking "barrier" is broken, and the frequency of parametric resonance peak surges to 3.5 times the frequency of the fundamental mode $f_{0,1}$. After the surge, we also note the presence of the Neimark-Sacker bifurcation nearby the internal resonance at $\omega_d/\omega_0 = 2.538$, which indicates the emergence of aperiodic oscillations [69], [79].

The experiments and simulations depicted in Figs. 3.1b and 3.3 demonstrate that, rather than being governed by just two DOFs, the complex motion of the graphene nanodrum around $2.5f_{0,1}$ is a combination of interactions between multiple modes of vi-

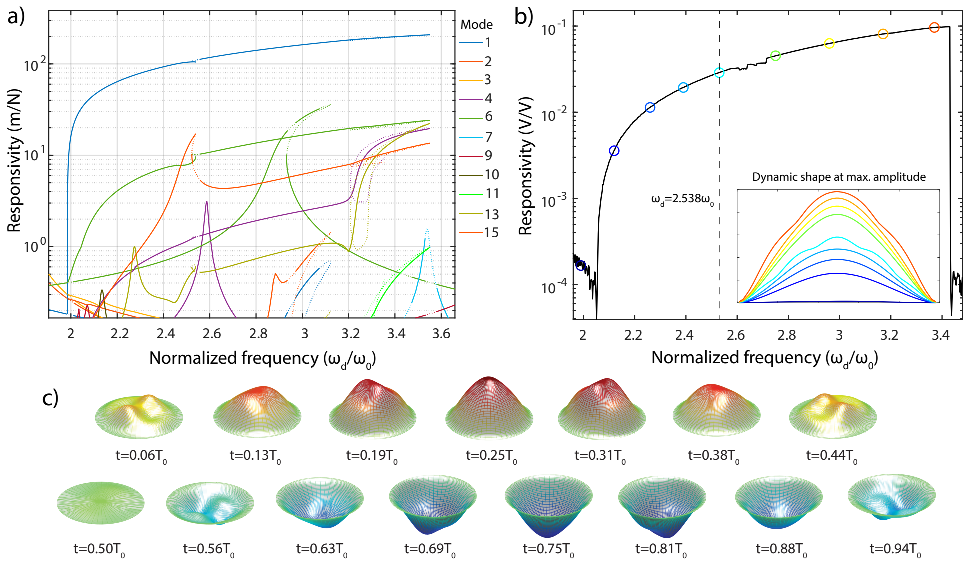

Figure 3.4: **Simulated overall nonlinear dynamic response of the graphene membrane at principal parametric resonance of $f_{0,1}$.** a) Simulated shape of the membrane at maximum amplitude level during its parametric resonance at specific drive frequencies, displayed on the experimental parametric resonance curve. Solid lines indicate stable solutions whereas dashed lines indicate unstable ones. b) Full simulated frequency response at the principal parametric resonance of mode $f_{0,1}$, showing activation of many other modes in the system during the strong parametric resonance, specially around the internal resonance region $\omega_d/\omega_0 = 2.538$. c) Shape of the membrane during a period of oscillation at internal resonance ($\omega_d/\omega_0 = 2.538$), displaying multiple mode shapes within a single period of oscillation with different frequencies. T_0 is a single period of mode $f_{0,1}$. Amplitude of the response is amplified for visual convenience.

bration. We examine the contribution of numerous vibrational modes in the vicinity of the first parametric resonance in order to trace the energy redistribution among various interacting modes. Fig. 3.4a shows strong activation of multiple modes at the internal resonance point, where axisymmetric modes $f_{0,2}$ and $f_{0,3}$ (mode numbers 6 and 15) with asymmetric mode $f_{2,1}$ (mode number 4) are most notably excited. Time responses of the modes during one period of $f_{0,1}$ oscillation at $\omega_d/\omega_0 = 2.538$ are also shown for convenience (Appendix B3). A more visual representation of the time signals can be obtained by using the modal amplitudes q from AUTO to superpose the FEM mode shapes ϕ, thereby reconstructing the total mechanical response and the deflection shape X of the graphene nanodrum during internal resonance (see Fig. 3.4b and 3.4c). If we analyze the nanodrum shape at its maximum amplitude level during an oscillation, we can see that the effective deflection shape is unique near the internal resonance point (Fig. 3.4b). Dissecting the total motion of the membrane by taking snapshots at different times during a single period of the fundamental mode $f_{0,1}$ (Fig. 3.4c) further reveals the strong influence of the multi-modal interaction. It is possible to clearly observe the emergence of other mode shapes during a single oscillation of $f_{0,1}$ parametric resonance. These simulations clearly showcase the energy pathways that lead to the aforementioned nonlinear dissipation phenomenon, not only at the clearly visible internal resonance, but also at responses that look regular, like the direct resonance of $f_{0,1}$. When the global frequency response per mode is analyzed, it is also possible to see the autoparametric activation of multiple modes around the $f_{0,1}$ where most of the energy ends up in $f_{0,3}$ (see Appendix B3).

3.4. DISCUSSION

We note that the favored energy pathways for each system will be distinct due to variations in pre-tension, geometry, and material properties. These physical parameters dictate the system's capacity to "internally resonate", due to their effects on the nonlinear terms and resonance frequencies. In the literature, it is common to model nonlinear systems by disregarding the effects of multi-modal interactions, especially if there are no other visible modes contributing to the measurement data. Most of the time, as discussed before, this results in using empirical fit parameters to explain the observations. In this case, the assumption is that, all the interactions effectively renormalize the terms in the single mode equation (generally being Duffing or Duffing-van der Pol). The downfall of this assumption is that, in reality, the effects of multi-modal interactions are amplitude and drive frequency dependent [67], whereas re-normalization through empirical fit parameters assumes constant effects. This means that such simplistic models, at best, will agree with the experiments only for a snapshot of frequency response and cannot explain the overall dynamics at higher drive levels and for wide frequency ranges. Utilizing a method that fully relies on physical parameters and includes as many modes as needed, automatically resolves this problem, while clearly displaying the enigmatic nature of these intermodal interactions and energy dissipation pathways.

In summary, we utilized a nonlinear ROM technique to characterize the multi-modal interactions of nanomechanical resonators. We used FEM simulations as the basis to develop our physics-based model, that relies purely on measurable quantities from experiments. We calculated the linear and nonlinear internal forces using FEM simulations to extract quadratic and cubic nonlinear terms for constructing the full nonlinear ROM. By simulating the response curves with the model and comparing the results to nonlinear dynamic measurements of a graphene nanodrum resonator, we showed that the model can replicate complex nonlinear intermodal interactions. Moreover, by tracking simultaneous activation of modal amplitudes, we have identified intermodal energy transfer pathways mediated by nonlinear couplings between multiple modes of vibration. Our study provides an efficient and accurate protocol for modelling complex nonlinear dynamics of nanomechanical resonators in a global manner, purely based on material and geometrical parameters. As a result, we anticipate that this protocol will not only aid in explaining the multi-mode nonlinear dynamics of nanoresonators, but will also serve as a framework for designing optimized nanoresonators that can take advantage of the powerful phenomena that nonlinear dynamics has to offer [80], [81].

3.5. APPENDIX B

3.5.1. B1: ANALYTICAL MODEL FOR AN IDEAL MEMBRANE WITH TWO-DEGREES-OF-FREEDOM

In order to benchmark the method provided in the main section, we use the Rayleigh-Ritz approach to obtain the equations of motion for a circular membrane [22], [61], [69]. The elastic strain energy of the drum is obtained as

$$U=\int_0^{2\pi}\int_0^R \frac{Eh}{2(1-\nu^2)}\Big(\epsilon_{rr}^2+\epsilon_{\theta\theta}^2+2\nu\epsilon_{rr}\epsilon_{\theta\theta}+\frac{1-\nu}{2}\gamma_{r\theta}^2\Big)r\,dr\,d\theta, \tag{3.10}$$

in which h is the thickness of the drum, R is the radius, E is the Young's modulus, and ν is the Poisson's ratio. Moreover, ϵ_{rr}, $\epsilon_{\theta\theta}$, and $\gamma_{r\theta}$ are the normal and shear strains. During axisymmetric oscillations $\gamma_{r\theta}=0$, and the normal strains are obtained in terms of the transverse deflection (w) and radial displacement (u) of the drum as follows

$$\epsilon_{rr}=\frac{\partial u}{\partial r}+\frac{1}{2}\Big(\frac{\partial w}{\partial r}\Big)^2+\Big(\frac{\partial w}{\partial r}\Big)\Big(\frac{\partial w_0}{\partial r}\Big), \tag{3.11}$$

$$\epsilon_{\theta\theta}=\frac{u}{r}. \tag{3.12}$$

In Eq.(4.4), w_0 is the initial transverse displacement of the drum associated with zero initial stress, and is equal to zero when assuming ideal symmetric membrane. By taking into account the modal interactions between the first two axisymmetric eigenmodes and fixed boundary conditions $(u=w=0)$, the solution is approximated as

$$w=q_1(t)J_0\Big(Z_1\frac{r}{R}\Big)+q_2(t)J_0\Big(Z_2\frac{r}{R}\Big), \tag{3.13}$$

$$u=u_0r+r(R-r)\sum_{j=1}^{n}y_j(t)r^{j-1}, \tag{3.14}$$

where u_0 is the initial radial displacement due to pre-tension n_0, and q_1 and q_2 are generalized coordinates associated with the first and the second axisymmetric mode of the drum, respectively. Moreover, J_0 is the Bessel function of order zero and Z_1 and Z_2 are its first two roots. We Taylor approximate $J_0\Big(Z_1\frac{r}{R}\Big)$ to 10th order and $J_0\Big(Z_2\frac{r}{R}\Big)$ to 14th order to accurately capture the mode shapes. In addition, y_j are the radial generalized coordinates and n is the number of these coordinates retained in the approximation where convergence is achieved at $n=8$.

The kinetic energy of the drum is then obtained as

$$T=\frac{1}{2}\rho h\int_0^{2\pi}\int_0^R \dot{w}^2 r\,dr\,d\theta, \tag{3.15}$$

in which the overdot represents differentiation with respect to time t, and ρ is the mass density.

Next, we obtain Lagrange equations as follows:

$$\frac{\partial\mathscr{L}}{\partial q_i}-\frac{d}{dt}\Big(\frac{\partial\mathscr{L}}{\partial\dot{q}_i}\Big)=0, \tag{3.16}$$

where $\mathscr{L}$ is the Lagrangian ($\mathscr{L} = T - U$), resulting in the equations:

$$m_1\ddot{q}_1 + k_1 q_1 + \alpha_{11}^{(1)} q_1^2 + \alpha_{12}^{(1)} q_1 q_2 + \alpha_{22}^{(1)} q_2^2 + b_{111}^{(1)} q_1^3 + b_{112}^{(1)} q_1^2 q_2 + b_{122}^{(1)} q_1 q_2^2 + b_{222}^{(1)} q_2^3 = 0, \quad (3.17)$$

$$m_2\ddot{q}_2 + k_2 q_2 + \alpha_{11}^{(2)} q_1^2 + \alpha_{12}^{(2)} q_1 q_2 + \alpha_{22}^{(2)} q_2^2 + b_{111}^{(2)} q_1^3 + b_{112}^{(2)} q_1^2 q_2 + b_{122}^{(2)} q_1 q_2^2 + b_{222}^{(2)} q_2^3 = 0, \quad (3.18)$$

in which $\alpha_{jk}^{(r)}$ and $b_{jkl}^{(r)}$ are the quadratic and cubic nonlinear terms. It is possible to express the coefficients in the equations of motion in terms of mechanical and geometric properties of the drum as follows

$$\omega_1 = \sqrt{\frac{k_1}{m_1}} = \frac{2.4}{R}\sqrt{\frac{n_0}{\rho h}} \quad (3.19a)$$

$$\omega_2 = \sqrt{\frac{k_2}{m_2}} = \frac{5.5}{R}\sqrt{\frac{n_0}{\rho h}}, \quad (3.19b)$$

$$b_{111}^{(1)} = 2.84\frac{Eh}{R^2}, b_{111}^{(2)} = -0.57\frac{Eh}{R^2} \quad (3.19c)$$

$$b_{222}^{(1)} = -3.32\frac{Eh}{R^2}, b_{222}^{(2)} = 22.76\frac{Eh}{R^2} \quad (3.19d)$$

$$b_{112}^{(1)} = -1.73\frac{Eh}{R^2}, b_{112}^{(2)} = 9.25\frac{Eh}{R^2} \quad (3.19e)$$

$$b_{122}^{(1)} = 9.25\frac{Eh}{R^2}, b_{222}^{(2)} = -9.96\frac{Eh}{R^2} \quad (3.19f)$$

in which the coefficients were evaluated assuming $\nu = 0.16$. The quadratic terms $\alpha_{jk}^{(r)}$ are all zero due to the ideal symmetric membrane assumption ($w_0 = 0$).

3.5.2. B2: NONLINEAR REDUCED-ORDER MODEL PARAMETERS FOR DIFFERENT NANOMECHANICAL RESONATORS

Here we provide the nonlinear reduced-order model parameters extracted using the STEP method [72], for the graphene nanodrum discussed in the main section, as well as a rectangular membrane and a string resonator. In the following tables, it is possible to find the definitions of the physical parameters for each model, dimensional prefactors for the terms in the nonlinear reduced-order model, and the dimensionless coefficients for the nonlinear terms. We note that for flat ideal circular, square and string resonators, the quadratic nonlinear terms are nonexistent for out-of-plane modes in the absence of in-plane modes.

REDUCED-ORDER MODEL PARAMETERS FOR THE EXPERIMENTAL GRAPHENE DRUM

Reduced-order model of the graphene drum provided here is based on a finite element (FE) model constructed in COMSOL, considering fixed boundary condition with plate elements. Eigenmodes of the graphene drum can be found in Fig. 3.5. The description of model parameters, scaling values and linear modal parameters can be found in Appendix Tables 3.2, 3.3 and 3.4. We construct the model using the first three axisymmetric and first four asymmetric out-of-plane modes of the structure, excluding their degenerates. Nonlinear coefficients can be found in Appendix Table 3.5.

Table 3.2: Parameters for the graphene drum resonator

Parameter	Formula	Units	Description
E	-	Pa	Young's modulus
h	-	m	Thickness
R	-	m	Radius
ν	-	-	Poisson's ratio
ρ	-	$\mathrm{kg/m^3}$	Density
σ	-	Pa	Stress
$\tilde{\rho}$	ρh	$\mathrm{kg/m^2}$	Mass per unit area
T_0	σh	$\mathrm{N\,m^{-1}}$	Membrane tension

Table 3.3: Scaling values for the graphene drum equations

	Linear		Nonlinear	
m_t	k_0	ω_0	a_dim	b_dim
$\pi R^2 h\rho$	T_0	$\dfrac{2.405}{R}\sqrt{\dfrac{T_0}{\tilde{\rho}}}$	$[-]$	$\dfrac{Eh}{R^2}$

Table 3.4: Dimensionless linear modal values for the experimental graphene drum from the main section. Eigenfrequencies are normalized w.r.t. the fundamental mode (ω_1). Modes: 1, 2, 4, 6, 7, 9, 15

	Eq. 1	Eq. 2	Eq. 3	Eq. 4	Eq. 5	Eq. 6	Eq. 7
m/m_t	0.204	0.195	0.183	0.103	0.192	0.118	0.0698
k/k_0	5.78	16.5	34.6	24.2	68.3	55.4	64.9
ω/ω_1	1	1.73	2.59	2.89	3.54	4.07	5.73

Table 3.5: Dimensionless nonlinear coefficients for the graphene drum ($\nu = 0.16$) from the main section. Modes: 1, 2, 4, 6, 7, 9, 15.

	Eq. 1	Eq. 2	Eq. 3	Eq. 4	Eq. 5	Eq. 6	Eq. 7
b_{111}	2.55	0	0.313	1.34	0.000204	0.000435	−0.529
b_{112}	0	8.57	−0.000307	−0.000596	−0.426	−4.05	0.000196
b_{113}	0.942	−0.000283	9.79	1.07	−0.00111	0.000244	−0.0467
b_{114}	4.02	−0.000585	1.07	10.8	0.00124	−0.000745	2.96
b_{115}	0.00058	−0.434	−0.00109	0.00124	12	0.71	0.000527
b_{116}	0.00128	−4.05	0.000289	−0.000762	0.711	15.9	0.0028
b_{117}	−1.61	0.000168	−0.0469	2.96	0.000479	0.0028	14.2
b_{122}	8.61	0	−5.82	3.82	0.00154	0.00208	−2.56
b_{123}	−0.143	−11.8	0.349	0.0771	−13.8	7.28	0.0707
b_{124}	0.00129	7.69	0.0838	0.167	0.621	−14.5	0.08
b_{125}	−0.826	0.174	−13.7	0.625	0.434	0.0744	2.17
b_{126}	−8.12	0.0522	7.31	−14.5	0.0669	0.26	0.184
b_{127}	−0.0667	−5.07	0.0861	0.0629	2.17	0.158	0.361
b_{133}	9.88	0.000849	1.46	1.37	−0.000543	0.00217	−7.65
b_{134}	2.13	0.000409	2.83	6.92	0.00248	−0.000509	4.82
b_{135}	−0.0277	−13.7	0.22	−0.000755	1.95	6.94	−0.0145
b_{136}	−0.00152	7.33	0.085	0.019	6.94	−9.79	−0.00623
b_{137}	−0.0863	−0.000881	−15.3	4.82	0.0112	−0.00304	10.5
b_{144}	10.8	−0.000906	3.54	17.4	0.00168	−0.000612	8.08
b_{145}	0.0254	0.634	0.0135	0.133	−1.84	2.25	−0.0204
b_{146}	0.0829	−14.4	0.0383	0.167	2.25	34	−0.00671
b_{147}	5.92	−0.00501	4.86	16.3	0.00322	0.0132	28.8
b_{155}	12.1	−0.000487	1.18	−1.01	−0.00161	0.00579	−11.1
b_{156}	1.45	0.02	7.02	2.27	0.197	0.293	−0.336
b_{157}	−0.032	2.16	−0.000708	−0.0264	−22.1	−0.336	0.136
b_{166}	16.1	0.00254	−4.79	16.8	0.00614	−0.0112	2.66
b_{167}	−0.033	0.161	−0.00144	−0.0053	−0.335	5.38	0.144
b_{177}	14.4	−0.00684	5.31	14.3	0.00216	0.0112	3.13
b_{222}	0	18.7	−0.000908	−0.00143	1.94	−6.99	0.000362
b_{223}	−5.73	−0.00272	45.2	6.43	−0.00445	−0.00177	6.38
b_{224}	3.83	−0.00433	6.42	16	0.00159	−0.00127	3.57
b_{225}	0.00146	5.81	−0.00434	0.00156	47.7	4.2	−0.00925
b_{226}	0.00194	−21	−0.00157	−0.00127	4.21	53	0.0126
b_{227}	−2.48	0.000901	6.38	3.55	−0.00939	0.0125	22.2
b_{233}	0.00075	45.2	−0.00485	−0.00484	31.9	−5.51	−0.00498
b_{234}	0.00452	12.9	−0.00523	−0.0825	20.3	7.73	−0.0346
b_{235}	−13.5	−0.224	64	20.3	−0.399	−0.0729	15.6
b_{236}	7.3	0.0157	−10.9	7.74	−0.0876	−0.285	−9.19
b_{237}	−0.0112	12.8	−0.0207	−0.0566	15.6	−9.18	−0.158
b_{244}	−0.000933	16	−0.00287	−0.00374	−3.94	−14.1	−0.00715
b_{245}	0.605	0.00898	20.3	−7.81	0.0907	0.00222	−2.75
b_{246}	−14.3	−0.0382	7.73	−28.1	0.00247	0.15	−11.7
b_{247}	0.0374	7.29	0.0448	0.237	−2.76	−11.8	0.376
b_{255}	−0.000489	47.8	0.00469	−0.00145	0.0154	10.7	−0.012
b_{256}	−0.00483	8.51	−0.00451	−0.0111	21.5	5.05	0.000509
b_{257}	2.13	−0.0207	15.6	−2.74	0.00764	0.00618	−12.7
b_{266}	0.00243	53.3	−0.0148	0.00474	2.42	−66.2	−0.018
b_{267}	−0.108	−0.0164	−9.17	−11.7	0.0066	0.0415	−29.3
b_{277}	−0.00664	22.3	−0.00488	−0.0109	−6.38	−14.7	−0.00534
b_{333}	0.476	−0.00144	44.9	4.06	−0.00568	−0.00114	0.176
b_{334}	1.35	−0.00473	12.2	45.4	−0.000223	−0.0106	8.8
b_{335}	−0.000782	31.8	−0.0168	−0.000288	121	11.2	−0.00672
b_{336}	0.00211	−5.46	−0.00299	−0.0106	11.2	54.8	−0.00819
b_{337}	−7.59	−0.00504	0.53	8.78	−0.00705	−0.00823	45.1
b_{344}	3.5	−0.00279	45.4	0.37	−0.00526	−0.00348	5.32
b_{345}	−0.00534	20.2	0.0276	−0.0768	5.01	58.3	−0.0532
b_{346}	−0.00706	7.68	−0.00618	−0.0376	58.3	12.7	0.00249
b_{347}	4.81	−0.000293	17.6	10.5	−0.0412	0.0192	4.01
b_{355}	1.15	0.00491	121	2.55	0.000372	−0.002	−6.49
b_{356}	6.9	−0.0452	22.4	58.3	−0.145	−0.213	−14
b_{357}	−0.00073	15.5	0.00302	−0.0546	−13	−14	−0.085
b_{366}	−4.85	−0.0145	54.9	6.4	−0.0298	0.00973	11.9
b_{367}	−0.00578	−9.12	−0.00329	0.00184	−14	23.8	−0.0382
b_{377}	5.24	−0.00472	45.1	2.09	−0.00347	0.0116	−2.47
b_{444}	5.72	−0.00118	0.121	26.5	0.00194	−0.00152	13.7
b_{445}	0.00157	−3.92	−0.00516	0.00524	57.3	−4.5	0.0103
b_{446}	−0.000414	−14	−0.00338	−0.00593	−4.5	61.5	0.0181
b_{447}	8.05	−0.00703	5.31	41.1	0.0101	0.0182	70.8
b_{455}	−1.05	−0.00139	2.54	57.3	0.00456	−0.00335	−11.8
b_{456}	2.22	−0.00729	58.3	−8.97	0.0408	0.0648	8.01
b_{457}	0.0154	−2.73	−0.0417	0.0565	−23.6	8.01	0.0482
b_{466}	16.5	0.00502	6.39	61.5	−0.00738	−0.0574	24.7
b_{467}	0.0212	−11.6	0.0228	0.0718	8.01	49.5	0.129
b_{477}	14.1	−0.0106	2.08	70.8	−0.00654	0.0288	77.4
b_{555}	−0.000543	0.0125	0.000385	0.00193	116	2.28	−0.00666
b_{556}	0.00566	10.7	−0.00135	−0.00352	6.83	105	−0.0293
b_{557}	−10.9	−0.012	−6.49	−11.8	−0.0234	−0.0292	61.7
b_{566}	0.00617	2.45	−0.0296	−0.00728	105	42.2	−0.017
b_{567}	−0.308	−0.00115	−14	8.01	−0.0505	−0.0185	−4.96
b_{577}	0.00192	−6.34	−0.00334	−0.00672	61.8	−2.49	0.0524
b_{666}	−0.00265	−21.9	0.0039	−0.0176	14.1	99.4	0.0251
b_{667}	2.89	−0.0179	11.9	24.7	−0.0172	0.077	67.3
b_{677}	0.0108	−14.5	0.0118	0.0285	−2.49	67.3	0.0274
b_{777}	1.13	−0.000123	−0.814	25.8	0.0211	0.00682	81.4

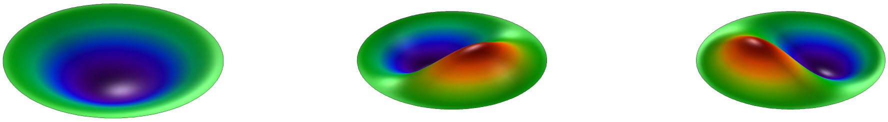

(a) 1st mode (b) 2nd mode (c) 3rd mode

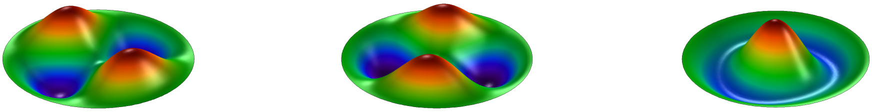

(d) 4th mode (e) 5th mode (f) 6th mode

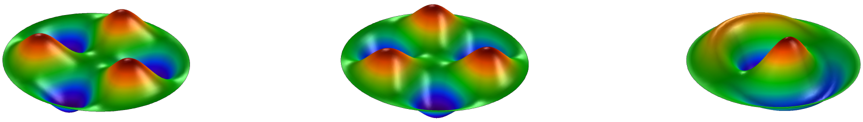

(g) 7th mode (h) 8th mode (i) 9th mode

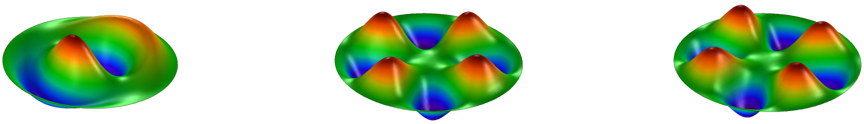

(j) 10th mode (k) 11th mode (l) 12th mode

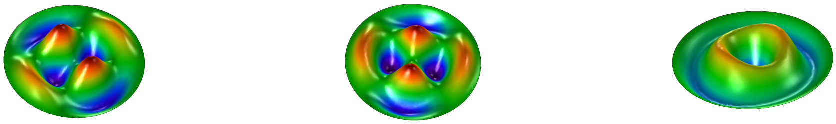

(m) 13th mode (n) 14th mode (o) 15th mode

Figure 3.5: **Eigenmodes of the graphene drum resonator.**

REDUCED-ORDER MODEL PARAMETERS FOR A SQUARE MEMBRANE RESONATOR

Reduced-order model of an ideal square membrane provided here is based on an FE model constructed in COMSOL, considering pinned boundary conditions with membrane elements. Eigenmodes of the square drum can be found in Fig. 3.6. The description of model parameters, scaling values and linear modal parameters can be found in Appendix Tables 3.6, 3.7 and 3.8. We construct the model using the first eleven out-of-plane modes of the structure, excluding their degenerates, resulting in seven modes. Nonlinear coefficients can be found in Appendix Table 3.9.

Table 3.6: Parameters for a square membrane and string resonators

Parameter	Formula	Units	Description
E	-	Pa	Young's modulus
h	-	m	Thickness
L	-	m	Length
ν	-	-	Poisson's ratio
ρ	-	$\mathrm{kg/m^3}$	Density
σ	-	Pa	Stress
$\tilde{\rho}$	ρh	$\mathrm{kg/m^2}$	Mass per unit area
T_0	σh	$\mathrm{N\,m^{-1}}$	Membrane tension

Table 3.7: Scaling values for a square membrane resonator

Linear			Nonlinear	
m_t	k_0	ω_0	a_dim	b_dim
$L^2 h\rho$	T_0	$\frac{\pi}{L}\sqrt{\frac{2T_0}{\tilde{\rho}}}$	$[-]$	$\frac{\pi}{1.27-0.97\nu}\frac{Eh}{L^2}$

Table 3.8: Dimensionless linear modal values of a square membrane resonator for modes: 1, 2, 4, 5, 7, 9, 11.

	Eq. 1	Eq. 2	Eq. 3	Eq. 4	Eq. 5	Eq. 6	Eq. 7
m/m_t	0.25	0.215	0.25	0.206	0.154	0.227	0.248
k/k_0	4.93	10.6	19.7	20.3	19.8	38.2	44.2
ω/ω_0	1	1.58	2	2.24	2.55	2.92	3

Table 3.9: Dimensionless nonlinear coefficients for a square membrane resonator modelled with modes: 1, 2, 4, 5, 7, 9, 11.

	Eq. 1	Eq. 2	Eq. 3	Eq. 4	Eq. 5	Eq. 6	Eq. 7
b_{111}	3.65	0	0	−0.0807	0	−0.000131	−0.0466
b_{112}	0	11.6	0	−0.000267	1.17	−1.17	−0.000234
b_{113}	0	0	15.2	−0.000269	0	0	−0.00112
b_{114}	−0.242	0	−0.000418	16.4	−0.000231	−0.000154	−0.635
b_{115}	0	1.15	0.000103	−0.000291	12.9	−1.27	0.00107
b_{116}	0	−1.13	−0.000234	−0.000123	−1.27	31.8	0.00211
b_{117}	−0.144	−0.000263	−0.00117	−0.634	0.000812	0.00159	27.4
b_{122}	11.6	−0.000387	10.4	2.87	−0.000952	−0.0015	0.367
b_{123}	−0.0597	20.7	−0.303	−0.0311	−13.7	−8.35	−0.109
b_{124}	−0.0514	5.63	−0.0362	−0.385	4.47	7.54	0.179
b_{125}	2.29	−0.057	−14.1	4.49	−0.193	−0.0697	−18
b_{126}	−2.32	−0.126	−8.16	8	−0.0441	−0.494	−9.19
b_{127}	0.0561	0.791	0.0117	0.0806	−18.2	−8.97	−0.397
b_{133}	15.2	−0.000448	0.00201	1.2	0.00178	−0.00327	8.13
b_{134}	−0.019	0.00178	2.29	−0.186	0.000313	0.00695	−0.0058
b_{135}	−0.0147	−14	−0.121	−0.00515	10.3	−9.72	−0.16
b_{136}	−0.0233	−8.18	−0.14	−0.0121	−9.85	−3.8	−0.0321
b_{137}	0.0116	0.00107	16.5	−0.00781	0.00765	−0.00699	−0.232
b_{144}	16.4	0	0	2.26	−0.00141	0.00465	−19.8
b_{145}	−0.0133	4.48	0.00381	−0.175	3.1	−8.76	0.0714
b_{146}	−0.0633	8.01	0.00551	−0.26	−8.47	19.2	0.227
b_{147}	−1.16	0.00215	−0.00516	−39.3	−0.000571	0.0115	−0.279
b_{155}	12.9	−0.00323	5.31	1.64	−0.00101	−0.00147	2.64
b_{156}	−2.53	−0.0488	−9.79	−8.34	−0.148	−0.267	−17.9
b_{157}	0.0263	−18.2	−0.0387	0.0259	5.39	−17.6	−0.312
b_{166}	31.8	0.0107	−1.71	9.94	0.0026	−0.0312	0.307
b_{167}	0.061	−9.15	0.000304	0.189	−17.8	1	−0.458
b_{177}	27.4	0	0.0117	0.2	0.0051	−0.0057	0.11
b_{222}	−0.000165	21.9	0	0.000103	−0.117	−1.95	0.000453
b_{223}	10.5	0.000308	58.2	2.24	0.00278	0.0003	8.15
b_{224}	2.91	0	2.24	58.7	−0.00307	0.00554	−6.02
b_{225}	−0.000944	−0.34	0.00268	−0.00286	51	−6.71	0.00785
b_{226}	−0.00146	−5.86	−0.000207	0.00451	−6.71	79.3	−0.000829
b_{227}	0.307	0.00135	8.17	−6.03	0.00768	−0.00178	69.9
b_{233}	−0.000749	58.2	−0.0025	−0.00113	−28.8	−2.03	−0.0032
b_{234}	−0.0416	4.4	−0.115	−0.19	−7.88	37.6	0.0978
b_{235}	−14.1	0.0428	−57.7	−7.9	−0.224	0.0697	−64.9
b_{236}	−8.21	−0.0898	−4.19	37.7	0.144	−0.495	11.6
b_{237}	−0.00833	16.4	−0.0144	0.0216	−64.9	11.6	−0.316
b_{244}	0	58.7	0.00345	0.00242	34.5	21.1	0.00102
b_{245}	4.56	−0.0935	−7.91	68.8	−0.267	−0.195	−26.9
b_{246}	8.12	−0.169	37.7	42	−0.116	−0.904	−58.8
b_{247}	0.0902	−12	0.0513	0.398	−26.9	−58.7	−0.63
b_{255}	−0.00367	51	−0.00805	−0.00674	−20.2	10.4	−0.0024
b_{256}	−0.000602	−13.5	0.0222	−0.0165	20.7	46	0.0198
b_{257}	−18.3	0.0616	−65	−26.9	0.146	0.128	−15.4
b_{266}	0.0114	79.4	0.00916	0.0192	23.2	4.87	−0.0265
b_{267}	−9.2	0.121	11.6	−59.1	0.0295	0.535	72.6
b_{277}	0.00143	70	−0.00657	−0.02	−7.5	36.4	−0.0217
b_{333}	0.000617	−0.0005	58.5	−0.00202	0.00316	0.000402	0.00416
b_{334}	1.21	0	−0.00648	67	−0.00399	0.00373	4.26
b_{335}	0.00161	−28.9	0.00964	−0.00411	96.5	3.74	0.011
b_{336}	−0.0036	−2.01	−0.000215	0.00201	3.72	145	−0.00439
b_{337}	8.21	−0.00274	0.0113	4.26	0.0106	−0.00483	156
b_{344}	0	0.00294	67	0.00108	0.00533	−0.000892	−0.00772
b_{345}	0.00929	−7.9	−0.0623	−0.089	10.9	−16.8	−0.0892
b_{346}	−0.0278	37.8	−0.0846	−0.116	−16.8	2	0.0116
b_{347}	0.00647	0.0126	8.55	0.122	0.00104	−0.0017	−0.208
b_{355}	5.3	−0.00847	96.5	5.51	0.028	−0.0255	71.2
b_{356}	−9.82	0.0311	7.38	−16.9	−0.134	−0.235	−19.5
b_{357}	−0.0299	−65.1	0.00507	0.00618	143	−19.5	−0.193
b_{366}	−1.73	0.0104	145	1.16	−0.0114	−0.097	−12.7
b_{367}	−0.0406	11.6	0.0688	−0.0194	−19.6	−25.1	−0.472
b_{377}	0.0107	−0.00793	156	0.0176	0.00823	−0.0476	0.137
b_{444}	0.767	0.000402	0.000369	81.4	−0.00372	0.0116	−7.64
b_{445}	−0.00148	34.5	0.00503	−0.0106	112	41	0.0106
b_{446}	0.00254	21.2	−0.00315	0.0327	40.9	192	−0.0431
b_{447}	−20.1	0.00305	−0.00774	−22.9	0.0118	−0.0465	253
b_{455}	1.66	−0.00814	5.52	112	−0.00863	−0.0149	−9.73
b_{456}	−8.43	−0.114	−16.9	81.7	−0.224	−0.459	−80.8
b_{457}	0.0719	−26.9	−0.00488	0.178	−19.3	−80.8	−0.367
b_{466}	9.98	0.0206	1.16	192	0.0156	0.393	−103
b_{467}	0.195	−59.1	−0.00207	0.455	−80.9	−205	−0.59
b_{477}	0.215	−0.0217	0.0231	252	−0.043	0.00334	0.049
b_{555}	−0.000449	−6.75	0.00986	−0.00293	76.1	−9.91	0.0205
b_{556}	0.00139	10.4	−0.0263	−0.0158	−29.7	158	−0.0479
b_{557}	2.57	−0.00312	71.3	−9.74	0.0581	−0.0474	240
b_{566}	0.00579	23.2	−0.0138	0.0161	158	−0.405	−0.0349
b_{567}	−17.9	0.118	−19.6	−81.1	−0.0376	0.243	−0.642
b_{577}	0.00484	−7.5	0.00627	−0.0436	240	−0.186	−0.00717
b_{666}	−0.0145	1.63	−0.0311	0.139	−0.136	357	−0.105
b_{667}	0.147	−0.0237	−12.7	−103	−0.0374	−0.317	406
b_{677}	−0.00576	36.6	−0.0549	0.00193	−0.251	406	0.145
b_{777}	−0.0396	−0.00622	0.0474	0.0102	−0.00117	0.0459	295

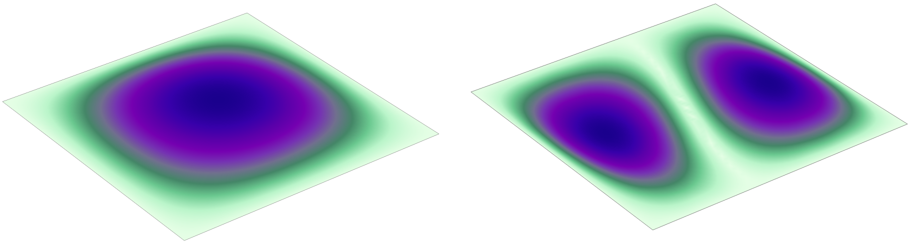

(a) 1st mode (b) 2nd mode

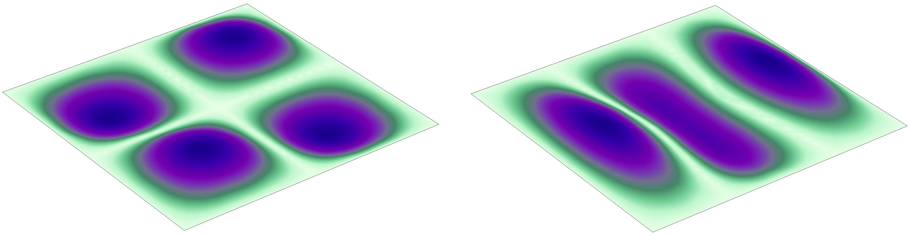

(c) 4th mode (d) 5th mode

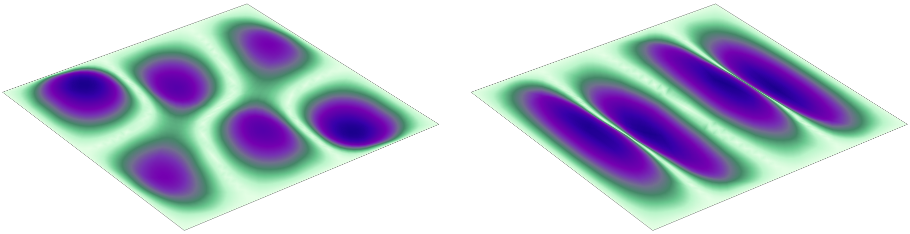

(e) 7th mode (f) 9th mode

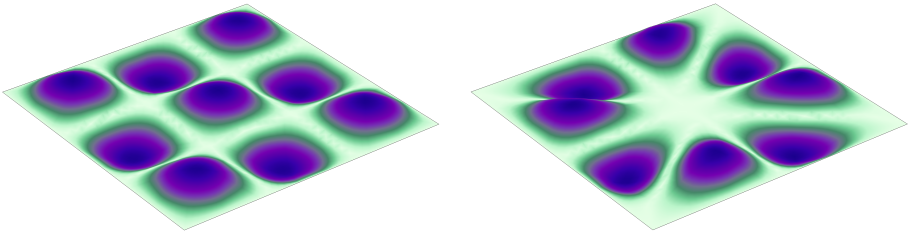

(g) 11th mode (h) 12th mode

Figure 3.6: **Eigenmodes of a square membrane resonator.**

REDUCED-ORDER MODEL PARAMETERS FOR A STRING RESONATOR

Reduced-order model of an ideal string resonator provided here is based on an FE model constructed in COMSOL, considering pinned boundary condition with truss elements. The description of model parameters, scaling values and linear modal parameters can be found in Appendix Tables 3.6, 3.10 and 3.11. We construct the model using the first three out-of-plane and first three in-plane modes of the structure. Nonlinear coefficients can be found in the Appendix Tables 3.12 and 3.13.

Table 3.10: Scaling values for a string resonator

	Linear				Nonlinear	
m_t	k_{0_out}	k_{0_in}	ω_{0_out}	ω_{0_in}	a_dim	b_dim
ρAL	$\dfrac{\sigma A}{L}$	$\dfrac{EA}{L}$	$\dfrac{1}{2L}\sqrt{\dfrac{\sigma}{\rho}}$	$\dfrac{1}{L}\sqrt{\dfrac{E}{\rho}}$	$\dfrac{EA}{L^2}$	$\dfrac{EA}{L^3}$

Table 3.11: Dimensionless linear modal values of a string resonator. Eigenfrequencies are normalized w.r.t. the fundamental mode (ω_1). Note that Eq. 4, Eq. 5 & Eq. 6 describe in-plane modes.

	Eq. 1	Eq. 2	Eq. 3	Eq. 4	Eq. 5	Eq. 6
m/m_t	0.5	0.5	0.499	0.5	0.501	0.497
k/k_0	4.93	19.7	44.4	4.97	19.9	44.6
ω/ω_1	1	2	3	23.6	47.2	70.9

Table 3.12: Quadratic nonlinear coefficients for a string resonator modelled with modes: first three out-of-plane modes (correspond to 1, 2, 3 in the table) and first three in-plane modes (correspond to 4, 5, 6 in the table)

	Eq. 1	Eq. 2	Eq. 3	Eq. 4	Eq. 5	Eq. 6
a_{11}	0	0	0	7.75	−0.000 153	−0.0014
a_{12}	0	0	0	0	0	0
a_{13}	0	0	0	46.5	−93.1	0.006 46
a_{14}	15.5	0	46.5	0	0	0
a_{15}	−0.000 152	0	−93.1	0	0	0
a_{16}	−0.001 32	0	0.008 06	0	0	0
a_{22}	0	0	0	0	−62.1	0
a_{23}	0	0	0	0	0	0
a_{24}	0	0	0	0	0	0
a_{25}	0	−124	0	0	0	0
a_{26}	0	0	0	0	0	0
a_{33}	0	0	0	0.000 349	−0.001 73	−209
a_{34}	46.5	0	−0.001 16	0	0	0
a_{35}	−93.1	0	−0.001 73	0	0	0
a_{36}	−0.001 08	0	−418	0	0	0
a_{44}	0	0	0	0	−186	0
a_{45}	0	0	0	−372	0	1.12×10^3
a_{46}	0	0	0	0	1.12×10^3	0
a_{55}	0	0	0	0	0	0
a_{56}	0	0	0	1.12×10^3	0	0.0162
a_{66}	0	0	0	0	−0.0111	0

Table 3.13: Cubic nonlinear coefficients for a string resonator modelled with modes: first three out-of-plane modes (that correspond to 1, 2, 3 in the table) and first three in-plane modes (that correspond to 4, 5, 6 in the table)

	Eq. 1	Eq. 2	Eq. 3	Eq. 4	Eq. 5	Eq. 6
b_{111}	18.3	0	18.3	0	0	0
b_{112}	0	146	0	0	0	0
b_{113}	54.8	0	328	0	0	0
b_{114}	0	0	0	48.7	−48.8	0.00533
b_{115}	0	0	0	−48.8	195	146
b_{116}	0	0	0	0.00403	146	437
b_{122}	146	0	219	0	0	0
b_{123}	0	438	0	0	0	0
b_{124}	0	0	0	0	0	0
b_{125}	0	0	0	0	0	0
b_{126}	0	0	0	0	0	0
b_{133}	328	0	−0.0227	0	0	0
b_{134}	0	0	0	146	−292	−437
b_{135}	0	0	0	−292	−0.00655	876
b_{136}	0	0	0	−437	876	−0.0632
b_{144}	48.7	0	73	0	0	0
b_{145}	−97.5	0	−292	0	0	0
b_{146}	0.00747	0	−437	0	0	0
b_{155}	195	0	−0.00386	0	0	0
b_{156}	292	0	876	0	0	0
b_{166}	437	0	−0.0141	0	0	0
b_{222}	0	292	0	0	0	0
b_{223}	219	0	1.31×10^3	0	0	0
b_{224}	0	0	0	292	0	−292
b_{225}	0	0	0	0	781	0
b_{226}	0	0	0	−292	0	1.75×10^3
b_{233}	0	1.31×10^3	0	0	0	0
b_{234}	0	0	0	0	0	0
b_{235}	0	0	0	0	0	0
b_{236}	0	0	0	0	0	0
b_{244}	0	292	0	0	0	0
b_{245}	0	0	0	0	0	0
b_{246}	0	−583	0	0	0	0
b_{255}	0	781	0	0	0	0
b_{256}	0	0	0	0	0	0
b_{266}	0	1.75×10^3	0	0	0	0
b_{333}	0.00417	0	1.48×10^3	0	0	0
b_{334}	0	0	0	438	−439	0.0182
b_{335}	0	0	0	−439	1.76×10^3	−0.0141
b_{336}	0	0	0	0.00627	0.00105	3.93×10^3
b_{344}	73	0	438	0	0	0
b_{345}	−292	0	−877	0	0	0
b_{346}	−437	0	0.0373	0	0	0
b_{355}	0.000582	0	1.76×10^3	0	0	0
b_{356}	876	0	−0.0161	0	0	0
b_{366}	−0.011	0	3.93×10^3	0	0	0
b_{444}	0	0	0	292	0	−290
b_{445}	0	0	0	0	2.34×10^3	0
b_{446}	0	0	0	−875	0	5.24×10^3
b_{455}	0	0	0	2.34×10^3	0	-3.51×10^3
b_{456}	0	0	0	0	-7.02×10^3	0
b_{466}	0	0	0	5.24×10^3	0	0.502
b_{555}	0	0	0	0	4.7×10^3	0
b_{556}	0	0	0	-3.51×10^3	0	2.1×10^4
b_{566}	0	0	0	0	2.1×10^4	0
b_{666}	0	0	0	0.132	0	2.35×10^4

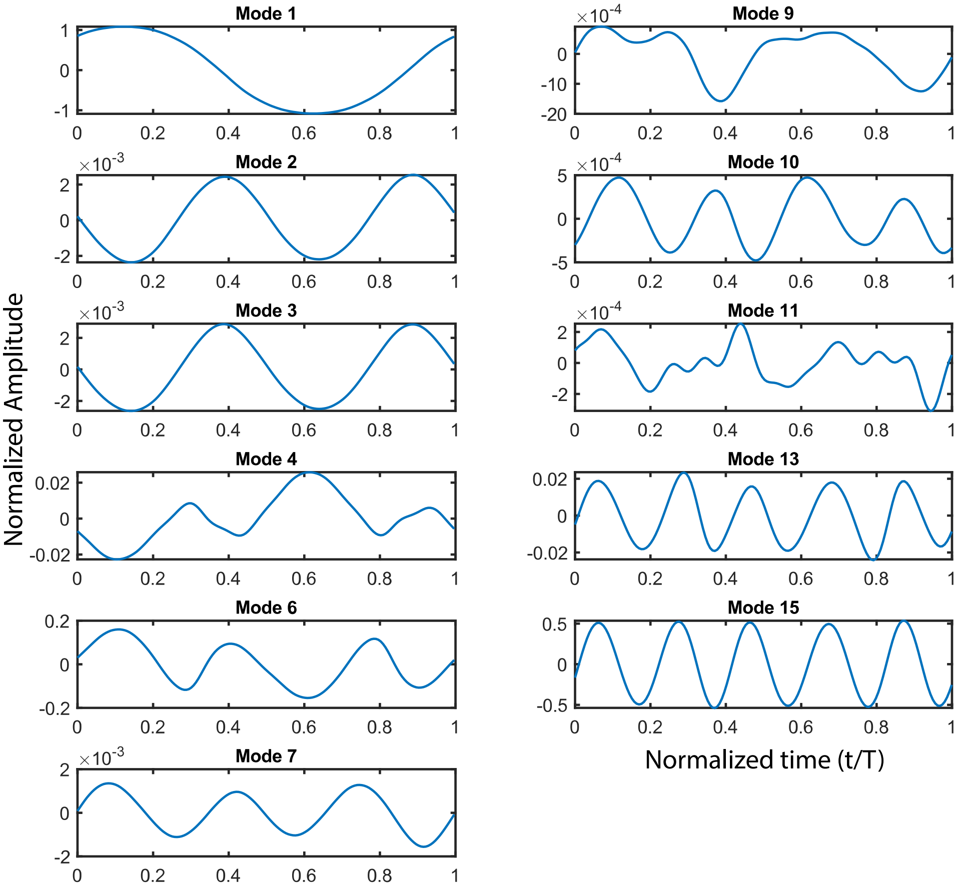

Figure 3.7: **Time responses of each mode during a period of oscillation for the graphene drum undergoing internal resonance at $\omega_d/\omega_0 = 2.538$.**

3.5.3. B3: DYNAMIC RESPONSE OF THE GRAPHENE DRUM DURING INTERNAL RESONANCE

In Chapter 2 main section, experiments were displayed where complex nonlinear phenomena occur, one of which is internal resonance caused by the interaction of the parametric resonance of the first mode with other modes of vibration. In the simulations, these observations were replicated. Here, we further investigate this response. In Fig. 3.7, we show the time response of each mode during once cycle of the internal resonance at $\omega_d/\omega_0 = 2.538$. It is possible to observe strong activation of multiple modes. The dominant modes are the first three axisymmetric modes $f_{0,1}$, $f_{0,2}$ and $f_{0,3}$ (mode numbers 1, 6, 15) together with asymmetric mode $f_{2,1}$ (mode number 4). This is also clear in the overall frequency responses in Appendix Figs. 3.8 and 3.9 with all the simulated modes.

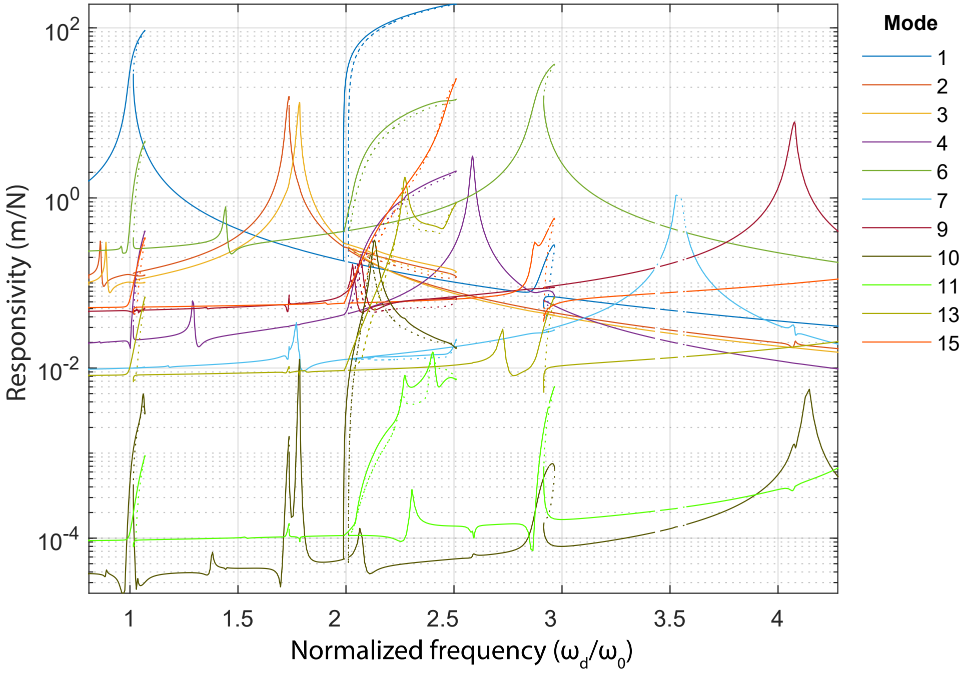

Figure 3.8: **Simulated modal frequency response for excitation level $\beta = 14.32$ and $\gamma = 2.5$, before the surge.**

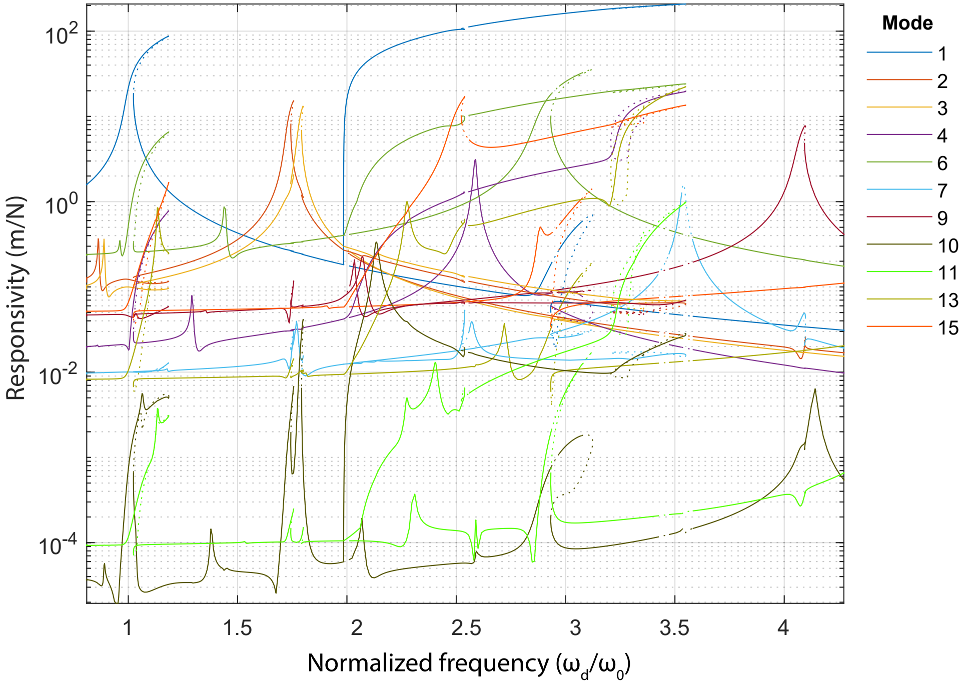

Figure 3.9: **Simulated modal frequency response for excitation level $\beta = 26.22$ and $\gamma = 3.2$, after the surge.**

4

SYMMETRY-BREAKING INDUCED FREQUENCY COMBS IN GRAPHENE RESONATORS

Nonlinearities are inherent to the dynamics of two-dimensional materials. Phenomena like intermodal coupling already arise at amplitudes of only a few nanometers, and a range of unexplored effects still awaits to be harnessed. Here, we demonstrate a route for generating mechanical frequency combs in graphene resonators undergoing symmetry-breaking forces. We use electrostatic force to break the membrane's out-of-plane symmetry and tune its resonance frequency towards a one-to-two internal resonance, thus achieving strong coupling between two of its mechanical modes. When increasing the drive level, we observe splitting of the fundamental resonance peak, followed by the emergence of a frequency comb regime. We attribute the observed physics to a non-symmetric restoring potential, and show that the frequency comb regime is mediated by Neimark bifurcation of the periodic solution. These results demonstrate that mechanical frequency combs and chaotic dynamics in 2D material resonators can emerge near internal resonances due to symmetry-breaking.

This chapter has been published in Nano Letters 2022, 22, 15, 6048–6054

4.1. INTRODUCTION

NANOMECHANICAL resonators made of two-dimensional (2D) materials are ideal for exploring nonlinear dynamic phenomena. Owing to their atomic thickness and high flexibility, forces in the pN range can already trigger large-amplitude oscillations in these membranes and drive them into nonlinear regime [22], [26]. Tension modulation via electrostatic actuation [82]–[84] and opto-thermal forces [59], [85] serve as practical knobs to tune mechanical nonlinearity of 2D material membranes, and can lead to a wealth of nonlinear phenomena including multi-stability [44], parametric resonance [59], [67], parametric amplification [86], [87], high-frequency tuning [40], [88], stochastic switching [89], and mode coupling [90], [91].

Amongst different nonlinear phenomena that emerge in 2D material membranes, mode coupling is particularly interesting as it allows for the transfer of energy between vibrational states of single [90] or coupled 2D resonators [92]. Mode coupling is also closely linked to nonlinear dissipation [52], [67], and can be tuned utilizing internal resonance (IR); a condition at which two or more resonance frequencies become commensurate. The application of IR in mechanical resonators spans from frequency division [93] and time-keeping [49], [94] to enhancing the sensitivity of scanning probe techniques [95].

Here, we present a mechanism for generating frequency combs by symmetry-breaking, that exploits internal resonances of a few-nm-thick graphene resonator. We make use of the extreme flexibility of graphene to controllably break its out-of-plane symmetry by bending it using electrostatic force, and achieve one-to-two (1:2) IR between its distinct mechanical modes. Unlike recent demonstrations of frequency comb generation in graphene that require strong coupling of the suspended membrane with a high quality factor SiN_x substrate [96], here we show that by careful tuning of the intermodal coupling between two modes of vibration in a single resonator, frequency combs can be generated. As a result of this 1:2 modal interaction, we observe splitting of the resonance peak at a critical gate voltage and drive level, leading to equally spaced spectral lines near the fundamental resonance. By using an analytical model that accounts for the broken symmetry and comprises quadratic coupling terms, we account for the characteristic dependence of the frequency comb region on the membrane tension and deflection amplitude, and confirm that symmetry-broken mechanics lies at the root of the observations.

4.2. MEASUREMENTS

Experiments are performed on a 15 nm thick exfoliated graphene flake, transferred over a circular cavity of 8 μm diameter and 220 nm depth forming a drum resonator. The motion of graphene is read-out in a Fabry-Pérot interferometer where a red helium-neon laser ($\lambda = 633$ nm) is used to probe the motion [66], [97], (see Fig. 4.1a, c). The drum is driven opto-thermally using a power modulated blue laser ($\lambda = 485$ nm), and to control the static deflection of the drum, a local gate electrode is placed at the bottom of the cavity, see Fig. 4.1b. Moreover, to reduce damping by the surrounding gas, the sample is measured in a vacuum chamber with pressure $\leq 10^{-4}$ mbar.

By sweeping the modulation frequency f of the blue laser using a Vector Network Analyzer (VNA), we observe multiple directly-driven resonances, appearing as pronounced peaks in the resonator's spectral response (Fig. 4.1d). Among them, the primary and secondary axisymmetric modes of the drum can be readily identified at $f_{0,1} = 7.0\,\mathrm{MHz}$ ($Q_{0,1} \approx 80$) and $f_{0,2} = 15.8\,\mathrm{MHz}$ ($Q_{0,2} \approx 40$), with $f_{0,2}/f_{0,1} = 2.25$, close to the theoretically predicted ratio of 2.29 for a membrane [98]. We note that the resonance frequencies depend strongly on the membrane tension, which we can tune via the electrostatic force generated by the electrostatic gate electrode.

4.2.1. FREQUENCY RESPONSE OF THE SYMMETRY-BROKEN NANODRUM

By sweeping the gate voltage V_g, we control the tension in the membrane and alter the out of plane offset (see Appendix C1). The electrostatic force pulls the drum out of its initial flat configuration, and breaks its out-of-plane symmetry [99]. This broken-symmetry can have significant influence on the dynamics of the resonator, especially in the nonlinear regime, where the resonant response deviates from the common Duffing model, because it introduces quadratic terms in the nonlinear stiffness [70].

We note that increasing V_g causes the resonance frequencies of the drum to shift at different rates (see Appendix Figure 4.5). At a certain critical voltage $V_{\mathrm{IR}} = 7\,\mathrm{V}$ we observe (Fig. 4.1e) splitting of the fundamental resonance peak at f_{IR}=22.73 MHz, which we attribute to the occurrence of a 1:2 internal resonance with a higher mode, since it occurs when the frequency of a higher mode at 44 MHz is exactly twice that of the fundamental mode, see Fig. 4.2a. Besides splitting, the height of both resonance peaks also diminishes close to V_{IR}, providing evidence for the presence of 1:2 IR and energy redistribution between the interacting modes.

By driving the drum at elevated blue laser powers and performing upward frequency sweeps, we observe in Fig. 4.2b a butterfly-shaped response, consisting of two Duffing-like asymmetric resonances, one of which bending to lower and the other to higher frequency, indicating that one of the split peaks experiences a spring softening, and the other a spring hardening nonlinearity (similar responses have been observed in other nonlinear resonators undergoing IR [50], [100]–[102]). Interestingly, at the maximum drive level (10 dBm), the strong coupling between the resonant modes yields the emergence of a third peak in the middle of the split region at frequency f_{IR} = 22.73 MHz (see Fig. 4.2c).

4.2.2. EMERGENCE OF THE FREQUENCY COMB

In order to investigate this unconventional response in depth, we drive the graphene drum to the critical voltage V_{IR} required to observe the split peak at f_{IR}, and used a Zurich UHFLI to analyze the fast oscillations of the drum at high drive powers. By simultaneously tracing the response spectrum while sweeping the driving frequency around f_{IR} we noticed that for driving frequencies outside the region where the middle peak was spotted, the motion is harmonic. However, close to f_{IR}, the spectral response suddenly changes and a frequency comb is observed consisting of multiple equally spaced peaks near f_{IR} (see Fig. 4.2d and Fig. 4.2e and Appendix C2).

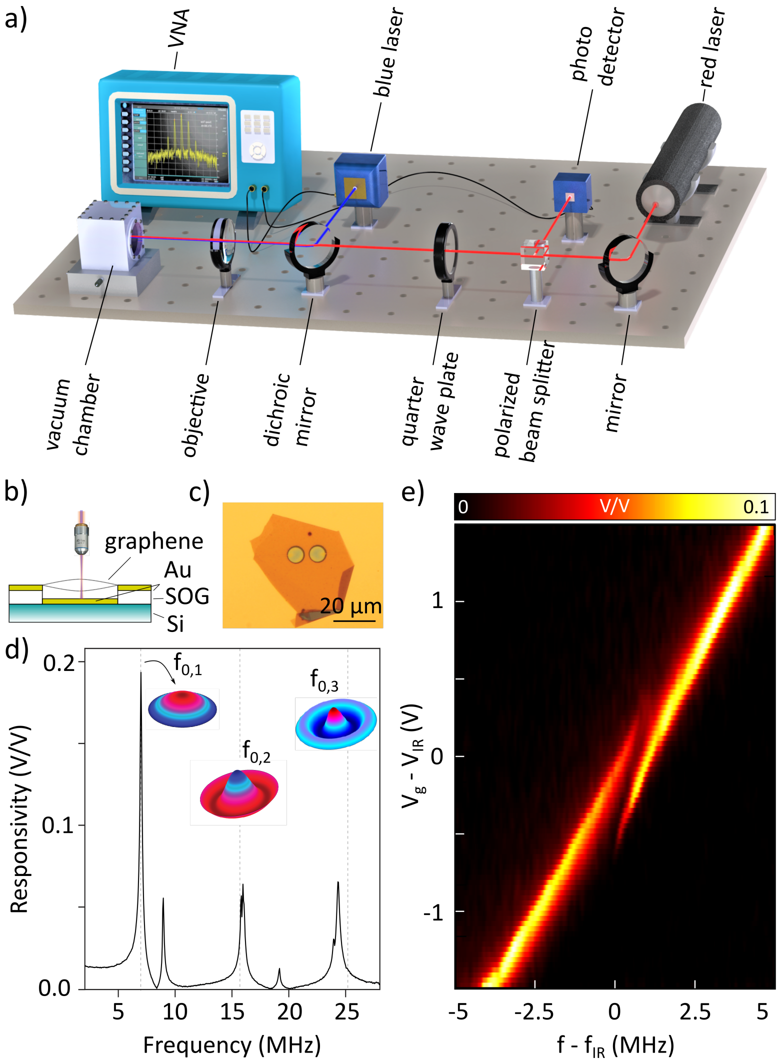

Figure 4.1: **Graphene drum measurements.** (a) Schematic of the optical set-up for actuating and detecting the motion of graphene. The drum is actuated via a blue laser at a certain frequency set by a Vector Network Analyzer (VNA), and the motion is read-out using a red laser. (b) Schematic of the resonating graphene drum with electrical contacts. (c) Optical micrograph of the graphene drum. (d) Frequency response of the resonator at neutral gate voltage (V_g=0 V). Here, Finite Element Simulations are performed to determine the frequencies of axisymmetric modes of vibration. (e) Variation of the fundamental frequency of the drum $f_{0,1}$ as a function of the gate voltage V_g, showing a state of splitting at V_{IR} ~ 7 V and frequency f_{IR} = 22.73 MHz.

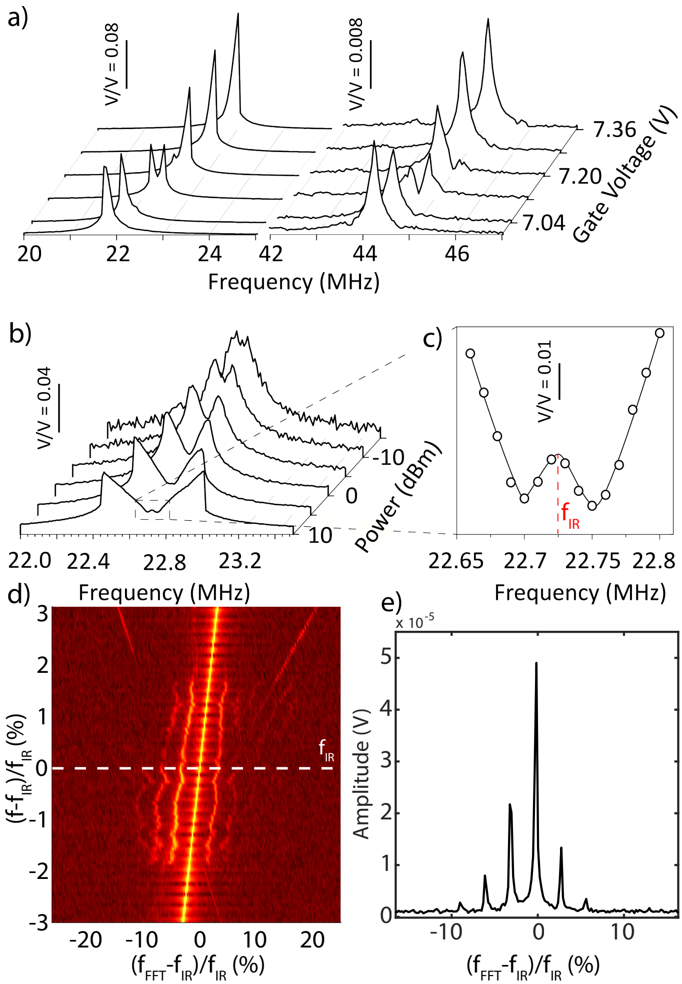

Figure 4.2: **Measured intermodal coupling of the graphene resonator.** (a) Evolution of the fundamental and a higher resonance peaks close to the gate voltage of 7.1 V, measured via VNA, at -10 dBm drive level. (b) Evolution of the 1:2 IR response upon increasing the drive power. (c) A third peak emerges at f_{IR}. (d) Fast Fourier Transform (FFT) measurements at high drive powers while sweeping the blue laser modulation frequency f, showing the presence of sidebands at f_{IR}. The white dashed line in (d) is a line-cute of the FFT map, that is zoomed in on (e) to show equally spaced sideband frequencies.

4.3. THEORETICAL MODEL: 1:2 INTERNAL RESONANCE

To explain the nonlinear physics associated with the observed dynamics and frequency comb near IR in a system with broken-symmetry, we present an analytical model to derive the system's Lagrangian and obtain the governing equations of motion (See Appendix C3). For the model, we accounted up to third order nonlinearities, since the graphene drum we study, outside the internal resonance regime, exhibits a slight Duffing response even at the highest drive levels. We approximate the coupled motion by only considering the drum's first two axisymmetric modes of vibration with frequencies $f_{0,1}$ and $f_{0,2}$ (see Fig. 4.1d). For an ideal circular membrane, the ratio of these first two axisymmetric modes can be tuned to approach $f_{0,2}/f_{0,1} \approx 2$ by changing the tension distribution. These variations in tension distribution might originate from variations in the electrostatic force if the distance to the gate electrode is non-uniform due to membrane deflection, wrinkling or buckling. Moreover, to account for the broken-symmetry mechanics, we model the drum with a static deflection from its undeformed state, that has the shape of its fundamental mode shape [61], with an amplitude W_0. This leads to the presence of both quadratic and cubic coupling terms in the equations of motion. However, we note that not all the terms in a 1:2 IR are resonant [67], and retain only the relevant terms to obtain the following set of simplified equations near the IR (See Appendix C4):

$$\ddot{x} + (k_x + T_x)\,x + \gamma x^3 + \tau_x \dot{x} + 2\alpha x q = F\cos(\Omega t), \tag{4.1}$$

$$\ddot{q} + \left(k_q + T_q\right) q + \tau_q \dot{q} + \alpha x^2 = 0. \tag{4.2}$$

Here, x and q are the generalized coordinates which represent the first and second axisymmetric mode of the graphene membrane respectively, k_x and k_q are the intrinsic mode stiffness and T_x and T_q represent added stiffness due to electrostatic tuning of the tension. τ_x and τ_q are the linear damping coefficients of the generalized coordinates. Moreover, γ is the Duffing coefficient, and α is the coupling strength that can be determined analytically in terms of the offset shape and modes of vibration (See Appendix C3). Finally, F is the forcing amplitude and $\Omega = 2\pi f_d$ is the excitation frequency. All the terms in Eqs. 4.1 and 4.2 are mass normalized.

4.3.1. SIMULATIONS

In order to investigate the resonant interaction numerically, we time-integrate the equations of motion. We start by recording the time response of the system at Ω far from resonance and sweep Ω through the 1:2 IR condition. Simulations are performed first at a low driving level that is associated with the linear harmonic oscillator response and then F is increased until the specific characteristics of the nonlinear interaction such as mode splitting appear. We perform our simulations using nonlinear parameters $\gamma = 5.78 \times 10^{30}$ $(\mathrm{Hz/m})^2$, $\alpha = 1.97 \times 10^{24}$ $(\mathrm{Hz}^2/\mathrm{m})$. These values correspond to the analytical model of a 15 nm thick drum with a diameter of 8 μm assuming Young's modulus of $E = 1$ TPa, and initial axisymmetric offset amplitude of 90 nm.

Fig. 4.3a shows the modelled variation of the resonance frequency as a function of the applied tension (T_x). By changing the tension T_x, the fundamental resonance frequency $f_{0,1}$ is tuned and a peak splitting, similar to that in Fig. 4.1e, is observed near the internal resonance frequency f_{IR}.

The splitting phenomenon becomes more apparent at elevated drive powers (see Fig. 4.3b), similar to the experimental observations in Fig. 4.2c. This leads to the emergence of a similar butterfly-shaped responsivity x/F, as the nonlinear coupling becomes stronger at higher drive levels, where energy leaks to the interacting mode. The butterfly shaped split is a direct consequence of the 1:2 IR and can be understood by obtaining the nonlinear frequency response function of equations (4.1) and (4.2) analytically (See Appendix C3). Interestingly, we also note the presence of the third middle peak in our simulation. In Fig. 4.3c, it can be seen that this peak indeed appears within the split region, at zero detuning from IR condition, confirming that 1:2 IR that follows from the equations of motion Eqs. 4.1 and 4.2, can be held accountable for our experimental observations.

In Fig. 4.3c it can be also noted that when driving near f_{IR} the second generalized coordinate q shows an enhanced amplitude, with a response that resembles that of x. It is important to note that in the experiments, the middle peak observed at f_{IR} is only due to the fundamental amplitude x, since our measurements are performed in a homodyne detection scheme.

4.3.2. NEIMARK BIFURCATION AND QUASI-PERIODIC RESPONSE

To better understand the mechanism that lies at the centre of our observation, we investigated the stability of the solution branches using a numerical continuation software package (AUTO). We found that the middle peak appears in a region that is confined between two Neimark bifurcations (red dashed lines in Fig. 4.3c and Appendix C4). Similar to the Hopf bifurcation, at which a fixed point becomes a limit cycle, at a Neimark bifurcation (also known as the secondary Hopf bifurcation) a periodic orbit becomes a quasi-periodic orbit [103]. Quasi-periodic motion is characterized by a closed invariant curve in the Poincaré map of the phase space that is known to result in amplitude-modulated motion, and thus the emergence of frequency combs in the spectral response [61]. To investigate the spectral characteristics of the quasi-periodic oscillations, we swept the excitation frequency Ω in the spectral neighborhood of the region confined by the two Neimark bifurcations, and analyzed the time response of the nonlinear equations, similar to [102]. Fig. 4.3d shows the frequency content of the simulated time signal inside and outside this region. It can be observed that the frequencies around f_{IR} are discretely separated from each other, creating a frequency comb that was nonexistent before reaching the onset of Neimark bifurcation, resembling the frequency comb in Fig. 4.2d. We also show that the time-dependent motion becomes amplitude modulated when entering the Neimark bifurcation region (see Fig. 4.3e), while having constant amplitude outside of that region. Interestingly, numerical simulations also show signatures of chaotic states upon amplification of the drive level, suggesting that 1:2 IR and broken-symmetry mechanics can represent the onset of a transition from quasi-periodic to chaotic oscillations in 2D material resonators (see Fig. 4.4a), and can be tuned by manipulating the intermodal couplings and vibrational states of the drum. However we note that, although the numerical model does capture the most relevant features of the experimental system near the onset of IR, this does not guarantee that this correspondence continues at higher driving levels up to the onset of chaos, where other nonlinearities could also play a role. Further experiments will be therefore needed to prove the presented route to

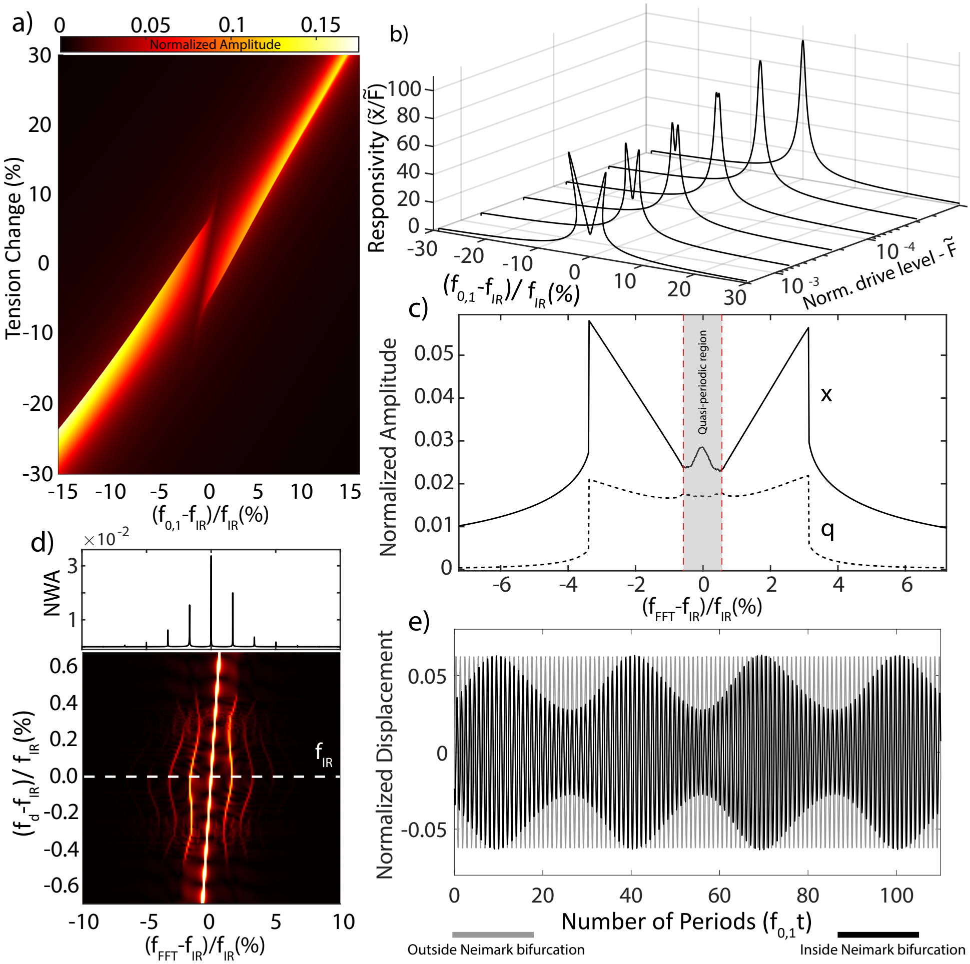

Figure 4.3: **Modal interaction simulations at the normalized drive level $\tilde{F} = F/(2\pi f_{0,1} h) = 0.0015$, where h is the thickness of the drum. Generalized coordinates are also normalized with respect to the thickness, such that $\tilde{x} = x/h$ and $\tilde{q} = q/h$.** (a) Frequency response of the fundamental mode as the tension of the membrane is increased. At zero detuning from IR, mode splitting occurs. (b) Frequency response simulations with different drive levels at zero detuning from IR. As the drive level is increased, nonlinear coupling becomes stronger, and both softening and hardening nonlinearities emerge. (c) After a critical drive level, Neimark bifurcations emerge (depicted by red dashed lines) and at the region confined by these bifurcations, the steady state oscillations become quasi-periodic, generating frequency combs around the resonance frequency. (d) FFT map at the vicinity of IR and critical force level. Frequency combs emerge at the center of the split region, where equally spaced comb elements appear, surrounding the main resonance peak. Inset above is the FFT at the IR condition, showing the normalized wave amplitude (NWA), representing the white dashed line cut of the FFT map. (e) In time domain, this bifurcation leads to amplitude-modulated response.

chaos near broken-symmetry induced 1:2 IR.

4.4. DISCUSSION

By simulating the equations of motion at IR while sweeping the parameters, it is also possible to show that the Neimark bifurcations and thus frequency comb generation is sensitive to mechanical parameters of the system. At 1:2 IR, where the Neimark bifurcation is activated, any change in mechanical properties of the drum will be reflected in the frequency spectrum, as a change in the comb intensity, spacing, and population. Figs. 4.4b and 4.4c reveal the sensitivity of these combs to the drum offset and tension, which were obtained by sweeping the initial offset (broken-symmetry) amplitude and T_x. These combs only appear if there is sufficient quadratic nonlinear coupling induced by the broken symmetry, since the terms responsible of the internal resonance are directly related to the membrane offset and diminish in the absence of it (See Appendix C3). If there is no broken symmetry, the system is symmetric upon inverting the x and q coordinates and all forces F_{total} obey $F_{total}(x,q) = -F_{total}(-x,-q)$, such that there are only odd (linear and cubic) terms in the equations of motion and therefore no 1:2 interaction and associated combs. Increases in the membrane offset influences both comb spacing and population. Furthermore, near IR, the frequency comb can be used as a sensitive probe for changes in the parameters of the two interacting modes. Any shift in the resonance frequency of the coupled modes results in changes in comb spacings, making it possible to simultaneously probe changes in both frequencies by solely measuring the response of the fundamental mode after the Neimark bifurcation. External parameters like drive power and drive frequency are also observed to influence frequency comb region, and serve as controls for tuning comb intensity, spacing, and population (See Appendix C5).

In summary, we demonstrate a route for generating frequency combs in the nonlinear response of graphene drums that utilizes broken symmetry and 1:2 internal resonance. Unlike other methods that use multiple wave mixing [104], [105], resonant nonlinear friction [106], or SNIC bifurcation [53], to generate mechanical frequency combs, the presented method makes use of an electrostatic gate to controllably tune frequency combs that are mediated by broken-symmetry. When the drum is brought close to the broken-symmetry induced 1:2 IR, we observe strong splitting of the fundamental resonance peak, exhibiting both softening and hardening nonlinearity. Between the split peaks, we observe resonant interactions when driving at relatively high powers, that are generated by Neimark bifurcations of the periodic motion. This regime hosts quasi-periodic oscillations that are held accountable for the observed frequency combs. The experimentally observed phenomena were explained using a continuum mechanics model of a deflected drum with 1:2 IR between its first two axisymmetric modes. Emerging from the inherent geometric nonlinearities, mechanical frequency combs are closely linked to the mechanical properties of 2D materials, including tension, Young's modulus and broken-symmetry, and thus can be utilized for probing these properties and tracing their variations with frequency and drive levels [96]. There are many examples in recent years where internal resonance in NEMS/MEMS systems has been utilized to enhance the frequency stability of resonant sensors [49], [107]–[109]. In these systems, it has also been shown that frequency combs can be used as an alternative approach for resonance fre-

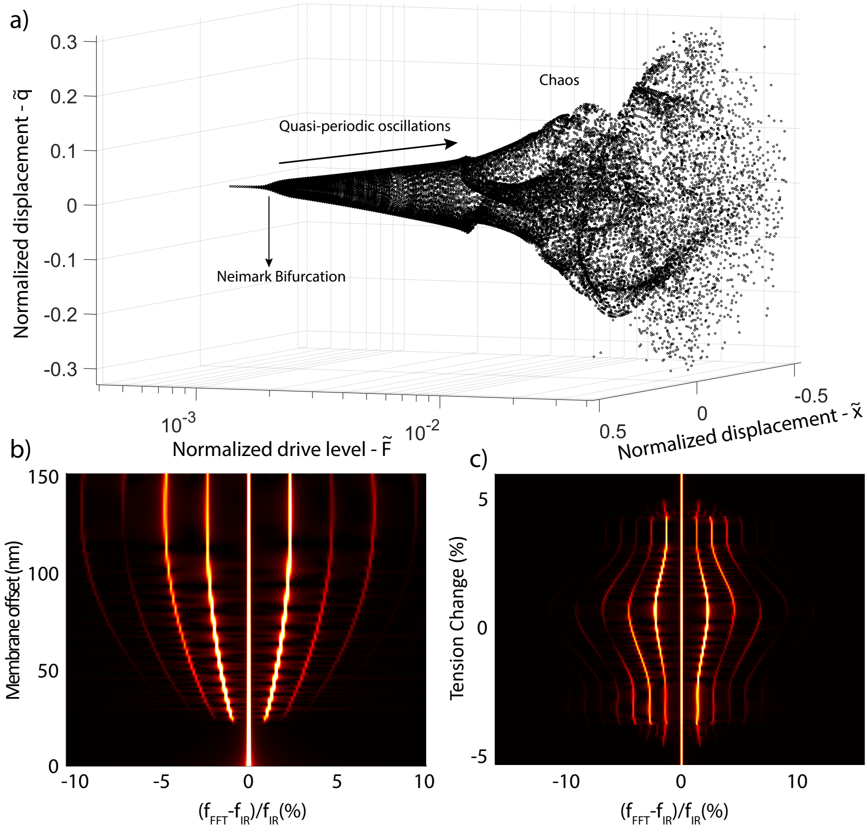

Figure 4.4: **Numerical simulations showing the evolution of phase spaces and sensitivity of frequency comb generation in a graphene drum with broken-symmetry and 1:2 IR to (b) offset amplitude (c) tension variation at the drive level $\tilde{F} = 0.0025$.** a) Bifurcation diagram of the graphene drum at 1:2 IR, showcasing a quasi-periodic route to chaos. b) Offset amplitude W_0 has been swept while the FFT of the time signal is being extracted in each step. As the offset increases, so does the boundaries of Neimark bifurcation and comb population. c) Added stiffness due to the tension change, T_x, has been swept while the FFT of the time signal is being extracted in each step, as the added tension moves the resonance frequencies with respect to the 1:2 IR condition.

quency tracking [110]. The internal resonance mechanism described here complements available toolsets in utilizing modal interactions of micro and nanomechanical systems and paves the way towards controllable use of IR for sensing physical properties of 2D materials and mechanical frequency comb generation.

4.5. APPENDIX C

4.5.1. C1: EVOLUTION OF THE OVERALL FREQUENCY RESPONSE WITH GATE VOLTAGE

In Fig. 4.5a (bottom panel) we show the evolution of the resonance frequencies of our graphene drum as a function of the applied gate voltage, and in top panel we show the frequency spectrum at V_g=1.9 V. We observe that change of the gate voltage changes the resonance frequencies at different rates, providing the possibility to obtain IR conditions. ~ 3 V is a striking feature of this mapping where there is an abrupt jump in the resonance frequencies. The observation coincides with a rapid change in the observed color of the drum (Fig. 4.5b), which points towards a rapid adjustment in the equilibrium position of the oscillator, i.e. snap-through instability (buckling). This is expected, if the membrane cavity is sealed very well in the atmospheric pressure, where it bulges upwards inside the vacuum chamber due to the pressure difference. This means that center of the membrane is above the surface level of the substrate confirming the presence of initial static deflection. The electrostatic attraction between the membrane and the bottom of the cavity, above the threshold voltage, slowly lowers the center of the membrane, until a critical voltage where an instant jump in the resonance frequencies occurs.

4.5.2. C2: ADDITIONAL EXPERIMENTAL RESULT

Here, we provide additional experimental result of the same device with different tension and pressure levels, where the 1:2 IR condition was met (Fig. 4.6a). Similar to the main results, we see a nonlinear splitting of the peak as the drive level is increased. Furthermore, in the center of the splitting, the third peak is observed due to Neimark bifurcaitons. The bifurcation gives birth to quasi-periodic motion, which is measured, observed as an amplitude modulated response (see Fig. 4.6b).

4.5.3. C3: EQUATIONS OF MOTION

To obtain the governing equations of the circular drum, we use the Rayleigh-Ritz approach. The elastic strain energy of the circular drum is obtained as

$$U = \int_0^{2\pi}\int_0^R \frac{Eh}{2(1-\nu^2)}\left(\epsilon_{rr}^2 + \epsilon_{\theta\theta}^2 + 2\nu\epsilon_{rr}\epsilon_{\theta\theta} + \frac{1-\nu}{2}\gamma_{r\theta}^2\right) r\,dr\,d\theta, \tag{4.3}$$

in which h is the thickness of the drum, R is the radius, E is the Young's modulus, and ν is the Poisson's ratio. Moreover, ϵ_{rr}, $\epsilon_{\theta\theta}$, and $\gamma_{r\theta}$ are the normal and shear strains. During axisymmetric oscillations $\gamma_{r\theta} = 0$, and the normal strains are obtained in terms of the transverse deflection (w) and radial displacement (u) of the drum as follows

$$\epsilon_{rr} = \frac{\partial u}{\partial r} + \frac{1}{2}\left(\frac{\partial w}{\partial r}\right)^2 + \left(\frac{\partial w}{\partial r}\right)\left(\frac{\partial w_0}{\partial r}\right), \tag{4.4}$$

$$\epsilon_{\theta\theta} = \frac{u}{r}. \tag{4.5}$$

In equation (4.4), w_0 is the initial transverse displacement of the drum associated with zero initial stress. Assuming modal interactions between the first two axisymmetric

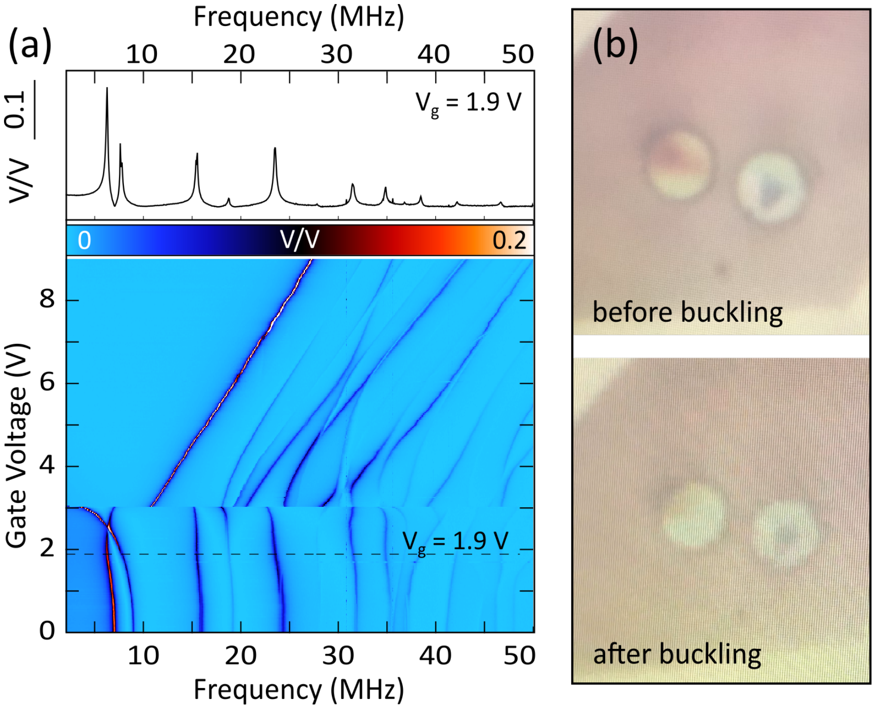

Figure 4.5: **Graphene membrane subjected to electrostatic force.** (a) Evolution of the resonance frequencies of the membrane as a function of the gate voltage: The resonator showcases several resonance peaks which evolve by applying gate voltage. Note the sudden jump in the resonance frequencies close to the gate voltage of ~ 3 V which suggest a state of buckling instability. (b) Snapshots of the membrane under the test (left circular object), before and after the buckling, taken by an optical camera.

eigenmodes and fixed boundary conditions ($u = w = 0$), the solution is approximated as

$$w = x(t)J_0\left(\beta_1\frac{r}{R}\right) + q(t)J_0\left(\beta_2\frac{r}{R}\right), \tag{4.6}$$

$$u = u_0 r + r(R-r)\sum_{j=1}^{n} y_j(t)r^{j-1}, \tag{4.7}$$

where u_0 is the initial radial displacement due to pre-tension n_0, and x and q are generalized coordinates associated with the first and the second axisymmetric mode of the drum, respectively. Moreover, J_0 is the Bessel function of order zero and β_1 and β_2 are its first two roots. In addition, y_j are the radial generalized coordinates and n is the number of these coordinates retained in the approximation. Moreover, we assume that the initial offset w_0 has the same form of the first axisymmetric mode with known amplitude W_0, thus:

$$w_0 = W_0 J_0\left(\beta_1\frac{r}{R}\right), \tag{4.8}$$

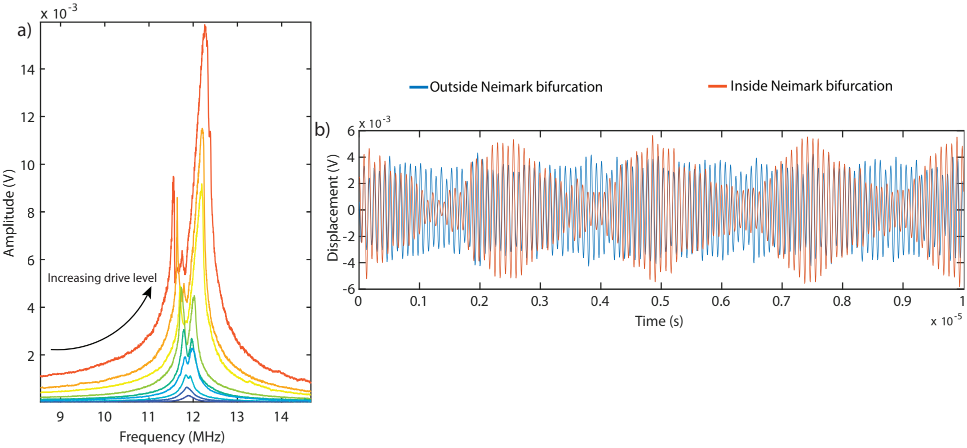

Figure 4.6: **Additional experimental results at 1:2 IR.** a) As the drive level is increased, the nonlinear splitting occurs. At higher levels, the central peak is also visible. b) Time signal inside and outside the Neimark bifurcation region. Inside the Neimark bifurcation response becomes quasi-periodic, displaying an ampltiude modulation.

The kinetic energy of the drum is then obtained as

$$T = \frac{1}{2}\rho h \int_0^{2\pi} \int_0^R \dot{w}^2 r dr d\theta, \tag{4.9}$$

in which the overdot represents differentiation with respect to time t, and ρ is the mass density. Next, Lagrange equations of motion are obtained [22] leading to the following set of coupled equations

$$\ddot{x} + \omega_1^2 x + \alpha_{11}^{(1)} x^2 + \alpha_{12}^{(1)} xq + \alpha_{22}^{(1)} q^2 + \gamma_{111}^{(1)} x^3 + \gamma_{112}^{(1)} x^2 q + \gamma_{122}^{(1)} xq^2 + \gamma_{222}^{(1)} q^3 = 0, \tag{4.10}$$

$$\ddot{q} + \omega_2^2 q + \alpha_{11}^{(2)} x^2 + \alpha_{12}^{(2)} xq + \alpha_{22}^{(2)} q^2 + \gamma_{111}^{(2)} x^3 + \gamma_{112}^{(2)} x^2 q + \gamma_{122}^{(2)} xq^2 + \gamma_{222}^{(2)} q^3 = 0, \tag{4.11}$$

in which $\alpha_{lm}^{(k)}$ and γ_{lm}^{k} are the quadratic and cubic nonlinear terms. It is worth noting that in equations (4.10) and (4.11) not all terms are resonant. To recover the resonant terms under 1:2 IR condition ($\omega_2 \simeq 2\omega_1$), we assume harmonic motion of the form $x \approx \cos(\omega_1 t)$ and $q \approx \cos(2\omega_1 t)$ as a first approximation. Inserting these relations in equations (4.10) and (4.11) shows that the terms $x^3 = \frac{3}{4}\cos(\omega_1 t) + \frac{1}{4}\cos(3\omega_1 t)$ and $xq = \frac{1}{2}(\cos(\omega_1 t) + \cos(3\omega_1 t))$ in the first equation of motion are trivially resonant. The same holds for the term $x^2 = \frac{1}{2}(1 + \cos(2\omega_1 t))$ which can be viewed as a resonant term in equation (4.11). In a similar fashion it can be shown that the cubic coupling terms xq^2 and $q^2 x$ are dispersive terms. Therefore, the governing equations of motion can reduce to

$$\ddot{x} + \omega_1^2 x + \alpha_{12}^{(1)} xq + \gamma_{111}^{(1)} x^3 = 0, \tag{4.12a}$$

$$\ddot{q} + \omega_2^2 q + \alpha_{11}^{(2)} x^2 = 0. \tag{4.12b}$$

Equations (4.12) are the normal form of a coupled oscillator undergoing 1:2 IR, and assuming that the second mode does not surpass its Duffing nonlinearity. It is interesting to note that frequencies ω_1 and ω_2, the coupling term $\alpha_{12}^{(1)} = 2\alpha_{11}^{(2)} = 2\alpha$, and the Duffing nonlinearity $\gamma_{111}^{(1)} = \gamma$ can be expressed in terms of mechanical and geometric properties of the drum as follows

$$\omega_1 = \frac{2.4}{R}\sqrt{\frac{n_0}{\rho h}} \tag{4.13a}$$

$$\omega_2 = \frac{5.5}{R}\sqrt{\frac{n_0}{\rho h}}, \tag{4.13b}$$

$$\alpha = 10.794\frac{\pi E h W_0}{R^2}, \tag{4.13c}$$

$$\gamma = 0.9\frac{\pi E h}{R^2}, \tag{4.13d}$$

in which α and γ are evaluated assuming $\nu = 0.16$. We note that the Duffing nonlinearity γ depends on the Young's modulus and Poisson's ratio of the drum [22] while the quadratic coupling α in addition depends on the initial deformation w_0. In other words, in the absence of W_0, mechanically, no quadratic coupling exists between the first two eigenmodes of the drum. Moreover, as mentioned above, one can show that in the 1:2 internal resonance scenario, the full model (equations (4.10) and (4.11)) and the normal form model (equations (4.12)) behave the same qualitatively where they both replicate the observed behavior (Fig. 4.7), with only differences in the peak frequencies and the amplitudes due to dispersive terms. Both models display a butterfly shaped response, where left-hand side of the resonance undergoes softening and right-hand side undergoes hardening. This is a direct outcome of 1:2 IR and can be intuitively understood by assuming harmonic motion of the form $x = Xcos(\Omega t + \theta)$, $q = Qcos(2\Omega t + \psi)$. One can see from equations (4.1) and (4.2) in the main text that

$$X^2[(\omega_1^2 - \Omega^2) + Q\alpha + \frac{3}{4}\gamma X^2]^2 + \tau_x^2\Omega^2 X^2 = F^2, \tag{4.14a}$$

$$Q = \frac{\alpha X^2}{2(4\Omega^2 - 2\Omega\tau_q - \omega_2^2)} \tag{4.14b}$$

where $\omega_1^2 = k_x + T_x$ and $\omega_2^2 = k_q + T_q$, assuming $\psi = 2\theta$. We note that equations (4.14a) and (4.14b) are approximate solutions that are found by only accounting for the fundamental harmonics and discarding higher order harmonics. By inserting equation (4.14a) in (4.14b), one can see that the effective nonlinearity is $\gamma_{eff} = \frac{\alpha^2 X^2}{2(4\Omega^2 - 2\Omega\tau_q - \omega_2^2)} + \frac{3}{4}\gamma X^2$. Recalling that close to 1:2 IR, $\omega_2 = 2\omega_1$, for $\Omega < \omega_1$ and by assuming relatively small Duffing constant γ and linear damping coefficient τ_q, effective nonlinearity becomes $\gamma_{eff} < 0$ and thus the response is softening at the left side of the resonance, whereas at the right side where $\Omega > \omega_1$, the effective nonlinearity becomes $\gamma_{eff} > 0$, showing a hardening response. This gives rise to the butterfly shaped split observed in the experiments.

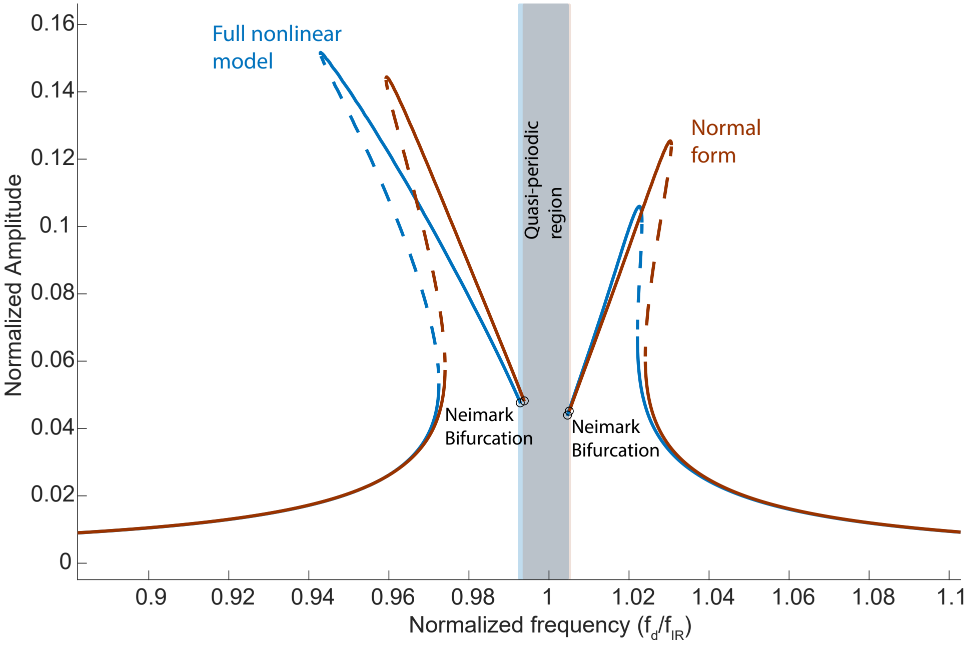

Figure 4.7: **Comparison of full model (equations (4.10) and (4.11)) to normal form model (equation (4.12)).** Solid lines depict stable solutions whereas dashed lines depict unstable solutions. Black circles depict the boundaries of the Neimark bifurcation. Physical parameters that are mentioned in the main paper were used in both simulations, with drive $\tilde{F} = 0.002$.

4.5.4. C4: ADDITIONAL SIMULATIONS

Following on simulations in Figure 4.3, here we provide additional simulations. Fig. 4.8 shows the frequency response at the internal resonance condition, obtained by the numerical continuation software (AUTO). The Neimark bifurcations are obtained at the points where the motion becomes quasi-periodic in the time integration simulations, also shown in the main text. Furthermore, we investigate the evolution of the phase space as the drive frequency passes the 1:2 IR condition (Fig. 4.9). It is possible to observe that, the periodic motion of the resonator turns to quasi-periodic oscillation (which can be also seen from the Poincaré maps) when the bifurcation is triggered (at $f_d/f_{IR} = 0.9951$). The phase space afterwards shows an ergodic behavior till $f_d/f_{IR} = 1.0043$ where the system regains its stable periodic motion through the second Neimark bifurcation. Increasing the drive levels further increases the complexity of the Poincaré maps (Fig. 4.10) as the system starts to exhibit chaotic oscillations.

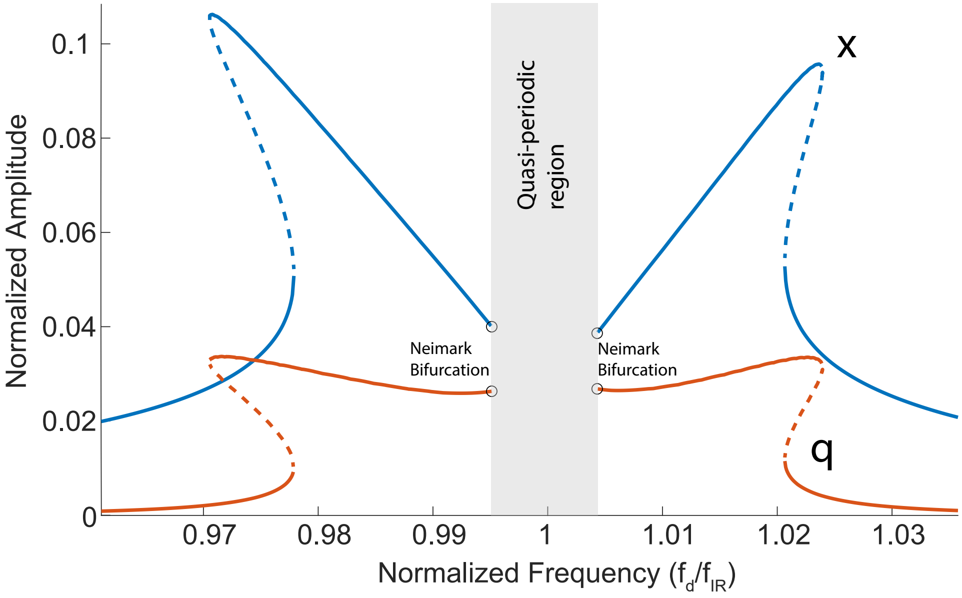

Figure 4.8: **Frequency response curves obtained by numerical continuation.** Solid lines depict stable solutions whereas dashed lines depict unstable solutions. Black circles depict the boundaries of the Neimark bifurcation.

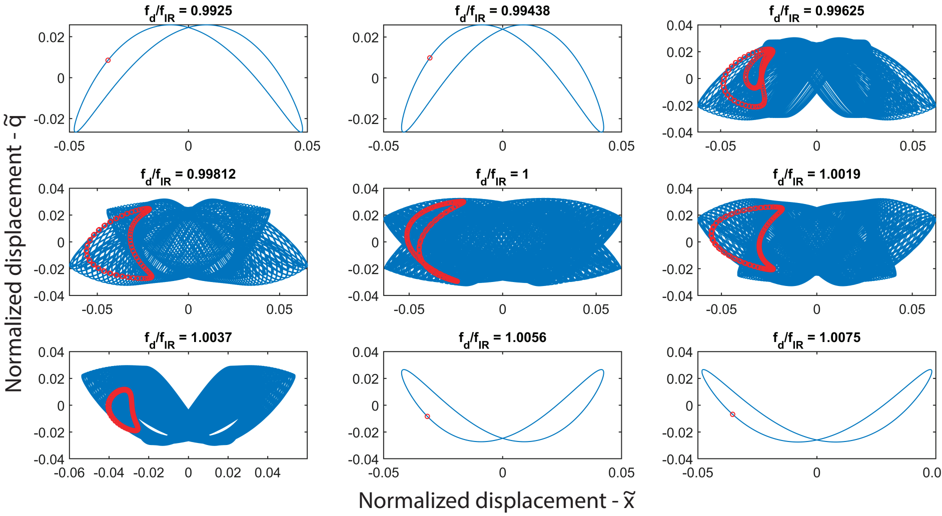

Figure 4.9: **Evolution of the phase space as the resonator passes through the IR condition.** Poincaré maps are extracted(by taking snapshots at every drive period) on top of the phase spaces, indicated by red circles. ($\tilde{F} = 0.0015$)

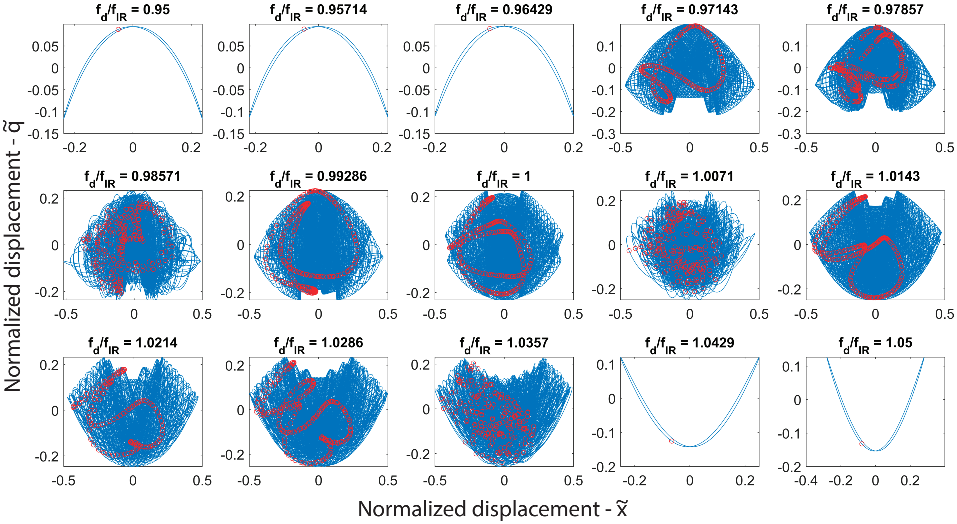

Figure 4.10: **Evolution of the phase space at a higher drive level, showing increasingly complex Poincaré maps.**($\tilde{F} = 0.02$)

4.5.5. C5: Sensitivity of the frequency combs to the external drive at 1:2 IR

The sensitivity of the comb spacing to the drive frequency can be also studied using our model. In Fig. 4.11a it is possible to trace the evolution of the frequency combs as the drive level is increased. Higher drive levels enlarge the Neimark bifurcation region and enrich the spectral response by increasing the comb population, until a certain drive level where the response of the system becomes chaotic. In Fig. 4.11b and c we show the variation of comb spacing (Δf) with respect to the drive frequency in the region mediated by Neimark bifurcations, in experiment (from the measurements in Fig. 4.2d) and simulations (from the results in Fig. 4.3d). It can be seen that the comb spacing is sensitive to the drive frequency.

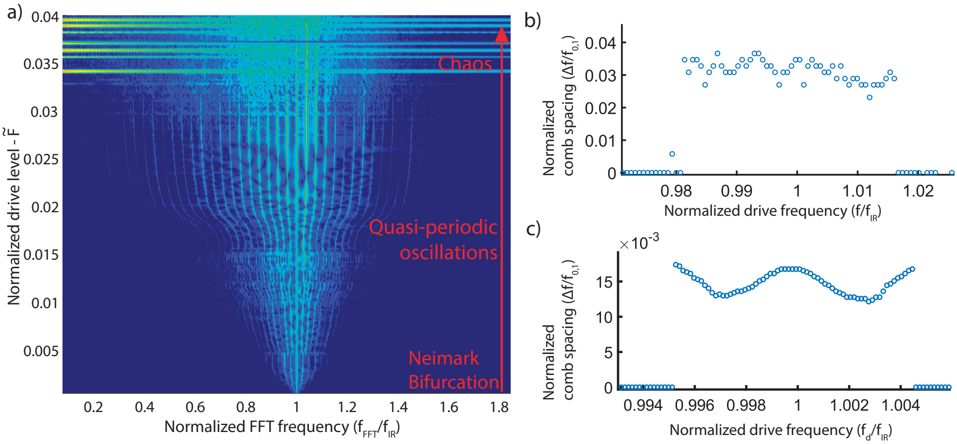

Figure 4.11: **Evolution of the frequency comb.** (a) As the drive level is increased, the Neimark bifurcation is triggered, giving birth to the frequency comb region. Comb population increases further at high drive levels until the response becomes chaotic. (b) Experimental frequency spacings of the frequency comb as the drive frequency is swept through the 1:2 IR, derived from the results of Fig. 4.2d. (c) Simulated frequency spacings of the frequency comb as the drive frequency is swept through the 1:2 IR, derived from the results of Fig. 4.3d.

5

NONLINEAR NANOMECHANICAL COUPLING TO ANTIFERROMAGNETIC ORDER VIA MAGNETOSTRICTION

Nanomechanical resonances of two-dimensional (2D) materials are probes for condensed-matter physics, offering new insights into the magnetic and electronic phase transitions. Despite extensive research, the influence of second-order phase transitions on nonlinear dynamics of 2D membranes has remained largely unknown. Here, we investigate nonlinear magneto-mechanical coupling to antiferromagnetic order in suspended $FePS_3$*-based heterostructure membranes. By analyzing the motion of these membranes as a function of temperature, we observe renormalization of both nonlinear stiffness and damping close to the Néel temperature* T_N*. We explain these observations with an analytical magnetostriction model, describing the nonlinear dissipation mechanism arising in our measurements. Our findings thus provide previously unexplored insights into the thermodynamics and magneto-mechanical energy dissipation mechanisms in nanomechanical resonators due to the phase change of materials.*

The contents of this chapter are from a manuscript under preparation, in collaboration with Makars Šiškins (who has major contributions in the making of this chapter), Maurits Houmes, Samuel Mañas-Valero, Eugenio Coronado, Yaroslav M. Blanter, Herre S. J. van der Zant, Peter G. Steeneken and Farbod Alijani.

5.1. INTRODUCTION

THE mechanical properties of two-dimensional (2D) materials have been extensively studied [111], [112] due to their potential for use in a variety of applications, such as sensing [10], [112], [113] and energy transduction [32], [65], [66]. Different degrees of freedom are utilized in coupling the motion dynamics of such devices to both internal and external stimuli [65], [66], ranging from coupling to photons [114], [115], phonons [31], [116], [117] and electrons [118]–[120], to an interaction between multiple resonators at a distance [92], [117]. Owing to their small mass and ultra-thin nature, these membranes can easily operate in a nonlinear regime of motion, where elastic effects [22], internal resonances [67], [69] and various internal dissipation mechanisms [26], [31], [32], [67] dictate their motion dynamics.

Recently, there has been a growing interest to use nanomechanical vibrations of 2D materials as practical knobs to infer the elastic and thermodynamic properties of these membranes [66]. Examples include nonlinear dynamic characterization of their elastic properties [22], probing magnetic [121]–[127] and electronic phase transitions [120], [121]. Among them, the ability of these membranes to detect magnetic phase change in the absence of an applied magnetic field [121], [123], [125] has opened up new avenues for developing self-sensitive magnetic nano-electromechanical (NEMS) devices [65], [66]. This approach relies on the coupling between the magnetic and mechanical properties of the 2D material, which allows for highly sensitive detection of magnetisation [122], [127] and thermodynamics of magnetic phases [121], [123]. Yet, the consequences of the magneto-mechanics in nonlinear motion regime of these membranes have remained largely unexplored.

Here, we investigate the nonlinear coupling mechanisms between nanomechanics and antiferromagnetic order in membranes made of $FePS_3$-based heterostructures. We study the changes in both nonlinear stiffness and nonlinear damping as a result of the antiferromagnetic phase transition near the Néel temperature T_N of $FePS_3$ [121], [128]. Consequently, we substantiate these observations with a magnetostriction model, revealing and providing a description of the magneto-mechanical dissipation mechanism, as a previously unexplored source of nonlinear damping in 2D material membranes.

5.2. MEASUREMENTS OF GRAPHENE/$FePS_3$ HETEROSTRUCTURE NANORESONATORS

To create a freestanding membrane, we suspend 9.5 ± 0.6 nm thin layer of $FePS_3$ over a pre-defined circular cavity of $r = 1.5\ \mu$m in radius in a Si/SiO_2 substrate (Fig. 5.1a). To improve thermal management in the $FePS_3$ layer [129] and electrically contact it, we cover the membrane with multi-layer graphene (MLG) of 2.0 ± 0.7 nm thickness which acts as an excellent heat sink [130], [131]. These MLG/$FePS_3$ heterostructure membranes are then placed into a closed-cycle cryostat chamber with optical access and cooled to cryogenic temperatures. At a specific temperature T set by the local sample heater, we measure the amplitude x of the membrane's fundamental mode of vibration in response to the low-power opto-thermal drive using a laser interferometry technique [97], [121] (see Methods and Fig. 5.1a-c). We then fit the measured resonance peak (gray-filled circles) to the linear harmonic oscillator model (solid blue line) and extract the corresponding

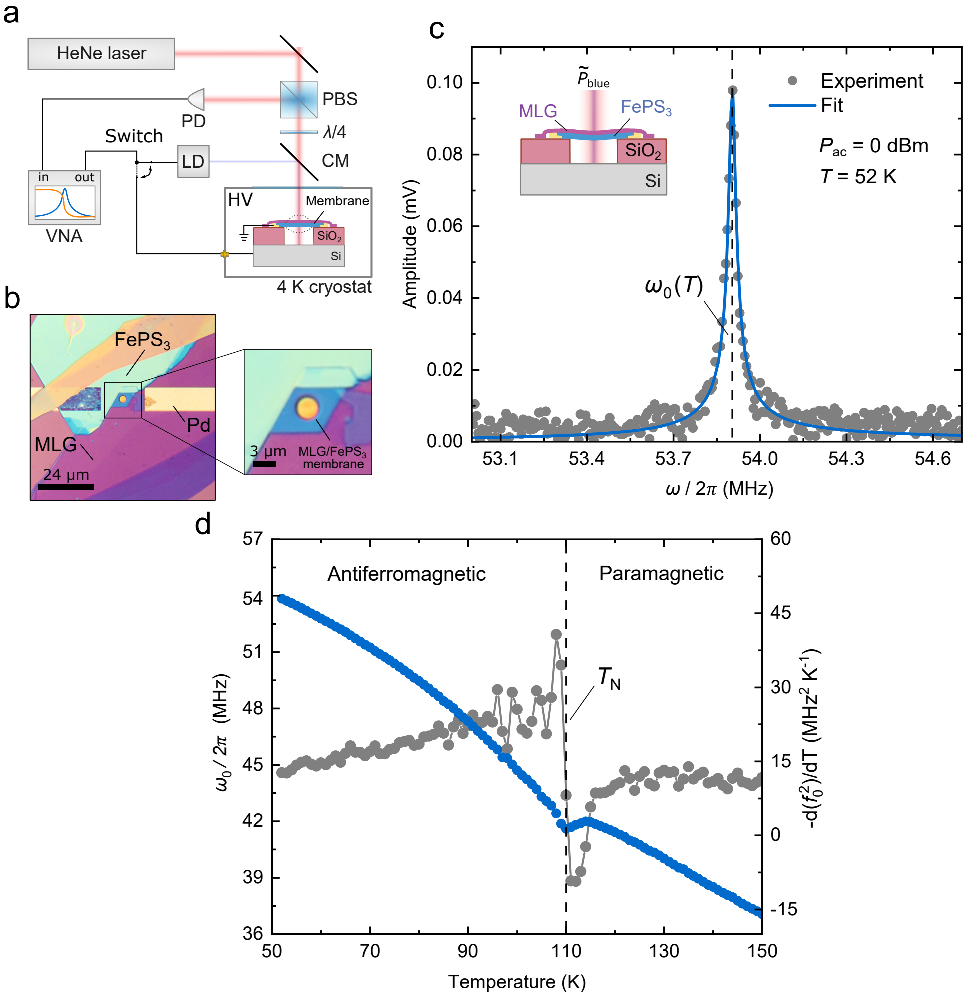

Figure 5.1: **Membrane resonator made of MLG/FePS$_3$ heterostructure.** (a) Schematic of the laser interferometer measurement setup (see Methods). PD is the photodiode, LD - the laser diode CM - the cold (dichroic) mirror, PBS - the polarized beam splitter, VNA - the vector network analyzer. (b) Optical image of the sample. (c) The measured resonance peak amplitude of the fundamental membrane mode of vibration (filled gray dots). The solid blue line is fit to the linear damped harmonic oscillator model. The inset shows the schematic of the device cross-section. A vertical dashed line indicates extracted ω_0. (d) The resonance frequency ω_0 as a function of temperature, extracted from the fit similar to (c) (filled blue dots). Connected gray dots are the corresponding derivative of the f_0^2 with respect to temperature. A vertical dashed line indicates extracted T_N.

resonance frequency $\omega_0(T) = 2\pi f_0(T)$, as shown in Fig. 5.1c.

5.2.1. LINEAR VIBRATIONS NEAR PHASE TRANSITION

Following this procedure, we measure $\omega_0(T)$ in the temperature range from 52 to 150 K as shown in Fig. 5.1d. In the vicinity of $T \sim 110$ K (vertical dashed line in Fig. 5.1d) the resonance frequency $\omega_0(T)$ exhibits the anomaly related to antiferromagnetic-to-paramagnetic phase transition. This becomes even more prominent in the temperature derivative of $f_0^2(T)$ (filled gray circles in Fig. 5.1d) - a quantity which is related to specific heat $c_v(T)$ of the material through thermal expansion coefficient and thermodynamic relations [121]. Thus, the temperature of the discontinuity in $-\frac{\mathrm{d}f_0^2(T)}{\mathrm{d}T}$ can be used as a measure of T_N at the transition from magnetic to non-magnetic state [121], [123]. This is further supported by the fact that the measured T_N also corresponds to a peak in inverse quality factor $Q^{-1}(T)$ (see Appendix D1), which is expected to arise due to the increased thermoelastic damping contribution near the phase transition [92], [121], [123].

5.2.2. NONLINEAR VIBRATIONS NEAR PHASE TRANSITION

After characterising the dynamics of the membrane in the linear regime at a low optothermal driving force, we increase the driving power of the VNA P_{ac} from 0 to 8 dBm to achieve higher force levels and observe nonlinear hardening behavior. Fig. 5.2a displays an apparent Duffing response at $T = 52$ K and $P_\mathrm{ac} = 8$ dBm, revealing bi-stable amplitude branches that depend on the direction of the frequency sweep, indicating the presence of nonlinear stiffness [22]. Furthermore, the responsivity of this Duffing response decays as the drive levels are further increased (Fig. 5.2d), implying the presence of nonlinear damping [67].

To investigate the temperature dependence of the nonlinear resonance, we measure the normalized amplitude of membrane motion A_n around $\omega_0(T)$ at 8 dBm of power using backward frequency sweeps in the temperature range from 52 to 150 K and plot it in Fig. 5.2b versus the difference between the driving frequency ω and the measured $\omega_0(T)$ in linear regime (Fig. 5.1d). In the vicinity of the phase transition temperature T_N, we observe changes in the nonlinear frequency response of the membrane that seem to be peculiar to the coupling to magnetic phase transition. Two major observations can be made here. Firstly, the central position of the resonance peak at a higher driving power is shifted near the T_N, indicating a change in linear membrane stiffness k_1, and thus the strain [121] (Figs. 5.2b and c). Secondly, the backbone slope of the Duffing response notably, changes depending on the magnetic state of the membrane, again, with the largest effect near T_N, indicating a change in nonlinear membrane stiffness k_3 [22] (see Fig. 5.2c). We have also performed additional control experiments on multiple samples using both optical and electrical excitation, where V_ac signal is applied between the Si backgate of the chip and the conducting top layer of MLG, and confirm that these observations are reproducible and independent of the method of excitation (see Appendix D2).

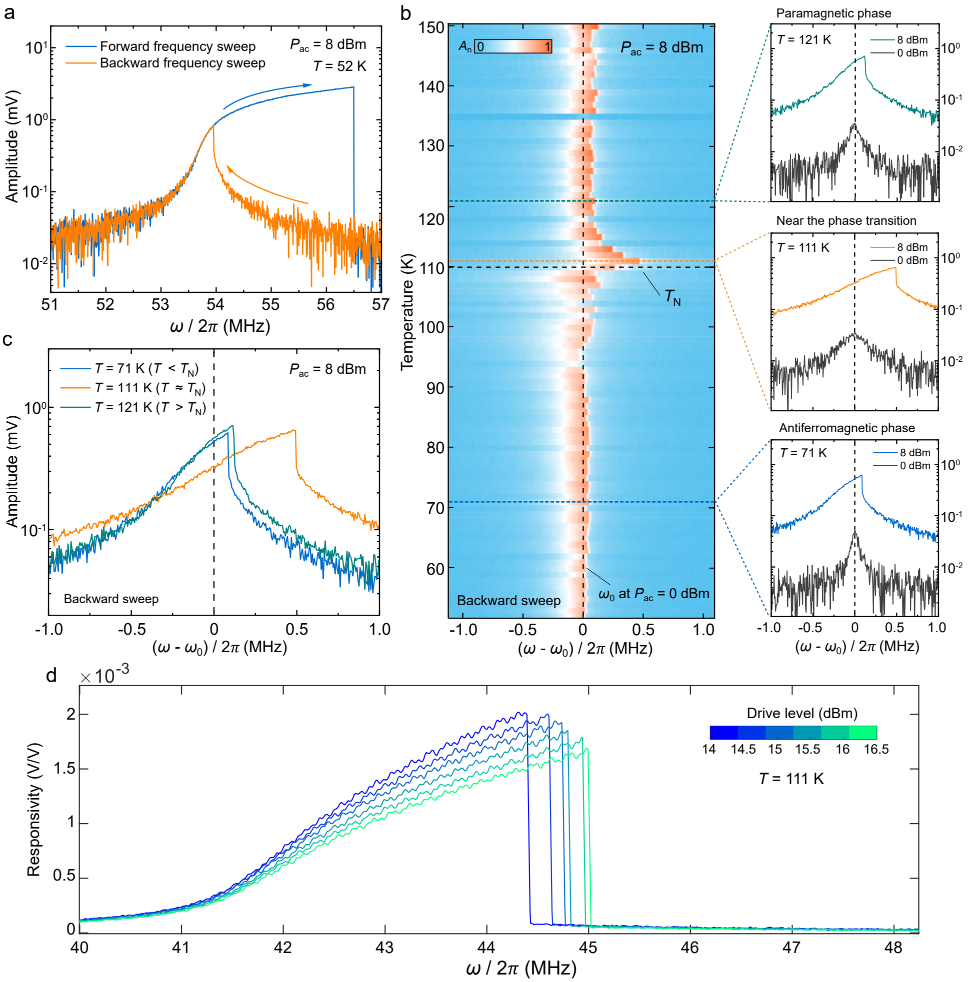

Figure 5.2: **Nonlinear dynamics of the MLG/FePS$_3$ membrane.** (a) The measured Duffing response of the resonance peak from Fig. 5.1c at a higher excitation power (P_{ac} = 8 dBm). (b) Left panel: The colour map of the normalized amplitude measured as a function of temperature in backward frequency sweep regime around linear resonance frequency ω_0 from Fig. 5.1d. The Néel temperature T_N from Fig. 5.1d is indicated with a black dashed horizontal line. Right panel: the measured amplitude around ω_0 from the right panel for P_{ac} = 0 and 8 dBm at three temperature points corresponding to different magnetic phases. (c) The measured frequency responses at 8 dBm for the same temperature points from (b) superimposed for comparison. (d) Responsivity measurements in nonlinear regime for various drive levels, at T = 111 K.

5.3. NONLINEAR PARAMETER EXTRACTION

To carefully assess the findings of our experimental data, we fit the measured frequency response curves to the Duffing-van der Pol oscillator model and extract the model parameters (see Appendix D3 and D4) for a given temperature range, as depicted in Fig. 5.3a:

$$\ddot{x}+\omega_0^2 x+\gamma x^3=\bar{F_\omega}\cos(\omega t)-\frac{\omega_0}{Q}\dot{x}-\xi_{\mathrm{nl}}x^2\dot{x}, \tag{5.1}$$

where $\bar{F_\omega}$ is the drive force amplitude, γ is the nonlinear stiffness and ξ_{nl} is the nonlinear damping term of van der Pol type [67], [132], all mass normalized. We start by extracting the linear resonance frequency $f_0 = \omega_0/2\pi$, as a function of the drive levels, as it can increase at higher drive powers (Fig. 5.3b). Then, we extract the nonlinear stiffness term γ (Fig. 5.3c) using the slope of the backbone curve. Consequently, we fix this value to fit the forward frequency sweep response for extracting ξ_{nl} (Fig. 5.3d).

Extracted parameters reveal that, at a higher driving power and as the temperature decreases, a notable anomalous peak with a consequent sharp drop is observed in γ at $T < T_{\mathrm{N}}$ (Fig. 5.3c). This feature is also accompanied by a peak in ξ_{nl} at approximately the same temperature (Fig. 5.3d), indicating a prominent increase in the nonlinear dissipation in the antiferromagnetic phase regime. Furthermore, the shift in f_0 is quantified, and it can be seen that it peaks around $T \approx T_{\mathrm{N}}$ (Fig. 5.3b).

5.4. THEORETICAL MODEL

We make an attempt to understand these observations with a theoretical model, by considering the elastic potential energy of the membrane U_{el}, the magnetic free energy U_{m} of FePS$_3$ and magneto-mechanical coupling via spontaneous magnetostriction U_{ms} [121], [127], [133] (see Appendix D5):

$$\begin{aligned}U_{\mathrm{T}} =& U_{\mathrm{el}}+U_{\mathrm{m}}+U_{\mathrm{ms}}\\ =& \left[\frac{k_1}{2}x^2+\frac{k_3}{4}x^4\right]+\\ & \left[U_{\mathrm{m},0}+\frac{a}{2}(T-T_{\mathrm{N}})L^2+\frac{B}{4}L^4\right]+\left[\frac{\lambda_{ij}\sigma_{ij}(x)}{2}L^2\right],\end{aligned} \tag{5.2}$$

where x is the motion amplitude, k_1 and k_3 are the linear and nonlinear stiffnesses, $\sigma_{ij}(x)$ is the amplitude-dependent stress tensor, L the antiferromagnetic order parameter in the direction of an easy-axis of FePS$_3$, λ_{ij} the magnetostriction tensor, $U_{\mathrm{m},0}$ is the magnetic energy at paramagnetic state, and a, B are phenomenological positive constants [133], [134]. By minimizing equation (5.2) with respect to L at $x = 0$, the ground state order parameter L_0 is obtained (see Appendix D5). When the membrane is in motion $\sigma = \sigma_0 + \sigma_\omega(x)$; σ_0 captures the pre-stress and other static stress contributions where $\sigma_\omega(x)$ is the oscillatory part of the stress. Therefore, the magnetic system will be out of equilibrium, such that $L(x) \simeq L_0 + L_\omega(x)$, and thus becomes stress and amplitude dependent. Subsequently, the rate of $L(x)$ approaching the ground state L_0 (Fig. 5.4a) can be set by the kinetic equation [135]–[137]:

$$\frac{\mathrm{d}L}{\mathrm{d}t}=-\kappa\frac{\partial U_{\mathrm{T}}}{\partial L}, \tag{5.3}$$

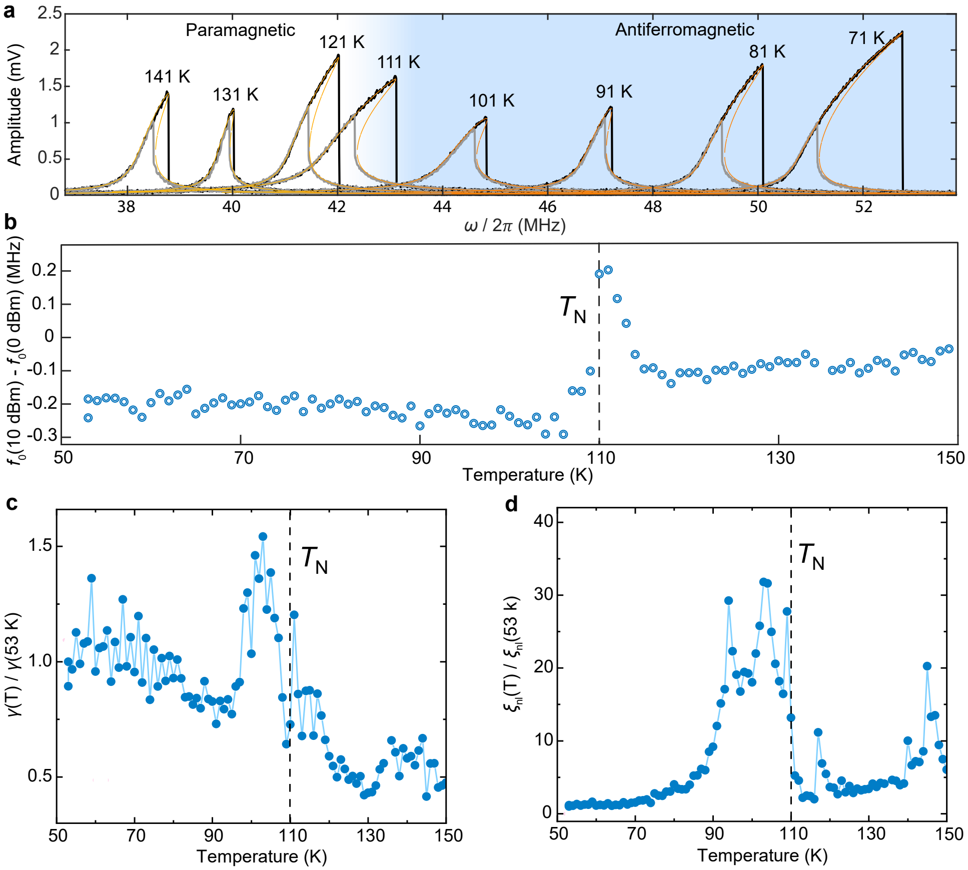

Figure 5.3: **Fits of the experimental frequency response curves to the Duffing-van der Pol model.** (a) Fit of the equation (5.1) (orange solid lines) to the frequency response measurements for forward (black solid lines) and backward sweeps (gray solid lines) at $P_{ac} = 10$ dBm for different temperatures. The light blue region indicates the antiferromagnetic phase of the membrane. (b) Linear resonance frequency $2\pi f_0 = \omega_0$ fits at 10 dBm drive level plotted relative to 0 dBm drive level linear resonance frequency fits, with respect to temperature. (c) Connected blue dots are the measured $\gamma(T)$, extracted from the fits similar to (a) and normalized by the 53 K data point. (d) Connected blue dots are the measured $\xi_{nl}(T)$, extracted from the fits similar to (a) and normalized by the 53 K data point.

where t is the time and κ is the phenomenological kinetic coefficient. By linearizing equation (5.3) via Taylor expanding around L_0 (see Appendix D5), we obtain:

$$\frac{dL_\omega}{dt} \cong -\frac{L_\omega}{\tau} - \kappa\lambda L_0 \sigma_\omega(x), \tag{5.4}$$

where $\tau = \frac{1}{2\kappa a(T_N^* - T_N)}$ is the magnetic relaxation time constant of the FePS$_3$ membrane [135], [136], [138]. Although typically magnetic relaxations are fast (in the order of picoseconds) in antiferromagnets [139]–[141], in case of FePS$_3$, long nanosecond-scale relaxation times are required to relax the magnetic sub-lattice near the T_N due to the strongly coupled ordering of spins to the slow process of interlayer shear [138] (see Appendix D5). $L_\omega(x)$ term then induces oscillations in $L(x)$ at frequency 2ω, as $\dot{L}_\omega \propto \sigma_\omega$ where $\sigma_\omega \propto x^2$, which can lag the membrane motion at sufficiently large τ [138] producing a delay in the coupled magneto-mechanical system (see Appendix D5).

In order to theoretically investigate the consequences of this delay in the dynamics, we look into the steady-state response of the driven coupled magnetomechanical system. To do this, we extract the equation of motion associated with the generalized coordinate x, by defining the Lagrangian as $\mathscr{L} = \frac{1}{2}m\dot{x}^2 - U_T$ (See Appendix D5). Thus, using the Lagrange equations, $\frac{d}{dt}\frac{\partial \mathscr{L}}{\partial \dot{x}} - \frac{\partial \mathscr{L}}{\partial x} = 0$, equation of motion governing x becomes :

$$m\ddot{x} + k_1 x + k_3 x^3 + \frac{\lambda}{2} L_0^2 \frac{\partial \sigma(x)}{\partial x} + \lambda L_0 L_\omega \frac{\partial \sigma(x)}{\partial x} = F_\omega \cos(\omega t) - \left(\eta_{nl} x^2 + \frac{m\omega_0}{Q}\right)\dot{x}, \tag{5.5}$$

where m is the effective mass of the resonator, $k_1 = m\omega_0^2$ is the linear non-magnetic stiffness and k_3 is the nonlinear non-magnetic Duffing constant. We consider a periodic forcing with amplitude F_ω that is driving the system, together with a linear dissipation related to quality factor Q and an intrinsic non-magnetic nonlinear damping with intensity η_{nl}. Solving the coupled system i.e. equations (5.4) and (5.5) using the harmonic balance method (see Appendix D5) we obtain the steady-state amplitude equation that is of the same form of the steady-state amplitude equation of the Duffing-van der Pol equation (see Appendix D3), however the linear and nonlinear parameters are rescaled due to the magneto-mechanical coupling, resulting in k_1^*, the renormalized linear stiffness:

$$k_1^* = \begin{cases} k_1 + \lambda L_0^2 \frac{Ec_3}{2r^2} & T < T_N^* \\ k_1 & T > T_N^*, \end{cases} \tag{5.6}$$

k_3^*, the renormalized nonlinear stiffness of Duffing type:

$$k_3^* = \begin{cases} k_3 - \frac{\lambda^2}{12B}\frac{E^2 c_3^2}{r^4}\frac{1}{1+4\omega^2\tau^2} & T < T_N^* \\ k_3 & T > T_N^*, \end{cases} \tag{5.7}$$

and η_{nl}^*, the renormalized nonlinear damping of van der Pol type [67], [132]:

$$\eta_{nl}^* = \begin{cases} \eta_{nl} + \frac{\lambda^2}{2B}\frac{E^2 c_3^2}{r^4}\frac{\tau}{1+4\omega^2\tau^2} & T < T_N^* \\ \eta_{nl} & T > T_N^*, \end{cases} \tag{5.8}$$

where E is the Young's modulus and c_3 a numerical factor that depends on membrane's Poisson's ratio and its geometry [22].

There are couple of important consequences of these renormalizations. The renormalization of k_1 can lead to its increase or decrease, depending on the sign of λ, and as the temperature is decreased beyond $T_\mathrm{N}^* = T_\mathrm{N} - \frac{\lambda_{ij}\sigma_{ij}(x)}{a}$. The T_N^* shift due to increased stress/strain was previously demonstrated by applying a purely static external force [121]. Likewise, at high amplitude oscillations, the dynamic change of the stress/strain via a modulated force results in an additional effective static strain and related stress term (see Appendix D5), which can reach up to 0.03% in similar systems [84]. The contribution of the order parameter on effective linear stiffness we show here, $k_1^* \propto L_0^2$, is studied and described with detail in a previous work [127].

Unlike the renormalization of k_1, which is independent of dynamics of the order parameter L, the renormalization of the nonlinear parameters k_3 and η_nl arise from the oscillations in L. As a result, both k_3^* and η_nl^* are functions of characteristic times of the coupled dynamic system, ω and τ. From equation 5.7, it is possible to see that when $T < T_\mathrm{N}^*$, k_3^* starts decaying with $k_3^* \propto -\frac{1}{1+4\omega^2\tau^2}$. Assuming a temperature dependent non-magnetic $k_3(T)$, that is monotonically increasing with the decrease in temperature (similar to what is measured in the experiments (Fig. 5.3c), this decay of magnetic origin in k_3^* will generate a local peak at $T \approx T_N^*$.

Furthermore, the renormalized nonlinear damping, $\eta_\mathrm{nl}^* \propto \frac{\tau}{1+4\omega^2\tau^2}$, at $T < T_\mathrm{N}^*$, peaks at $2\omega\tau = 1$ (see Appendix D5), resembling a Debye peak, whose maximum does not appear to be at $\omega = 1/\tau$ but rather at $2\omega = 1/\tau$, and decreases for smaller and larger τ. This behaviour can be understood intuitively as follows: if the oscillations are at a much faster timescale of the coupled reservoir, such that $2\omega \gg 1/\tau$, the reservoir does not have enough time to relax and dissipate energy. On the contrary, when the oscillations are at a much slower timescale than the coupled reservoir $2\omega \ll 1/\tau$, the reservoir almost perfectly follows the oscillations, as if it is in equilibrium, with almost no delay, again resulting in minimal dissipation [132]. Thus, the magnetic nonlinear damping contribution is only significant when the period of oscillations are comparable to two times the magnetic relaxation time such that $2\omega\tau \simeq 1$.

For convenience, we plot the derived magnetostrictive model of equations (5.7) and (5.8) in Fig. 5.4b and c. We assume temperature dependence for k_3 from equation (5.7) which is dominated by non-magnetic effects, as observed in the experiments (Fig. 5.3c), producing the additional background-slope in $k_3^*(T)$ below and above the T_N^*. As shown in Fig. 5.4b with solid magenta line, equation (5.7) reproduces the measured decrease of k_3^* in the proximity of T_N^*. At the same time, our model in Fig. 5.4c reproduces the measured peak in $\eta_\mathrm{nl}^*(T)$ at $2\omega_0\tau = 1$. Notably, in a hypothetical case where τ is insignificantly short, i.e. $\tau = 0$ in equations (5.7) and (5.8), the model still predicts the decrease in $k_3^*(T)$ at the T_N^* albeit discontinuous, while magnetic contribution to $\eta_\mathrm{nl}^*(T)$ vanishes, as shown in Fig. 5.4b and c with dashed gray lines.

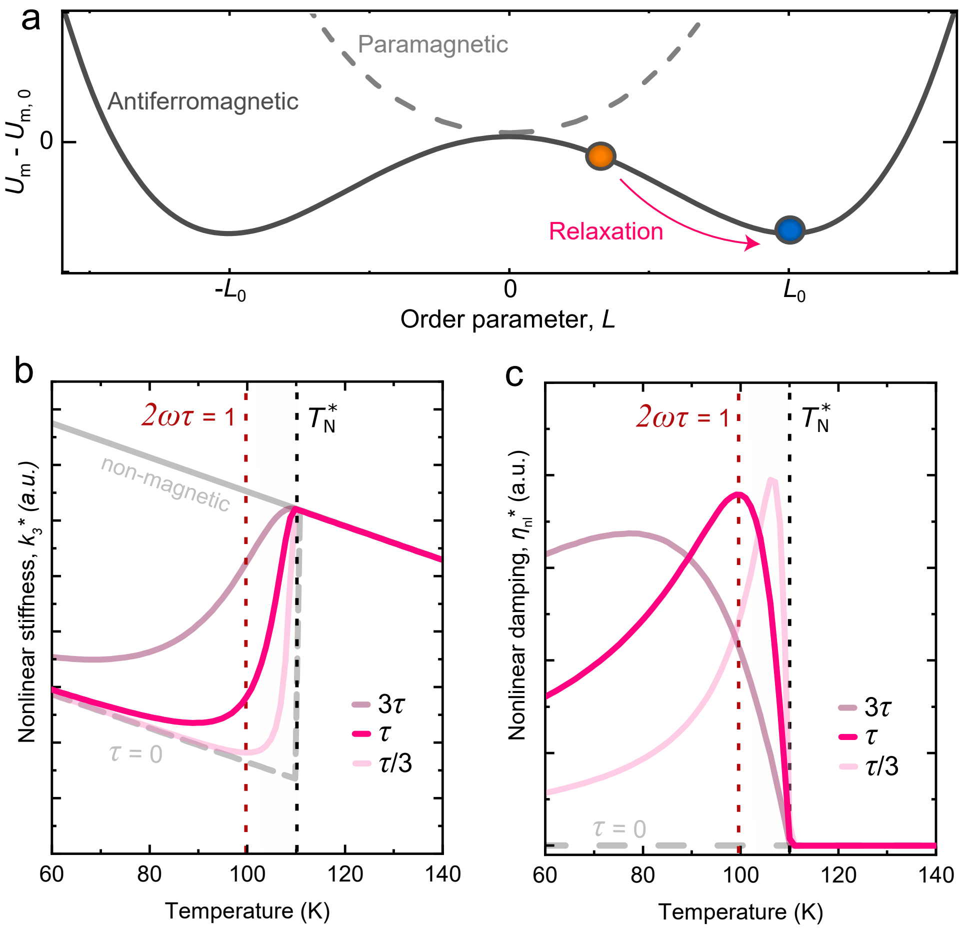

Figure 5.4: **Theoretical model.** (a) Schematic of the magnetic free energy of the system with un-relaxed (orange dot) and relaxed ground (blue dot) states indicated. (b) Effective nonlinear stiffness with respect to temperature from the equation (5.7) (solid magenta lines), assuming a linearly decreasing $k_3(T)$, at different magnetic relaxation times τ. The light gray line indicates the non-magnetic $k_3(T)$ slope that is extracted by a linear fit to $T > 110$ K region in Fig. 5.3c. (c) Effective nonlinear damping from the equation (5.8) (solid magenta lines), at different magnetic relaxation times τ. Both in (b) and (c) dashed gray line indicates the scenario where τ is insignificantly short, i.e. $\tau = 0$.

5.5. MICROSCOPIC ORIGIN OF NONLINEAR DAMPING

When discussing the physical interpretation of the origin of this nonlinear damping, its microscopic mechanism should be envisioned as a consequence of a nonlinear oscillator's excited vibrational modes scattering off its own magnetic energy reservoir [31], [58]. This interaction then is accompanied by the energy transfer of two oscillation quanta ($2\omega_0$) for nonlinear damping [58]. Interestingly, the mechanism also finds its macroscopic similarities to magnetic internal friction arising due to a delay in Young's modulus relaxation near the T_N occurring in large-scale bulk of magnetic solids [135]–[137], [142]–[145] with a crucial distinction at the nanoscale that it affects principally different mechanical properties at twice the rate in the membrane case. Our analysis predicts the observed nonlinear effect appearing solely as a result of modulation of antiferromagnetic order parameter $L(x)$ with dynamic strain via magnetostriction, delayed possibly by spin-shear relaxation τ [138], which is supported by the fact that $\lambda = 0$ would varnish all magnetic contributions to both k_3^* and η_nl^*. Perhaps, the same spin-shear relaxation mechanism and corresponding slow τ could also affect linear thermoelastic damping contribution near the T_N [121] in case thermal relaxation in these membranes becomes limited by an interlayer shear [138]. Yet, the latest experiments show that thermal relaxation time-scales in membranes of $FePS_3$ are up to two orders of magnitude slower [146] than spin-shear relaxation-related τ considered in this work. Therefore, the presence of substantial linear thermoelastic damping and observed nonlinear damping near the T_N are not a direct consequence of one another [121], [146] in the absence of higher-order geometric nonlinearities.

However, an indication for the presence of more intricate magneto-mechanical interactions in the system is the discrepancy between the experiment and the model of $k_3^*(T)$ shown in Fig. 5.4b, where we observe a peak-like feature near $2\omega_0\tau \simeq 1$, hinting that the dynamics of the magnetic system around ground state L_0 could be even higher order. We also note that the role of other nonlinear effects, like nonlinearities in optothermal response [60], [147], and resulting nonlinear terms in the magnetostrictive actuation force [146] could be partly responsible for the observed changes in nonlinear stiffness near the magnetic phase transition. Nevertheless, quantitatively confirming either of these hypotheses would require further experimental evidence which lies outside the scope of this work.

In conclusion, we demonstrate that the nonlinear dynamics of optothermally driven nanomechanical $FePS_3$-based heterostructure membrane resonators changes substantially near the antiferromagnetic phase transition. We describe a magnetostrictive mechanism that can account for the observed temperature dependence of the nonlinear parameters and formulate a theoretical model to understand the phenomenon. Utilizing the analytical magnetostriction model near the Néel temperature T_N, we demonstrate that the previously unexplored magneto-mechanical dissipation mechanism could possibly affect nonlinear dynamics of magnetic membranes significantly, even in the absence of a magnetic field. We anticipate that our results can offer new understanding of the thermodynamics and energy dissipation mechanisms due to magneto-mechanical interactions in 2D materials, which is important for the development of novel magnetic NEMS and spintronic devices.

5.6. METHODS

5.6.1. SAMPLE FABRICATION AND CHARACTERISATION

We pre-pattern a diced Si/SiO_2 wafer with circular holes using e-beam lithography and reactive ion etching. The holes have a radius of $r = 1.5$ μm and a cavity depth of 285 nm, and the SiO_2 layer acts as electrical insulation between the 2D material membranes and the bottom Si electrode. For electrostatic experiments, Pd electrodes are patterned on top of Si/SiO2 chips using a lift-off technique to establish electrical contact with some samples. To create suspended membranes, thin flakes of $FePS_3$ and graphite crystals are mechanically exfoliated and transferred onto the chip using the all-dry viscoelastic stamping method [148] immediately after exfoliation. Flakes of van der Waals crystals are exfoliated from high-quality synthetically grown crystals with known stoichiometry, and deterministic stacking is performed to form heterostructures. To prevent degradation, samples are kept in an oxygen-free or vacuum environment directly after the fabrication. AFM height profile scans and inspection are performed in tapping mode on a Bruker Dimension FastScan AFM. We typically use cantilevers with spring constants of $k_c = 30\text{–}40\ \mathrm{N\,m^{-1}}$ for inspection. Error bars on reported thickness values are determined by measuring multiple profile scans of the same flake.

5.6.2. LASER INTERFEROMETRY MEASUREMENTS

The sample is mounted on a xy piezo-positioning stage inside a dry optical 4 K cryostat Montana Instruments Cryostation s50. Temperature sweeps are carried out using a local sample heater at a rate of $\sim 3\ \mathrm{K\,min^{-1}}$ while maintaining the chamber pressure below 10^{-6} mbar. During data acquisition, the temperature is maintained constant with $\sim$ 10 mK stability. A power-modulated blue diode laser with a wavelength of 405 nm is used to optothermally excite the membrane's motion, and the resulting membrane displacement is measured using an interferometric detection with a He–Ne laser beam of 632 nm. The interferometer records the interfering reflections from the membrane and the Si electrode underneath, and the data is processed by a vector network analyzer Rohde & Schwarz ZNB4. All measurements are conducted with incident laser powers of $P_{\mathrm{red}} \leq 8\ \mu$W and $P_{\mathrm{blue}} \leq 35\ \mu$W, with a laser spot size of 1 μm.

5.7. APPENDIX D

5.7.1. D1: MECHANICAL DISSIPATION IN THE LINEAR REGIME

We plot the mechanical dissipation, the inverse of the quality factor, $Q^{-1}(T)$, of the MLG/FePS$_3$ resonator from Fig. 5.1 of the main section in Appendix Fig. 5.5. A notable peak is visible at T_N = 110 K. We attribute this observation to an increase of the thermoelastic damping [149], [150] expected near the T_N in magnetic resonators as $Q^{-1} \propto c_v(T)T$, where $c_v(T)$ is the temperature-dependent specific heat of FePS$_3$ [92], [121], [123].

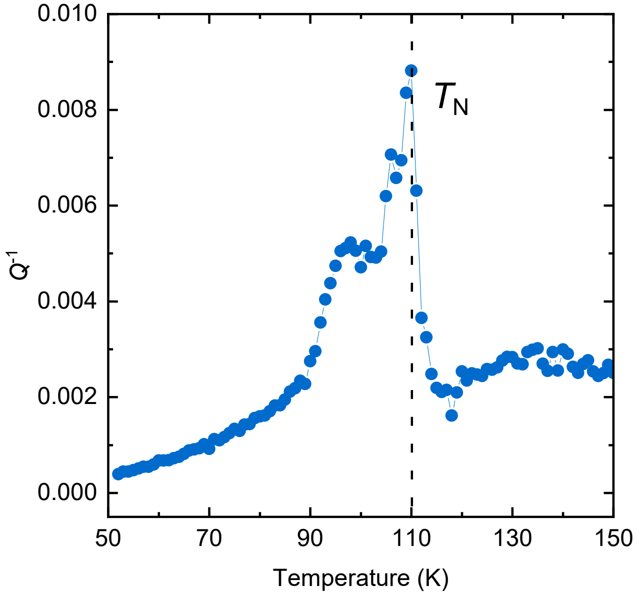

Figure 5.5: **Inverse quality factor Q^{-1} of the MLG/FePS$_3$ membrane from Fig. 5.1 of the main section.**

5.7.2. D2: REPRODUCIBILITY OF THE RESULTS

To check the reproducibility of the results in the main section, we did additional experiments with more samples, using both optical and electrical excitation. In the latter case, we applied an oscillating electric potential between the Si backgate of the chip and the multilayer graphene that is covering the FePS$_3$ membrane. Regardless of the excitation method, at the phase transition temperature, the shift in the linear resonance frequency f_0 that is reported in the main section at high amplitude oscillations was consistently observed (Appendix Figs. 5.6 and 5.7). Similarly, the anomalies in nonlinear stiffness and enhancement of nonlinear damping was also observed in both cases, supporting that the origin of these observations is the nonlinear magneto-mechanical coupling and not the method of excitation.

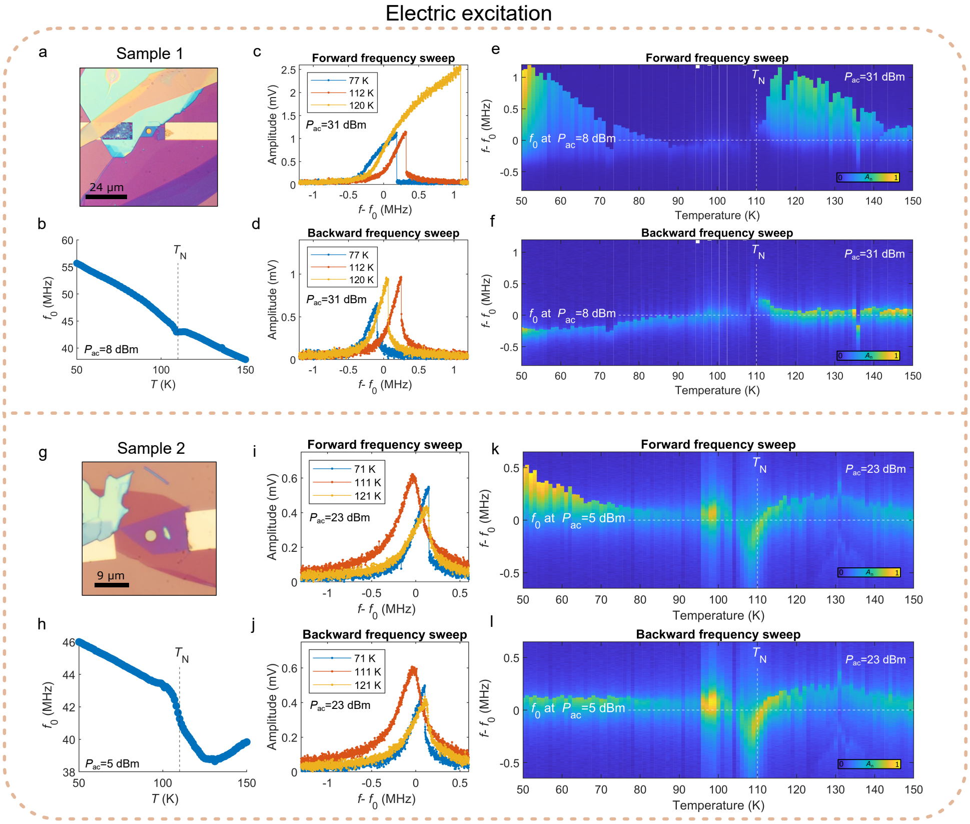

Figure 5.6: **Additional measurements of FePS$_3$-Graphene resonators, electrostatically excited.** Sample 1 is the device presented in the main text. (a) and (g) are the optical microscope images of the nanodrums. (b) and (h) display the linear resonance frequencies with respect to the temperature. (c), (d), (i) and (j) are the forward and backward frequencies sweeps of the drums at three different temperatures, one before the phase transition (blue), one at the phase transition (red) and one right after the phase transition (yellow). (e), (f), (k) and (l) are the forward and backward frequency sweeps with the full temperature range.

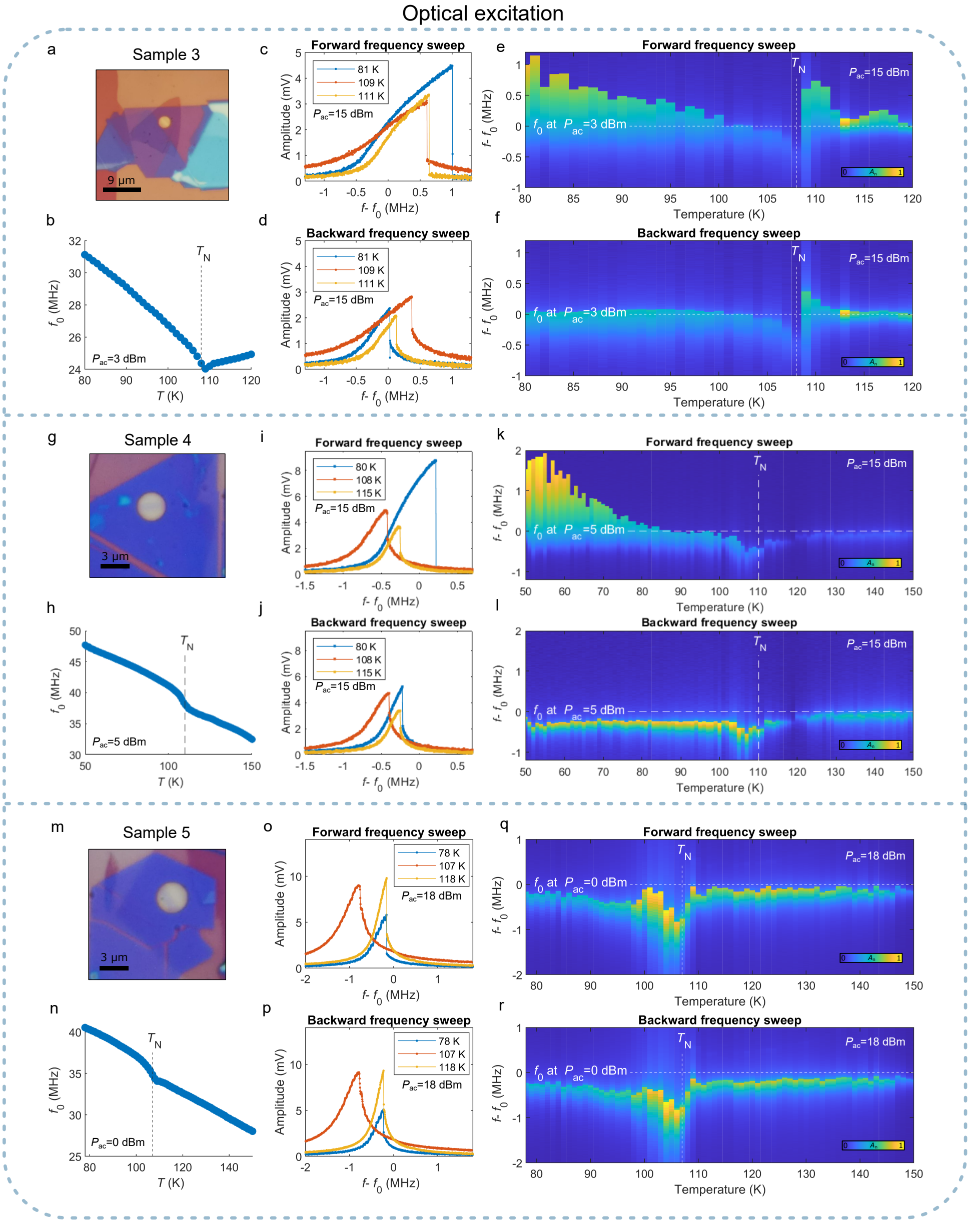

Figure 5.7: **Additional measurements of FePS$_3$-Graphene resonators, optothermally excited.** (a), (g) and (m) are the optical microscope images of the nanodrums. (b), (h) and (n) display the linear resonance frequencies with respect to the temperature. (c), (d), (i), (j), (o) and (p) are the forward and backward frequencies sweeps of the drums at three different temperatures, one before the phase transition (blue), one at the phase transition (red) and one right after the phase transition (yellow). (e), (f), (k), (l), (q) and (r) are the forward and backward frequency sweeps with the full temperature range.

5.7.3. D3: STEADY-STATE EQUATIONS FOR THE DUFFING-VAN DER POL OSCILLATOR

We use the method of harmonic balancing to obtain the steady-state amplitude of the Duffing-van der Pol oscillator:

$$\ddot{x} + \omega_0^2 x + \gamma x^3 = \frac{F_\omega}{m}\cos(\omega t) - \frac{\omega_0}{Q}\dot{x} - \xi_{\mathrm{nl}} x^2 \dot{x}, \tag{5.9}$$

We approximate the motion by a single harmonic such that $x \approx \bar{X}\cos(\omega t - \theta)$ where $\bar{X}$ is the steady-state amplitude. Plugging x, $\dot{x}$ and $\ddot{x}$ into the equation of motion in Eq. (5.9) results in an expression that consists of coefficients $\cos(\omega t)$, $\sin(\omega t)$, $\cos(3\omega t)$ and $\sin(\omega t)$, such that $R_1\cos(\omega t) + S_1\sin(\omega t) + R_2\cos(3\omega t) + S_2\sin(3\omega t) = 0$. Since we are interested in the fundamental harmonic ω, we solve for $R_1 = 0$ and $S_1 = 0$ to obtain the steady-state amplitude:

$$\begin{aligned} R_1 = &-\frac{F_\omega}{m} + \bar{X}\omega_0^2\cos(\theta) - \bar{X}\omega^2\cos(\theta) + \frac{3}{4}\bar{X}^3\gamma\cos(\theta)^3 + \frac{1}{Q}\bar{X}\omega_0\omega\sin(\theta) \\ &+\frac{1}{4}\bar{X}^3\xi_{\mathrm{nl}}\omega\cos(\theta)^2\sin(\theta) + \frac{3}{4}\bar{X}^3\gamma\cos(\theta)\sin(\theta)^2 + \frac{1}{4}\bar{X}^3\xi_{\mathrm{nl}}\omega\sin(\theta)^3 = 0 \end{aligned} \tag{5.10}$$

$$\begin{aligned} S_1 = &-\frac{1}{Q}\bar{X}\omega_0\omega\cos(\theta) - \frac{1}{4}\bar{X}^3\xi_{\mathrm{nl}}\omega\cos(\theta)^3 + \bar{X}\omega_0^2\sin(\theta) - \bar{X}\omega^2 sin(\theta) \\ &+\frac{3}{4}\bar{X}^3\gamma cos(\theta)^2\sin(\theta) - \frac{1}{4}\bar{X}^3\xi_{\mathrm{nl}}\omega\cos(\theta)\sin(\theta)^2 + \frac{3}{4}\bar{X}^3\gamma\sin(\theta)^3 = 0 \end{aligned} \tag{5.11}$$

By solving R_1 and S_1 together, we obtain the equation for the steady-state amplitude:

$$\left(\bar{X}^3\frac{3\gamma}{4} + \bar{X}\left(\omega_0^2 - \omega^2\right)\right)^2 + \omega^2\left(\bar{X}^3\frac{\xi_{\mathrm{nl}}}{4} + \bar{X}\frac{\omega_0}{Q}\right)^2 = \left(\frac{F_\omega}{m}\right)^2, \tag{5.12}$$

which can be expressed as a hexic equation in a:

$$\bar{X}^6\left(\frac{9\gamma^2}{16} + \frac{\xi_{\mathrm{nl}}^2\omega^2}{16}\right) + \bar{X}^4\left(\frac{3\gamma(\omega_0^2 - \omega^2)}{2} + \frac{\xi_{\mathrm{nl}}\omega_0\omega^2}{2Q}\right) + \bar{X}^2\left(\left(\frac{\omega_0\omega}{Q}\right)^2 + (\omega_0^2 - \omega^2)^2\right) = \left(\frac{F_\omega}{m}\right)^2. \tag{5.13}$$

5.7.4. D4: EXTRACTING EXPERIMENTAL PARAMETERS

In Chapter 5, to monitor the change in the stiffness and dissipation of the resonator, we fit the experimental frequency responses to the equation (5.13), to extract Q, γ, ξ_{nl}, F_ω/m and ω_0. The fitting is done sequentially. First, Q factors are extracted from the linewidths of linear resonance curves at low drive levels, before the onset of nonlinearity. Next, ω_0 can be extracted from the peak frequency at low drive levels, assuming it stays constant with increasing drive levels. However we have observed a dependency on drive level, possibly due to overheating from the optothermal drive, thus instead, we extracted ω_0 for each drive level separately. At the drive levels where the response is nonlinear, we correct for the ω_0 using the inflection of the nonlinear resonance curve, such that $f_{dd}(\omega) = \frac{d^2a}{d\omega^2}$ where $f_{dd}(\omega_0) \approx 0$ or the low saddle-node point obtained in the reverse sweep. After obtaining Q and ω_0, it is possible to extract F_ω/m by fitting the off-resonance response to a linear harmonic oscillator model, such that $\ddot{x} + \frac{\omega_0}{Q}\dot{x} + \omega_0^2 x = \frac{F_\omega}{m}$. After obtaining all the linear parameters, it is possible to extract nonlinear parameters γ and ξ_{nl}. Normalized Duffing coefficient γ can be extracted using the slope of the square of the frequency response, since $\gamma = (8\omega_0/3)(\omega_{max} - \omega_0)/a_{max}^2$ [23], where ω_{max} is the frequency and a_{max} is the amplitude of the experimental nonlinear resonance peak. Finally, we find ξ_{nl} by matching the peak amplitude, by using an optimizer to minimize the objective $f_{obj} = |a_{max}^{sim}(\xi_{\mathrm{nl}}) - a_{max}|$, where a_{max}^{sim} is the peak amplitude of the simulated model. In Appendix Fig. 5.8, we provide additional examples of the fitted curves for convenience.

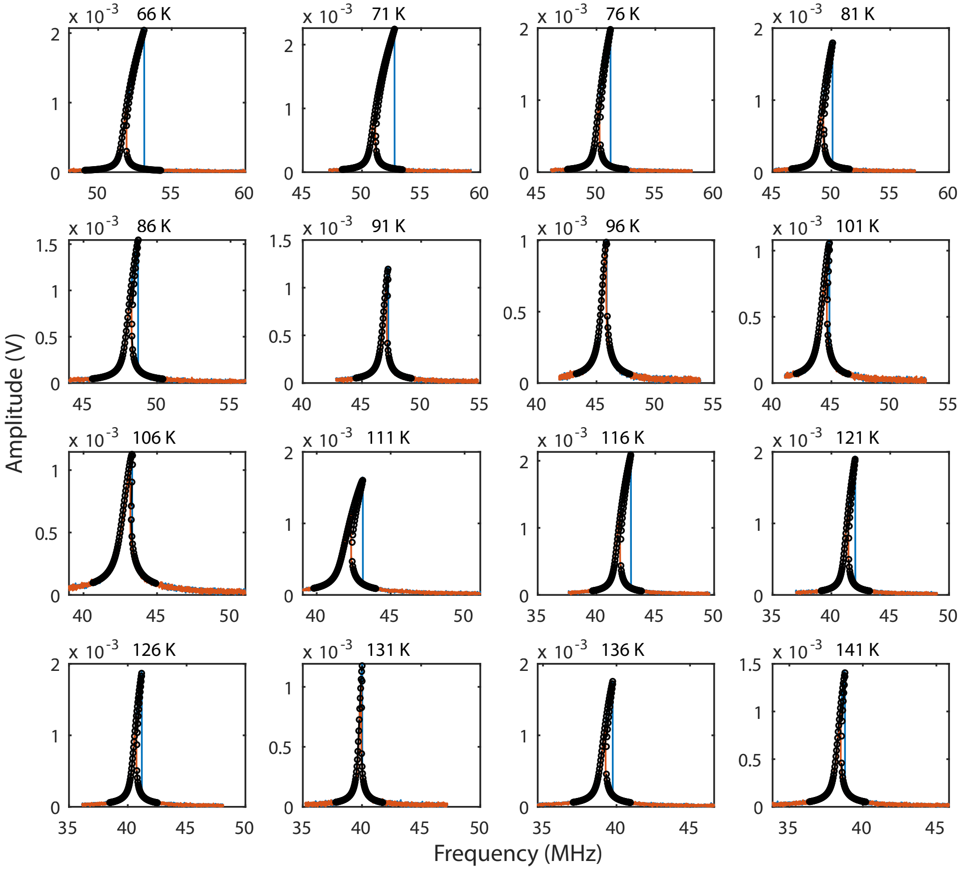

Figure 5.8: **Model fits to the experimental data for various temperatures at 10 dBm drive level.** Blue line is the experimental forward frequency sweep response, where orange line is in the reverse sweep response. Black line with connected dots is the simulated model response with fitted parameters.

5.7.5. D5: MAGNETOSTRICTIVE MODEL

DYNAMICS OF ANTIFERROMAGNETIC ORDER PARAMETER

The total potential energy of the system can be written down as follows:

$$U_{\mathrm{T}} = U_{\mathrm{el}} + U_{\mathrm{m}} + U_{\mathrm{ms}}, \tag{5.14}$$

where U_{el} is elastic potential energy, U_{m} free energy of an antiferromagnet and U_{ms} is magnetostrictive coupling energy term. These take form of:

$$\begin{aligned} U_{\mathrm{el}} &= \frac{k_1}{2}x^2 + \frac{k_3}{4}x^4 \\ U_{\mathrm{m}} &= U_{\mathrm{m},0} + \frac{A}{2}L^2 + \frac{B}{4}L^4 \\ U_{\mathrm{ms}} &= \frac{\lambda}{2}L^2\sigma(x), \end{aligned} \tag{5.15}$$

where k_1 and k_3 are linear and nonlinear stiffness, $U_{\mathrm{m},0}$ is the magnetic free energy in a disordered state, $L = M_1 - M_2$ is an antiferromagnetic order parameter along the easy-axis of antiferromagnet defined as a difference of counter-aligned spin sub-lattice magnetisations $M_{1,2}$, while A and B are phenomenological constants, λ is a phenomenological magnetostrictive coefficient, and $\sigma(x)$ is the bi-axial stress modulated by the membrane deflection x.

Let us first consider magnetic energy terms $U_{\mathrm{m}} + U_{\mathrm{ms}}$ that describe the antiferromagnetic phase:

$$U_{\mathrm{m}} + U_{\mathrm{ms}} = U_{\mathrm{m},0} + \frac{A}{2}L^2 + \frac{B}{4}L^4 + \frac{\lambda}{2}L^2\sigma(x). \tag{5.16}$$

Furthermore, we consider the ground state of magnetic system, in which case L shall take the value at a minimum of its magnetic energy U_{m} in zero stress conditions $\sigma = 0$. This energy minimum thus shall have extrema that satisfy $\frac{\partial(U_{\mathrm{m}} - U_{\mathrm{m},0})}{\partial L} = 0$, where $A > 0$ condition describes a disordered (paramagnetic) phase and $A < 0$ condition - an ordered (antiferromagnetic) phase. Consequently, $A = 0$ describes the transition between these phases. We thus define antiferromagnetic transition temperature or Néel temperature T_{N} such that it leads to $A = 0$ at T_{N} as:

$$A = a(T - T_{\mathrm{N}})^{2\beta}, \tag{5.17}$$

where a is a positive phenomenological constant, T is temperature and $\beta = 0.5$ the critical exponent. By plugging equation (5.17) to (5.15), we re-write the total potential energy as follows:

$$\begin{aligned} U_{\mathrm{T}} &= U_{\mathrm{el}} + U_{\mathrm{m}} + U_{\mathrm{ms}} \\ &= \left[\frac{k_1}{2}x^2 + \frac{k_3}{4}x^4\right] + \left[U_{\mathrm{m},0} + \frac{a}{2}(T - T_{\mathrm{N}})L^2 + \frac{B}{4}L^4\right] + \left[\frac{\lambda}{2}L^2\sigma(x)\right], \end{aligned} \tag{5.18}$$

By minimizing U_{T} with respect to L, we next find the values of order parameter at the ground state as follows:

$$\frac{\partial U_{\mathrm{T}}}{\partial L} = a(T - T_{\mathrm{N}})L + BL^3 + \lambda L\sigma(x) = 0, \tag{5.19}$$

which leads to the antiferromagnetic order parameter at the ground state at $\sigma = \sigma_0$:

$$L_0 = \pm\sqrt{\frac{a(T_\mathrm{N} - T) - \lambda\sigma_0}{B}} = \pm\sqrt{\frac{a(T^*_\mathrm{N} - T)}{B}}. \tag{5.20}$$

This means that magnetostriction produces the rescaled Néel temperature T^*_N as a function of σ_0:

$$T^*_\mathrm{N} = T_\mathrm{N} - \frac{\lambda\sigma_0}{a}. \tag{5.21}$$

Furthermore, assuming the total stress $\sigma(x) = \sigma_0 + \sigma_\omega(x)$, where σ_0 is the static stress and $\sigma_\omega(x)$ the dynamic stress that is modulated due to the membrane motion of amplitude x, a stressed antiferromagnet at motion, i.e. $\sigma(x) \neq 0$, produces the following relation between L and T_N:

$$L(x) = \pm\sqrt{\frac{a(T_\mathrm{N} - T) - \lambda\sigma(x)}{B}}. \tag{5.22}$$

Here, an important observation from equation (5.22) is that $L(x)$ is a function of stress $\sigma(x)$, and thus membrane deflection x. Consequently, $L(x)^2$ from equation (5.22) takes the form:

$$L(x)^2 = \frac{a(T_\mathrm{N} - T) - \lambda\left(\sigma_0 + \sigma_\omega(x)\right)}{B} \cong \left(L_0 + L_\omega(x)\right)^2, \tag{5.23}$$

where $L_\omega(x)$ is the dynamic term of the antiferromagnetic order parameter L. Since membrane deflection x is modulated at a frequency $f = \omega/2\pi$, elastic waves are excited in the antiferromagnet through the magnetostrictive coupling, where time dependence of L is related to energy U_T by the kinetic equation [135]–[137]:

$$\frac{dL}{dt} = -\kappa\frac{\partial U_\mathrm{T}}{\partial L}, \tag{5.24}$$

where κ is the kinetic coefficient, that is assumed to be free of anomalies near T_N. Since from equation (5.23) $L = L_0 + L_\omega$ is a sum of the equilibrium L_0 and the additional dynamic term L_ω produced by the small stresses σ_ω, we expand $\frac{\partial U_\mathrm{T}}{\partial L}$ using Taylor series around L_0:

$$\frac{dL}{dt} \cong -\kappa\left[\frac{\partial U_\mathrm{T}}{\partial L}|_{L_0} + \frac{\partial^2 U_\mathrm{T}}{\partial L^2}|_{L_0}(L - L_0) + \ldots\right], \tag{5.25}$$

and obtain (assuming $L_\omega \ll L_0$):

$$-\frac{dL_\omega}{dt} \cong 2\kappa B L_0^2 L_\omega + \kappa\lambda\sigma_\omega(x)L_0. \tag{5.26}$$

As originally shown by Landau and Khalatnikov [135], the time constant τ, that describes the relaxation of an antiferromagnetic order parameter due to its dynamic term [136], [137], can be defined from equation (5.26) as:

$$\tau = \begin{cases} \frac{1}{2\kappa a\left(T^*_\mathrm{N} - T\right)} & T < T^*_\mathrm{N} \\ \infty & T > T^*_\mathrm{N} \end{cases} \tag{5.27}$$

Coupled dynamics of the mechanical mode and the order parameter

In order to obtain the steady state response of the mechanical degree of freedom x, that is coupled to the magnetic order, we define the Lagrangian $\mathscr{L}=\frac{1}{2}m\dot{x}^2-U_T$, and use the Lagrange equation as follows:

$$\frac{d}{dt}\frac{\partial\mathscr{L}}{\partial\dot{x}}-\frac{\partial\mathscr{L}}{\partial x}=0, \tag{5.28}$$

which yields

$$m\ddot{x}+k_1x+k_3x^3+\lambda(L_0+L_\omega)^2\frac{\partial\sigma(x)}{\partial x}=0, \tag{5.29}$$

where $k_1=m\omega_0^2$. Assuming that $L_0>>L_\omega$ and including linear dissipation related to the quality factor Q, an intrinsic nonlinear dissipation of the van der Pol type with constant intensity $\eta_{\rm nl}$ and periodic forcing with the amplitude F_ω with frequency ω and phase ψ, coupled equations of motion can be written in the following form:

$$m\ddot{x}+k_1x+k_3x^3+\frac{\lambda}{2}L_0^2\frac{\partial\sigma(x)}{\partial x}+\lambda L_0L_\omega\frac{\partial\sigma(x)}{\partial x}=F_\omega\cos(\omega t+\psi)-(\eta_{\rm nl}x^2+\frac{m\omega_0}{Q})\dot{x}, \tag{5.30}$$

$$\dot{L}_\omega=-2\kappa BL_0^2L_\omega-\kappa\lambda L_0\sigma_\omega(x), \tag{5.31}$$

where $k_1=m\omega_0^2$.

To proceed further, we define $\sigma(x)$ as:

$$\sigma(x)=\frac{E}{(1-\nu)}\epsilon(x)=\frac{E}{(1-\nu)}\left[\epsilon_0+\epsilon_\omega(x)\right]=\sigma_0+\sigma_\omega(x), \tag{5.32}$$

where ϵ_0 and $\epsilon_\omega(x)=\frac{c_3}{2}\frac{(1-\nu)}{r^2}x^2$ are the static and dynamic strain terms, respectively. Moreover, r is the radius of the membrane, E is the Young's Modulus and c_3 is a dimensionless parameter that depends on the geometry and the Poisson's ratio of the membrane [22], [84]. Assuming the steady state is a periodic motion in the form of $x=\bar{X}\cos\omega t$, equation (5.32) leads to the static and dynamic stress terms:

$$\sigma_0=\frac{E}{(1-\nu)}\epsilon_0+E\frac{c_3}{4r^2}\bar{X}^2, \tag{5.33}$$

$$\sigma_\omega(x)=E\frac{c_3}{4r^2}\bar{X}^2\cos2\omega t. \tag{5.34}$$

To solve for the steady state response of the mechanical degree-of-freedom that is coupled to the magnetic order, we start by solving the first order differential equation (5.31). Using equations (5.27) and (5.34), we obtain the steady-state solution for L_ω in terms of τ:

$$L_{\omega ss}=-\frac{a^2C_{\rm nl}\tau\kappa L_0\lambda(2\tau\omega\sin2\omega t+\cos2\omega t)}{2\left(1+4\tau^2\omega^2\right)}, \tag{5.35}$$

where $C_{\rm nl}=E\frac{c_3}{2r^2}$.

Consequently, to apply harmonic balancing to equation 5.30, we keep the assumption of periodic motion at the steady state in the form of $x=\bar{X}\cos\omega t$ and plug in the steady state solution of L_ω, such that $L_\omega=L_{\omega ss}$. Considering only the fundamental harmonic ω, we find:

$$\left[\frac{3}{4}\left(k_3-\frac{C_{\mathrm{nl}}^2\lambda^2}{3B\left(1+4\tau^2\omega^2\right)}\right)\bar{X}^3+(C_{\mathrm{nl}}L_0^2\lambda+m(\omega_0^2-\omega^2))\bar{X}\right]\cos\omega t- \tag{5.36}$$

$$\left[\frac{\omega}{4}\left(\eta_{\mathrm{nl}}+\frac{2\tau C_{\mathrm{nl}}^2\lambda^2}{B\left(1+4\tau^2\omega^2\right)}\right)\bar{X}^3+\frac{m\omega_0\omega}{Q}\bar{X}\right]\sin\omega t=F_\omega\cos\psi\cos\omega t-F_\omega\sin\psi\sin\omega t$$

By equating the coefficients of the fundamental harmonic, namely $\sin\omega t$ and $\cos\omega t$ on both sides, we obtain the following steady-state amplitude-frequency equation:

$$\left(\frac{3}{4}\left(k_3-\frac{C_{\mathrm{nl}}^2\lambda^2}{3B\left(1+4\tau^2\omega^2\right)}\right)\bar{X}^3+(C_{\mathrm{nl}}L_0^2\lambda+m(\omega_0^2-\omega^2))\bar{X}\right)^2 \tag{5.37}$$

$$+\omega^2\left(\frac{1}{4}\left(\eta_{\mathrm{nl}}+\frac{2\tau C_{\mathrm{nl}}^2\lambda^2}{B\left(1+4\tau^2\omega^2\right)}\right)\bar{X}^3+\frac{m\omega_0}{Q}\bar{X}\right)^2=F_\omega^2. \tag{5.38}$$

From this equation, it is possible to see that the coupling to the magnetic order leads to a nonlinear damping term η_{nl}^* of van der Pol type [67] at $T<T_{\mathrm{N}}^*$ such that:

$$\boxed{\begin{cases}\eta_{\mathrm{nl}}^*=\eta_{\mathrm{nl}}+E^2\frac{c_3^2}{2r^4}\frac{\tau\lambda^2}{B(1+4\tau^2\omega^2)} & T<T_{\mathrm{N}}^*\\ \eta_{\mathrm{nl}}^*=\eta_{\mathrm{nl}} & T>T_{\mathrm{N}}^*\end{cases}}. \tag{5.39}$$

Similarly, due to the same coupling, the nonlinear stiffness of the Duffing type is rescaled, such that:

$$\boxed{\begin{cases}k_3^*=k_3-E^2\frac{c_3^2}{12r^4}\frac{\lambda^2}{B(1+4\tau^2\omega^2)} & T<T_{\mathrm{N}}^*\\ k_3^*=k_3 & T>T_{\mathrm{N}}^*\end{cases}}. \tag{5.40}$$

And finally, the linear stiffness is rescaled as:

$$\boxed{\begin{cases}k_1^*=k_1+\lambda L_0^2\frac{Ec_3}{2r^2} & T<T_{\mathrm{N}}^*\\ k_1^*=k_1 & T>T_{\mathrm{N}}^*\end{cases}}. \tag{5.41}$$

It is worth noting from equation (5.39) that η_{nl}^* is significant near $2\tau\omega\approx1$ and peaks at $2\tau\omega=1$. In previous work of Zhou, F. et al [138], it was shown that in FePS$_3$ the longest magnetostriction-caused lattice relaxation time constant is related to a modulation of monoclinic lattice angle by interlayer spin-shear coupling, which can be in order of several tens of nanoseconds near T_{N}. These relaxation timescales are indeed expected to lead to $2\tau\omega\approx1$ and thus possibly cause significant nonlinear damping within the measured range of ω.

By fitting experimental data from Zhou, F. et al [138] to equation (5.27) (see Appendix Fig. 5.9), we plot the expected temperature dependence of $k_3^*(T)$ and $\eta_{\mathrm{nl}}^*(T)$ (assuming a minor temperature dependence of $k_3(T)$ due to other effects of non-magnetic nature) in main section Fig. 5.4b and c.

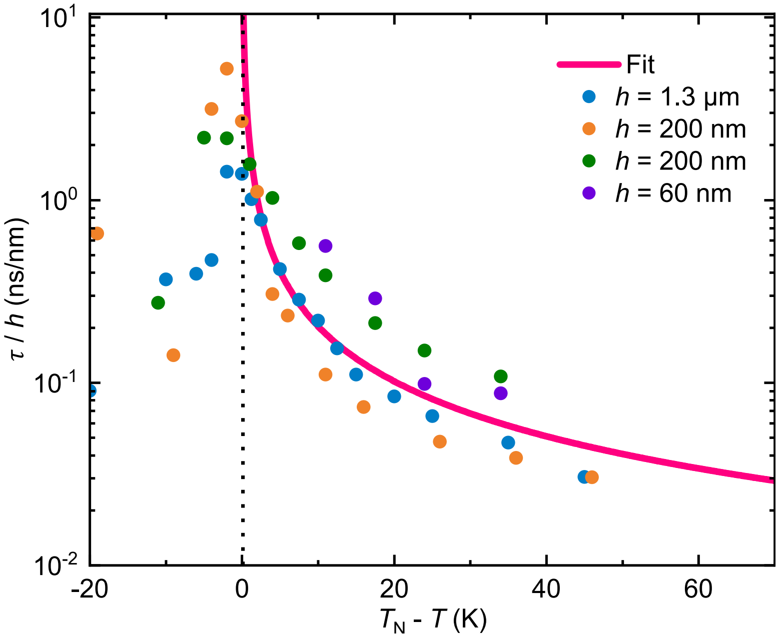

Figure 5.9: **Thickness-normalized relaxation time constants $\tau(T)$ reported on samples of various thicknesses from Zhou, F. et al [138].** Solid magenta line - fitted to equation (5.27).

6

CONCLUSION AND OUTLOOK

THE aim of this thesis was to explore mode coupling driven nonlinear dissipation pathways in 2-D material resonators. We have studied the nonlinear dissipation in these resonators in various conditions, such as different drive levels and frequencies as well as different tensions, electrostatic fields and temperatures, while trying to explain our observations with theoretical and numerical models. I now will summarize the results of those studies and provide an outlook to future routes for extending this work and initial steps taken in that direction during my PhD thesis research.

NONLINEAR MODE COUPLING AND DISSIPATION

In Chapter 2, we started by studying the effects of intermodal coupling on nonlinear dissipation, where we have investigated the nonlinear dynamic response of a optothermally excited graphene nanodrum resonator undergoing a parametric-direct internal resonance. We analyzed the dissipation in the system near the internal resonance and observed a dramatic increase in the nonlinear dissipation rate. To understand our observations, we built a coupled nonlinear two degrees-of-freedom model of the resonator, that showed good agreement with the experimental observations. The model revealed the connection between the observed nonlinear dissipation and drive frequency, coupling strength and Q factor of the coupled mode.

The resulting expression for the nonlinear damping was very intuitive and captured the core of the dissipation mechanism in a simple way. When calculated on the internal resonance point, it is exactly proportional to the square of the coupling strength between modes and Q factor of the coupled mode, $\tau_{nl} \propto \alpha^2 Q_2$. If we put it into words, this mathematical expression is almost equivalent to a quantity that defines how efficiently each oscillation of the first mode can be transferred and stored in the second mode. I believe this is the fundamental question of dissipation through intermodal couplings. However, to understand the effects of this phenomenon globally, this question had to be asked for every mode in the system that is activated.

And this we did by developing a multi-modal reduced-order modeling procedure in Chapter 3, that relied on purely physical and measurable parameters using finite element simulations to understand global dynamic response of nonlinear nanoresonators. We have compared our simulations to experiments on a graphene resonator in a wide range of frequencies and drive levels and found good qualitative description of the complicated nonlinear dynamics of the structure.

It is remarkable that through this method, only based on material and geometric parameters, we could determine the strength of these energy pathways virtually in any nanoresonator. Obviously at this point, we had to ask for the aid of numerical continuation simulations to make sense of the model, as the coupled equations become very crowded and cannot be solved as simply as the two-degree-of-freedom scenario. Anyhow, simulations are still effective in displaying how the energy is distributed, as well as detecting bifurcations.

NONLINEAR MODE COUPLING AND FREQUENCY COMBS

In Chapter 4, we investigated an exotic nonlinear dynamic phenomenon emerging from the nonlinear coupling of internal modes due to symmetry-breaking forces. By using electrostatic forces, we broke the out-of-plane symmetry of a graphene nanodrum resonator while tuning its resonance frequencies towards a one-to-two internal resonance, activating a strong energy pathway among its two eigenmodes. At the high drive levels, we observed the emergence of quasi-periodic oscillations that generate mechanical frequency combs. To explain the observations, we constructed a continuum mechanics model of the deflected drum which showed good agreement with the experiments, revealing the origin of the frequency comb: Neimark bifurcation of the periodic solution.

Here the mechanical frequency comb is a direct result of purely the nonlinear dynamics of the resonator, without the need of a collective response of a resonator and a complicated feedback circuit, nor a multi-frequency drive. In principle, the concept can be applied to any nonlinear resonator which could be tuned to satisfy the one-to-two internal resonance condition and utilized in sensing applications to downscale and track the frequencies of the system. We also pushed our simulations to even stronger nonlinear regime and showed that a quasi-periodic route to chaos can occur in such a system [103].

NONLINEAR COUPLING TO THE MAGNETIC ORDER

And finally in Chapter 5, we have investigated the nonlinear coupling not among eigenmodes, but between the mechanics and microscopic physics of a 2-D material resonator. We probed the nonlinear dynamics of $FePS_3$-based heterostructure membranes undergoing phase transition at the Néel temperature, where they change their magnetic order, from antiferromagnetic to paramagnetic. In our experiments, we observed dramatic changes in the nonlinear stiffness and damping during this phase transition.

We have provided a possible explanation to these observations using an analytical magnetostriction model that attributes the observed phenomena to the magneto-mechanical coupling of the structure. Yet we also note that it was previously shown that there is an influence on the heat capacity of these membranes at the phase transition [121], so the effect of thermoelasticity could be equally important in these observations. Anyhow, the results make it clear that the changes in the magnetic order of the material can directly reflect on the linear and nonlinear dynamics of these resonators, where the dynamic response can be used as a probe for the physics. Whether it is the slowing down of the magnetic relaxation time or a peak in the thermal time constant at the phase transition, it results in nonlinear dissipation, in a thematic consistency with the work.

6.1. OUTLOOK

Nonlinear phenomena in nanoscale is rich. As promised in the introduction, through various studies, we have demonstrated examples of nonlinear dissipation pathways in 2-D resonators emerging due to nonlinear coupling of the internal mechanical modes to each other and to microscopic physics. It is important to mention that by no means the full spectrum of nonlinear dissipation effects was covered here. One can simply argue that any mechanism that introduces an effective delay between stresses and the strains can possibly result in nonlinear dissipation at high amplitudes via geometric nonlinearity, besides their effects on linear dissipation. However the nonlinear mechanism we studied here was perhaps one of the most fundamental to all structures, as it is purely based on geometry. Hopefully through this work, we have made clear the importance of the geometric nonlinearity in the context of nonlinear dissipation. Our studies expand beyond what is delivered in this work, as many interesting ideas emerged during the process. Before the final words, in this section, I feel compelled to share certain concepts that we have partially explored.

6.1.1. FREQUENCY STABILITY OF NONLINEAR 2-D MEMBRANE RESONATORS

For sensing and time keeping applications, currently nonlinear resonators aren't the first devices of choice, due to the amplitude-frequency noise conversion of the Duffing response at high amplitudes. However it has been also shown that the nonlinear modal interactions might have the capability to stabilize these frequency fluctuations [49]. We made similar suggestions in Chapter 2 while investigating the nonlinear dissipation that is related to 2:1 parametric-direct internal resonance that we show is dependent on amplitude and drive frequency.

Hypothetically, one can already talk about a stabilizing effect in the vicinity of the internal resonance where the nonlinear dissipation peaks. As we mentioned many times, one of the consequences of nonlinear dissipation is the reduction in the responsivity of the resonator. Naturally, the frequency where the nonlinear dissipation peaks in the system will be the point where it least responds to fluctuations in the force, thus acting as a more stable operation frequency.

In this direction, inspired by the multi-modal interactions we saw in many devices, we have made initial measurements of frequency stability in graphene nanoresonators, in order to study the effects of multi-modal interactions on the frequency stability [151]. In fact, we have observed an unexpected trend in the frequency stability of these resonators, with a minimum Allan deviation in arbitrary frequencies on the nonlinear resonance curve (Fig. 6.1). We suspect that this might be a consequence of the nonlinear intermodal interactions, and if so, this mechanism can be further utilized by tuning/engineering the tension and the geometry of these devices.

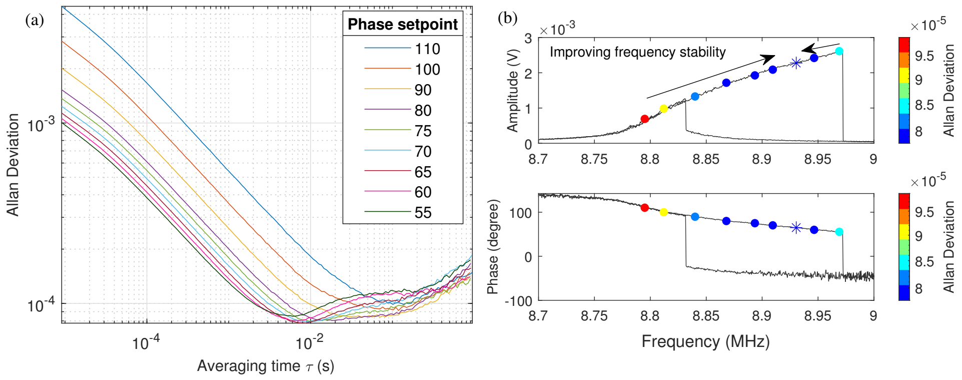

Figure 6.1: **Frequency stability of a nonlinear graphene nanoresonator (adapted from [151]).** a) Allan deviation of the nanodrum with respect to different phase set points while controlled by a phase-locked-loop. b) Open-loop frequency response measurements of the drum, displaying the minimum Allan deviation at different drive frequencies.

6.1.2. FERMI-PASTA-ULAM-TSINGOU PHYSICS IN NANORESONATORS

In chapter 3 we showed that a plethora of nonlinear dynamic phenomena that nanoresonators exhibit could be linked to their physical and material properties. This opens up the way for the study of fundamental nonlinear dynamics problems in nanomechanical systems, such as the famous Fermi-Pasta-Ulam-Tsingou (FPUT) problem, as the desired nonlinear coupling parameters could be achieved in real life nanoresonators. For graphene resonators, even if FPUT behaviour was studied numerically [34], the experimental realization is difficult due to low Q factors. Recently, an FPUT-like behavior was observed in Brownian dynamics of carbon nanotubes [152], yet the tailoring of such devices for desired nonlinear parameters is very challenging due to fabrication difficulties.

A good alternative for this study are the Si_3N_4 string resonators, as they are the best representation of the original FPUT system (which was a chain of mass-spring systems), and can provide very high Q factors and a lot of freedom in manufacturing. We made preliminary experiments on Si_3N_4 string resonators, where we observed signatures of multi-modal interactions both in frequency response and ringdown measurements, and provide exemplary measurements in Figs. 6.2 and 6.3. In the frequency response measurements (Fig. 6.2a), due to very high Q factors, even at the lowest drive levels of the piezoelectrically actuated base, strings show a Duffing response. Furthermore, as the drive levels were increased, signatures of internal resonance, such as the reduction in responsivity and locking of the peak nonlinear resonance frequency, were observed.

Moreover, we measured an exotic response of the strings at high drive levels, where the harmonics of the fundamental frequency were activated. This is specifically interesting because in strings, harmonics correspond to resonance frequencies of the modes as eigenfrequencies are at the integer harmonics of the fundamental mode. In the ringdown measurements (Fig. 6.3a), it is possible to observe an anomalous region where the harmonics of the fundamental mode interacts in the high amplitude regime, and after the energy of harmonics diminishes, only then the amplitude starts to decays with a con-

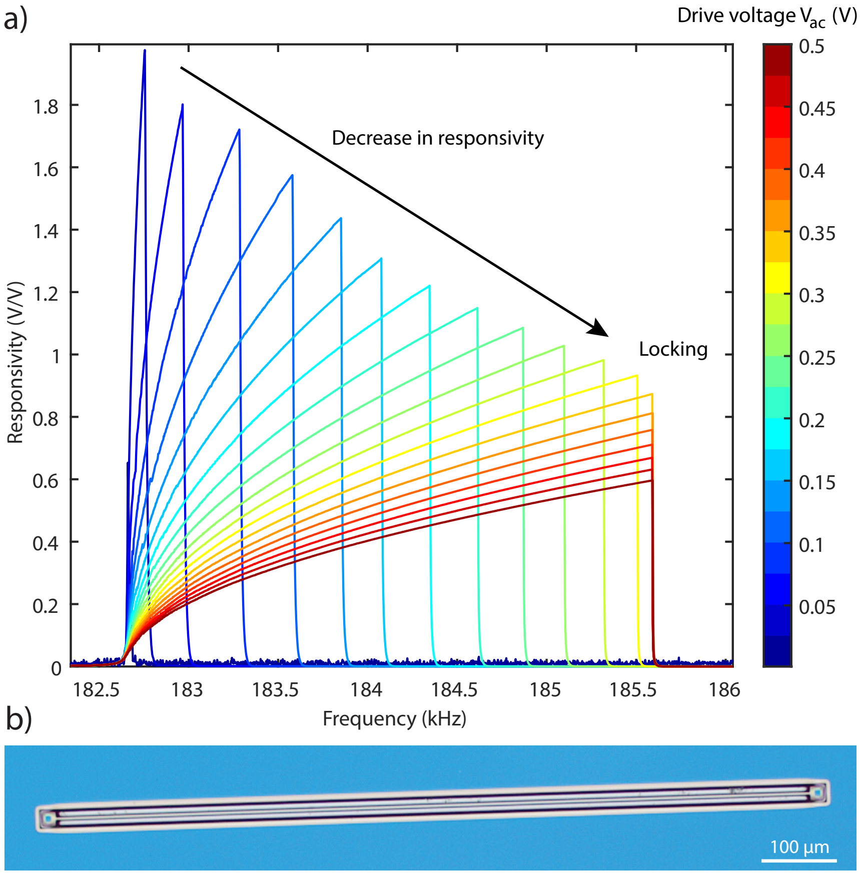

Figure 6.2: **Frequency response measurements of a Si_3N_4 resonator.** a) Responsivity measurement of a 1100 μm Si_3N_4 string resonator. b) Microscope image of a 1100 μm Si_3N_4 string resonator.

stant rate. We check the frequencies of the system by applying Fast-Fourier-Transform (FFT) at different drive frequencies (forward sweep) on the Duffing curve, and see the emergence of many other frequencies after a specific drive frequency (Fig. 6.3b). Although the observation is very interesting, we are suspicious that these results might be the outcomes of sensing errors at high amplitudes (such as optical nonlinearities and sensor saturation) and has to be investigated further (resonators were measured using a Polytec Vibrometer and a Zurich Instruments Lock-in Amplifier).

Despite these results, a long term energy recurrence behaviour, which is the core of FPUT problem, was not observed. Yet we suspect that with the careful design of geometry and the tension in these devices, nanomechanical manifestation of many fundamental nonlinear dynamics problems could be achieved, including FPUT behaviour [153].

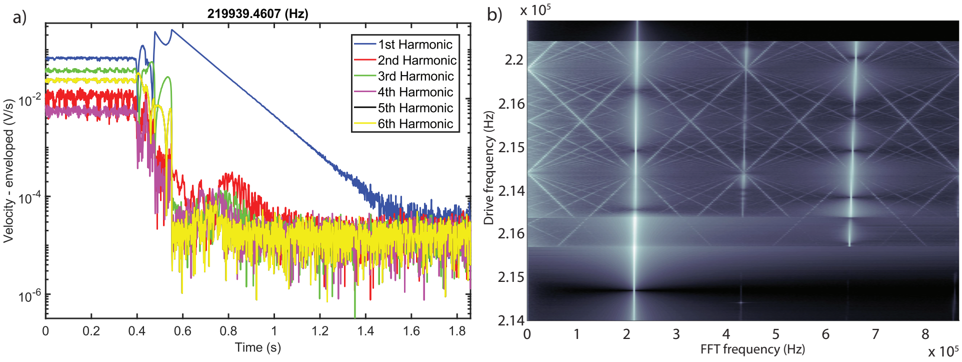

Figure 6.3: **Time response measurements of a Si$_3$N$_4$ resonator.** a) Nonlinear ringdown measurements of a 1100 μm from the Duffing response at a high drive voltage of V_{ac} = 10 V. b) Fast-Fourier-Transform (FFT) measurements with different drive frequencies on the Duffing response.

6.1.3. NONLINEAR DYNAMIC RESPONSE DUE TO HIGHER ORDER NONLINEARITIES OF EXTERNAL POTENTIALS

We only covered geometric nonlinearities in this thesis, however nonlinearities from external potentials can easily influence the dynamics of nanoresonators, one of which is the electric fields. Electrostatic fields are very frequently used to tune the resonance frequencies of these devices or even shown to nullify the hardening nonlinearity, as the electrostatic potential creates a nonlinear softening effect on the resonator [44]. If we think of a common design, where the resonator is suspended over a gate electrode, depending on the distance, the dominant order of nonlinearity will be different, as the electrostatic force is proportional to inverse of the distance squared. Most of the time, the nonlinearity that is observed are at most of third order. This is most probably because, as the voltage is increased and distance is closed between the resonator and the gate electrode, there is an immense increase in the Joule dissipation due to moving charges under the strong electric field and thus the motion of the resonator is diminished, failing to activate the higher order nonlinearities.

However, by taking advantage of the material properties of 2-D materials, this dissipation effect can be minimized, for instance, in the case of resonators made of graphene that is encapsulated in hexagonal boron nitride [154]. These structures can have superior electron mobility and thus can retain their motion even under strong electric fields. As a result, the effects of higher order nonlinearities are visible in the motion, where the resonance curve transitions from softening to hardening multiple times. This means that, just for a single frequency it could have up to 7 solutions (four stable and three unstable), with multiple zero dispersion points [25], creating interesting possibilities in terms of nonlinear dynamics. In Fig. 6.4 we provide exemplary numerical continuation simulations, modeling such a device.

From a different perspective the nonlinear dynamics response under nonlinear potentials can also be used for characterizing the nonlinear force itself. An example could be the quantum mechanical Casimir effect [155], which results in a force that depends on the fourth power of distance squared inverse. It is an attractive force between two un-

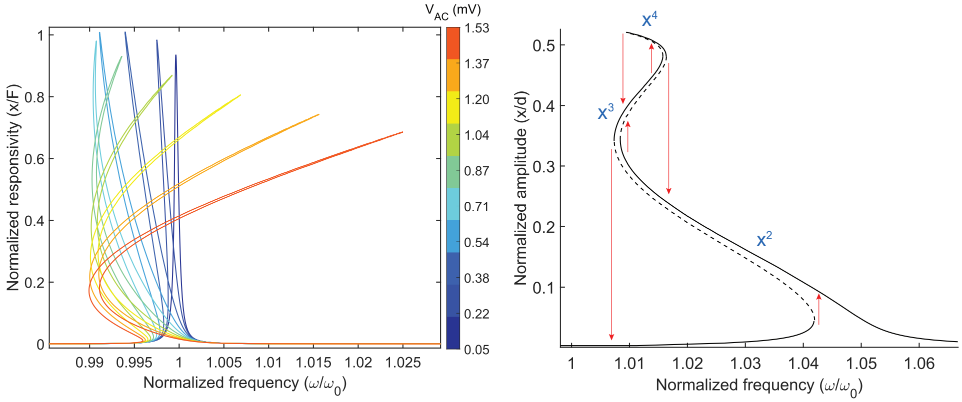

Figure 6.4: **Numerical continuation simulations of a electrostatically driven nanodrum, where the electrostatic force is modelled as** $F_e = c_{el}\frac{(V_{ac}+V_{dc})^2}{(1+x)^2}$**.** c_{el} is the coefficient of electrostatic force, V_{ac} is the AC voltage and V_{dc} is the DC voltage. a) Responsivity of the electrostatically driven nanodrum, displaying linear, softening and hardening responses as the drive level is increased. b) Frequency response of a nanodrum where the gap between the nanodrum and the electrostatic gate has been tuned to activate multiple nonlinear regimes of the nanodrum at high amplitudes.

charged conductive plates that can be explained by quantum fluctuations, a force that can be detected in very short distances. In principle, the higher order nonlinearities it introduces can be identified in the dynamics of a nanoresonator, which then can be used for its characterization. The idea of utilizing nonlinear dynamics to characterize nanoscale forces is not new, and in fact has been recently utilized in Atomic Force Microscopy [156]. However, the possibilities with 2-D mechanical resonators remain to be investigated.

ACKNOWLEDGEMENTS

I Think most would agree that doing a PhD extends beyond mastering your chosen field. I have decided to walk this path because of my deep passion to understand nature and was able to see meaning in life that way. However this journey quickly turned out to be one where you are tested not only in your intelligence, but in many other aspects, such as willpower, emotional resilience, determination, discipline, social skills, even your physical condition, as the journey itself leads to a rather "unnatural" lifestyle when compared to the rest of the society (not that the society lives a healthy lifestyle, but anyway). Yet, I believe one really gets to know oneself through enduring challenges in all aspects of life. The key to growth lies outside of the comfort zone, and believe me, doing a PhD is not comfortable. I must say that the idea of who I thought I was before and after this journey is quite different. I think that the people who made this journey possible in the first place, and much more pleasant along the way, deserve to be the subject of its final words.

Farbod, we met for the first time in your faculty famous "Engineering Dynamics" class during my master's studies, which earned you the best lecturer of 3ME award couple of times. Already at the moment I saw the way the class was taught, I was delighted, your delivery of the content was very clear and passionate. Furthermore, you made the structure of the course such that you could happily interact with the students and have in-depth discussions already in the classroom, and still deliver all the content you had to deliver in time. And in the end, we had to apply all the things we have learned in a project (dynamics of a motorbike), which really solidified all the learning. I think that was the secret.

Already close to the end of my master's studies, you have approached me with the opportunity to represent you in front of a committee with lots of big names, to present and defend your crazy 3D AFM idea. I had to train and prepare for that 5 minute pitch for more than a month. I think that pitch was one of the longer 5 minutes I had in my life. Couple of months later, instead, you got the ERC grant, and I still remember that day, because we had a football match where the students played against the staff, and I think you got the good news just before the game, and that was the only time I saw you running that fast, with the joy of the good news. You approached me to ask if I wanted to be the first PhD of this project, ENIGMA, and I gladly accepted, as it was the perfect combination of my interests: nonlinear dynamics, mechanics and physics.

I always felt your support and that you believed in me. From day one, you entrusted me to build the foundations of your first big project, where I had to manage hundreds of thousand euros to build a laser interferometry setup to measure 2D materials (which I believe is slightly stressful for someone who just got their master's degree), for my own research and all other researchers that would join the project later. Now the ENIGMA setup has resulted in many amazing results and publications from many researchers.

After building the setup, my real quest has started, to find the origins of nonlinear damping in graphene. As a first step, you wanted me to start investigating the viscoelasticity of the drums, as it can give rise to nonlinear damping, which you thought was a "low hanging fruit". Well you know it now, but you didn't know back then; that if something is straightforward and easy, I will have little motivation doing it. So instead, I secretly started working on nonlinear mode coupling and interactions more and more. Maybe if it was someone else in your place, I would be in trouble, but you quickly recognized the way my mind works (and I know that secretly, you also liked this topic much more), and let me pursue these things instead, which led to our first publication.

There were times that I had results and progress each and everyday. And there were times where I had nothing for weeks and you had to pop up constantly in my office to say "Paper, done?", "Simulations, done?", "Experiments, done?" with a smile on your face, to keep me going. Either way, you were always positive, motivating and uplifting with the way you supervised me. I feel incredibly lucky to have had you as a supervisor. I have learned a lot in these past years, and I am grateful for every bit of it. You have undoubtedly made a significant mark on my life and I will always remember these days with great joy.

Peter, my journey in the DMN group started with you. At the end of the first year of my master's studies, I was looking for a project that excited me, and surely Peter had one, "Exploring the dynamics of diamagnetically levitated objects". What is cooler than magnetically levitating stuff? Probably not many things. I remember the first day I came to your office to discuss the project. Funny enough, just after the meeting, you came downstairs with me to the optics lab, and literally taught me how to deal with the electronics. We made the first measurements on the levitating graphite plate together that day, by exciting the magnets with the magnetic fields generated by the coil we placed around them. I wasn't aware of this at that time, but now I see that this was a mystical event, because I haven't seen any other full professors instructing their students one on one in the lab ever again.

And then after my master's studies, you became my PhD promotor, in the ENIGMA project. This time, instead of the role of the first supervisor, you have helped my work immensely with your very careful and critical perspective. I really appreciated the dynamic I had with you and Farbod, as you both provided very different perspectives that in the end helped my works to be whole. I think you are an incredible role model for an emerging scientist with your sincere passion and interest in knowledge. In many cases, still to this day, you still send mails late night about a simulation or calculations about some idea, out of self interest. I think good science can only be made if you have this sincere passion about it. And it is evident that you never lost this passion. It was an honor to work with you. It was also a great surprise to me that my promotor was a strong chess player, and even had a proposition about defending a chess position in his own PhD defense. Yet somehow, all this time, we only played a single game of chess (with the pocket chess set I brought to the NMC conference in Switzerland), which ended in a draw, where I barely survived by finding a perpetual check. For that reason, unlike you, I have avoided putting a chess position to defend in my propositions, as it might have been pretty hard to defend against you.

Speaking of defending, I would like to thank the committee members before whom I will defend my thesis: **Prof. Mark Dykman**, **Prof. Elke Scheer**, **Prof. Yaroslav Blanter**,

Dr. Selim Hanay, **Dr. Gerard Verbiest** and the reserve member **Prof. Matthijs Langelaar**. I am grateful for the time and effort you have dedicated for reviewing my work.

Now is the time to acknowledge those who have accompanied me on the journey through my PhD, those with whom I've shared laughter, work, and suffering. First and foremost, my office mate, the king of AFM dynamics, **Abhilash**. When Pierpaolo departed from our group, I inherited his desk, which faced yours. You mentioned in your own PhD thesis that I occupied the most coveted desk in PME and spent my time playing chess, but we both know that's far from the truth. You were the one tucked away in the furthest corner of the office, secluded in a cubicle with its own door. It's a mystery how you managed to produce such outstanding research while seemingly dividing your attention between anime and TV series. I suppose you were a genius after all. Jokes aside, you were an exceptionally hardworking and exemplary researcher. Whenever I mentioned to others that we shared an office, they would immediately recognize you as "the serious, hardworking guy." Instead of Abhilash, I sometimes called you "Abi", which means 'big brother' in Turkish, a term that showed my respect for you as well as our friendship. I'm tempted to mention all the amusing incidents we've been through, yet I refrain, fearing that these tales might overshadow the scientific content in this book. Following your PhD, you chose a life of enjoyment after the past four years of hardship, in other words, you started working in ASML, and within a month, you appeared five years younger and ten times happier (not to mention five times wealthier). I am so happy to see that you are doing great, and I am convinced that your life will only get better.

Next, I must mention **Irek**, the maestro of the bacteria percussion band. Our paths crossed even before Farbod hired you as the second PhD student in the ENIGMA project. I had the pleasure of witnessing your presentations during DMN meetings during your master's studies. You were almost like an experienced businessman. Your exceptional skills in delivery and selling an idea were so good, I mistook you for a native English speaker, initially thought you were from England (which you were pretty suprised about), much far away from your actual homeland in Poland. When Farbod hired you, I was quite happy, because I knew how great of a job you did during your master's degree. You immediately started helping me to build the ENIGMA setup, and I am pretty sure without you, it would have taken much longer. As our taste in music aligned, when no one was around, we would blast our favorite metal song at the lab and continue working on the setup. We even won the PME talent show with our ridiculous cover of "Enter Sandman". To be honest, I felt a bit let down when you stopped working on nonlinear dynamics. Instead, one afternoon, you and Farbod decided to put germs (infecting our beautiful setup) on some graphene drums and somehow now you have a very successful start-up company based on measuring the bacteria with graphene drums and laser interferometry. I believe that the ones that make the effort to try extraordinary things are always rewarded in science, and this was a perfect example of it. I wish you the best in all your future endeavors, and I thank you for agreeing to be my paranymph for the defense!

Next, I'd like to acknowledge my dear friends from our research group dynamics of micro and nanosystems, starting with Farbod's crew or perhaps the "Farbots" ("Farbot" was the name of the resonant robot that one of our students designed for his master's project). **Xianfeng**, the master of diamagnetic levitation, I am grateful that you have built upon what I started in my master's thesis work, elevating it to remarkable heights (or must I say "levitating"), which resulted in a series of exceptional publications. Besides research, we became quite close friends as we shared most of our coffee breaks. You even gave me the honor of being your paranymph for your PhD defense. Despite your calm appearance, you always caught me off guard with your edgy jokes that seemed to come out of nowhere. But perhaps most importantly, I will never forget the ancient Chinese story you shared with me, "old cow and the young grass". **Zichao**, my comrade in nonlinear dynamics, I will always cherish the discussions we had about life and the intricacies of our field after a hard day's work in the office. I wish someone had recorded our discussions; I believe they would have made a very successful podcast. I will always remember you with the precision you aim to achieve in your scientific work, similar to how you perceive and live life, which is inspiring. **Ali**, my other comrade in nonlinear dynamics. Your expertise in simulations and theory was just enough to be able to keep dodging making experiments for ENIGMA, which in the end worked out pretty well to be honest, you produced very nice papers. And now, you are going to be done soon and you already have a job ready for you in a bank, who would have guessed! I wish you all the best in your next journey. **Sandro**, the other maestro of the graphene band, also the bass player for many other bands, including mine, once upon a time. I will always remember the time we performed those songs from RATM, Metallica etc. in the PME Christmas event, which was a shocker for the most of the audience. Good luck with your company, I believe in you guys (do not forget me when you get rich though)!

Obviously there are many dear friends outside our inner circle of ENIGMA, which made every day much better. I would like to mention them, starting with a friend that liked basketball so much that he decided his English name to be **Curry** (inspired by his favorite player, Stephen Curry). **Hanqing**, the man that does it all, hard work, sports, games, socializing, and always with a good mood and smiles. Most of the time you were the first one to come to office and the last one to leave, but you never accepted that you were a hardworker. We had countless brainstorming sessions on life and helped each other look from the perspectives that we wouldn't be able to do so by ourselves. The Chinese food you made the day you invited me and Abhilash to eat was probably the best Chinese food I ever had, so I think you are an exceptional chef! We spent so many fun and valuable moments together, playing video games, doing sports or just having dinner after work. You were always very stylish, even so that girls kept coming to you, asking "Where did you buy your clothes?", and you would say "Oh, my girlfriend bought it". Do not forget our 200 € bet, I am sure I am going to win though. I am sure you are going to be very successful in your new position, Dr. Liu!

Vincent, you always got my spirits up whenever I saw you in 3ME, even from miles away, with your big smile. If it wasn't for your exceptional master's project work, the third chapter of this thesis wouldn't be possible. I am proud that we were able to finish the paper finally. Thanks for your hard work.

These next people really like SiN resonators. First is the "Dalao", or that is what the Chinese guys call him. It means the big boss. **Minxing**, my dear friend, you are indeed such a boss. You had the most difficult experimental challenges in your pursuit of measuring the Casimir force, but you never gave up. You helped everyone whenever you could, with your superb fabrication skills, and also by handing out awesome SiN resonators. You even helped me pursue my dream of observing the FPUT phenomenon by making some awesome high Q micro/nanomechanical resonators for me. You always had the hot news about the stocks or the crypto market, you knew where the money is at all the time. I really hope that you fulfil your dream of measuring Casimir forces using nonlinear dynamics. And never forget I will always be there if you need a little bit of nonlinear dynamics support. Best of luck in finishing your PhD, you are very close now!

Andrea, the human being with the most gorgeous hair in the university. I said human, because even the girls envy you (I heard it with my own ears!). I always appreciated your professionalism while keeping the good vibes and humor. Your work that is inspired by spiderwebs was so cool (who doesn't love spiders anyway). Best of luck in your defense, but probably by the time you read this, you will be called Dr. Cupertino.

Matthijs, the man who has a story about literally anything. Your general knowledge of things always amazed me, you made lunch breaks so much for fun and informative! I also really appreciated your scientific approach in general and the way you worked was very inspiring.

Next is our DMN postdocs. The mastermind of nonlinear dynamics simulations, **Pierpaolo**. You were one of the first people that got me exposed to nonlinear dynamics, perhaps that is why I liked it this much. Still to this day, whenever I have a question about some nonlinear dynamics simulation, you are one of the first that comes to my mind. Now you are a professor back in Italy, yet luckily we keep meeting in nonlinear dynamics conferences, and whenever I see you, my day always gets brighter.

Tomas, thanks for helping Ties and me about stability of resonators. It is amazing that you are a professor now, and not so far away, just at the next faculty. Your students are very lucky my friend!

Sadatal, it was always amusing watching you and Matthijs drowning us with new knowledge, in any topic I could imagine, during lunch breaks. Good luck with your company!

Hadi, if it wasn't for you, I probably would delay testing those graphene chips with the electrostatic gate, therefore we wouldn't have the frequency comb paper. It would be such a shame. Thanks for making it possible.

Daniel, one of the most extraordinary people I have ever met. I don't have many friends who casually pilots planes for fun, while living on a boat, doing research. Good luck with everything back in Australia!

And of course we have the TNW crew, **Makars, Martin, Robin, Maurits** and **Gabriele**. I will start with the legendary duo, **Makars** and **Martin**. **Makars**, I was always amazed at how you could turn any discussion or idea into one that included 2D materials. I remember when I first started my PhD, you were ordering all kinds of weird crystals and secretly exfoliating them in the lab after hours (probably to avoid endangering us). You always had a story about a certain scientific topic, often quite funny ones about eccentric professors. You could talk about literally anything: music, video games, modern art, you name it. But beyond all that, you were a very dedicated and hardworking scientist. We spent your last couple of months in Delft together; during your short postdoc, we shared an office, where we worked on the phase transition paper, which, to be honest, turned out quite nice. I learned a lot from you.

And **Martin**, the grandmaster of 2D material fabrication, I can't even begin to comprehend how many people have had successful papers thanks to you and your skills in fabrication. I am particularly proud of the experiments in my first paper, which showcases one of the most beautiful wide frequency range nonlinear dynamics responses of graphene, coming from a graphene drum you helped me fabricate! Luckily, we were also neighbors, which made me all the more appreciative of your hard work. I remember in the last years of your PhD, you were almost always back from the lab around 23:00. That dedication is apparent from your publication record; you had 32 papers in your list of publications in your PhD thesis. THIRTY-TWO! Whenever I give this information in an academic environment, people just can't believe. You were super smart, yet humble, and very kind to everyone (perhaps sometimes too humble). You guys are the perfect professor material, and I truly believe that both of you will be very successful on this path. Your future students are very lucky.

Robin, another guy who made our (the next generation of PhDs) job much harder (maybe the main guy, because you perhaps set the bar for Makars and Martin). You did so much with the dynamics of 2D material resonators that we had to be extra creative to find new directions! Your extensive work on nonlinear dynamics guided me a lot during my own work (a shout-out to **Dejan** too, especially for his paper on nonlinear dynamic characterization).

Gabriele, I can't thank you enough for motivating me to start going to gym. I will always remember your positive attitude and kindness.

Maurits, the man with the unique style, the sunglasses enthusiast. You would wear them in any condition (indoors, outdoors, almost during the meetings), and if you took them out, perhaps half of the people wouldn't recognize you. It was a pleasure to work with you on the phase transition paper. Thank you for all the discussions about magnetic phase transitions.

I would also like to express my gratitude to **Gerard** and **Richard** for their critical insights and detailed feedback during my presentations to the group, especially in the early stages of my PhD. The weekly morning meetings were invaluable, it is a shame that we can't have them anymore, as the group grew so fast. **Richard**, throughout my PhD, we addressed the challenging FPUT problem in nanomechanical resonators with you. Now, as I started my postdoc journey with you, we are tackling yet another formidable challenge together: designing, fabricating and testing record aspect ratio photonic crystal lightsails, to be propelled by light, aiming for interstellar travel! It is pretty apparent that you have an appetite for only the most difficult problems, and I must say, I share that sentiment entirely.

There are many wonderful people entered my PhD journey in a later stage, but they really made the coffee breaks just better: **Lucas**, **Megha**, **Ruben**, **Frederike**, **Malte**, **Inge**, **Xiliang**, **Endre**, **Paulina**, **Hande**, **Hava**, **Tufan**, **Nils**, **Stijn** and many others... It was a pleasure getting caught in between **Ruben** and **Frederike**'s endless discussions on random projects. **Xiliang**, you might be secretly Turkish, I say this due to the natural talent you have while using niche Turkish "expressions". Thank you **Endre** for being a really motivating gym buddy. **Lucas** and **Megha**, I really enjoy working with both of you in the Starshot project. **Lucas**, prepare your luggage, we're taking off for Proxima Centauri b soon. Feel free to bring your saxophone along as well, I am pretty sure aliens appreciate some good music (at least they did like it in the Mos Eisley cantina).

Thanks to **Abdullah** and **Gürhan** for giving me the opportunity to complain about my research a bit in my native tongue every day, before they left their place to **Hande**, **Hava** and **Tufan**. Best of luck to both of you in your new jobs.

Damla, isn't it remarkable how life works? Imagine taking a random selfie with a stranger ten years ago, only to meet again on the other side of the world. Thank you for the coffee breaks that provided a much needed change of scenery from my office (I didn't usually go to Coffee Star), where I could momentarily set aside my research worries and listen about your work on climate change and 'decision making under deep uncertainty', a concept that sounded like our PhD journeys. I truly beelieve (not a typo) that your research tackling climate change is not only admirable but also a reflection of your kind soul and unique perspective on life, which I have learned a lot from. And of course I have to mention your beautiful **Şimşek**, the cutest and most vicious (when she smelled some good food) dog in Delft. Or should I have said Dr. Şimşek (MD), because whenever someone felt bad, she would immediately understand. Her treatment was to jump on top of people and sit for hours until she makes sure that they got all the good "energies" (and I must say it was probably ten times more effective than the Dutch treatment system based on paracetamol).

Thank you all once again (and all the ones I forgot to include) for the nice discussions that made my days much better.

Next I would like to mention my master's students, **Ties**, **Tim** and **Bart**.

Ties, you definitely were an exceptional student with ultimate autonomy. Your topic, frequency stability of graphene resonators, was quite a challenge due to the sensitivities of the atomically thin membranes. Somehow you basically covered all the possible grounds with your efforts in experiments, theory and simulations. The way you worked was extremely careful, structured and systematical. The results you have obtained were very interesting and suggested very promising research directions. You really were displaying signs of an independent researcher (according to Just Herder, the sole purpose of doing a PhD is to become an independent researcher) already at the master's level.

Tim, you have covered a topic which was so dear to my heart. The FPUT paradox. It was my dream to show it in nanomechanical systems, and you did an excellent job on creating the framework to analyze nonlinear dynamics of nanomechanical strings, which is a system that very much resembles the original FPUT system. Even though most probably you were going through the hardest times of your life due to special reasons, you have almost never skipped a meeting and kept making progress and ended up delivering an exceptional thesis. I have rarely witnessed such dedication and discipline.

Bart, you took on a tough experimental challenge, at the crossroads of Tim and Ties's work, where you had to explore energy transfer mechanisms (which can be quite exotic) during nonlinear oscillations in nanoresonators, experimentally. Even though the road is tough, you never gave up and kept going. I am sure you are going to make it very soon to the finish line.

Even though I was your supervisor, you guys taught me a lot. I hope I was able to teach you something as well. I wish you all great success in life.

Next, I would like to mention the people who make our applied research possible, our all-mighty technicians, **Patrick**, **Rob**, **Spiridon**, **Bradley** and **Gideon**. I thank you for your support across my journey, from my master's project to my PhD project, and even now my postdoc project.

Next, I would like to thank all the PME staff, especially **Eveline**, **Marli** and **Marianne**. **Eveline**, I will never forget your help and support, especially during my master's studies. You always were on the students' side, being an exceptional problem solver (instead of a problem maker, which I think is the more common practice). Please never stop singing and keep shocking all the new students that will join PME with your beautiful voice. **Marli** and **Marianne** thanks for helping us, the ENIGMA team, virtually with any office related issue we have encountered.

Next, I would like to thank acknowledge couple of scientists outside the DMN group that provided guidance along the path. **Ori**, thank you very much for your guidance and discussions on nonlinear dynamics. My first paper wouldn't be possible without you. While writing our first paper, the things I learned from your expertise on nonlinear dynamics also aided me a lot in my later works. **Alejandro**, I really appreciate all the advice and help that you provided without hesitation whenever we had an FEM or mechanics related question. I also would like to thank **Prof. Mehmet Ali Alpar** (whose lectures deepened my passion for physics during my bachelor's studies) for pointing me to a dictionary that **Prof. Bülent Sankur** initiated (https://www.terimler.org), where I could find the Turkish translations of many field specific technical terms, which greatly assisted me in writing the Turkish summary at the start of this thesis. While initially attempting to write the summary in Turkish, I felt quite embarrassed when I struggled to find the appropriate technical terms and I suspect that many of my peers would encounter similar difficulties in their own native languages. I am grateful for your efforts. And finally, I would like to thank **Prof. Marco Amabili** for emphasizing the importance of nonlinear damping to various scientific communities, with his famous words: "When nonlinear stiffness changes 5% people go crazy, but when nonlinear damping changes 50%, no one cares!?" (numbers are not exact, but you get the idea).

Next are the people that became my second family in the Netherlands.

Derin, we met during the very first days of my master's studies, which coincided with the start of your bachelor's in aerospace, at the orientation for international students. We immediately connected over shared hobbies and similar thought processes, including our somewhat crooked Stoic outlook on life, and from that day on, we were inseparable. We made it a point to share at least one meal together every weekend, exchanging stories from our week, and even now, we meet every weekend to play tennis. We've always motivated each other on to improve. Since our low points tend to be quite similar, we've become adept at noticing each other's patterns and became the voice of reason for one another. You always lifted my spirits and never allowed me to feel down. If I was ill, you would show up at my door with a collection of fruits, ginger, and medicine without me saying a single word. Starting a new life far away from our families and comfort of home was challenging for both of us, yet I always felt as though I had a brother by my side. I hope I was able to be the same for you. Thank you for your unwavering friendship and for being my paranymph.

Sarah, our paths crossed while we were both immersed in our master's projects, working in the same office. It was over lunch breaks, through mutual venting about the trials of work and life, that our bond deepened. It seems adversity has a way of drawing people together. You possess a brilliance and kindness that surpasses even your own awareness. Each time we talk, I eagerly share my stupid ideas and stories with you, knowing you will always smack some sense in me. Thanks for forcing me to go out of my "cave" while I was "rotting" at home during the weekends. Thanks for taking me to concerts that I would never go by myself, all of which I enjoyed a lot. Thanks for always cheering me up and motivating me and letting me believe that I can always do better (even while bouldering, but maybe you can skip that from now on because I keep getting injured when you do that). I am deeply grateful for your friendship.

Savio, **Erdi** and **Arie**, even though I may be the worst friend, even though I keep missing your calls and am late to respond, you never let me fade away. We went through thick and thin together during our master's studies forming a strong friendship. Whenever we meet, it feels as if no time has passed since those days. I always cherish the memories of the adventures we had during our studies and travels around Europe. I am lucky to have you guys.

And finally I would like to acknowledge the people who supported me on every single step with their unconditional love, my dear family, my sister **Derya**, my mother **Deniz** and my father **Atilla**, in Turkish.

Doktora maceramın son noktası olan tezimin son sözlerini canım aileme ayırdım.

Canım kardeşim, **Derya**. Sen henüz altı yaşlarındayken ben üniversiteye başladım. Önce İstanbul'da köprünün diğer tarafına geçtim, sonrasında kendimi Avrupa'nın diğer ucunda buldum. Hayatta anlam bulduğum şeyi yapmak için çıktığım bu yolculuk hayatımın en değerlileriyle aramıza mesafeler soktu. Ama ne kadar uzakta olsam da, ne olursa olsun bil ki her şeye karşı, her adımında hep yanında olacağım. Olduğun dürüst, iyi kalpli ve akıllı insan ile gurur duyuyorum. İyi ki kardeşimsin, seni çok seviyorum.

Canım annem ve babam, **Deniz** ve **Atilla**. Küçüklüğümden beri beni etrafımdaki dünyadan korkutmak yerine onu sevmeye, incelemeye ve anlamaya teşvik ettiniz. İkinizin de doğaya olan sevgisi, saygısı ve ilgisi benim içimde de doğaya karşı büyük bir sevgi ve ilgi uyandırdı. Bana küçük yaştan bilimin önemini aşıladınız. İstekli ve tutkulu olduğumu gördüğünüz her şeyin peşinden gitmeme izin verdiniz, bana hep destek oldunuz. Ve yine sizin fedakarlıklarınız ve emekleriniz sayesinde hiç bir kaygı duymadan hayatımı sevdiğim şeye, bilime adayabildim. Karşılıksız sevginiz ve desteğiniz olmasaydı buralara gelebilir miydim bilmiyorum, kendimi çok şanslı hissediyorum. Hayatımda zorlandığım anlarda iki tümce yankılanır hep zihnimde, ve endişelerimin hepsi yok olur. Biri babamın "ne yaparsan yap, ne olursa olsun arkandayım", diğeri ise annemin "ne başardığın ya da başaramadığın önemli değil, sen önemlisin, ve sonuç ne olursa olsun seni seviyoruz" sözü. İyi ki ailemsiniz, sizleri çok seviyorum.

BIBLIOGRAPHY

[1] P. Simon and M. D. Laplace, *A Philosophical Essay on Probabilities* (Dover Books on Mathematics Ser.). Jan. 1996, ISBN: 978-0-486-28875-8. DOI: `10.1604/9780486288758`.

[2] S. H. Strogatz, *Nonlinear Dynamics and Chaos: With Applications to Physics, Biology, Chemistry, and Engineering, Second Edition.* CRC Press, Mar. 2015, ISBN: 978-0-8133-4910-7.

[3] S. H. Strogatz, *Sync: The Emerging Science of Spontaneous Order.* Mar. 2003, ISBN: 978-0-7868-6844-5. DOI: `10.1604/9780786868445`.

[4] J. Zhu, X. Liu, Q. Shi, *et al.*, “Development trends and perspectives of future sensors and mems/nems”, *Micromachines*, vol. 11, no. 1, p. 7, Dec. 2019, ISSN: 2072-666X. DOI: `10.3390/mi11010007`. [Online]. Available: `http://dx.doi.org/10.3390/mi11010007`.

[5] L. Wei, X. Kuai, Y. Bao, *et al.*, “The recent progress of mems/nems resonators”, *Micromachines*, vol. 12, no. 6, p. 724, Jun. 2021, ISSN: 2072-666X. DOI: `10.3390/mi12060724`. [Online]. Available: `http://dx.doi.org/10.3390/mi12060724`.

[6] K. S. Novoselov, A. K. Geim, S. V. Morozov, *et al.*, “Electric field effect in atomically thin carbon films”, *Science*, vol. 306, no. 5696, pp. 666–669, Oct. 2004, ISSN: 0036-8075. DOI: `10.1126/science.1102896`. eprint: `http://science.sciencemag.org/content/306/5696/666.full.pdf`. [Online]. Available: `http://dx.doi.org/10.1126/science.1102896`.

[7] A. K. Geim and K. S. Novoselov, “The rise of graphene - nature materials”, *Nature*, vol. 6, no. 3, pp. 183–191, Mar. 2007. DOI: `10.1038/nmat1849`. [Online]. Available: `https://www.nature.com/articles/nmat1849`.

[8] K. Cao, S. Feng, Y. Han, *et al.*, “Elastic straining of free-standing monolayer graphene”, *Nature Communications*, vol. 11, no. 1, p. 284, Jan. 2020, ISSN: 2041-1723. DOI: `10.1038/s41467-019-14130-0`. [Online]. Available: `https://doi.org/10.1038/s41467-019-14130-0`.

[9] D. H. Shin, H. Kim, S. H. Kim, *et al.*, “Graphene nano-electromechanical mass sensor with high resolution at room temperature”, *iScience*, vol. 26, no. 2, p. 105 958, 2023, ISSN: 2589-0042. DOI: `https://doi.org/10.1016/j.isci.2023.105958`. [Online]. Available: `https://www.sciencedirect.com/science/article/pii/S2589004223000354`.

[10] I. E. Rosłoń, A. Japaridze, P. G. Steeneken, C. Dekker, and F. Alijani, “Probing nanomotion of single bacteria with graphene drums”, *Nat. Nanotechnol.*, vol. 17, no. 6, pp. 637–642, Apr. 2022. DOI: `10.1038/s41565-022-01111-6`.

[11] A. D. Smith, F. Niklaus, A. Paussa, *et al.*, “Piezoresistive properties of suspended graphene membranes under uniaxial and biaxial strain in nanoelectromechanical pressure sensors”, *ACS Nano*, vol. 10, no. 11, pp. 9879–9886, Nov. 2016. DOI: `10.1021/acsnano.6b02533`.

[12] S.-E. Zhu, M. K. Ghatkesar, C. Zhang, and G. C. A. M. Janssen, “Graphene based piezoresistive pressure sensor”, *Appl. Phys. Lett.*, vol. 102, no. 16, p. 161 904, Apr. 2013. DOI: `10.1063/1.4802799`.

[13] R. N. Patel, J. P. Mathew, A. Borah, and M. M. Deshmukh, “Low tension graphene drums for electromechanical pressure sensing”, *2D Mater.*, vol. 3, no. 1, p. 011 003, Jan. 2016. DOI: `10.1088/2053-1583/3/1/011003`.

[14] Y.-M. Chen, S.-M. He, C.-H. Huang, *et al.*, “Ultra-large suspended graphene as a highly elastic membrane for capacitive pressure sensors”, *Nanoscale*, vol. 8, no. 6, pp. 3555–3564, 2016. DOI: `10.1039/c5nr08668j`.

[15] M. Šiškins, M. Lee, D. Wehenkel, *et al.*, “Sensitive capacitive pressure sensors based on graphene membrane arrays”, *Microsyst. Nanoeng.*, vol. 6, no. 1, p. 102, Nov. 2020, ISSN: 2055-7434. DOI: `10.1038/s41378-020-00212-3`. [Online]. Available: `https://doi.org/10.1038/s41378-020-00212-3`.

[16] R. J. Dolleman, D. Davidovikj, S. J. Cartamil-Bueno, H. S. J. van der Zant, and P. G. Steeneken, “Graphene squeeze-film pressure sensors”, *Nano Lett.*, vol. 16, no. 1, pp. 568–571, Dec. 2015, ISSN: 1530-6984. DOI: `10.1021/acs.nanolett.5b04251`. [Online]. Available: `https://doi.org/10.1021/acs.nanolett.5b04251`.

[17] X. Fan, F. Forsberg, A. D. Smith, *et al.*, “Graphene ribbons with suspended masses as transducers in ultra-small nanoelectromechanical accelerometers”, *Nature Electronics*, vol. 2, no. 9, pp. 394–404, 2019.

[18] G.-H. Lee, D. K. Efetov, W. Jung, *et al.*, “Graphene-based josephson junction microwave bolometer”, *Nature*, vol. 586, no. 7827, pp. 42–46, 2020.

[19] J. S. Bunch, A. M. van der Zande, S. S. Verbridge, *et al.*, “Electromechanical resonators from graphene sheets”, *Science*, vol. 315, no. 5811, pp. 490–493, 2007, ISSN: 0036-8075. DOI: `10.1126/science.1136836`. eprint: `http://science.sciencemag.org/content/315/5811/490.full.pdf`.

[20] M. Takamura, H. Okamoto, K. Furukawa, H. Yamaguchi, and H. Hibino, “Energy dissipation in graphene mechanical resonators with and without free edges”, *Micromachines*, vol. 7, no. 9, 2016, ISSN: 2072-666X. DOI: `10.3390/mi7090158`. [Online]. Available: `https://www.mdpi.com/2072-666X/7/9/158`.

[21] R. A. Norte, J. P. Moura, and S. Gröblacher, “Mechanical resonators for quantum optomechanics experiments at room temperature”, *Phys. Rev. Lett.*, vol. 116, p. 147 202, 14 Apr. 2016. DOI: `10.1103/PhysRevLett.116.147202`. [Online]. Available: `https://link.aps.org/doi/10.1103/PhysRevLett.116.147202`.

[22] D. Davidovikj, F. Alijani, S. J. Cartamil-Bueno, H. S. Van Der Zant, M. Amabili, and P. G. Steeneken, “Nonlinear dynamic characterization of two-dimensional materials”, *Nature Communications*, vol. 8, no. 1, pp. 1–7, Dec. 2017, ISSN: 20411723. DOI: `10.1038/s41467-017-01351-4`. [Online]. Available: `www.nature.com/naturecommunications`.

[23] R. Lifshitz and M. C. Cross, “Nonlinear dynamics of nanomechanical and micromechanical resonators”, *Review of nonlinear dynamics and complexity*, vol. 1, pp. 1–52, 2008. DOI: `https://doi.org/10.1002/9783527626359.ch1`.

[24] T. Manzaneque, M. K. Ghatkesar, F. Alijani, M. Xu, R. A. Norte, and P. G. Steeneken, “Resolution limits of resonant sensors”, *Phys. Rev. Appl.*, vol. 19, p. 054 074, 5 May 2023. DOI: `10.1103/PhysRevApplied.19.054074`. [Online]. Available: `https://link.aps.org/doi/10.1103/PhysRevApplied.19.054074`.

[25] S. Rosenberg and O. Shoshani, “Zero-dispersion point in curved micro-mechanical beams”, *Nonlinear Dynamics*, vol. 107, no. 1, pp. 1–14, Jan. 2022, ISSN: 1573-269X. DOI: `10.1007/s11071-021-07015-9`. [Online]. Available: `https://doi.org/10.1007/s11071-021-07015-9`.

[26] A. Eichler, J. Moser, J. Chaste, M. Zdrojek, I. Wilson-Rae, and A. Bachtold, “Nonlinear damping in mechanical resonators made from carbon nanotubes and graphene”, *Nature Nanotechnology*, vol. 6, no. 6, pp. 339–342, May 2011, ISSN: 1748-3395. DOI: `10.1038/nnano.2011.71`. [Online]. Available: `https://doi.org/10.1038/nnano.2011.71`.

[27] S. Zaitsev, O. Shtempluck, E. Buks, and O. Gottlieb, “Nonlinear damping in a micromechanical oscillator”, *Nonlinear Dynamics*, vol. 67, no. 1, pp. 859–883, 2012.

[28] M. Amabili, “Derivation of nonlinear damping from viscoelasticity in case of nonlinear vibrations”, *Nonlinear Dynamics*, vol. 97, no. 3, pp. 1785–1797, 2019.

[29] L. Catalini, M. Rossi, E. C. Langman, and A. Schliesser, “Modeling and observation of nonlinear damping in dissipation-diluted nanomechanical resonators”, *Phys. Rev. Lett.*, vol. 126, no. 17, p. 174 101, 17 Apr. 2021. DOI: `10.1103/physrevlett.126.174101`. [Online]. Available: `https://link.aps.org/doi/10.1103/PhysRevLett.126.174101`.

[30] A. Croy, D. Midtvedt, A. Isacsson, and J. M. Kinaret, “Nonlinear damping in graphene resonators”, *Phys. Rev. B*, vol. 86, p. 235 435, 23 Dec. 2012.

[31] J. Atalaya, T. W. Kenny, M. Roukes, and M. Dykman, “Nonlinear damping and dephasing in nanomechanical systems”, *Physical Review B*, vol. 94, no. 19, p. 195 440, 2016.

[32] J. Güttinger, A. Noury, P. Weber, *et al.*, “Energy-dependent path of dissipation in nanomechanical resonators”, *Nat. Nanotech.*, vol. 12, no. 7, pp. 631–636, Jul. 2017, ISSN: 17483395. DOI: `10.1038/nnano.2017.86`. [Online]. Available: `www.nature.com/naturenanotechnology`.

[33] E. Fermi, P. Pasta, S. Ulam, and M. Tsingou, *Studies of the nonlinear problems*, May 1955. DOI: `10.2172/4376203`. [Online]. Available: `https://www.osti.gov/biblio/4376203`.

[34] D. Midtvedt, A. Croy, A. Isacsson, Z. Qi, and H. S. Park, “Fermi-pasta-ulam physics with nanomechanical graphene resonators: Intrinsic relaxation and thermalization from flexural mode coupling”, *Phys. Rev. Lett.*, vol. 112, p. 145 503, 14 Apr. 2014. DOI: `10.1103/PhysRevLett.112.145503`. [Online]. Available: `https://link.aps.org/doi/10.1103/PhysRevLett.112.145503`.

[35] M. Amabili, P. Balasubramanian, I. Bozzo, *et al.*, “Nonlinear dynamics of human aortas for material characterization”, *Physical Review X*, vol. 10, no. 1, p. 011 015, 2020.

[36] B. Divinskiy, S. Urazhdin, S. O. Demokritov, and V. E. Demidov, “Controlled nonlinear magnetic damping in spin-hall nano-devices”, *Nature Communications*, vol. 10, no. 1, p. 5211, Nov. 2019, ISSN: 2041-1723. DOI: `10.1038/s41467-019-13246-7`.

[37] Z. Leghtas, S. Touzard, I. M. Pop, *et al.*, “Confining the state of light to a quantum manifold by engineered two-photon loss”, *Science*, vol. 347, no. 6224, pp. 853–857, 2015.

[38] X. Dong, M. I. Dykman, and H. B. Chan, “Strong negative nonlinear friction from induced two-phonon processes in vibrational systems”, *Nature Communications*, vol. 9, no. 1, p. 3241, Aug. 2018, ISSN: 2041-1723. DOI: `10.1038/s41467-018-05246-w`.

[39] X. Song, M. Oksanen, M. A. Sillanpää, H. Craighead, J. Parpia, and P. J. Hakonen, “Stamp transferred suspended graphene mechanical resonators for radio frequency electrical readout”, *Nano letters*, vol. 12, no. 1, pp. 198–202, 2012.

[40] B. Sajadi, F. Alijani, D. Davidovikj, J. Goosen, P. G. Steeneken, and F. van Keulen, “Experimental characterization of graphene by electrostatic resonance frequency tuning”, *Journal of Applied Physics*, vol. 122, no. 23, p. 234 302, 2017.

[41] M. Lee, D. Davidovikj, B. Sajadi, *et al.*, “Sealing graphene nanodrums”, *Nano letters*, vol. 19, no. 8, pp. 5313–5318, 2019.

[42] J. M. L. Miller, A. Ansari, D. B. Heinz, *et al.*, “Effective quality factor tuning mechanisms in micromechanical resonators”, *Applied Physics Reviews*, vol. 5, no. 4, p. 041 307, 2018.

[43] P. Weber, J. Guttinger, I. Tsioutsios, D. E. Chang, and A. Bachtold, “Coupling graphene mechanical resonators to superconducting microwave cavities”, *Nano letters*, vol. 14, no. 5, pp. 2854–2860, 2014.

[44] C. Samanta, N. Arora, and A. K. Naik, “Tuning of geometric nonlinearity in ultrathin nanoelectromechanical systems”, *Applied Physics Letters*, vol. 113, no. 11, p. 113 101, 2018. DOI: `10.1063/1.5026775`. eprint: `https://doi.org/10.1063/1.5026775`. [Online]. Available: `https://doi.org/10.1063/1.5026775`.

[45] F. Yang, F. Rochau, J. S. Huber, *et al.*, “Persistent response and nonlinear coupling of flexural modes in ultra-strongly driven membrane resonators”, *arXiv preprint at https://arxiv.org/abs/2003.14207*, 2020.

[46] A. H. Nayfeh and D. T. Mook, *Nonlinear Oscillations* (Wiley Classics Library). Wiley-VCH, Mar. 1995, vol. 57, ISBN: 978-0-471-12142-8. DOI: `10.1604/9780471121428`.

[47] H. J. R. Westra, M. Poot, H. S. J. van der Zant, and W. J. Venstra, "Nonlinear modal interactions in clamped-clamped mechanical resonators", *Phys. Rev. Lett.*, vol. 105, p. 117 205, 11 Sep. 2010.

[48] C. Van der Avoort, R. Van der Hout, J. Bontemps, *et al.*, "Amplitude saturation of mems resonators explained by autoparametric resonance", *Journal of Micromechanics and Microengineering*, vol. 20, no. 10, p. 105 012, 2010.

[49] D. Antonio, D. H. Zanette, and D. López, "Frequency stabilization in nonlinear micromechanical oscillators", *Nature communications*, vol. 3, no. 1, pp. 1–6, 2012.

[50] A. Eichler, M. del Álamo Ruiz, J. A. Plaza, and A. Bachtold, "Strong coupling between mechanical modes in a nanotube resonator", *Phys. Rev. Lett.*, vol. 109, p. 025 503, 2 Jul. 2012. DOI: `10.1103/PhysRevLett.109.025503`. [Online]. Available: `https://link.aps.org/doi/10.1103/PhysRevLett.109.025503`.

[51] C. Chen, D. H. Zanette, D. A. Czaplewski, S. Shaw, and D. López, "Direct observation of coherent energy transfer in nonlinear micromechanical oscillators", *Nature Communications*, vol. 8, no. 1, p. 15 523, May 2017, ISSN: 2041-1723. DOI: `10.1038/ncomms15523`. [Online]. Available: `https://doi.org/10.1038/ncomms15523`.

[52] O. Shoshani, S. W. Shaw, and M. I. Dykman, "Anomalous decay of nanomechanical modes going through nonlinear resonance", *Scientific reports*, vol. 7, no. 1, pp. 1–8, 2017.

[53] D. A. Czaplewski, C. Chen, D. Lopez, *et al.*, "Bifurcation generated mechanical frequency comb", *Phys. Rev. Lett.*, vol. 121, p. 244 302, 24 Dec. 2018. DOI: `10.1103/PhysRevLett.121.244302`. [Online]. Available: `https://link.aps.org/doi/10.1103/PhysRevLett.121.244302`.

[54] D. A. Czaplewski, S. Strachan, O. Shoshani, S. W. Shaw, and D. López, "Bifurcation diagram and dynamic response of a mems resonator with a 1: 3 internal resonance", *Applied Physics Letters*, vol. 114, no. 25, p. 254 104, 2019.

[55] F. Yang, F. Rochau, J. S. Huber, *et al.*, "Spatial modulation of nonlinear flexural vibrations of membrane resonators", *Physical review letters*, vol. 122, no. 15, p. 154 301, 2019.

[56] S. Houri, D. Hatanaka, M. Asano, and H. Yamaguchi, "Demonstration of multiple internal resonances in a microelectromechanical self-sustained oscillator", *Phys. Rev. Applied*, vol. 13, p. 014 049, 1 Jan. 2020.

[57] H. J. R. Westra, D. M. Karabacak, S. H. Brongersma, M. Crego-Calama, H. S. J. van der Zant, and W. J. Venstra, "Interactions between directly- and parametrically-driven vibration modes in a micromechanical resonator", *Phys. Rev. B*, vol. 84, p. 134 305, 13 Oct. 2011.

[58] M. Dykman and M. Krivoglaz, "Spectral distribution of nonlinear oscillators with nonlinear friction due to a medium", *physica status solidi (b)*, vol. 68, no. 1, pp. 111–123, 1975.

[59] R. J. Dolleman, S. Houri, A. Chandrashekar, F. Alijani, H. S. Van Der Zant, and P. G. Steeneken, "Opto-thermally excited multimode parametric resonance in graphene membranes", *Scientific reports*, vol. 8, no. 1, pp. 1–7, 2018.

[60] R. J. Dolleman, D. Davidovikj, H. S. J. van der Zant, and P. G. Steeneken, "Amplitude calibration of 2d mechanical resonators by nonlinear optical transduction", *Applied Physics Letters*, vol. 111, no. 25, p. 253 104, 2017.

[61] M. Amabili, *Nonlinear Vibrations and Stability of Shells and Plates*. Cambridge University Press, Jan. 2010, ISBN: 978-0-511-61969-4. DOI: `http://dx.doi.org/10.1017/CBO9780511619694`.

[62] J. Guckenheimer and P. Holmes, *Nonlinear Oscillations, Dynamical Systems, and Bifurcations of Vector Fields* (Applied Mathematical Sciences). Springer New York, 2013, ISBN: 9781461270201.

[63] J. Chaste, A. Eichler, J. Moser, G. Ceballos, R. Rurali, and A. Bachtold, "A nanomechanical mass sensor with yoctogram resolution", *Nature Nanotechnology*, vol. 7, no. 5, pp. 301–304, May 2012, ISSN: 1748-3395. DOI: `10.1038/nnano.2012.42`. [Online]. Available: `https://doi.org/10.1038/nnano.2012.42`.

[64] F. Fogliano, B. Besga, A. Reigue, *et al.*, "Ultrasensitive nano-optomechanical force sensor operated at dilution temperatures", *Nature Communications*, vol. 12, no. 1, p. 4124, Jul. 2021, ISSN: 2041-1723. DOI: `10.1038/s41467-021-24318-y`. [Online]. Available: `https://doi.org/10.1038/s41467-021-24318-y`.

[65] A. Bachtold, J. Moser, and M. Dykman, "Mesoscopic physics of nanomechanical systems", *Rev. Mod. Phys.*, vol. 94, no. 4, Dec. 2022. DOI: `10.1103/revmodphys.94.045005`.

[66] P. G. Steeneken, R. J. Dolleman, D. Davidovikj, F. Alijani, and H. S. J. van der Zant, "Dynamics of 2D material membranes", *2D Mater.*, vol. 8, no. 4, p. 042 001, Aug. 2021, ISSN: 2053-1583. DOI: `10.1088/2053-1583/ac152c`. [Online]. Available: `https://doi.org/10.1088/2053-1583/ac152c`.

[67] A. Keşkekler, O. Shoshani, M. Lee, H. S. J. van der Zant, P. G. Steeneken, and F. Alijani, "Tuning nonlinear damping in graphene nanoresonators by parametric–direct internal resonance", *Nat. Commun.*, vol. 12, no. 1, p. 1099, Feb. 2021, ISSN: 2041-1723. DOI: `10.1038/s41467-021-21334-w`. [Online]. Available: `https://doi.org/10.1038/s41467-021-21334-w`.

[68] M. Wang, D. J. Perez-Morelo, D. Lopez, and V. A. Aksyuk, "Persistent nonlinear phase-locking and nonmonotonic energy dissipation in micromechanical resonators", *Phys. Rev. X*, vol. 12, p. 041 025, 4 Dec. 2022. DOI: `10.1103/PhysRevX.12.041025`. [Online]. Available: `https://link.aps.org/doi/10.1103/PhysRevX.12.041025`.

[69] A. Keşkekler, H. Arjmandi-Tash, P. G. Steeneken, and F. Alijani, "Symmetry-breaking-induced frequency combs in graphene resonators", *Nano Letters*, vol. 22, no. 15, pp. 6048–6054, Aug. 2022, ISSN: 1530-6984. DOI: `10.1021/acs.nanolett.2c00360`. [Online]. Available: `https://doi.org/10.1021/acs.nanolett.2c00360`.

[70] J. S. Ochs, G. Rastelli, M. Seitner, M. I. Dykman, and E. M. Weig, “Resonant nonlinear response of a nanomechanical system with broken symmetry”, *Phys. Rev. B*, vol. 104, p. 155 434, 15 Oct. 2021. DOI: 10.1103/PhysRevB.104.155434. [Online]. Available: https://link.aps.org/doi/10.1103/PhysRevB.104.155434.

[71] B. Sajadi, S. Wahls, S. van Hemert, P. Belardinelli, P. G. Steeneken, and F. Alijani, “Nonlinear dynamic identification of graphene’s elastic modulus via reduced order modeling of atomistic simulations”, *Journal of the Mechanics and Physics of Solids*, vol. 122, pp. 161–176, 2019, ISSN: 0022-5096. DOI: https://doi.org/10.1016/j.jmps.2018.09.013. [Online]. Available: https://www.sciencedirect.com/science/article/pii/S0022509618305180.

[72] A. A. Muravyov and S. A. Rizzi, “Determination of nonlinear stiffness with application to random vibration of geometrically nonlinear structures”, *Computers & Structures*, vol. 81, no. 15, pp. 1513–1523, 2003, ISSN: 0045-7949. DOI: https://doi.org/10.1016/S0045-7949(03)00145-7. [Online]. Available: http://www.sciencedirect.com/science/article/pii/S0045794903001457.

[73] B. Sajadi, S. van Hemert, B. Arash, P. Belardinelli, P. G. Steeneken, and F. Alijani, “Size- and temperature-dependent bending rigidity of graphene using modal analysis”, *Carbon*, vol. 139, pp. 334–341, 2018, ISSN: 0008-6223. DOI: https://doi.org/10.1016/j.carbon.2018.06.066. [Online]. Available: https://www.sciencedirect.com/science/article/pii/S0008622318306328.

[74] A. Castellanos-Gomez, V. Singh, H. S. J. van der Zant, and G. A. Steele, “Mechanics of freely-suspended ultrathin layered materials”, *Annalen der Physik*, vol. 527, no. 1-2, pp. 27–44, 2015. DOI: https://doi.org/10.1002/andp.201400153. eprint: https://onlinelibrary.wiley.com/doi/pdf/10.1002/andp.201400153.

[75] A. Isacsson, A. W. Cummings, L. Colombo, L. Colombo, J. M. Kinaret, and S. Roche, “Scaling properties of polycrystalline graphene: A review”, *2D Materials*, vol. 4, no. 1, p. 012 002, Dec. 2016. DOI: 10.1088/2053-1583/aa5147. [Online]. Available: https://dx.doi.org/10.1088/2053-1583/aa5147.

[76] A. Sarafraz, A. Givois, I. Roslon, *et al.*, “Dynamics of pressurized ultra-thin membranes”, *arXiv.org*, Dec. 2022. DOI: 10.48550/arXiv.2212.05464. [Online]. Available: https://arxiv.org/abs/2212.05464v2.

[77] M. P. Mignolet, A. Przekop, S. A. Rizzi, and S. M. Spottswood, “A review of indirect/non-intrusive reduced order modeling of nonlinear geometric structures”, *Journal of Sound and Vibration*, vol. 332, no. 10, pp. 2437–2460, 2013, ISSN: 0022-460X. DOI: https://doi.org/10.1016/j.jsv.2012.10.017. [Online]. Available: https://www.sciencedirect.com/science/article/pii/S0022460X12008188.

[78] E. J. Doedel, A. R. Champneys, F. Dercole, *et al.*, “Auto-07p: Continuation and bifurcation software for ordinary differential equations”, 2007.

[79] G. Gobat, V. Zega, P. Fedeli, C. Touzé, and A. Frangi, “Frequency combs in a mems resonator featuring 1:2 internal resonance: Ab initio reduced order modelling and experimental validation”, *Nonlinear Dynamics*, vol. 111, no. 4, pp. 2991–3017, Feb. 2023, ISSN: 1573-269X. DOI: 10.1007/s11071-022-08029-7. [Online]. Available: https://doi.org/10.1007/s11071-022-08029-7.

[80] S. Dou, B. S. Strachan, S. W. Shaw, and J. S. Jensen, “Structural optimization for nonlinear dynamic response”, *Philosophical Transactions of the Royal Society A: Mathematical, Physical and Engineering Sciences*, vol. 373, no. 2051, p. 20 140 408, 2015. DOI: 10.1098/rsta.2014.0408. eprint: https://royalsocietypublishing.org/doi/pdf/10.1098/rsta.2014.0408. [Online]. Available: https://royalsocietypublishing.org/doi/abs/10.1098/rsta.2014.0408.

[81] L. L. Li, P. M. Polunin, S. Dou, *et al.*, “Tailoring the nonlinear response of mems resonators using shape optimization”, *Applied Physics Letters*, vol. 110, no. 8, p. 081 902, 2017. DOI: 10.1063/1.4976749. eprint: https://doi.org/10.1063/1.4976749. [Online]. Available: https://doi.org/10.1063/1.4976749.

[82] C. Chen, S. Rosenblatt, K. I. Bolotin, *et al.*, “Performance of monolayer graphene nanomechanical resonators with electrical readout”, *Nat. Nanotechnol.*, vol. 4, no. 12, pp. 861–867, Sep. 2009. DOI: 10.1038/nnano.2009.267.

[83] V. Singh, S. Sengupta, H. S. Solanki, *et al.*, “Probing thermal expansion of graphene and modal dispersion at low-temperature using graphene nanoelectromechanical systems resonators”, *Nanotechnology*, vol. 21, no. 16, p. 165 204, Mar. 2010, ISSN: 1361-6528. DOI: 10.1088/0957-4484/21/16/165204. [Online]. Available: http://www.ncbi.nlm.nih.gov/pubmed/20351404.

[84] X. Zhang, K. Makles, L. Colombier, *et al.*, “Dynamically-enhanced strain in atomically thin resonators”, *Nat. Commun.*, vol. 11, no. 1, p. 5526, Nov. 2020. DOI: 10.1038/s41467-020-19261-3.

[85] H. Arjmandi-Tash, A. Allain, Z. (Han, and V. Bouchiat, “Large scale integration of CVD-graphene based NEMS with narrow distribution of resonance parameters”, *2D Materials*, vol. 4, no. 2, p. 025 023, Feb. 2017. DOI: 10.1088/2053-1583/aa57c6. [Online]. Available: https://doi.org/10.1088/2053-1583/aa57c6.

[86] J. P. Mathew, R. N. Patel, A. Borah, R. Vijay, and M. M. Deshmukh, “Dynamical strong coupling and parametric amplification of mechanical modes of graphene drums”, *Nature nanotechnology*, vol. 11, no. 9, pp. 747–751, 2016.

[87] P. Prasad, N. Arora, and A. Naik, “Parametric amplification in mos 2 drum resonator”, *Nanoscale*, vol. 9, no. 46, pp. 18 299–18 304, 2017.

[88] A. M. Eriksson, D. Midtvedt, A. Croy, and A. Isacsson, “Frequency tuning, nonlinearities and mode coupling in circular mechanical graphene resonators”, *Nanotechnology*, vol. 24, no. 39, p. 395 702, Oct. 2013, ISSN: 13616528. DOI: 10.1088/0957-4484/24/39/395702. [Online]. Available: https://doi.org/10.1088/1361-6528/aa722e.

[89] R. J. Dolleman, P. Belardinelli, S. Houri, H. S. van der Zant, F. Alijani, and P. G. Steeneken, “High-frequency stochastic switching of graphene resonators near room temperature”, *Nano letters*, vol. 19, no. 2, pp. 1282–1288, 2019.

[90] C. Samanta, P. R. Yasasvi Gangavarapu, and A. K. Naik, “Nonlinear mode coupling and internal resonances in MoS2 nanoelectromechanical system”, *Applied Physics Letters*, vol. 107, no. 17, p. 173 110, Oct. 2015, ISSN: 00036951. DOI: 10.1063/1.4934708. [Online]. Available: http://dx.doi.org/10.1063/1.4934708%20http://aip.scitation.org/doi/10.1063/1.4934708.

[91] S. S. P. Nathamgari, S. Dong, L. Medina, *et al.*, “Nonlinear mode coupling and one-to-one internal resonances in a monolayer ws2 nanoresonator”, *Nano letters*, vol. 19, no. 6, pp. 4052–4059, 2019.

[92] M. Šiškins, E. Sokolovskaya, M. Lee, *et al.*, “Tunable strong coupling of mechanical resonance between spatially separated FePS$_3$ nanodrums”, *Nano Lett.*, vol. 22, no. 1, pp. 36–42, Dec. 2021, ISSN: 1530-6984. DOI: 10.1021/acs.nanolett.1c03010. [Online]. Available: https://doi.org/10.1021/acs.nanolett.1c03010.

[93] K. R. Qalandar, B. Strachan, B. Gibson, *et al.*, “Frequency division using a micromechanical resonance cascade”, *Applied Physics Letters*, vol. 105, no. 24, p. 244 103, 2014.

[94] J. Yu, H.-K. Kwon, G. D. Vukasin, T. W. Kenny, and H. Cho, “Frequency stabilization in an encapsulated high-q micromechanical resonator via internal resonance”, in *2020 IEEE 33rd International Conference on Micro Electro Mechanical Systems (MEMS)*, IEEE, 2020, pp. 1191–1194.

[95] A. Chandrashekar, P. Belardinelli, S. Lenci, U. Staufer, and F. Alijani, “Mode coupling in dynamic atomic force microscopy”, *Physical Review Applied*, vol. 15, no. 2, p. 024 013, 2021.

[96] R. Singh, A. Sarkar, C. Guria, *et al.*, “Giant Tunable Mechanical Nonlinearity in Graphene-Silicon Nitride Hybrid Resonator”, *Nano Letters*, vol. 20, no. 6, pp. 4659–4666, 2020, ISSN: 15306992. DOI: 10.1021/acs.nanolett.0c01586. arXiv: 1904.01613.

[97] D. Davidovikj, J. J. Slim, S. J. Cartamil-Bueno, H. S. J. van der Zant, P. G. Steeneken, and W. J. Venstra, “Visualizing the motion of graphene nanodrums”, *Nano Lett.*, vol. 16, no. 4, pp. 2768–2773, Mar. 2016, ISSN: 15306992. DOI: 10.1021/acs.nanolett.6b00477. arXiv: 1602.00135. [Online]. Available: https://pubs.acs.org/doi/abs/10.1021/acs.nanolett.6b00477.

[98] S. S. Rao, *Vibration of continuous systems.* John Wiley & Sons, 2019.

[99] A. Eichler, J. Moser, M. Dykman, and A. Bachtold, “Symmetry breaking in a mechanical resonator made from a carbon nanotube”, *Nature communications*, vol. 4, no. 1, pp. 1–7, 2013.

[100] A. H. Ramini, A. Z. Hajjaj, and M. I. Younis, “Tunable resonators for nonlinear modal interactions”, *Scientific reports*, vol. 6, no. 1, pp. 1–9, 2016.

[101] K. Asadi, J. Yeom, and H. Cho, “Strong internal resonance in a nonlinear, asymmetric microbeam resonator”, *Microsystems & Nanoengineering*, vol. 7, no. 1, pp. 1–15, 2021.

[102] G. Gobat, V. Zega, P. Fedeli, L. Guerinoni, C. Touzé, and A. Frangi, "Reduced order modelling and experimental validation of a mems gyroscope test-structure exhibiting 1:2 internal resonance", *Scientific Reports*, vol. 11, no. 1, p. 16 390, Aug. 2021, ISSN: 2045-2322. DOI: `10.1038/s41598-021-95793-y`. [Online]. Available: `https://doi.org/10.1038/s41598-021-95793-y`.

[103] A. H. Nayfeh and B. Balachandran, *Applied nonlinear dynamics: analytical, computational, and experimental methods*. John Wiley & Sons, 2008.

[104] A. Ganesan, C. Do, and A. Seshia, "Phononic frequency comb via intrinsic three-wave mixing", *Physical review letters*, vol. 118, no. 3, p. 033 903, 2017.

[105] A. Ganesan, C. Do, and A. Seshia, "Excitation of coupled phononic frequency combs via two-mode parametric three-wave mixing", *Physical Review B*, vol. 97, no. 1, p. 014 302, 2018.

[106] M. I. Dykman, G. Rastelli, M. L. Roukes, and E. M. Weig, "Resonantly induced friction and frequency combs in driven nanomechanical systems", *Physical review letters*, vol. 122, no. 25, p. 254 301, 2019.

[107] A. Sarrafan, S. Azimi, F. Golnaraghi, and B. Bahreyni, "A nonlinear rate microsensor utilising internal resonance", *Scientific Reports*, vol. 9, no. 1, p. 8648, Jun. 2019, ISSN: 2045-2322. DOI: `10.1038/s41598-019-44669-3`. [Online]. Available: `https://doi.org/10.1038/s41598-019-44669-3`.

[108] E. Hacker and O. Gottlieb, "Internal resonance based sensing in non-contact atomic force microscopy", *Applied Physics Letters*, vol. 101, no. 5, p. 053 106, 2012. DOI: `10.1063/1.4739416`. eprint: `https://doi.org/10.1063/1.4739416`. [Online]. Available: `https://doi.org/10.1063/1.4739416`.

[109] T. Miao, X. Zhou, X. Wu, *et al.*, "Nonlinearity-mediated digitization and amplification in electromechanical phonon-cavity systems", *Nature Communications*, vol. 13, no. 1, p. 2352, Apr. 2022, ISSN: 2041-1723. DOI: `10.1038/s41467-022-29995-x`. [Online]. Available: `https://doi.org/10.1038/s41467-022-29995-x`.

[110] A. Ganesan and A. Seshia, "Resonance tracking in a micromechanical device using phononic frequency combs", *Scientific Reports*, vol. 9, no. 1, p. 9452, Jul. 2019, ISSN: 2045-2322. DOI: `10.1038/s41598-019-46003-3`. [Online]. Available: `https://doi.org/10.1038/s41598-019-46003-3`.

[111] C. Androulidakis, K. Zhang, M. Robertson, and S. Tawfick, "Tailoring the mechanical properties of 2D materials and heterostructures", *2D Mater.*, vol. 5, no. 3, p. 032 005, Jun. 2018. DOI: `10.1088/2053-1583/aac764`.

[112] H. Jiang, L. Zheng, Z. Liu, and X. Wang, "Two-dimensional materials: From mechanical properties to flexible mechanical sensors", *InfoMat*, vol. 2, no. 6, pp. 1077–1094, Dec. 2019. DOI: `10.1002/inf2.12072`.

[113] M. C. Lemme, S. Wagner, K. Lee, *et al.*, "Nanoelectromechanical sensors based on suspended 2D materials", *Research*, vol. 2020, p. 8 748 602, Jul. 2020. DOI: `10.34133/2020/8748602`.

[114] J. N. Kirchhof, Y. Yu, G. Antheaume, *et al.*, “Nanomechanical spectroscopy of 2D materials”, *Nano Lett.*, vol. 22, no. 20, pp. 8037–8044, Oct. 2022. DOI: `10.1021/acs.nanolett.2c01289`.

[115] I. S. Arribas, T. Taniguchi, K. Watanabe, and E. M. Weig, “Radiation pressure backaction on a hexagonal boron nitride nanomechanical resonator”, 2023, Preprint at arXiv:2302.04291.

[116] R. De Alba, F. Massel, I. R. Storch, *et al.*, “Tunable phonon-cavity coupling in graphene membranes”, *Nat. Nanotech.*, vol. 11, no. 9, pp. 741–746, Jun. 2016, ISSN: 17483395. DOI: `10.1038/nnano.2016.86`. [Online]. Available: `www.nature.com/naturenanotechnology`.

[117] G. Luo, Z.-Z. Zhang, G.-W. Deng, *et al.*, “Strong indirect coupling between graphene-based mechanical resonators via a phonon cavity”, *Nat. Commun.*, vol. 9, p. 383, Jan. 2018. DOI: `10.1038/s41467-018-02854-4`.

[118] C. Chen, V. V. Deshpande, M. Koshino, *et al.*, “Modulation of mechanical resonance by chemical potential oscillation in graphene”, *Nat. Phys.*, vol. 12, no. 3, pp. 240–244, Dec. 2015. DOI: `10.1038/nphys3576`.

[119] S. Sengupta, H. S. Solanki, V. Singh, S. Dhara, and M. M. Deshmukh, “Electromechanical resonators as probes of the charge density wave transition at the nanoscale in $NbSe_2$”, *Phys. Rev. B*, vol. 82, no. 15, p. 155 432, Oct. 2010. DOI: `10.1103/physrevb.82.155432`.

[120] M. Lee, M. Šiškins, S. Mañas-Valero, E. Coronado, P. G. Steeneken, and H. S. J. van der Zant, “Study of charge density waves in suspended 2H-TaS_2 and 2H-$TaSe_2$ by nanomechanical resonance”, *Appl. Phys. Lett.*, vol. 118, no. 19, p. 193 105, May 2021. DOI: `10.1063/5.0051112`.

[121] M. Šiškins, M. Lee, S. Mañas-Valero, *et al.*, “Magnetic and electronic phase transitions probed by nanomechanical resonators”, *Nat. Commun.*, vol. 11, no. 1, p. 2698, Jun. 2020. DOI: `10.1038/s41467-020-16430-2`.

[122] S. Jiang, H. Xie, J. Shan, and K. F. Mak, “Exchange magnetostriction in two-dimensional antiferromagnets”, *Nat. Mater.*, vol. 19, no. 12, pp. 1295–1299, Jun. 2020. DOI: `10.1038/s41563-020-0712-x`.

[123] M. Šiškins, S. Kurdi, M. Lee, *et al.*, “Nanomechanical probing and strain tuning of the Curie temperature in suspended $Cr_2Ge_2Te_6$-based heterostructures”, *npj 2D Mater. Appl.*, vol. 6, p. 41, Jun. 2022. DOI: `10.1038/s41699-022-00315-7`.

[124] T. Zhang, H. Wang, X. Xia, *et al.*, “A monolithically sculpted van der waals nano-opto-electro-mechanical coupler”, *Light Sci. Appl.*, vol. 11, p. 48, Mar. 2022. DOI: `10.1038/s41377-022-00734-7`.

[125] J. López-Cabrelles, S. Mañas-Valero, I. J. Vitórica-Yrezábal, *et al.*, “Chemical design and magnetic ordering in thin layers of 2D metal–organic frameworks (MOFs)”, *J. Am. Chem. Soc.*, vol. 143, no. 44, pp. 18 502–18 510, Nov. 2021. DOI: `10.1021/jacs.1c07802`.

[126] X. Li, X. Sha, N. Yan, and T. Zhang, “Mechanical detection of magnetic phase transition in suspended CrOCl heterostructures”, *Magnetochemistry*, vol. 8, no. 12, p. 170, Nov. 2022. DOI: `10.3390/magnetochemistry8120170`.

[127] M. J. A. Houmes, G. Baglioni, M. Šiškins, *et al.*, “Magnetic order in 2D antiferromagnets revealed by spontaneous anisotropic magnetostriction”, 2023, Preprint at arXiv:2303.11234.

[128] J.-U. Lee, S. Lee, J. H. Ryoo, *et al.*, “Ising-type magnetic ordering in atomically thin $FePS_3$”, *Nano Lett.*, vol. 16, no. 12, pp. 7433–7438, Nov. 2016. DOI: `10.1021/acs.nanolett.6b03052`.

[129] F. Kargar, E. A. Coleman, S. Ghosh, *et al.*, “Phonon and thermal properties of quasi-two-dimensional $FePS_3$ and $MnPS_3$ antiferromagnetic semiconductors”, *ACS Nano*, vol. 14, no. 2, pp. 2424–2435, Jan. 2020. DOI: `10.1021/acsnano.9b09839`.

[130] X. Xu, L. F. C. Pereira, Y. Wang, *et al.*, “Length-dependent thermal conductivity in suspended single-layer graphene”, *Nat. Commun.*, vol. 5, no. 1, p. 3689, Apr. 2014. DOI: `10.1038/ncomms4689`.

[131] R. J. Dolleman, S. Houri, D. Davidovikj, *et al.*, “Optomechanics for thermal characterization of suspended graphene”, *Phys. Rev. B*, vol. 96, no. 16, p. 165 421, Oct. 2017. DOI: `10.1103/physrevb.96.165421`.

[132] S. Schmid, L. G. Villanueva, and M. L. Roukes, *Fundamentals of Nanomechanical Resonators*. Springer International Publishing, 2016. DOI: `10.1007/978-3-319-28691-4`.

[133] L. D. Landau, L. P. Pitaevskii, and E. M. Lifshitz, *Electrodynamics of continuous media*, 2nd ed. New York: Butterworth, 1984, vol. 8.

[134] L. D. Landau, “On the theory of phase transitions”, *Zh. Eksp. Teor. Fiz.*, vol. 7, pp. 19–32, 1937, [*Ukr. J. Phys.* **53**, 25 (2008)].

[135] L. D. Landau and I. M. Khalatnikov, “On the anomalous absorption of sound near a second order phase transition point”, *Dokl. Akad. Nauk SSSR*, vol. 96, p. 469, 1954.

[136] K. P. Belov, G. I. Katayev, and R. Z. Levitin, “Internal friction anomalies in ferromagnets and antiferromagnets near the Curie point”, *J. Appl. Phys.*, vol. 31, no. 5, S153–S156, May 1960. DOI: `10.1063/1.1984642`.

[137] K. P. Belov, G. I. Kataev, and R. Z. Levitin, “Anomalies in internal friction and modulus of elasticity in ferromagnetic near the Curie point”, *J. Exptl. Theoret. Phys. (U.S.S.R.)*, vol. 37, pp. 938–943, 1959.

[138] F. Zhou, K. Hwangbo, Q. Zhang, *et al.*, “Dynamical criticality of spin-shear coupling in van der Waals antiferromagnets”, *Nat. Commun.*, vol. 13, no. 1, Nov. 2022. DOI: `10.1038/s41467-022-34376-5`.

[139] P. Němec, M. Fiebig, T. Kampfrath, and A. V. Kimel, “Antiferromagnetic opto-spintronics”, *Nat. Phys.*, vol. 14, no. 3, pp. 229–241, Mar. 2018. DOI: `10.1038/s41567-018-0051-x`.

[140] D. Afanasiev, J. R. Hortensius, M. Matthiesen, *et al.*, “Controlling the anisotropy of a van der Waals antiferromagnet with light”, *Sci. Adv.*, vol. 7, no. 23, eabf3096, Jun. 2021. DOI: `10.1126/sciadv.abf3096`.

[141] D. Khusyainov, T. Gareev, V. Radovskaia, *et al.*, “Ultrafast laser-induced spin-lattice dynamics in the van der Waals antiferromagnet $CoPS_3$”, 2023, Preprint at arXiv:2302.12104.

[142] H. Warlimont and W. Martienssen, Eds., *Springer Handbook of Materials Data* (Springer Handbooks), 2nd ed. Cham, Switzerland: Springer International Publishing, Aug. 2018.

[143] G. Hausch, “Magnetic exchange energy contribution to the elastic constants and its relation to the anomalous elastic behaviour of invar alloys”, *Phys. Status Solidi A*, vol. 15, no. 2, pp. 501–510, Feb. 1973. DOI: `10.1002/pssa.2210150215`.

[144] G. Hausch, “Magnetovolume effects in invar alloys: Pressure dependence of the Curie temperature”, *Phys. Status Solidi A*, vol. 16, no. 2, pp. 371–376, Apr. 1973. DOI: `10.1002/pssa.2210160204`.

[145] E. Postolache, D. Powell, G. Popov, R. C. Rai, M. Greenblatt, and J. Brill, “Comparison of Young’s modulus and specific heat anomalies at the magnetic transition in α'-NaV_2O_5”, *Solid State Sci.*, vol. 2, no. 8, pp. 759–766, Dec. 2000. DOI: `10.1016/s1293-2558(00)01086-4`.

[146] G. Baglioni, M. Šiškins, M. J. A. Houmes, *et al.*, “Thermo-magnetostrictive effect for driving antiferromagnetic 2D material resonators”, *Nano Lett.*, Jul. 2023. DOI: `10.1021/acs.nanolett.3c01610`.

[147] R. A. Barton, I. R. Storch, V. P. Adiga, *et al.*, “Photothermal self-oscillation and laser cooling of graphene optomechanical systems”, *Nano Lett.*, vol. 12, no. 9, pp. 4681–4686, Aug. 2012. DOI: `10.1021/nl302036x`.

[148] A. Castellanos-Gomez, M. Buscema, R. Molenaar, *et al.*, “Deterministic transfer of two-dimensional materials by all-dry viscoelastic stamping”, *2D Mater.*, vol. 1, no. 1, p. 011 002, Apr. 2014. DOI: `10.1088/2053-1583/1/1/011002`.

[149] R. Lifshitz and M. L. Roukes, “Thermoelastic damping in micro- and nanomechanical systems”, *Phys. Rev. B*, vol. 61, no. 8, pp. 5600–5609, Feb. 2000. DOI: `10.1103/physrevb.61.5600`.

[150] Y. Sun and M. Saka, “Thermoelastic damping in micro-scale circular plate resonators”, *J. Sound Vib.*, vol. 329, no. 3, pp. 328–337, Feb. 2010. DOI: `10.1016/j.jsv.2009.09.014`.

[151] T. Verschuren, *Frequency stability of graphene nonlinear resonators.* TU Delft, Oct. 2020. [Online]. Available: `http://resolver.tudelft.nl/uuid:96b47031-ff15-4057-ab33-1ac4863119be`.

[152] A. W. Barnard, M. Zhang, G. S. Wiederhecker, M. Lipson, and P. L. McEuen, “Real-time vibrations of a carbon nanotube”, *Nature*, vol. 566, no. 7742, pp. 89–93, 2019.

[153] T. Jansen, *Mode coupling in nanomechanical string resonators: Towards Fermi-Pasta-Ulam-Tsingou mechanics.* TU Delft, Jul. 2021. [Online]. Available: `http://resolver.tudelft.nl/uuid:02016e06-fa3d-47c1-8417-bc9bc0080059`.

[154] M. Müller, R. Dolleman, A. Keşkekler, *et al.*, "Ballistic graphene for high q-factor mechanical resonators", *In preparation*,

[155] H. B. Chan, V. A. Aksyuk, R. N. Kleiman, D. J. Bishop, and F. Capasso, *Science*, vol. 291, no. 5510, pp. 1941–1944, Mar. 2001. DOI: `10.1126/science.1057984`. [Online]. Available: `http://dx.doi.org/10.1126/science.1057984`.

[156] A. Chandrashekar, P. Belardinelli, M. A. Bessa, U. Staufer, and F. Alijani, "Quantifying nanoscale forces using machine learning in dynamic atomic force microscopy", *Nanoscale Adv.*, vol. 4, pp. 2134–2143, 9 2022. DOI: `10.1039/D2NA00011C`. [Online]. Available: `http://dx.doi.org/10.1039/D2NA00011C`.

CURRICULUM VITÆ

Ata KEŞKEKLER

11-11-1994	Born in Istanbul, Türkiye.

2008–2012	High School Adile Mermerci Anadolu Lisesi, Istanbul, Türkiye
2012–2016	BSc in Mechatronics Engineering, Minor: Physics (High Honors) Sabanci University, Istanbul, Türkiye
2016–2018	MSc in Precision and Microsystems Engineering (Cum Laude) Delft University of Technology, Delft, the Netherlands
2018–2023	PhD in Mechanical Engineering Delft University of Technology, Delft, the Netherlands *Thesis:* Nonlinear coupling and dissipation in two-dimensional resonators *Promotors:* Prof. dr. P. G. Steeneken & Dr. Farbod Alijani
2023–Present	Postdoctoral Researcher Delft University of Technology, Delft, the Netherlands *Project:* Breakthrough Starshot: Development and validation of photonic crystal lightsails for laser propulsion in spacecraft applications *Supervision:* Dr. Richard Norte

LIST OF PUBLICATIONS

JOURNAL ARTICLES

7. M. Šiškins, **A. Keşkekler**, M. J. A. Houmes, S. Mañas-Valero, E. Coronado, Y. M. Blanter, H. S. J. van der Zant, P. G. Steeneken, F. Alijani, *Nonlinear dynamics and magneto-elasticity of nanodrums near the phase transition*, Under review, Preprint: arXiv:2309.09672.

6. M. Müller, R. J. Dolleman, **A. Keşkekler**, F. Alijani, L. Banszerus, N. Borchers, K. Watanabe, T. Taniguchi, J. Güttinger, C. Stampfer, *Ballistic graphene for high Q-factor mechanical resonators*, Manuscript under preparation.

5. **A. Keşkekler**, V. Bos, A. M. Aragón, P. G. Steeneken, F. Alijani, *Characterizing multi-mode nonlinear dynamics of nanomechanical resonators*, Under review, Preprint: arXiv:2304.01419.

4. **A. Keşkekler**, H. Arjmandi-Tash, P. G. Steeneken, F. Alijani, *Symmetry-breaking-induced frequency combs in graphene resonators*, Nano letters 22 (15), 6048-6054.

3. X. Chen, N. Kothari, **A. Keşkekler**, P. G. Steeneken, F. Alijani, *Diamagnetically levitating resonant weighing scale*, Sensors and Actuators A: Physical 330, 112842.

2. **A. Keşkekler**, O. Shoshani, M. Lee, H. S. J. van der Zant, P. G. Steeneken, F. Alijani, *Tuning nonlinear damping in graphene nanoresonators by parametric–direct internal resonance*, Nature communications 12 (1), 1099.

1. X. Chen, **A. Keşkekler**, F. Alijani, P. G. Steeneken, *Rigid body dynamics of diamagnetically levitating graphite resonators*, Applied Physics Letters 116 (24).

PATENTS

1. F. Alijani, P. G. Steeneken, N. Kothari, **A. Keşkekler**, *Sensor equipped with at least one magnet and a diamagnetic plate levitating above said at least one magnet and method to measure a parameter of an object using such a sensor*, WO2021006727A1.